DISSERTATION

submitted to the

Combined Faculty of Natural Sciences and Mathematics

of the Ruperto Carola University of Heidelberg, Germany

for the degree of

Doctor of Natural Sciences

presented by

M. Sc. (Molecular Biosciences) Natalie Garg

born in Karlsruhe, Germany

Oral examination: February 20th, 2020

Development of fully-human macrophage-modulatory antibodies for cancer immunotherapy

Referees:

Prof. Dr. Peter Angel

Prof. Dr. Juergen Krauss

Summary

Tumor-associated macrophages (TAMs) contribute to tumor progression and foster the immunosuppressive tumor microenvironment. Several immunotherapeutic approaches to target TAMs are being developed, including the blockade of monocyte recruitment to the tumor site in order to reduce the number of pro-tumorigenic TAMs. Chemokine (C-C motif) ligand 2 (CCL2) and semaphorin 3A (Sema3A) secreted by tumor cells have been found to play crucial roles in the attraction of monocytes via the respective receptors C-C chemokine receptor type 2 (CCR2) and neuropilin 1 (NRP1) expressed on monocytes.

In this project, we selected fully human CCL2- and NRP1-targeting antibody fragments by means of phage display and further characterized them in the immunoglobulin 1 (IgG1) format. We demonstrated antigen specificity by ELISA, surface plasmon resonance spectroscopy and flow cytometry. Since we could not show blocking of the NRP1 – Sema3A interaction by the NRP1-specifc antibodies, these antibodies were not developed further. In contrast, we observed blocking of the CCL2 – CCR2 interaction by flow cytometry and confirmed the blockade of intracellular CCR2-dependent signaling mediated by our lead candidate anti-CCL2 antibody. Moreover, we demonstrated reduced CCL2-dependent migration of monocytes in the presence of the CCL2-specific antibody.

In addition, since recent reports showed that systemic administration of anti-CCL2 antibodies led to increased CCL2 production, we aimed to develop a system that allows for local and intratumoral delivery of the CCL2-neutralizing antibody fragment. To achieve this, we designed chimeric antigen receptor (CAR) constructs that enable simultaneous expression of the CAR and soluble secretion of our anti-CCL2 lead candidate. We demonstrated cell-surface expression of the CAR molecule and functionality of the CAR T cells. However, although simultaneous expression of the CAR and secretion of anti-CCL2 scFv was successfully proved for transfected HEK293T cells, we failed to detect scFv secretion from primary human T cells transduced with the same constructs. We assume that the amount of secreted scFv from T cells was below the detection limit of our assays. Thus, future work is warranted that shows that CAR T cells are able to produce sufficient amounts of anti-CCL2 scFv within the tumor and that this way of scFv delivery is superior to systemic administration routes.

Zusammenfassung

Tumorassoziierte Makrophagen (TAMs) tragen zur Tumorprogression bei und fördern das immunsuppressive Tumormikromilieu. Verschiedene TAM-gerichtete immuntherapeutische Ansätze werden entwickelt, einschließlich der Blockade der Monozytenrekrutierung zu Tumoren, um die Anzahl pro-tumorigener TAMs zu verringern. Es wurde festgestellt, dass von Tumorzellen sekretierte Moleküle wie C-C-Chemokinligand 2 (CCL2) und Semaphorin 3A (Sema3A) eine entscheidende Rolle spielen bei der Anlockung von Monozyten über ihre jeweiligen Monozyten-exprimierten Rezeptoren, C-C Chemokinrezeptor Typ 2 (CCR2) und Neuropilin 1 (NRP1).

In diesem Projekt wurden vollständig humane CCL2- und NRP1-spezifische Antikörperfragmente mittels Phagen-Display selektiert und im Immunglobulin 1 (IgG1) -Format charakterisiert. Wir konnten die Antigenspezifität nachweisen mittels ELISA, Oberflächenplasmonen-resonanzspektroskopie und Durchflusszytometrie. Da wir keine Blockierung der NRP1 – Sema3A Wechselwirkung durch die NRP1-spezifischen Antikörper zeigen konnten, wurden diese Antikörper nicht weiterentwickelt. In Gegenwart des CCL2-spezifischen Antikörpers beobachteten wir eine Blockierung der CCL2 – CCR2 Interaktion sowie der intrazellulären CCR2-abhängigen Signalübertragung und zeigten eine verringerte CCL2-gerichtete Migration der Monozyten.

Da kürzlich veröffentlichte Berichte zeigten, dass die systemische Verabreichung von anti-CCL2 Antikörpern zu einer erhöhten CCL2 Produktion führte, wollten wir ein System entwickeln, welches die intratumorale Abgabe des CCL2-spezifischen Antikörperfragments ermöglicht. Hierfür, generierten wir chimäre Antigenrezeptor (CAR)-Konstrukte, welche die gleichzeitige Expression des CAR und die lösliche Sekretion des anti-CCL2 Antikörperfragments ermöglichen. Wir demonstrierten die Expression des CAR Moleküls auf der Zelloberfläche und die Funktionalität der CAR T-Zellen. Obwohl die anti-CCL2 scFv Sekretion für transfizierte HEK293T-Zellen erfolgreich gezeigt wurde, konnten wir keine Sekretion aus transduzierten T-Zellen nachweisen. Wir gehen davon aus, dass die Menge an sekretiertem scFv durch T-Zellen unterhalb der Nachweisgrenze unseres Assays lag. Zukünftig soll gezeigt werden, dass CAR T-Zellen in der Lage sind, ausreichende Mengen an anti-CCL2 scFv im Tumor zu produzieren, und dass diese Art der scFv-Abgabe den systemischen Verabreichungswegen überlegen ist.

Table of content

Abbreviations

°C	degree Celsius
(B-)ALL	B cell actute lymphoblastic leukemia
(p)ERK	(phosphorylated) extracellular-signal regulated kinase
A	Adenine/ Alanine
AA	amino acid
ABC	activated B-cell
Amp(R)	ampicillin (resistance)
APC	allophycocyanin / antigen presenting cell
APS	ammonium peroxidsulfate
AU	absorbance unit
BCR	B cell receptor
bp	base pair
BSA	bovine serum albumin
C	Cytosine
CAIX	carbonic anhydrase 9
CAR	chimeric antigen receptor
Cat. No.	catalog number
CCL	(C-C motif) chemokine ligand
CCR	C-C chemokine receptor
CD	cluster of differentiation
cDNA	complementary deoxyribonucleic acid
CDR	complementarity determining region
CH	heavy chain constant domain
CIP	alkaline phosphatase from calf intestine
CL	light chain constant domain

c-myc	myelocytomatosis oncogene
CO_2	carbon dioxide
cPPT	central polypurine tract
CSF1(R)	colony-stimulating factor 1 (receptor)
CTLA4	cytotoxic T lymphocyte-associated protein 4
CUB	complement C1r/C1s, Uegf, Bmp1
CXCL	(C-X-C motif) ligand
D	diversity gene segment
Da	Dalton
ddH_2O	double distilled water
DGV	double gene vector
DLBCL	diffuse large B cell lymphoma
DMEM	Dulbecco's Modified Eagle's Medium
DMSO	dimethyl sulfoxide
DNA	deoxyribonucleic acid
dNTP	deoxynucleoside triphosphate
DTT	dithiothreitol
E. coli	Escherichia coli
E:T	effector to target
EC50	half maximal efective concentration
ECL	enhanced chemiluminescence
EDC	1-Ethyl-3-(3-dimethylaminopropyl)
EDTA	ethylenediaminetetraacetic acid
EF1α	elongation factor-1 alpha
EGF	epidermal growth factor
EGM2	endothelial cell growth medium 2
ELISA	enzyme linked immunosorbent assay

env	envelope
Fab	antigen binding fragment
Fc	fragment crystallizable
FCS	fetal calf serum
FDA	U.S. Food and Drug Administration
FITC	fluorescein isothiocyanate
FPLC	fast protein liquid chromatography
Fv	variable fragment
fw	forward primer (sense)
g	gravitational constant
G	Guanine
G418	Geneticin
GAPDH	glyceraldehyde 3-phosphate dehydrogenase
Gas6	growth-arrest-specific gene-6
GCB	germinal center B-cell
GD2	disialoganglioside
GLuc	gaussia luciferase
GmbH	Gesellschaft mit beschränkter Haftung
GM-CSF	granulocyte macrophage colony-stimulating factor
Go	goat
h	hour
HAL9/10	human antibody libraries 9/10
HEK	human embryonic kidney
hFc	human fragment crystallizable
His	histidine
HRP	horseradish peroxidase
HSA	human serum albumin

HUVEC	human umbilical vein endothelial cells
IFNγ	interferon gamma
Ig	immunoglobulin
IGHV	heavy chain V gene segment
IL	interleukin
IL-13Rα2	interleukin-13 receptor subunit alpha-2
IMAC	immobilized metal affinity chromatography
IPTG	isopropyl β-D-1-thiogalactopyranoside
IRES	internal ribosomal entry site
IU	infectious units
J	joining gene segment
ka	association rate constant
Kana(R)	kanamycin (resistance)
K_D	equilibrium dissociation constant / equilibrium binding constant
kd	dissociation rate constant
L	liter
LB medium/agar	lysogeny broth medium / agar
LB-A/-K medium/ agar	LB medium / agar with ampicillin or kanamycin
LIF	leukemia inhibitory factor
LPS	lipopolysaccharide
LTR	long terminal repeat
LYNDAL	LYmph Node Derived Antibody Libraries
M	molar (mol/L) / marker
mAb	monoclonal antibody
MAM	meprin, A-5 protein, and receptor protein-tyrosine phosphatase mu
MAPK	mitogen-acitvated protein kinase
MCP-1	monocyte chemotactic protein-1

M-CSF	macrophage-colony stimulating factor
mFc	murine fragment crystallizable
MFI	median fluorescence intensity
MHC	major histocompatibility complex
min	minute
MOI	multiplicity of infection
MPBS	milk phosphate buffered saline
mRNA	messenger ribonucleic acid
ms	mouse
MW	molecular weight
N	Asparagine
NC	negative control
NCBI	national center for biotechnology information
NCT	national center for tumor diseases
NF-κB	nuclear factor-κB
NHL	non-Hodgkin lymphoma
NHS	N-Hydroxysuccinimid
NK	natural killer
NO	nitrogen species
NRP1	neuropilin 1
nt	nucleotide
OD_{600}	optical density at 600 nm wavelength
ori	origin of replication
pA	polyadenylation signal
PAGE	polyacrylamide gel electrophoresis
PAMP	pathogen-associated molecular pattern
PBMC	peripheral blood mononuclear cell

PBS(-T)	phosphate buffered saline (with Tween 20)
PCR	polymerase chain reaction
PD-1	programmed cell death protein 1
PD-L1	programmed-death ligand 1
PDZ	PSD-95, Disc-large, and ZO-1
PE	phycoerythrin
PEG	polyethylene gylcol
PEI	polyethylenimine
pen/strep	penicillin/streptomycin
PGF2	placental growth factor 2
PGK	phosphoglycerate kinase
pH	potentia Hydrogenii
PHA-P	phytohaemagglutinin P (PHA-P)
PI3K	phosphoinositide 3-kinase
PRR	pattern recognition receptor
rel.	relative
R_L	ligand immobilization level
R_{max}	maximum response level
RNA	ribonucleic acid
ROS	reactive oxygen species
rpm	revolutions per minute
RPMI-1640	Roswell Park Memorial Institute 1640 medium
RRE	rev response element
RT	room temperature
RU	response unit
rv	reverse primer (antisense)
scFv	single chain variable fragment

SD	standard deviation
SDS	sodium dodecyl sulfate
SEC	size exclusion chromatography
Sema3A	semaphorin 3A
Siglec	sialic acid-binding immunoglobulin-like lectin
SIRPα	signal regulatory protein α
S_m	stoichiometric ratio
SOC	super optimal broth supplemented with glucose
SOCS3	suppressor of cytokine signaling 3
SP	signal peptide
SPR	Surface plasmon resonance
strep	streptavidin
SV	simian virus
T	Thymine
T2A	thosea asigna virus 2A
TAE	tris acetate EDTA buffer
TAM	tumor-associated macrophage
TCR	T cell receptor
TEMED	tetramethylethylenedamine
Th	T helper
TIM3	T cell immunoglobulin and mucin domain containing 3
TLR	toll-like receptor
Tm	melting temperature
TM	transmembrane
TMB	tetramethylbenzidine
TME	tumor microenvironment
TNF	tumor necrosis factor

Treg	regulatory T cell
Tris	tris(hydroxymethyl)aminomethane
Tryptone N1	TN1
TU	transducing units
U	enzyme unit
UV	ultraviolet
V	variable gene segment
v/v	volume per volume
VEGF(R)	vascular endothelial growth factor (receptor)
VH	heavy chain variable domain
VL	light chain variable domain
w/v	weight per volume
WPRE	woodchuck hepatitis virus posttranscriptional regulatory element
YT medium	yeast tryptone medium
YT-A medium	yeast tryptone medium with ampicillin
YT-AK medium	yeast tryptone medium with ampicillin and kanamycin
YT-GA medium/ agar	yeast tryptone medium / agar with glucose and ampicillin
YT-K agar	yeast tryptone agar with kanamycin
α	anti

1 Introduction

1.1 The innate and adaptive immune system

Our environment contains a vast number of pathogens and toxins challenging our immune system at a daily basis. Therefore, the immune system employs complex mechanisms to keep pathogens in check and usually eliminates them to avoid disease. At the same time, it is of utmost importance not to damage healthy tissues or beneficial microbes. There are two lines of defense for rapid and specific pathogen clearance: the innate and adaptive immune system [1].

The innate immunity represents the first line of defense which responds within hours after antigen contact. Pathogens share common structures, so called pathogen-associated molecular patterns (PAMPs), which are recognized by cells of the innate immune system via pattern recognition receptors (PRRs) [2]. Upon antigen detection, cytokines and chemokines are responsible for the rapid recruitment of additional immune cells to the site of infection. Numerous cell types constitute the innate immune system including macrophages, granulocytes (neutrophils, basophils, eosinophils), dendritic cells, mast cells and natural killer (NK) cells. Macrophages, neutrophils and dendritic cells engulf (phagocytose) and eliminate microbes. Granulocytes are additionally equipped with granules that contain lytic enzymes and cytokines which upon release help to defend against pathogens. Furthermore, NK cells play an important role in the lysis of virus-infected cells through the release of perforins and granzymes [1], [3]. In addition to the cellular components of the innate immune system, there is a network of soluble proteins that opsonize pathogens thereby marking them for phagocytosis. This so-called complement system can activate antigen presenting cells (APCs) of the adaptive immune system [4].

The adaptive immune system constitutes the second line of defense and sets in if the innate immune system is unsuccessful in eliminating a pathogen. In contrast to the innate immune response, the adaptive immune response is highly antigen-specific and it takes several days until the cells are fully activated and ready to participate in immune responses. Cells of the adaptive immunity include T lymphocytes (T cells) and B lymphocytes (B cells). T cells interact with macrophages and dendritic cells which function as APCs. Upon phagocytosis of pathogens, APCs present fragments thereof loaded onto class II major histocompatibility complex (MHC) molecules on their cell surface and thereby stimulate the adaptive immune system [1], [3]. In contrast, class I MHC molecules are expressed on the cell surface of all nucleated cells for identification of “self”-tissues and are responsible for presentation of intracellular peptides [2]. Each individual T cell

displays a unique T cell receptor (TCR) on its surface recognizing a specific peptide antigen fragment presented on MHC molecules. T cells can be subdivided into CD8+ cytotoxic T cells and CD4+ T-helper (Th) cells. Cytotoxic (effector) T cells have the potential to destroy infected cells or tumor cells presenting the cognate peptide antigen via MHC I molecules. Some of these effector cells differentiate to long-lived memory T cells that can be rapidly reactivated following subsequent encounters with the same antigen [1], [5]. Other than cytotoxic T cells, Th cells recognize antigen peptides presented by MHC II molecules and regulate and direct the immune response through the secretion of cytokines. Depending on the APC and the encountered cytokines CD4+ T cells differentiate to specific Th cell populations which are in turn characterized by different cytokine production and roles in the immune defense. Th1 cells kill bacteria or virus infected cells as well as tumor cells, Th2 cells aid B cell differentiation and antibody production, Th17 cells induce inflammatory responses at mucosal surfaces, Th9 cells mediate defense against helminths, follicular Th cells trigger B cell activation and germinal center formation and regulatory T cells (Tregs) dampen the immune activation.

In contrast to T cells, B cells recognize native and extracellular antigens through their surface-exposed immunoglobulin (B cell receptor, BCR) in an MHC independent manner. Upon antigen encounter and by the support of follicular Th cells, B cells are activated and differentiate to plasma cells or memory B cells. Plasma cells then secrete a soluble version of their immunoglobulin (antibody), which circulates through the blood stream and binds to antigens exposed on the surface of pathogens or soluble toxins. Memory B cells are long-lived and can quickly differentiate to plasma cells to produce antigen-specific antibodies upon re-encounter with the antigen [1], [5].

When antibodies bind to a pathogen, the exposed fragment crystallizable (Fc) region is recognized by cells of the innate immune system via Fc receptors and thereby elicits effector functions resulting in phagocytosis and destruction of the pathogens. There are five types of antibodies, namely IgA, IgD, IgE, IgG and IgM, which differ substantially in their functions and valency (number of antigen binding sites). The first antibodies to be produced during an immune response are IgM molecules which are pentamers and are primarily found in the blood and to a lesser extend in the lymph. All other antibody types are generated by class switching. IgG antibodies are the most common class found in blood plasma and efficiently opsonize pathogens for phagocytosis and activate the complement system. Based on structural and functional differences IgG antibodies are subdivided into four classes, IgG1, IgG2, IgG3 and IgG4 (numbered in reference to decreasing serum concentration). All IgG classes except IgG4 activate the complement cascade. IgG1 and IgG3 bind to all classes of Fcγ receptors (I, II and III), whereas IgG4 binds only

Fcγ receptor II and III and IgG2 binds only Fcγ receptor II. During an immune response, IgG1 and IgG3 are induced in response to protein antigen and IgG2 and IgG4 in response to polysaccharide antigens. IgA molecules can dimerize and are the most common antibodies in mucosal secretions and breast milk where they exert neutralizing functions. IgD is found at low levels in the serum and the function of these molecules remains unknown. IgE antibodies are present in the lowest serum concentration, are bound with high affinity by receptors on mast cells and play a role in allergic reactions [1], [6], [7].

Immunoglobulins are comprised of two identical heavy chains of the α, δ, ε, γ or μ isotype and light chains (either κ or λ light chain). In contrast, a TCR consist of an α and a β chain expressed in a complex with invariant CD3 chain molecules (CD3γε, CD3δε and two CD3ζ chains). Each chain is composed of an N-terminal variable domain and one or more C-terminal constant domains (immunoglobulin heavy chains contain three C-terminal constant domains). Within the BCR and TCR variable domains there are three hypervariable regions, called complementarity determining regions (CDRs), that protrude into the antigen-binding site and which make most of the contacts with an antigen. The CDR loops are flanked by less variable framework regions that are important for maintaining the immunoglobulin fold [7]. While each individual antigen receptor recognizes a unique antigen, the pool of all receptors together is able to detect a vast number of antigens. This diversity results from recombination of clustered variable (V), diversity (D) and joining (J) gene segments. During V(D)J recombination (D only present in the immunoglobulin heavy chain and TCR β chain) one of each gene is selected from a cluster of gene segments in the germline locus, while the addition or removal of nucleotides at the joining sites can further increase the variability of the newly arranged antigen receptor (junctional diversification) (*Figure 1*) [8], [9]. In germinal centers, which are microstructures within secondary lymphoid organs (lymph node and spleen), B cells proliferate, differentiate and maturate. Here, an additional process called somatic hypermutation occurs which further increases the receptor diversity through introduction of various point mutations in the V regions. Aided by follicular dendritic cells and follicular Th cells, B cells which have successfully gathered mutations that confer a higher specificity of their BCR to an antigen gain a survival advantage and finally differentiate [10], [11].

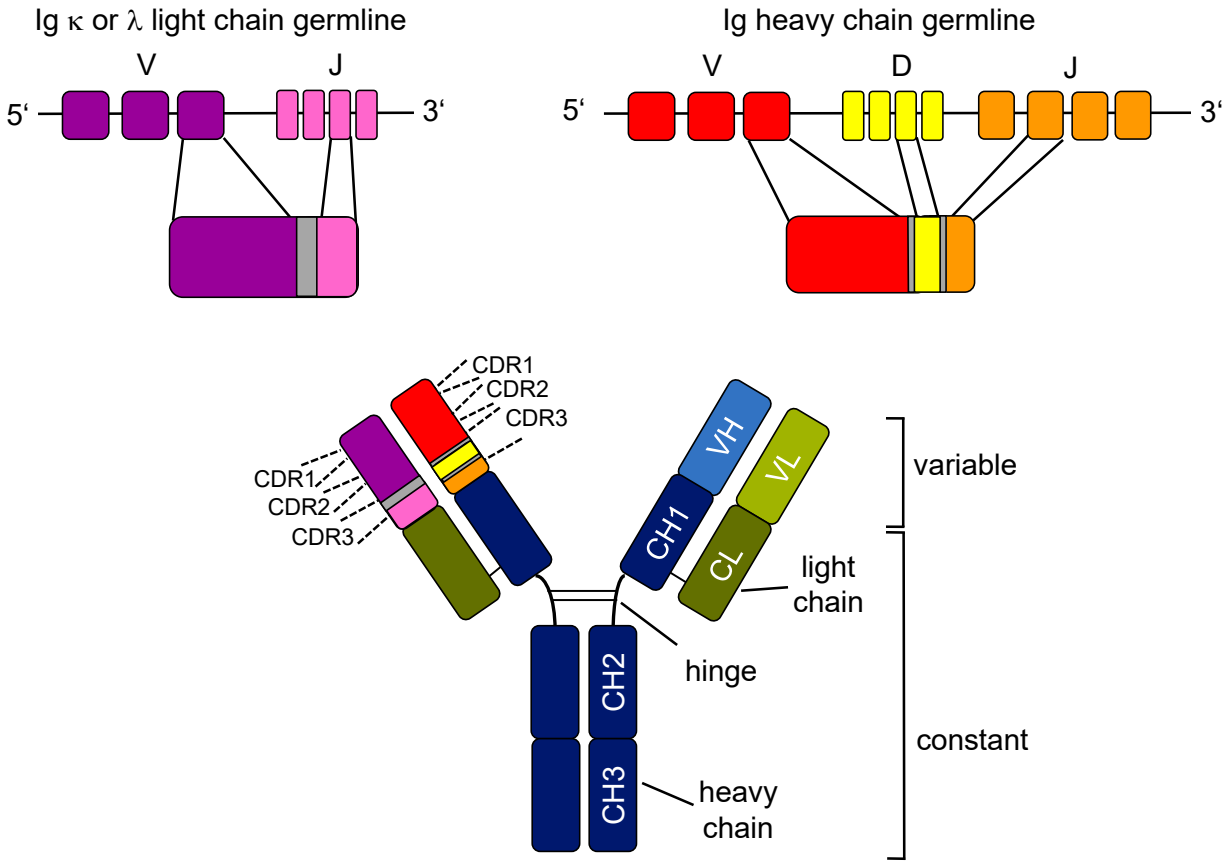

Figure 1. Antibody genetic encoding and structure. The germline (unrearranged) DNA of the immunoglobulin (Ig) heavy and light chain locus contains clusters of variable (V), diversity (D) (only heavy chain) and joining (J) gene segments. The variable region of the Ig heavy chain is generated by rearrangement and joining of each a single heavy chain D and J gene segment, followed by the joining of a single V gene segment. The variable region of the Ig κ or λ light chain is generated by joining of each a single V and J gene segment. During rearrangement, additional nucleotides may be added or removed at the joining sites (grey) in order to increase the diversity of the CDR3 loop. The constant regions of the heavy (CH1, CH2 and CH3) and the light (CL) chain are encoded downstream and are joined to the rearranged V(D)J genes by splicing. Figure adapted from Boyd and Joshi [12].

1.2 Macrophages as targets for cancer therapy

1.2.1 Macrophages and their role in the innate immune response

Monocytes and macrophages are cells of the myeloid lineage and have important functions in the innate immune response. According to the mononuclear phagocyte system, monocytes derive from precursors in the bone marrow, circulate in the blood and migrate into tissues where they differentiate to macrophages. During an immune response, monocytes are recruited to sites of infection or inflammation by various chemokines [13], [14]. Apart from the mononuclear phagocyte system, recent studies suggest the yolk sac or fetal liver as additional source of monocytes during embryonic development and that there are pre-macrophages which reside in certain adult tissues and can give rise to mature macrophages [15]–[17]. Macrophages phagocytose pathogens and produce cytokines to support the immune reaction. Based on the tissue they reside in and the environment they encounter, macrophages can exhibit different morphology and functionality [18].

Macrophages are classified into two groups: classically activated macrophages, called the M1 phenotype, and alternatively activated macrophages, called the M2 phenotype. Importantly, macrophages show a huge plasticity with diverse states ranging between M1 and M2 phenotype, whereby M1 and M2 macrophages can only be seen as opposite extremes. Polarization towards the M1 phenotype is mediated by bacterial lipopolysaccharides (LPS) as well as tumor necrosis factor (TNF) and interferon-gamma (IFNγ) secreted by cells of the innate and adaptive immune system. Upon activation, M1 macrophages support the immune response via secretion of pro-inflammatory cytokines (IL-1, IL-6, TNF), effector molecules (reactive oxygen and nitrogen species) and chemokines (C-X-C motif ligand (CXCL)9, CXCL10) [18]. M2 polarization of macrophages occurs in response to IL-4 and IL-13 secreted by Th2 cells, engagement of Fcγ receptors and toll-like receptors on the macrophage surface and anti-inflammatory cytokines including IL-10 and transforming growth factor-β (TGFβ). M2 macrophages are further subclassified into M2a, M2b, M2c and M2d according to the listed stimuli which trigger their polarization (*Table 1*) [19]. These macrophages generally induce anti-inflammatory, immunoregulatory and wound-healing processes [18], [20].

Table 1. Characteristics of classically activated M1 and alternatively activated M2 macrophages (Adapted from Poh and Ernst 2018 [19])

	Classically activated	**Alternatively activated**			
	M1	M2a	M2b	M2c	M2d
Stimuli inducing polari-zation	IFNγ LPS GM-CSF	IL-4 IL-13 Fungal/ helminth infection	IL-1R	IL-10 TGFβ Glucocorti-coids	IL-6 LIF Adenosine
Markers	CD40 CD80 CD68 MHC II IL-1R TLR2 TLR4 SOCS3	CD163 MHC II Scavenger receptor CD206	CD86 MHC II Mer tyrosine kinase	CD163 TLR1 TLR8	VEGF
Cytokine secretion	TNF IL-1 IL-6 IL-12 IL-23	IL-10 TGFβ	IL-1 IL-6 IL-10 TNF	IL-10 TGFβ	IL-10 IL-12 TNF TGFβ
Chemo-kine secretion	CCL10 CCL11 CCL5 CCL8 CCL4 CXCL9 CXCL10	CCL17 CCL22 CCL24	CCL1	CCR2	CCL5 CXCL10 CXCL16
Function	Inflammation, tissue damage, pathogen clearance	Allergic inflammation, tissue repair, tissue remodeling, fibrosis	Anti-inflammation, tissue remodeling, fibrosis	Anti-inflammation	Tissue repair, angiogenesis

1.2.2 Macrophages in the tumor microenvironment

Macrophages are the most abundant immune cells in solid tumors and can constitute up to 50 % of the tumor mass [21]. Their role in the tumor microenvironment is, however, diverse and depends on their phenotype. Some preclinical studies have shown that tumor-associated macrophages (TAMs) can exhibit anti-tumor characteristics. For example, in tumor tissues of colorectal cancer patients TAMs secreted pro-inflammatory cytokines thereby activating cytotoxic T cells [22]. It was not until the 1990s when several preclinical and clinical studies correlated TAM abundance with poor clinical prognosis. A key experiment to prove the pro-tumorigenic properties of macrophages was performed using a breast cancer mouse model, in which ablation of the colony-stimulating factor 1 (CSF1) gene resulted in reduction of macrophage number and concomitant suppression of tumor progression and metastasis [23]. Remarkably, a comprehensive analysis of 55 studies of different cancers correlated high TAM numbers with poor clinical outcome in breast, bladder, ovarian, gastric, oral and thyroid cancers [24]. Additional meta-analyses confirmed the correlation of TAM infiltration and poor prognosis for breast, gastric and non- small-cell lung cancer as well as for Hodgkin lymphoma [25]–[28].

Macrophages in the tumor microenvironment (TME) have been found to be mainly polarized towards the M2 phenotype. Apart from cytokines derived from tumor infiltrating immune cells and tumor cells, the hypoxic environment in solid cancers plays a pivotal role in macrophage recruitment and polarization (as discussed later) [29]. TAMs have been found to be pro-tumorigenic by inducing cancer initiation, tumor cell proliferation, angiogenesis, immune suppression, invasion and metastasis (*Figure 2*).

Chronic inflammation is linked to cancer initiation and is characterized by strong activation of nuclear factor-κB (NF-κB). Macrophages contribute to cancer initiation by creating a mutagenic environment through the secretion of pro-inflammatory molecules such as IL-6, tumor necrosis factor (TNF) as well as reactive oxygen species (ROS) and nitrogen species (NO) which may promote genomic instability [30]. Following cancer initiation, tumor cells express IL-10 and macrophage-colony stimulating factor (M-CSF), which leads to the increased secretion of growth-arrest-specific gene-6 (Gas6) by macrophages. Gas6 is the common ligand for the Tyro3, Ax1 and Mer receptors on cancer cells, all of which induce proliferation and survival. Additionally, macrophages directly promote tumor growth by production of growth factors, including epidermal growth factor (EGF), TNF and IL-6 [31]. Furthermore, progression of tumors requires the constant formation of new blood vessels, a process called angiogenesis. The “angiogenic swith”, a dramatic increase in newly formed blood vessels, is support by TAMs mainly via the expression of the

angiopoietin receptor TIE2 and secretion of pro-angiogenic factors such as vascular-endothelial growth factor (VEGF) or CXCL8 and CXCL12 [19], [30]. Moreover, TAMs generally exert an immunosuppressive function mediated by the release of IL-10, which induces Treg expansion. Additionally, up-regulation of programmed-death ligand (PD)-L1 on TAMs inhibits cytotoxic T cells [19], [30]. Macrophages further promote the most important cause for cancer mortality: metastasis. CSF1 secretion by tumor cells induces the production of EGF by TAMs which promotes tumor cell migration. Additionally, macrophages produce proteases which degrade the extracellular matrix, thereby allowing tumor cells to detach from the cell cluster and to migrate to other sites [19].

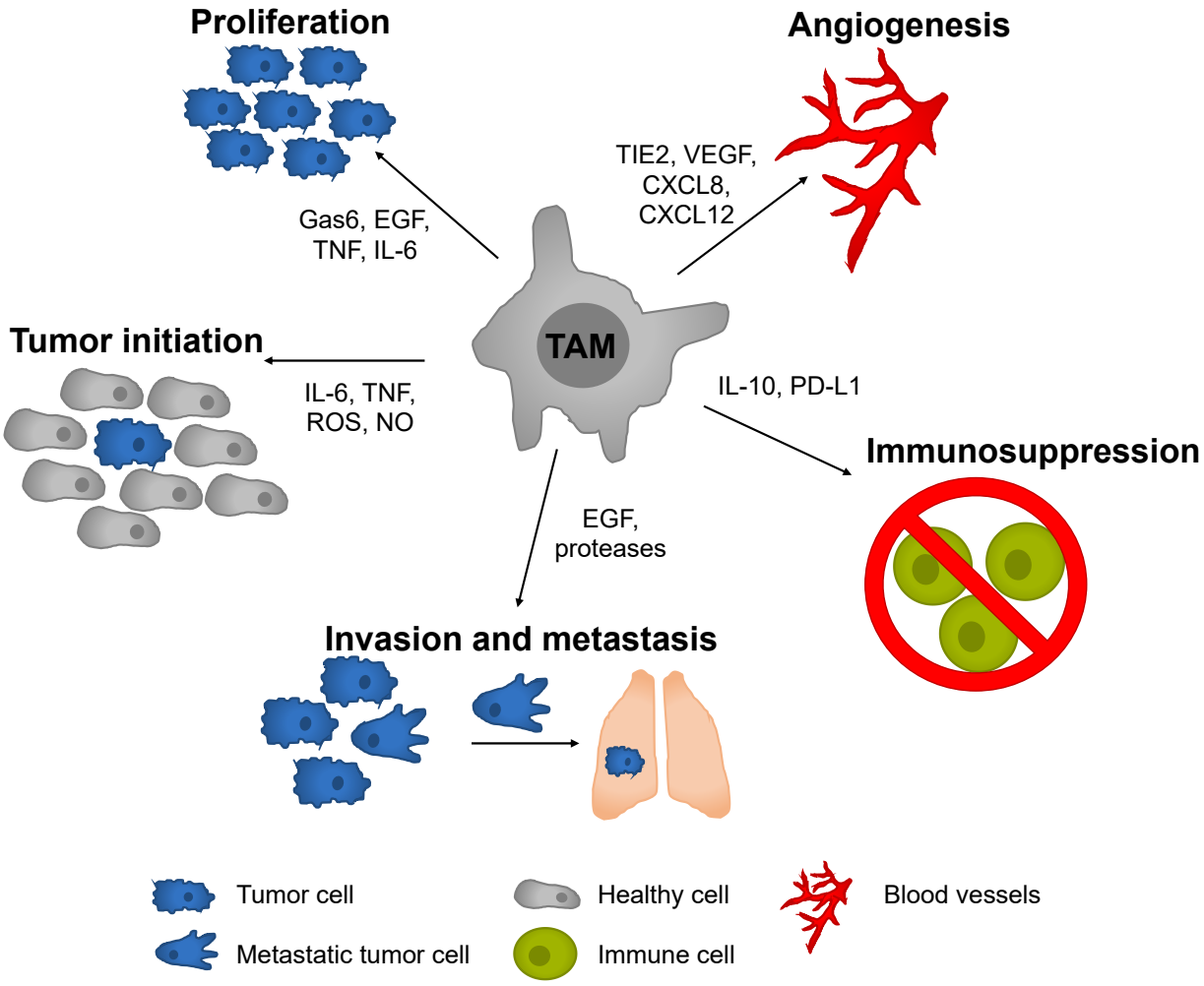

Figure 2. Roles of tumor-associated macrophages in the tumor microenvironment. In the tumor microenvironment, TAMs exert several pro-tumorigenic functions. They secrete pro-inflammatory cytokines, growth factors, pro-angiogenic and immunosuppressive factors. Thereby TAMs support cancer initiation, tumor cell proliferation, angiogenesis, immunosuppression as well as invasion and metastasis. Figure adapted from Schmidt *et al.* [31].

1.2.3 Macrophage-modulating cancer therapy

Due to their tumor-promoting properties, TAMs have become attractive targets for cancer therapy. Different approaches to target TAMs are currently under investigation in preclinical and clinical studies, including TAM depletion, reprogramming of TAMs into anti-tumoral phenotypes and inhibition of TAM recruitment (*Figure 3*). In the following section, the most advanced, clinically tested treatment approaches for macrophage modulation will be discussed.

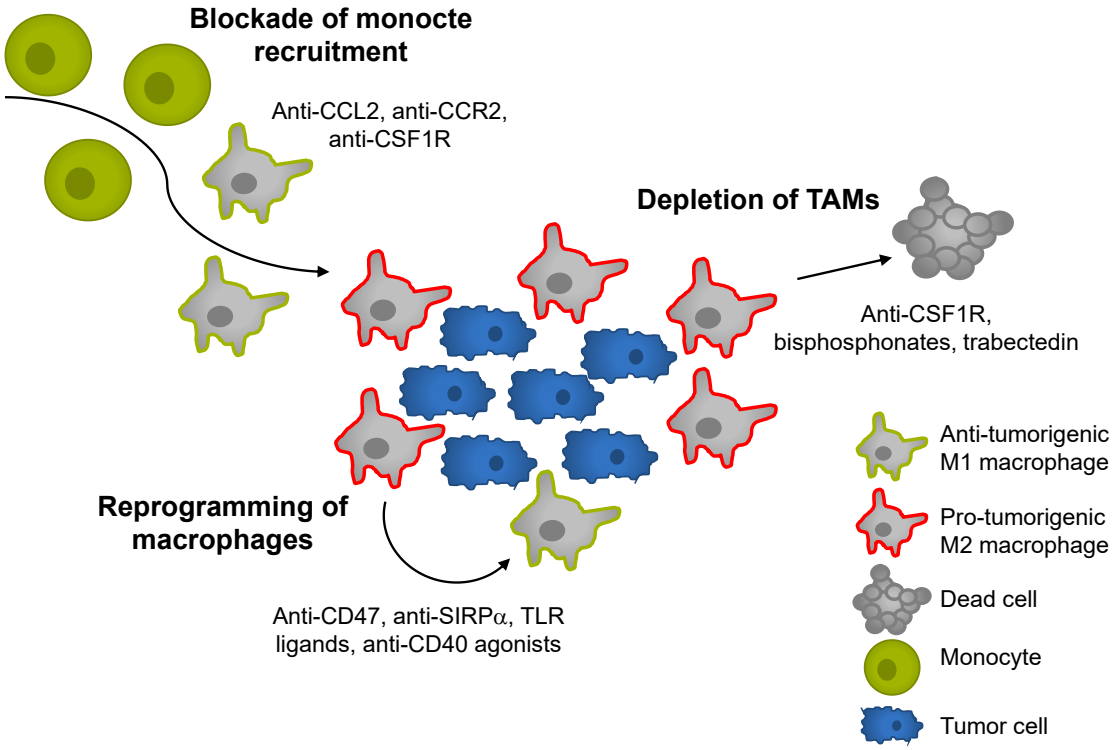

Figure 3. Therapeutic strategies targeting tumor-associated macrophages. Clinically evaluated treatment approaches targeting TAMs include depletion of TAMs using CSF1 receptor (CSF1R)-specific antibodies or small molecules and induction of apoptosis via bisphosphonates or trabectedin. Reprogramming of macrophages from a pro-tumorigenic M2 to an anti-tumorigenic M1 phenotype is currently under investigation using anti-CD47 and anti-SIRPα antibodies or fusion proteins as well as agonistic TLR ligands and agonistic CD40-specific antibodies. To reduce pro-tumorigenic TAMs in the tumor microenvironment, monocyte recruitment can be blocked and is clinically evaluated using CCL2-specific antibodies, small molecules inhibiting CCR2 or anti-CSF1R antibodies. Figure adapted from Josephs *et al.* [32].

One strategy is the depletion of macrophages to inhibit tumor progression and metastatic spread of tumor cells. Macrophages greatly depend on CSF1 receptor (CSF1R) signaling, therefore several antibodies and small molecules targeting CSF1R are tested in clinical trials to deplete macrophages and block their recruitment and survival. In total, there are five small molecules (PLX3397, JNJ-40346527, PLX7486, ARRY-382 and BLZ945) and three monoclonal antibodies (mAbs) (RG7155, IMC-CS4 and FPA008), all targeting CSF1R, under clinical investigation [30]. In a phase I and II study using PLX3397 in patients with tenosynovial giant cell tumors, a group of rare tumors that form in the joints and overexpress CSF1 and CSF1R, tumor regression was observed in 11 out of 14 patients [33]. In a phase II study of PLX3397 in glioblastoma patients, however, no benefit was observed in comparison to standard of care treatment [34]. Furthermore, in a phase I/II trial using JNJ-40346527 for treatment of Hodgkin lymphoma patients, over 50 % of patients responded with stable disease [35]. The CSF1R-targeting small molecules PLX7486, ARRY-382 and BLZ945 are currently being tested in phase I clinical trials for treatment of advanced-stage solid tumors [30]. Moreover, the humanized mAb RG7155 efficiently depleted CSF1R-expressing M2 macrophages in preclinical and clinical studies and resulted in 86 % objective response and 7 % complete response in patients with tenosynovial giant cell tumors [36]. Nevertheless, complete depletion of macrophages for a long period of time is problematic, therefore strategies of selectively depleting TAMs have been developed. Zoledronic acid and clodronate, belonging to the bisphosphonates, were reported to induce apoptosis in macrophages. Current studies are aiming to improve the delivery of these molecules by encapsulation. However, several clinical studies using zoledronic acid and clodronate reported inconsistent results. Consequently the route of administration of the drug needs to be further optimized [30]. Moreover, the DNA-binding agent trabectedin is an approved anti-tumor drug for soft tissue sarcoma and induces caspase-8 expression in TAMs thereby initiating apoptosis [37].

Reprogramming of pro-tumorigenic TAMs to an anti-tumorigenic M1 phenotype is a promising approach and for this purpose various antibodies, fusion proteins and small molecules are currently under clinical investigation. Many tumors overexpress CD47 which interacts with signal regulatory protein α (SIRPα) on the surface of macrophages and mediates a “do not eat me” signal [38]. Several preclinical studies have demonstrated anti-tumor effects of CD47 inhibition by restoring tumor cell phagocytosis and killing. Two CD47-targeting mAbs (Hu5F9-G4 and CC-90002) as well as a SIRPα-crystallizable fragment (Fc) fusion protein (TTI-621) are currently under phase I clinical investigation for treatment of solid and hematological tumors [30]. Furthermore, activation of pattern recognition receptors such as toll-like receptors (TLRs) is described to polarize macrophages towards the pro-inflammatory M1 phenotype during an innate immune

response. Consequently, TLR ligands have been developed to induce a switch of TAMs towards the anti-tumorigenic M1 phenotype [39]. Imiquimod, 852A and IMO-2055 are agonistic TLR ligands tested in clinical trials for the treatment of different cancers to evaluate their antitumoral and macrophage modulating effects [30]. An additional approach to reactivate the antitumoral potential of TAMs is the activation of CD40 signaling. CD40 is expressed on macrophages and interaction with CD40 ligand (CD40L) induces upregulation of MHC surface molecules as well as expression of pro-inflammatory cytokines [40]. Due to promising preclinical results of anti-CD40 agonistic antibodies in distinct tumor mouse models, two CD40-specific antibodies (CP-870,893 and RO7009789) have advanced into clinical trials [30]. CP-870,893 demonstrated anti-tumor activity when treating patients with solid tumors [41], [42].

Another strategy is to prevent formation of TAMs by inhibition of macrophage recruitment to the tumor. This inhibition is mainly addressed by blockade of the CC-chemokine ligand 2 (CCL2) – C-C chemokine receptor type 2 (CCR2) axis. CCL2 is the key chemoattractant for monocytes and is released by many tumor cells [43], [44]. In a clinical phase I trial treating patients with solid tumors, the CCL2-specific monoclonal antibody CNTO 888 (carlumab) was well tolerated. However, an increase in CCL2 levels expressed by the tumor was observed in response to the treatment [45]. Carlumab in combination with chemotherapy in a phase Ib trial demonstrated good safety but did not induce a significant anti-tumor response [46]. Moreover, no antitumoral response was observed in a phase II trial when using carlumab for treatment of patients with castration resistant prostate cancer [47]. More promising results were obtained in a phase Ib study combining a CCR2 inhibitor (PF-04136309) and chemotherapy for treatment of pancreatic adenocarcinoma. A partial tumor response was observed for 49 % of patients without showing increased toxicities [48]. Furthermore, an ongoing clinical trial of the CCR2 inhibitor CCX872 in the treatment of fifty patients with pancreatic cancer reported survival of 29 % of patients receiving CCX872 and chemotherapy at month 18. This is more favorable than overall survival rates of 18.6 % at month 18 for chemotherapy alone. In addition, circulating and inflammatory monocyte numbers were reduced following treatment with CCX872 [49]. Intervention of CCL2 – CCR2 signaling is challenged by compensatory mechanisms such as increased CCL2 concentrations in response to treatment with the CCL2 inhibitor carlumab [45]. Combinatorial therapies of CCL2 – CCR2 inhibition for example with checkpoint inhibition may reduce therapy resistance and have synergetic effects in restoring T cell function. Moreover, targeted delivery as opposed to systemic application of these drugs may circumvent compensatory mechanisms.

1.2.4 Macrophage recruitment to tumors

In order to advance the therapeutic approach of inhibiting macrophage recruitment and entrapment in the tumor, it is important to discuss the factors supporting these processes. A key player in monocyte recruitment to the tumor is CCL2. In addition to cytokines such as CCL2, CCL5 or CSF1 secreted by tumor cells and other cells in the TME, the hypoxic environment in solid tumors triggers the expression of chemoattractants by tumor cells, surrounding cells or macrophages themselves including VEGF, endothelial-monocyte-activating polypeptide II, endothelin-2, semaphorin 3A (Sema3A), stromal cell-derived factor 1 α, oncostatin M and eotaxin [29], [50]–[57]. Additionally, damage-associated molecular patterns such as extracellular DNA, RNA, adenosine triphosphate, or heat-shock proteins released from necrotic cells further attract macrophages [58]. Once inside the hypoxic tumor region, expression of CCR2, CCR5 and neuropilin-1 (NRP1) by TAMs is reduced, slowing down TAM migration and thereby trapping them at the tumor site [54], [59], [60]. Moreover, mitogen-activated protein kinase (MAPK) signaling, which is linked to macrophage migration, is blocked by upregulation of MAPK phosphatase 1 [29].

1.2.4.1 CC-chemokine ligand 2 structure and function

CCL2, also known as monocyte chemotactic protein-1 (MCP-1), was first isolated in 1989 from tumor cell supernatants and activated peripheral blood mononuclear cells (PBMCs) [43], [44]. Along this line, it has been shown that CCL2 attracts monocytes to the site of inflammation during an acute immune response [61]. The CCL2 cDNA encodes a 99 amino acid precursor protein with a 23 amino acid signal peptide. The mature protein is composed of 76 amino acids and has a molecular weight of approximately 13 kDa [62]. CCL2 is secreted by fibroblasts, astrocytes, mast cells, endothelial cells, osteoblasts, macrophages and lymphocytes in response to signals such as pro-inflammatory cytokines [62]. Importantly, CCL2 is expressed by a huge variety of human tumors, including prostate, breast and ovarian cancer. In most cancer cells the transcription factor NF-κB is constitutively activated and CCL2 possesses two NF-κB binding sites in the 5' untranslated region [63], [64]. Moreover, CCL2 is further upregulated in tumor cells in response to inflammatory molecules, such as IL-1, IL-6, TNF or TGFβ [65]. CCL2 is comprised of three distinct domains (*Figure 4*). First, a flexible N-terminal domain containing disulfide bonds between the N-terminal cysteines which triggers receptor binding and activation. Second, three anti-parallel β-pleated sheets and, third, an α-helix overlying these sheets [66].

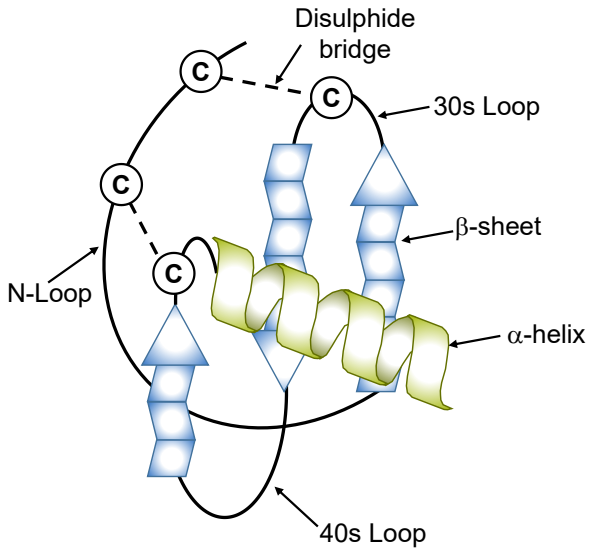

Figure 4. Schematic representation of CCL2. CCL2 is composed of an N-terminal loop (N-Loop) with two cysteine residues (C). Three anti-parallel β-sheets are connected by the 30s and 40s loops and are followed by an α-helix. The structure is stabilized by disulphide bonds between conserved cysteines. Figure adapted from Deshmane *et al.* [66].

Upon secretion of chemokines, chemokine receptor-expressing cells migrate along the chemical ligand gradient (chemokine gradient) towards high chemokine concentrations [66]. CCL2 is bound by its cognate receptor CCR2 which is expressed on monocytes, macrophages, lymphocytes and non-hematopoietic cells such as fibroblasts, endothelial cells and mesenchymal stem cells [62]. CCR2 expression has been found to be down-regulated during the differentiation of monocytes to macrophages [67]. CCR2 also interacts with other chemokines (CCL7, CCL8, CCL13), albeit not as efficiently as with CCL2 [68]. Chemokine receptors are seven-transmembrane receptors coupled to heterotrimeric G proteins and are therefore called G protein-coupled receptors. Upon activation of CCR2, downstream intracellular signal transduction via the MAPK signaling cascade results in the transmigration of monocytes [69]–[71]. Specifically, Ashida *et al.* have described a model to explain CCL2-dependent cell adhesion and migration. Following binding of CCL2 to CCR2, downstream signaling via extracellular signal-regulated kinase (ERK) results in integrin activation which mediates cell adhesion. Moreover, signaling via Rho, Rho kinase and p38 MAPK mediates chemotaxis [71]. Also of note, CCR2 triggers pro-inflammatory functions mediated by antigen-presenting cells and T cells as well as anti-inflammatory effects mediated by regulatory T cells [62].

High CCL2 expression has been correlated with high intratumoral macrophage density and poor clinical prognosis for many tumors, including breast, prostate, ovarian and non-small cell lung cancers [72]–[75]. Moreover, CCL2 has been found to polarize macrophages towards the pro-tumorigenic M2 phenotype by enhancing their IL-10 expression [76]. Importantly, CCL2 also

directly promotes tumor growth, survival and invasion [62]. Consequently, CCL2-targeted therapies have been evaluated in preclinical and clinical studies.

Inhibition of CCL2 using monoclonal antibodies neutralizing the murine homolog of CCL2, correlated with reduced tumor growth in mouse models representing prostate and lung cancer [77], [78]. Moreover, metastasis was reduced in a breast cancer mouse model upon intra peritoneal injection of a murine antibody targeting human CCL2 (MAB679, R&D Systems) [79]. In a xenograft mouse model of renal cell carcinoma, treatment with MAB679 resulted in reduced intratumoral TAM density [80]. Furthermore, in an *in vitr*o experiment, inhibition of CCL2 using a rabbit polyclonal anti-human CCL2 antibody (ab9669, Abcam) enhanced the expression of M1 phenotype markers and cytokines in human macrophages while M2 marker expression was reduced [76]. In addition, two phage display selected human antibodies against human CCL2 (MC8 and MC32) showed *in vitro* inhibition of monocyte chemotaxis [81]. To date, there are two therapeutic monoclonal antibodies to CCL2 which have advanced into clinical trials, namely ABN912 and carlumab. ABN912 is a human anti-human CCL2 IgG4 antibody developed by Novartis for the treatment of rheumatoid arthritis. The antibody was generated by immunization of genetically engineered mice containing human immunoglobulin genes. In a phase II trial in 45 patients with rheumatoid arthritis intravenous infusion of ABN912 showed no clinical improvement and resulted in increased CCL2 serum levels following treatment [82]. Carlumab is a phage display-derived human IgG1 antibody targeting human CCL2 and was developed by Centocor. CCL2 blockade using carlumab increased efficacy of chemotherapy in mouse models of ovarian cancer [83]. Clinical studies including the anti-CCL2 antibody carlumab showed less antitumoral efficacy compared to the preclinical studies indicating that clinical translation of this treatment approach needs further optimization [47]. Taken together, CCL2 appears as a promising target for anti-cancer therapy especially with regard to blocking the macrophage recruitment by the tumor.

1.2.4.2 Neuropilin 1 structure and function

NRP1 is a single-pass transmembrane, non-tyrosine kinase receptor of approximately 120 kDa. NRP1 consists of an N-terminal extracellular domain, a transmembrane domain and a short cytoplasmic tail containing a PDZ (PSD-95, Disc-large, and ZO-1)-binding motif to mediate protein-protein interactions (*Figure 5*). Within the extracellular domain there are two CUB (complement C1r/C1s, Uegf, Bmp1) domains (a1/ a2), two factor V/VIII coagulation factor homology domains (b1/ b2) as well as a MAM (meprin, A-5 protein, and receptor protein-tyrosine

phosphatase mu) domain (c), that causes receptor dimerization [84], [85]. In addition to the membrane-bound form, there are also soluble isoforms of NRP1 which potentially serve as decoy receptors [86]. NRP1 has diverse functions depending on the interacting ligand and cellular expression. NRP1 is expressed in the developing nervous system, lymphoid and myeloid cells, endothelial and tumor cells, including lung, breast, prostate, pancreatic and colon carcinomas, melanoma, astrocytoma and neuroblastoma [86], [87].

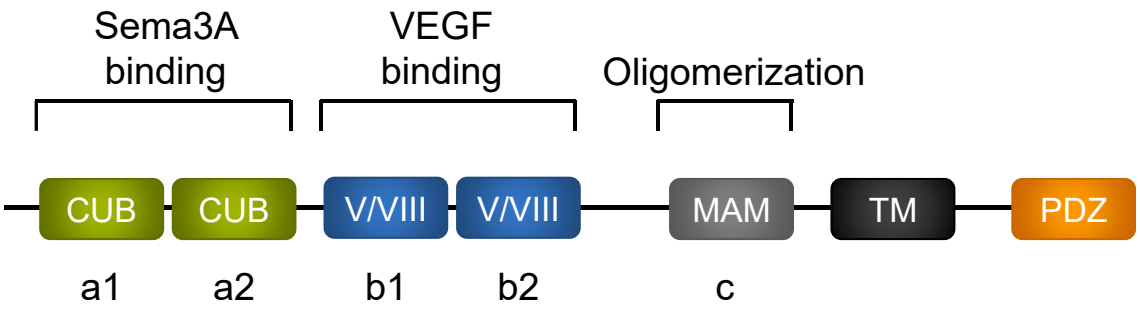

Figure 5. Schematic representation of NRP1. NRP1 is composed of an extracellular domain, a transmembrane (TM) domain and a cytoplasmic domain. Within the extracellular domain, two CUB domains (a1/a2) mediate Sema3A binding, two factor V/VIII homology domains (b1/b2) mediate VEGF binding and a MAM domain causes oligomerization. The short cytoplasmic domain contains a PDZ-binding motif which can mediate protein-protein interactions. Figure adapted from Pellet-Many *et al.* [88].

NRP1 was initially described to be expressed in axons and to serve as cell-surface receptor for class III semaphorins, primarily Sema3A [89]. Secreted Sema3A binds to the CUB domains of NRP1 and forms a holoreceptor complex with PlexinA1 or PlexinA2 resulting in axonal guidance [86]. Apart from this interaction, binding of NRP1 expressed on endothelial cells to $VEGF_{165}$, VEGF-B, and placental growth factor 2 (PGF2) via the b1/ b2 domains plays a role in angiogenesis [90]. Due to the interaction with different ligands and differential expression of NRP1 the physiological roles of this receptor are, to date, not fully understood.

Also in cancer cells, the roles of NRP1 are diverse. Many tumor cells overexpress NRP1, which has been linked to angiogenesis and subsequently tumor progression [91]. Indeed, the anti-NRP1 antibody MNRP1685A which blocks the binding of $VEGF_{165}$, VEGF-B, and PGF2 was evaluated in a clinical trial to treat patients with solid tumors. However, MNRP1685A did not achieve satisfactory clinical results and resulted in high proteinuria [92]. Importantly, several preclinical studies described a role of the NRP1 – Sema3A interaction in modulation of monocyte migration and macrophage reprogramming [54], [93]. Casazza *et al.* showed that tumor-derived Sema3A

recruits monocytes expressing NRP1 to the site of the tumor. Once inside the tumor, macrophages are arrested in an NRP1-independent manner in the hypoxic environment and are consequently polarized towards the pro-tumorigenic M2 phenotype. Interestingly, in orthotopic mouse models of lung and pancreatic cancer it was shown that NRP1-deficient TAMs did not enter the hypoxic tumor region and retained an anti-tumorigenic phenotype resulting in inhibition of tumor growth and metastasis [54].

Additionally, Chen *et al.* discovered that NRP1 overexpression in tumor tissues of cervical cancer patients correlated with increased intratumoral M2 macrophage density. Moreover, in a lung cancer mouse model under hypoxic conditions they found that increased NRP1 expression correlated with higher M2 macrophage density in the tumor and that inhibition of NRP1 expression in hypoxic tumor cells using small interfering RNA prevented monocyte recruitment and M2 macrophage polarization [93]. Taken together, there is increasing evidence that NRP1 modulates the migration of macrophages to the tumor site and their switch to a pro-tumorigenic phenotype, thus classifying NRP1 as a promising target for macrophage-modulatory cancer therapy.

1.3 Therapeutic antibodies

In 1975, Koehler and Milstein first described the hybridoma technology for the development of monoclonal antibodies which was fundamental for the development of modern therapeutic antibodies [94]. The hybridoma technology includes the immunization of an animal with the antigen, harvesting of splenocytes and fusion of antibody-producing B cells with an immortalized myeloma cell line. This results in immortalized antibody-producing hybridoma cells. By single cell selection of individual hybridoma clones, characteristics of monoclonal antibodies can be studied and upon identification of an appropriate clone, hybridoma cell lines can be cryopreserved for a long-lasting supply of monoclonal antibodies [94]. Furthermore, the generation of chimeric antibodies (murine variable antibody regions fused to human constant antibody region), humanized antibodies (murine CDR loops grafted on human framework regions and constant domains) and human antibodies (e.g. genetically modified mice carrying human V, D, J and constant domain gene segments) has reduced antibody immunogenicity and further accelerated the development of therapeutic antibodies [95].

In addition, the field of monoclonal antibody generation was further extended by new *in vitro* selection techniques such as phage display, which was invented by Smith and Winter in 1985 [96]. Phage display uses bacteriophages (viruses which infect bacteria) that are engineered to display

antibody fragments on their outside while encoding the specific antibody gene on their inside. Target antigen-specific phages can bind to immobilized antigen or antigen coupled to magnetic beads, while non-binding phages are removed by washing. Bound phages are eluted and amplified in bacteria. Several of these screening rounds (called biopanning) are used to enrich antigen-specific phages. After the final round of phage display, bacteria are infected, individual antibody fragments can be characterized and the DNA coding sequence can be recovered [96], [97]. As starting material for phage display, naïve, immune or synthetic antibody libraries may be used. Naïve libraries are generated from healthy donors and are “universal” libraries from which antibody fragments against (theoretically) all possible antigens can be isolated. In contrast, immune libraries are generated from immunized or diseased donors and are generally used to select antibody fragments against a particular antigen, for example a pathogen or a tumor marker. For the generation of these combinatorial libraries, antibody heavy and light chain variable regions are amplified from human B cell repertoires and cloned in random combinations into a phagemid vector system [98]. In contrast, fully synthetic antibody libraries are generated from optimized synthetic antibody frameworks and artificially diversified CDRs [99]. Apart from using phages for the presentation and selection of antibody fragments, other techniques like ribosome display and display on the cell surface of bacteria, yeast and mammalian cells have been developed [100]. However, phage display has become the most commonly used display platform since it is robust, rather inexpensive, allows automated screening and can be used to screen huge amounts of antibodies of up to 10^{11} clones [100].

Remarkably, these technological advances culminated in the approval of over 80 therapeutic monoclonal antibodies by the U.S. Food and Drug Administration and/or the European Commission, as of November 2019. Targeted immunotherapy with monoclonal antibodies is used to treat cancer as well as inflammatory, neurodegenerative and many other diseases [101], [102]. Although most approved antibodies are in the full-length IgG format, some therapeutic strategies require antibody formats that possess other pharmacokinetic properties or effector functions. By means of antibody engineering, recombinant antibodies as well as functional derivatives thereof can be generated (*Figure 6*). For example, full-length antibodies are characterized by long serum half-life and mediation of effector functions via the Fc region. However, due to their large molecular size, they show only limited tissue penetration. In contrast, single chain variable fragments (scFvs) have only short serum half-life and do not mediate effector functions, but efficiently penetrate tissue [103]. Moreover, antibody engineering allows for modifications to alter antibody effector functions and to develop for example antibody – toxin fusion proteins in order to generate antibodies according to the therapeutic need [103].

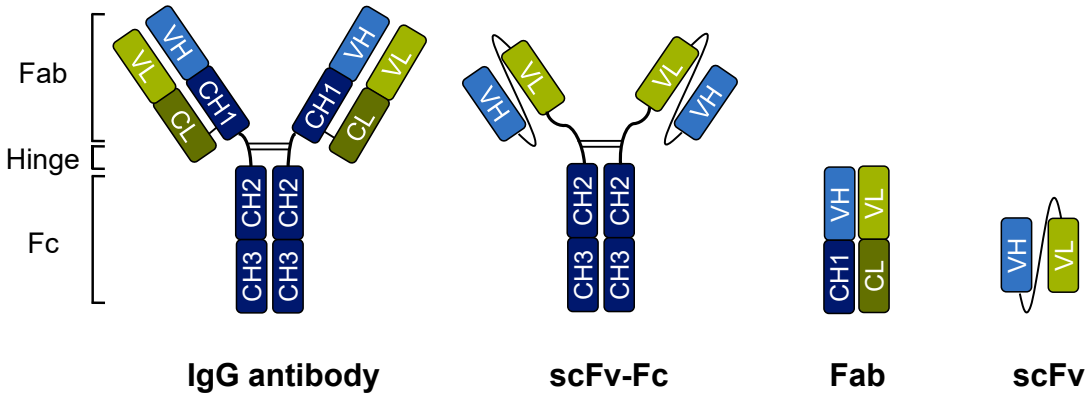

Figure 6. IgG antibody format and derivatives thereof. A full-length IgG antibody contains constant heavy (CH), constant light (CL) as well as variable heavy (VH) and variable light (VL) chain domains. IgG antibody-derived formats can be engineered to tailor drugs according to the therapeutic need. The alternative antibody formats exhibit different characteristics regarding tissue penetration, half-life and effector functions, which are mediated by the fragment crystallizable (Fc) region. The antigen binding fragment (Fab) encompasses only the variable antibody domains as well as the CL and CH1 domain that are linked with each other by natural disulfide bridges in the constant domains. Connection of the VH and VL domain via an artificial flexible linker results in a single chain variable fragment (scFv). Fusion of scFv to the antibody Fc region generates the antibody-like scFv-Fc format. Figure based on Carter *et al.* [104].

1.4 Chimeric antigen receptor T cells

In addition to antibody-based immunotherapy, cellular immunotherapies such as the adoptive cell therapy have achieved remarkable results regarding the treatment of cancer patients. Generally, there are three approaches of adoptive cell therapy all involving the isolation of immune cells from the cancer patient: First, tumor infiltrating B and T lymphocytes isolated from the tumor can be activated and expanded *ex vivo* before being retransferred into to the patient [105]. Second, T cells isolated from the peripheral blood can be engineered to express a modified TCR possessing a certain specificity against a target antigen of interest thereby allowing killing of target antigen-presenting tumor cells in an MHC-dependent manner [106], [107]. Third, T cells isolated from the peripheral blood can be engineered to express a so called chimeric antigen receptor (CAR) which comprises a tumor antigen-specific domain fused to TCR activation and signaling domains [108], [109]. CAR T cells combine the advantage of a predefined specificity with that of antigen recognition in an MHC-independent manner, thereby circumventing tumor escape mechanisms induced by MHC down-regulation [110].

A CAR molecule consist of an extracellular targeting domain (in most cases a scFv), a spacer domain, a transmembrane region and a cytoplasmic region containing one or more signaling domains (*Figure 7*) [111]. In the first generation of CARs, the scFv was fused via a spacer and a transmembrane domain to the CD3 zeta (ζ) chain of the TCR [109]. Upon specific binding of CAR T cells to antigen-expressing tumor cells, CAR T cells are activated by cytoplasmic signaling via the CD3ζ chain. Although CD3ζ is sufficient for activation, costimulatory molecules are required for serial killing of tumor cells and long-term expansion of CAR T cells. Costimulatory domains are commonly derived from CD28, OX40 and 4-1BB (CD137) [112]–[114]. 4-1BB was found to confer improved expansion, long-term *in vivo* persistence and reduced exhaustion of CAR T cells [115], [116]. Depending on the number of included costimulatory domains, CARs are classified as second generation (one costimulatory domain) or third generation (two costimulatory domains) CARs [117]. Furthermore, the spacer confers not only flexibility and length but critically defines the intercellular distance between CAR T cell and tumor cell which affects CAR activation and cytotoxicity. Commonly used spacers are composed of either a CD8α hinge, a CD28 hinge, an IgG1 or IgG4 Fc portion [118], [119].

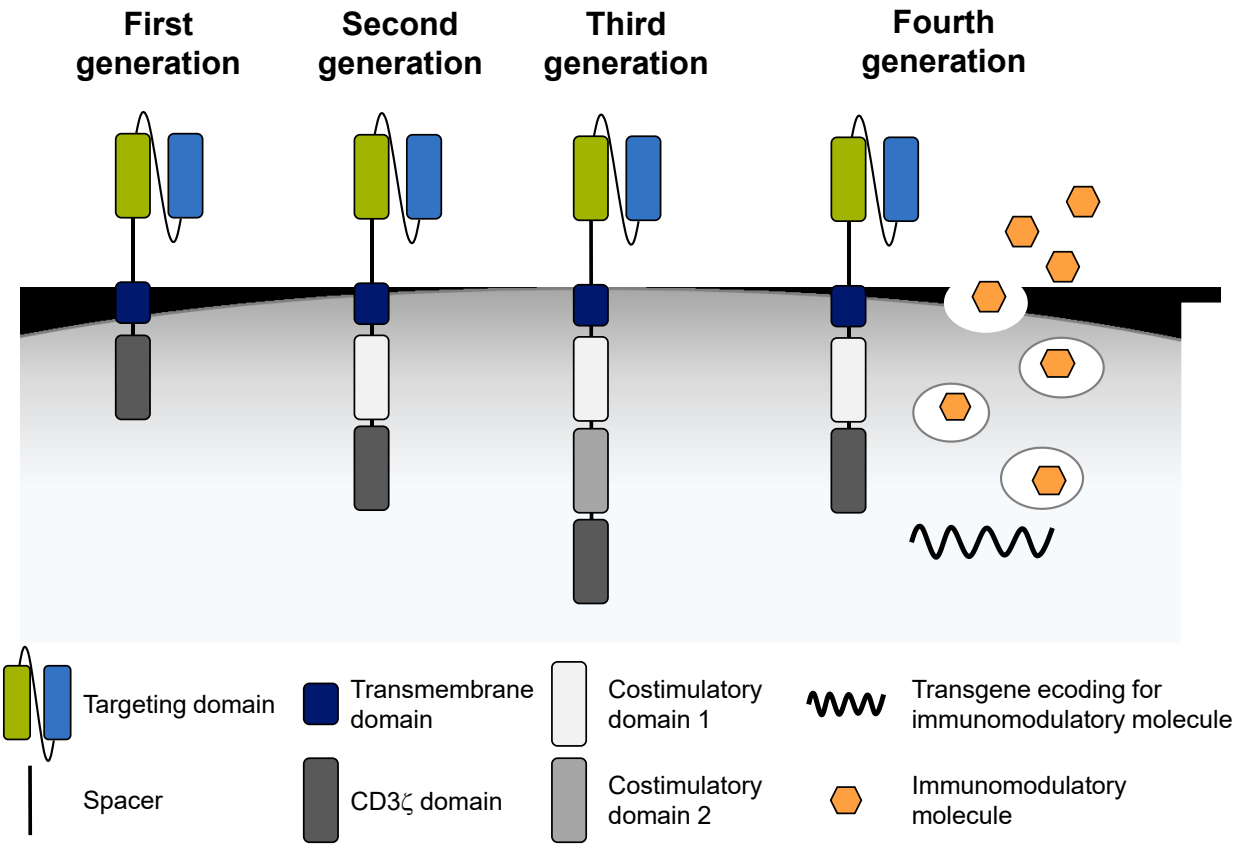

Figure 7. Structural representation of different CAR generations. CARs consist of an extracellular targeting domain, usually a scFv, a spacer which defines the intercellular distance between CAR T cell and tumor cell, a transmembrane domain, and the activation domain of the CD3ζ chain derived from the TCR (first generation) which can be linked to one (second generation) or two (third generation) costimulatory domains. Fourth generation CAR T cells are additionally engineered to encode immunomodulatory molecules such as cytokines or antibody fragments targeting immune checkpoints which are secreted by the CAR T cell. Figure based on Brentjens and Curran [117].

Over the past years, tremendous effort has been put into the development of CAR T cell therapies leading to the approval of two CD19-targeting CAR T cell therapies by the FDA. Tisagenlecleucel (Kymriah®, Novartis) was first approved in 2017 for the treatment of children and young adults suffering from pre-B cell acute lymphoblastic leukemia (ALL) [120]. Moreover, axicabtagene ciloleucel (Yescarta®, Kite Pharma) and tisagenlecleucel were approved in 2017 and 2018, respectively, for the treatment of relapsed and refractory large B cell lymphoma [120], [121]. Both CARs are of the second generation including either the 4-1BB (tisagenlecleucel) or the CD28 (axicabtagene ciloleucel) costimulatory domain [122]. Complete remission following treatment with tisagenlecleucel was observed in 90 % of patients with relapsed or refractory ALL, 43 % of patients with diffuse large B cell lymphoma (DLBCL) and 71 % of patients with follicular lymphoma [123], [124]. A clinical trial of axicabtagene ciloleucel in which patients with refractory large B cell lymphoma were treated resulted in 54 % complete remission [125]. Although CD19-targeted CAR T cell therapies show potent anti-tumor effects and sustained remissions, some patients with initial complete remission relapsed. This was either due to poor CAR T cell persistence or loss of the epitope in CD19 on malignant cells. These CD19 negative B cell cancers require alternative treatment options as for example the targeting of other B cell surface proteins [126].

Another targetable B cell surface protein is CD22. CD22 is a single-spanning sialic acid-binding immunoglobulin-like lectin (Siglec) transmembrane receptor which plays a critical role in B cell homeostasis by creating a threshold of antigen binding that needs to be achieved prior to activation of a B cell [127]. Cytoplasmic CD22 is expressed in precursor B cells, whereas surface CD22 expression is detected in immature and activated B cells. Along with the differentiation of activated B cells to plasma cells, CD22 expression is progressively downregulated. Importantly, CD22 is expressed in B-lymphoblastic leukemia and lymphomas as well as in mature B-cell leukemia and lymphomas [128]. Along this line, CD22-targeting CAR T cell therapies have advanced into the clinic. A clinical phase I trial using a novel CD22-directed CAR to treat patients with relapsed pre-B cell ALL, that was previously treated applying CD19-directed immunotherapy,

resulted in complete remission in 11 out of 15 (73 %) patients. Importantly, the CD22-targeting CAR T cell therapy demonstrated a similar safety profile and efficacy as the CD19-directed CAR T cell treatment. However, relapses were again observed in patients with previous complete remission most probably resulting from diminished CD22 expression on leukemic blast cells [129].

Apart from tumor escape mechanisms, a major hurdle that CAR T cell therapy needs to overcome is the immunosuppressive tumor microenvironment (TME) in solid tumors and lymphomas. Primarily, macrophages and regulatory T cells mediate suppression of anti-tumor effector T cells and immunosuppressive signaling via immune checkpoint molecules additionally reduce the efficacy of CAR T cell therapy [130]. To overcome these barriers set up by the TME, novel “fourth” generation of CARs are currently under development (*Figure 7*). These so called “armored” CAR T cells are genetically engineered to co-express immunomodulatory molecules such as cytokines or checkpoint inhibitors and allow local delivery of these molecules to the tumor. In this context, IL-12 secretion by carcinoembryonic antigen-targeting CAR T cells was reported to increase the recruitment of anti-tumorigenic macrophages to the tumor [131]. In addition, IL-12 secretion by VEGF receptor 2 (VEGFR2)-targeting CAR T cells resulted in tumor regression in multiple analyzed tumors in mice [132]. Moreover, IL-18 secretion increased the anti-tumor efficacy of CD19-directed CAR T cells in murine xenograft models [133], [134]. Furthermore, IL-15 secretion improved the anti-tumor efficacy of IL13 receptor subunit α2 (IL-13α2)-targeting CAR T cells in mouse models of glioblastoma [135]. IL-15 secreting CD19-direceted CAR T cells additionally showed prolonged *in vivo* persistence of the T cells in mouse models of leukemia [136]. Importantly, not only co-expressed cytokines but also co-expressed immune checkpoint inhibitors targeting programmed cell death protein 1 (PD-1), PD-1 ligand (PD-L1) and cytotoxic T-lymphocyte-associated protein 4 (CTLA4) improved anti-tumoral CAR T cell efficacy. Secretion of PD-1-blocking scFvs by either CD19- or Mucin 16 (ecto)-targeting CAR T cells enhanced the survival of mice bearing hematologic and solid tumors. In this context, PD-1-specific scFvs acted not only on the expressing CAR T cells themselves but also on tumor infiltrating bystander T cells [137]. In addition, secretion of anti-PD-L1 IgG antibodies from carbonic anhydrase IX (CAIX)-directed CAR T cells resulted in diminished tumor growth and reduced expression of PD-L1 on tumor cells in a humanized mouse model of clear cell renal cell carcinoma [138]. Moreover, IL-13α2-targeting CAR T cells co-expressing anti-CTLA4 minibodies resulted in inhibition of tumor growth and prolonged CAR T cells function in a mouse model of human glioma [139]. Taken together, the studies of “armored” CAR T cells consistently demonstrated improvement of anti-tumoral CAR T cell efficacy and therefore are most likely the next treatment modality to enter the clinics.

1.5 Diffuse large B cell lymphoma

Diffuse large B cell lymphoma (DLBCL) is the most common type of non-Hodgkin lymphoma (NHL) and accounts for 24 % of newly diagnosed cases of NHL in the United States each year [140], [141]. DLBCL is usually diagnosed by analyzing biopsies of abnormally enlarged lymph nodes and the International Prognostic Index supports clinicians to characterize prognosis based on various factors including age, disease spread and number of extranodal sites [142]. Most patients show lymphadenopathy, however, although being classified as a hematological cancer, DLBCL can frequently appear at extranodal sites including the kidneys, adrenal gland, brain, bones, and other soft tissues [141]. Generally, DLBCL is treated with chemoimmunotherapy (R-CHOP: rituximab, cyclophosphamide, doxorubicin, vincristine, and prednisone) resulting in high remission rates of approximately 50%-60% of patients. Unfortunately, 40 % of these patients relapse and experience a particularly poor prognosis [141], [143]. Based on the cell of origin DLBCL is classified as the germinal center B-cell (GCB)-like subtype or non-GCB DLBCL which contains the activated B-cell (ABC)-like subtype and remaining unclassifiable disease. ABC-like subtypes responded significantly poorer to standard-of-care treatment as compared to GCB DLBCL in several large patient studies [141].

DLBCL tumor cells express the B cell-specific surface molecules CD19 and CD22 [141]. Along this line, CD19-targeting CAR T cell therapy with tisagenlecleucel resulted in a complete response in 6 out of 14 patients suffering from DLBCL (43 %). Although only evaluated for this small patient cohort, immunohistochemical image analysis of lymph node and bone marrow biopsies revealed that patients, who did not respond, had higher levels of immune checkpoint proteins such as PD-1, lymphocyte-activation gene 3 and T-cell immunoglobulin and mucin domain 3 (TIM3) [124]. In a large clinical trial using tisagenlecleucel for treatment of 93 patients with relapsed or refractory DLBCL, 40 % of these patients showed complete remission out of which 79 % were relapse-free 12 months after initial response [144]. In addition, treatment of 77 DLBCL patients with axicabtagene ciloleucel resulted in 49 % complete response [125].

Although CAR T cell therapies show remarkable efficacy and persisting CAR T cell responses toward hematological tumors, the treatment is limited by adverse events such as cytokine release syndrome or neurologic toxicities. Cytokine release syndrome has been found not to result from CAR T cell-secreted cytokines but from macrophage-derived IL-6, IL-1 and nitric oxide [145]. Apart from inducing cytokine release syndrome, macrophages are the key player in the immunosuppressive tumor microenvironment, directly and indirectly inhibiting CAR T cell function [130]. Importantly, increased numbers of TAMs, especially of the M2 phenotype, were correlated

with poor prognosis in several studies analyzing DLBCL [146]–[150]. In addition, analysis of CCL2 expression in tumor cells of 221 DLBCL patients showed a correlation of high CCL2 levels with significantly poorer overall survival and progression free survival [151]. Along this line, fourth generation CAR T cell therapies which modulate the immunosuppressive tumor microenvironment may improve the clinical outcome.

1.6 Aim of the project

Pro-tumorigenic macrophages present in the tumor microenvironment have been found to support tumor initiation, progression and metastasis. Along this line, treatment approaches to target TAMs have shown promising results in preclinical studies. The aim of this project was the development of CCL2- and NRP1-targeting antibodies to inhibit monocyte migration to the tumor, thereby preventing the enrichment of pro-tumorigenic TAMs.

We set out to select fully-human CCL2- and NRP1-specific antibody fragments from immune and naïve antibody libraries by means of phage display. Following incorporation into full-length IgG molecules, we meant to analyze antibody specificity, affinity and functional characteristics.

For the local intratumoral application of our CCL2 neutralizing lead candidate antibody, we intended to engineer primary human T cells for co-expression of cell-surface exposed CD22-specific CAR molecules and soluble CCL2-specific scFv. Thus, the second study objective included the analysis of such “fourth” generation CAR T cells for CAR expression, scFv secretion, T cell expansion as well as target cell killing capacities. This novel combinatorial treatment approach may be of particular relevance for the treatment of DLBCL for which a correlation of increased CCL2 expression and TAM density has been correlated with poor prognosis.

2 Materials and Methods

2.1 Materials

2.1.1 Chemicals, reagents and commercial media

Table 2. List of used chemicals, reagents and commercial media

Chemical / Reagent / Commercial media	Supplier (Cat. No.)
10x Cut Smart buffer	New England Biolabs (B7204S)
10X DNase I Reaction Buffer	Invitrogen (Y02340)
10x T4 DNA ligase buffer	Thermo Fisher Scientific (B69)
2x Cell lysis buffer	Thermo Fisher Scientific (16189)
50x Tris acetate EDTA (TAE) buffer	AppliChem (A1691)
6x Loading dye	New England Biolabs (B70245)
Acetic acid	Carl Roth (7332.1)
Agar	Sigma-Aldrich (05039)
Agarose, universal	VWR Chemicals (35-1020)
Ammonium peroxidsulfate (APS)	Carl Roth (9592.2)
Ammoniumchlorid (NH_4Cl)	Carl Roth (K298.1)
Ampicillin sodium salt	Carl Roth (K029)
Aqua ad iniectabilia	Braun (2351744)
Bovine serum albumin (BSA)	Carl Roth (8076.2)
Bromphenol blue	AppliChem (7K005159)
Buffer solution pH 10	Carl Roth (P716.2)
Buffer solution pH 4	Carl Roth (P712.3)
Buffer solution pH 7	Carl Roth (A518.1)
Calciumchloride ($CaCl_2$)	Carl Roth (CN93.2)
Citric acid	Carl Roth (X863.2)
Coelenterazine	Biotium (B-10110-1)
cOmplete, EDTA free protease inhibitor cocktail	Roche (04693159001)
Coomassie Brillant Blue R 250	Carl Roth (3862.1)

D(+)-Glucose	Carl Roth (X997.2)
D(+)-Sucrose	Carl Roth (4621.2)
Dimethyl sulfoxide (DMSO)	Serva (20385.01)
Disodium hydrogen phosphate (Na_2HPO_4)	Carl Roth (P030.2)
Dithiothreitol (DTT)	Carl Roth (6908.3)
Dulbecco's Modified Eagle Medium (DMEM), high glucose	Sigma-Aldrich (D0819)
Dulbecco's Modified Eagle Medium (DMEM), without phenol red	Sigma-Aldrich (21063029)
Dulbecco's Phosphate Buffered Saline (PBS)	Sigma-Aldrich (D8537)
Endothelial Cell Growth Medium 2 (EGM2)	Promocell (C-22011)
Ethanol	Carl Roth (5054.4)
Ethylenediaminetetraacetic acid disodium salt dihydrate (EDTA)	Carl Roth (8043.2)
FACS clean	BD Biosciences (340345)
FACS flow	BD Biosciences (342003)
Fetal calf serum (FCS)	Sigma-Aldrich (F0804)
Freestyle F17 Medium	Life technologies (A13835)
GeneRuler 1 kb DNA Ladder	Thermo Fisher Scientific (SM0311)
Geneticin disulfate (G418)	Carl Roth (CP11.3)
Glycerol	Carl Roth (7530.4)
Glycine	Carl Roth (3908.2)
Heparin sodium salt	Sigma-Aldrich (H3149)
Human serum	Sigma-Aldrich (H4522)
Human serum albumin (HSA)	Sigma-Aldrich (A3782)
Hydrochloric acid, 2N (HCl)	Carl Roth (T134.1)
Hydrochloric acid, 37% (HCl)	Carl Roth (9277.1)
Imidazol	Carl Roth (X998.4)
Isopropanol	Carl Roth (9866.2)
Isopropyl β-D-1-thiogalactopyranoside (IPTG)	Carl Roth (2316.1)
Kanamycin sulfate	Carl Roth (T832.2)
Kolliphor P188	Sigma-Aldrich (K4894)
L-Glutamine	Sigma-Aldrich (G7513)
Magnesium sulfate ($MgSO_4$)	Carl Roth (0261.2)

Penicillin Streptomycin solution (pen/strep)	Sigma-Aldrich (P0781)
PeqGREEN DNA/RNA Dye	peqLab (37-5000)
PhosStop	Roche (04906845001)
Pierce BCA Protein Assay Kit	Thermo Fisher Scientific (23225)
Polybrene hexadimethrine bromide	Sigma (107689)
Polyethylene glycol 2 (PEG_2)	Novabiochem (8.51031.8500)
Polyethylene glycol 6000 (PEG_{6000})	Carl Roth (0158.1)
Polyethylenimine (PEI)	Polysciences (23966)
Potassium chloride (KCl)	Carl Roth (6781.1)
Potassium dihydrogen phosphate (KH_2PO_4)	Carl Roth (P018.1)
Powdered milk	Carl Roth (T145.2)
RIPA lysis and extraction buffer	Thermo Fisher Scientifc (89900)
Roswell Park Memorial Institute 1640 medium (RPMI-1640), Aqmedia	Sigma-Aldrich (R2405)
Rotiphorese 10x SDS PAGE	Carl Roth (3060.2)
Rotiphorese Gel A	Carl Roth (3037.1)
Rotiphorese Gel B	Carl Roth (3039.2)
Sodium acetate	Carl Roth (6773.1)
Sodium azide (NaN_3)	Sigma-Aldrich (52002)
Sodium chloride (NaCl)	Carl Roth (9265.2)
Sodium dihydrogen phosphate (NaH_2PO_4)	Carl Roth (K300.3)
Sodium dodecyl sulfate (SDS)	Carl Roth (2326.1)
Sodium hydroxide (NaOH)	Carl Roth (6771.1)
Spectra BR Multicolor Broad Range Protein Ladder	Thermo Fisher Scientific (26634)
Sulfuric acid (H_2SO_4)	Carl Roth (X873.1)
SYTOX Blue Dead Cell Stain	Invitrogen (S34857)
Tetramethylethylenedamine (TEMED)	Fluka (87689)
Tris Base	Calbiochem (648510)
Tris hydrochloride (Tris-HCl)	Carl Roth (9090.3)
Tris Pufferan	Carl Roth (4855.2)
Trypan blue	Life Technologies (15250-061)

Trypsin/EDTA	Life technologies (25300)
Tryptone N1 (TN1)	Organotechnic SAS (19553)
Tryptone/Peptone from casein	Carl Roth (8952.2)
Tween 20	Carl Roth (9127.1)
X-VIVO15	Lonza (BE02-060F)
Yeast extract	Carl Roth (2363.2)

2.1.2 Kits

Table 3. List of used kits

Kit	Supplier (Cat. No.)
Amine Coupling Kit	GE Life Science (BR100050)
ELISA MAX™ Deluxe Set Human MCP-1/CCL2	BioLegend (438804)
EndoFree Plasmid Maxi Kit	QIAGEN (12362)
EndoFree Plasmid Midi Kit	QIAGEN (12362)
Intracellular fixation and permeabilization buffer set	Thermo Fisher Scientific (88-8824-00)
KAPA HiFi PCR Kit	Roche (KK2101)
LEGENDplex HU Th1 Panel (5-plex)	BioLegend (740724)
Pierce BCA Protein Assay Kit	Thermo Fisher Scientific (23225)
Pierce ECL Western Blotting Substrate	Thermo Fisher Scientific (32106)
Pierce TMB Substrate Kit	Thermo Fisher Scientific (34021)
Plasmid Midi Kit	QIAGEN (12143)
QIAprep Spin Minprep Kit	QIAGEN (27106)
QIAquick Gel Extraction Kit	QIAGEN (28706)
QIAquick PCR Purification Kit	QIAGEN (28106)
RevertAid first strand cDNA synthesis kit	Thermo Fisher Scientific (K1612)
RNeasy Mini Kit	QIAGEN (74104)
T Cell TransAct, human	Miltenyi (130-111-160)
Zenon APC Human IgG Labeling Kit	Thermo Fisher Scientific (Z-25451)

2.1.3 Media, buffers and solutions

Table 4. List of used media, buffers and solutions

Medium/ Buffer/ Solution	Components
10x HBS-EP	0.1 M HEPES, 1.5 M NaCl, 30 mM EDTA, 0.5% (v/v) Tween 20% in ddH_2O, pH 7.4
10x PBS	1.4 mM NaCl, 27 mM KCl, 101 mM Na_2HPO_4, 18 mM KH_2PO_4 in ddH_2O
2x YT medium	16 g/L tryptone/peptone, 10 g/L yeast extract, 5 g/L NaCl in ddH_2O
2x YT-A/-AK medium	100 mg/L ampicillin (-A) or 100 mg/L ampicillin and 25 mg/L kanamycin (-AK) in 2x YT medium
2x YT-GA agar	15 g/L agar in 2x YT-GA medium
2x YT-GA medium	20 g/L glucose, 100 mg/L ampicillin in 2x YT medium
2x YT-K agar	15 g/L agar, 25 mg/L kanamycin in 2x YT medium
5x Laemmli buffer	250 mM Tris-HCl, 10% (w/v) SDS, 30% (v/v) glycerol, 0.05% (w/v) bromphenol blue in ddH_2O
BSA-PBS	2-4% (w/v) BSA in PBS
Coomassie Blue staining solution	60 mg/L Coomassie Brilliant Blue R 250, 35 mM HCl in ddH_2O
Flow cytometry buffer	2% (v/v) FCS, 1 g/L NaN_3 in PBS
Freezing medium	10% DMSO (v/v) in FCS
LB-A/-K agar	15 g/L agar in LB medium, 100 µg/mL ampicillin (-A) or kanamycin (-K)
LB-A/-K medium	10 g/L tryptone, 5 g/L yeast extract, 10 g/L NaCl in ddH_2O, 100 µg/mL ampicillin (-A) or kanamycin (-K)
M9 solution	58 g/L Na_2HPO_4, 30 g/L KH_2PO_4, 5 g/L NaCl, 10 g/L mM NH_4Cl in ddH_2O, adjust to pH7.2
Minimal agar	15 g/L agar, 2 g/L glucose, 1 mM $MgSO_4$, 2 mg/L thiamine, 100 ml M9 solution in ddH_2O
MPBS	2-4% (w/v) milk powder in PBS
PBST	0.05% (v/v) Tween 20 in PBS
PEI transfection reagent	0.1% (w/v) PEI dissolved at pH 2.0 in ddH_2O, adjust pH to 7.0
Periplasmic preparation buffer	30 mM Tris-HCl, 1 mM EDTA, 20% (w/v) sucrose in ddH2O, adjust to pH 8.0, add 5% (w/v) fresh lysozyme before use
Phage elution buffer	100 mM glycine-HCl, 0.5M NaCl in ddH_2O, adjust pH to 2.2

Phage neutralization buffer	1 M Tris-HCl in ddH_2O, adjust to pH 9.5
Phage precipitation buffer	2.5 M NaCl, 20% (w/v) PEG_{6000} in ddH_2O
Protein A binding buffer	100 mM NaH_2PO_4, 100 mM NaCl, 10 mM EDTA in ddH_2O, adjust to pH 7.0
Protein A elution buffer	0.1 M citric acid in ddH_2O, adjust to pH 3.0
Protein A neutralization buffer	1 M Tris Pufferan in ddH_2O, adjust to pH 9.0
Semi-dry blot buffer	48 mM Tris Pufferan, 39 mM glycine, 1.3 mM SDS, 20% (v/v) ethanol in ddH_2O, adjust to pH 9.0-9.4
Separating gel buffer	1 M Tris Pufferan in ddH_2O, adjust to pH 8.8
SOC medium	20 g/L tryptone, 5 g/L yeast extract, 2.5 mM KCl, 10 mM NaCl, 10 mM $MgSO_4$, 10 mM $MgCl_2$,20 mM glucose in ddH_2O
SP10 binding buffer	20 mM NaH_2PO_4, 500 mM NaCl,10 mM imidazol in ddH_2O, adjust to pH 7.4
SP500 elution buffer	20 mM NaH_2PO_4, 500 mM NaCl, 500 mM imidazol in ddH_2O, adjust to pH 7.4
SPR regeneration buffer	10 mM glycine in ddH_2O, pH 1.7
Stacking gel buffer	650 mM Tris Pufferan in ddH_2O, adjust to pH 6.8
Supplemented DMEM medium	10% (v/v) FCS, 1% (v/v) pen/strep in DMEM medium
Supplemented F17 medium	4 mM L-Glutamine, 0.1% (w/v) Kolliphor P188, 25 µg/mL G418 in F17 medium
Supplemented RPMI-1640 medium	10% (v/v) FCS, 1% (v/v) pen/strep in RPMI-1640 medium
Supplemented X-Vivo 15 medium	5% (v/v) FCS, 10 ng/mL IL-7, 10 ng/mL IL-15 in X-Vivo 15 medium
TN1 feeding medium	20% (w/v) TN1 in transfection medium
Transfection medium	4 mM L-Glutamine, 0.1% (w/v) Kolliphor P188 in F17 medium

2.1.4 Cell lines, primary cells and bacteria

Table 5. List of used cell lines, primary cells and bacteria

Cell line / Bacterial strain	Organism	Description	Supplier (Cat. No.)
HEK293-6E	*Homo sapiens*	Embryonic kidney cells constitutively expressing a truncated version of EBNA-1	National Research Council Canada
HEK293T	*Homo sapiens*	Embryonic kidney cells, expressing the SV40 T antigen	American Type Culture Collection (CRL-3216)
HUVEC2	*Homo sapiens*	Primary cells isolated from the umbilical cord vein of single donors	Promocell (C-12206)
K562	*Homo sapiens*	Myelogenous leukemia cell line	Kind gift of Prof. Schmitt, University Hospital Heidelberg
Nalm6	*Homo sapiens*	B cell precursors of acute lymphoblastic leukemia	German Collection of Microorganisms and Cell Cultures GmbH (ACC-128)
Peripheral blood mononuclear cells (PBMC)	*Homo sapiens*	Isolated from fresh blood or buffy coats of healthy donors by AG Krauss (NCT Heidelberg)	NCT Heidelberg (fresh blood), German Red Cross blood donor service Mannheim (buffy coats)
Raji	*Homo sapiens*	Burkitt's lymphoma B lymphocytes	Sigma Aldrich (85011429)
Raji-Gluc	*Homo sapiens*	Raji cells stably expressing gaussia luciferase	AG Krauss, NCT Heidelberg
Stbl 3	*Escherichia coli*	Bacterial strain used for selection after gateway cloning	New England BioLabs (C3040I)
TG1	*Escherichia coli*	Bacterial strain for phage display and scFv production	Agilent Technologies (200123)
THP1	*Homo sapiens*	Monocytic cell line established from an acute monocytic leukemia	German Collection of Microorganisms and Cell Cultures GmbH (ACC-16)

XL-1 Blue	*Escherichia coli*	Bacterial strain for DNA amplification	Stratagene (200228)

2.1.5 Bacteriophages

Table 6. List of used bacteriophages

Phage	Description	Supplier (Cat. No.)
VCSM13	Kanamycin resistant helper phage capable high single-stranded phagemid yields, derivative of M13KO7	Agilent Technologies (200251)

2.1.6 Vectors

Table 7. List of used vectors

Vector	Description	Supplier (Cat. No.)
pAB1	Bacterial expression of scFvs	Kind gift of Prof. Kontermann, University Stuttgart
pCMV6	Transient expression of mFc tagged antigens in mammalian cells	OriGene (PS100053)
pCMV-dR8.74 (Lentiviral helper plasmid #2)	Lentiviral packaging plasmid, used for lentiviral vector production	Kind gift of Dr. Schmidt, NCT Heidelberg
pCMX2.5-hIgG1-Fc	Transient expression of scFv-hFc in mammalian cells	
pConPlus IgG1	Transient expression of IgG1 heavy chain in mammalian cells	Lonza Group
pConPlus IgG1 [N297A]	Transient expression of IgG1 heavy chain with N297A substitution in mammalian cells	Lonza Group
pConPlus Kappa	Transient expression of kappa light chain in mammalian cells	Lonza Group
pConPlus Lambda	Transient expression of lambda light chain in mammalian cells	Lonza Group

pENTR1a (CD22-CD8-41BB-CD3ζ)	Gateway entry vector encoding anti-CD22 CAR based on the scFv SGIII (humanized RFB4 scFv), human CD8α hinge and transmembrane region, human 4-1BB (CD137) and CD3zeta signaling domains	AG Krauss, NCT Heidelberg, modified from pENTR1a (kind gift of Dr. Schmidt, NCT Heidelberg)
pHENIS	Phagemid vector encoding scFv fused to the phage coat protein pIII to enable scFv surface presentation	Kind gift of Prof. Kontermann, University Stuttgart
pMD2.G-VSV-G (Lentiviral helper plasmid #1)	Lentiviral envelope plasmid, used for lentiviral vector production	Kind gift of Dr. Schmidt, NCT Heidelberg
pRRL#5	Gateway destination vector for stable expression of lentiviral vectors in mammalian cells	Kind gift of Dr. Schmidt, NCT Heidelberg
pRRLSIN.cPPT.hEF1a.WPRE	Lentiviral vector for stable expression of gene of interest (e.g. CAR) in mammalian cells	AG Krauss, NCT Heidelberg, modified from pRRL#5
pSCon IgG1	Subcloning vector for antibody heavy chain	Lonza Group
pSCon Kappa	Subcloning vector for antibody kappa light chain	Lonza Group
pSCon Lambda	Subcloning vector for antibody lambda light chain	Lonza Group
αCD22CAR	Anti-CD22 CAR based on the scFv SGIII (humanized RFB4 scFv), human CD8α hinge and transmembrane region, human 4-1BB (CD137) and CD3zeta signaling domains	AG Krauss, NCT Heidelberg

2.1.7 Primers

Primers were purchased from Thermo Fisher Scientific.

Table 8. List of used primers

Name	Sequence 5'→3'	Description
4-1BB_rv	GCAGAAAGAAGCTCCTGTATATATTCA	Amplification and sequencing of CAR upstream to 4-1BB domain
BamHI_CD3zeta_Rev	TATAGGATCCGCGAGGGGGCAGGGCCTGC	Amplification of CAR and BamHI insertion
BamHI-IgGVHSP fw	TATAGGATCCATGGGATGGTCATGTATCATCC	Amplification of scFv and BamHI insertion
CCL2_fw	GAGAGGCTGAGACTAACCCAGA	Amplification of CCL2 cDNA
CCL2_NB7.E5_VH_Fw	TATAGTGCACTCGCAGGTCCAGCTGGTAC	Amplification of antibody heavy chain encoded in pAB1 and ApaLI insertion
CCL2_NB7.E5_VH_Rev	ACTCGAGACAGTGACCAG	Amplification of antibody heavy chain encoded in pAB1
CCL2_NB7.E5_VL_Fw	TATAGTGCACTCGGACATCGTGATGACCC	Amplification of antibody light chain encoded in pAB1 and ApaLI insertion
CCL2_NB7.E5_VL_Rev	TATACGTACGTTTGATTTCCAGC	Amplification of antibody light chain encoded in pAB1 and BsiWI insertion
CCL2_rev	ATCACAGCTTCTTTGGGACACT	Amplification of CCL2 cDNA
CD3z-XbaI-rev	TAATCTAGATTAGCGAGGGGGCAG	Amplification of CAR and XbaI insertion
CD8-fw	CGTGCGGCCGCATTCGTGC	Sequencing of CAR downstream to CD8α hinge
CH1 rev	TCAGGGCTCCGCTGTTCC	Sequencing of antibody heavy chain in pConPlus
CH2 forw	ACCCTGATGATCAGCAGAAC	Sequencing of antibody heavy chain in pConPlus
CH3 rev	AACACGTTGCCCTGCTGC	Sequencing of antibody heavy chain in pConPlus
cPPT Seq_fw	GTAGACATAATAGCAACAGACATAC	Sequencing downstream to cPPT element

Fdseqlong_rv	GTAAAACGACGGCCAGTGAATTC	Amplification of scFv encoded in pHENIS
GAPDH fw	CAAGGTCATCCATGACAACTTTG	Amplification of GAPDH cDNA
GAPDH rev	GTCCACCCTGTTGCTGTAG	Amplification of GAPDH cDNA
hEF1a fw	CAAGCCTCAGACAGTGGTTC	Amplification and sequencing of downstream to promoter
LMB2_rv	GTAAAACGACGGCCAGTGAATTC	Amplification of scFv in pAB1
LMB3long_fw	CAGGAAACAGCTATGACCATGATTAC	Amplification of scFv encoded in pHENIS
M13-RP	CAGGAAACAGCTATGACC	Sequencing of scFv encoded in pHENIS
NB7.E5 scFv_rev_2	AGATGAGTTTTTGTTCTGCGGC	Amplification of NB7.E5 cDNA
NB7.E5_scFv_fw_2	GTAGCAACTGCAACCGGTCA	Amplification of NB7.E5 cDNA
pConPluskappa forw	AGCAGCTGAAGAGCGGCA	Sequencing of antibody light chain in pConPlus
pConPluskappa rev	TCCTGCTCGGTGACGCTC	Sequencing of antibody light chain in pConPlus
pConPluslambda forw	GCCGTGACAGTGGCTTG	Sequencing of antibody light chain in pConPlus
pConPluslambda rev	AGGCGTCAGGCTCAGATAG	Sequencing of antibody light chain in pConPlus
PCR2	TTAGCTCACTCATTAGG	Sequencing of antibody heavy and light chain in pSCon
pENTR_anti	GATTTTGAGACACGGGCCAGA	Sequencing of CAR
pENTR_sense3	CATAAACTGCCAGGCATCAAACTAAG	Amplification and sequencing of CAR
prehFc_rev	GGTCCGGGAGATCATGAG	Sequencing of scFv in pCMX2.5-hIgG1-Fc
T2A-CAR fw	GCAGTCTGCTGACATGCGGTGACGTGGAAGAGAATCCCGGCCCTATGGAAAGGCACTGGATCTTTCTC	Amplification of CAR and insertion of T2A overhang

T2A-GSG-myc rev	CTTCCACGTCACCGCATGTCAGCAGACTGCCTCTGCCCTCTCCGGAGCCCAGATCCTCTTCTGAGATGAG	Amplification of scFv and insertion of T2A overhang
TATA+AgeI+NB7.E5 scFv_Fw	TATAACCGGTCAGGTCCAGCTGGTACAGTC	Amplification of scFv encoded in pAB1 and AgeI insertion
TATA+XbaI+Stop+myc_Rev	TATATCTAGATTACAGATCCTCTTCTGAGATGAG	Amplification of scFv encoded in pAB1 and XbaI insertion
WPRE_rev	AGCAACATAGTTAAGAATACCAGTC	Amplification and sequencing upstream to WPRE element
YU109A1 VL fw	TATAGTGCACTCGCAGCTTGTGCTGACTC	Amplification of antibody light chain encoded in pAB1 and ApaLI insertion
YU109A1 VL rev	TATACCTAGGACGGTCAGCATGG	Amplification of antibody light chain encoded in pAB1
YU109A1/B1/D1 VH rev	TATACTCGAGACGGTGACCATTGTCC	Amplification of antibody heavy chain encoded in pAB1
YU109A1/H1 VH fw	TATAGTGCACTCGGAGGTGCAGCTGGTGC	Amplification of antibody heavy chain encoded in pAB1 and ApaLI insertion
YU109B1 VL fw	TATAGTGCACTCGTCTTCTGAGCTGACTC	Amplification of antibody light chain encoded in pAB1 and ApaLI insertion
YU109B1/110D1 VH fw	TATAGTGCACTCGCAGGTGCAGCTGG	Amplification of antibody heavy chain encoded in pAB1 and ApaLI insertion
YU109B1/E1/110D1 VL rev	TATACCTAGGACGGTCAGCTTG	Amplification of antibody light chain encoded in pAB1
YU109D1 VH fw	TATAGTGCACTCGGAGGTGCAGCTGGTGG	Amplification of antibody heavy chain encoded in pAB1 and ApaLI insertion
YU109D1 VL fw	TATAGTGCACTCGCAGCCTGTGCTGACTC	Amplification of antibody light chain encoded in pAB1 and ApaLI insertion
YU109D1 VL rev	TATACCTAGGACGGTCAGCGTG	Amplification of antibody light chain encoded in pAB1
YU109E1 VH fw	TATAGTGCACTCGCAGGTACAGCTGCAGC	Amplification of antibody heavy chain encoded in pAB1 and ApaLI insertion
YU109E1 VL fw	TATAGTGCACTCGCAGGCTGTGCTGACTC	Amplification of antibody light chain encoded in pAB1 and ApaLI insertion

YU109E1/H1 VH rev	TATACTCGAGACGGTGACCAGGG TTC	Amplification of antibody heavy chain encoded in pAB1
YU109H1 VL fw	TATAGTGCACTCGGAAACGACAC TCACG	Amplification of antibody light chain encoded in pAB1 and ApaLI insertion
YU109H1 VL rev	TATACGTACGTTTGATATCCACTT TG	Amplification of antibody light chain encoded in pAB1 and BsiWI insertion
YU110B1 VH fw	TATAGTGCACTCGGAAGTGCAGC TGGTGG	Amplification of antibody heavy chain encoded in pAB1 and ApaLI insertion
YU110B1 VH rev	TATACTCGAGACGGTGACTAGGG TTC	Amplification of antibody heavy chain encoded in pAB1
YU110B1 VL fw	TATAGTGCACTCGCAGTCTGTGCT GACTC	Amplification of antibody light chain encoded in pAB1 and ApaLI insertion
YU110B1 VL rev	TATACCTAGGACGGTCAGCTTAGT C	Amplification of antibody light chain encoded in pAB1
YU110D1 VH rev	TATACTCGAGACGGTGACCGTGG TC	Amplification of antibody heavy chain encoded in pAB1
YU110D1 VL fw	TATAGTGCACTCGCAGGCTGGGC TGACTC	Amplification of antibody light chain encoded in pAB1 and ApaLI insertion

2.1.8 Antibodies

Table 9. List of used antibodies

Target structure, name, clonality	Host	Target	Conjugate	Supplier (Cat. No.)
CCL2, monoclonal	rabbit	human		Thermo Fisher Scientific (700489)
CCR2, monoclonal	mouse	human	PE	BioLegend (357205)
CD22, monoclonal	mouse	human	PE	BD (337899)
CD3, monoclonal	mouse	human	FITC	BioLegend (300406)
c-myc, monoclonal	mouse	human	HRP	Roche (11814150001)
c-myc, monoclonal	mouse	human		Roche (11667149001)
ERK1/2 phospho (Thr202/Tyr204), monoclonal	mouse	human		BioLegend (369501)

ERK1/2, monoclonal	rat	human		BioLegend (686902)
GAPDH, monoclonal	mouse	human	HRP	Proteintech (HRP-60004)
HSV-1/2 glycoprotein B, HDIT101 IgG, monoclonal	humanized	human		Heidelberg ImmunoTherapeutics GmbH, Heidelberg
HSV-1/2 glycoprotein B, mAb2c IgG, monoclonal	mouse	human		AG Krauss, NCT Heidelberg
IgG $(Fab')_2$ fragment, polyclonal	goat	rabbit	HRP	Jackson ImmunoResearch (111-035-047)
IgG $(Fab')_2$ fragment, polyclonal	goat	human	HRP	Jackson ImmunoResearch (109-035-006)
IgG Fc gamma, polyclonal	rabbit	human	FITC	Jackson ImmunoResearch (309-096-008)
IgG Fc gamma, polyclonal	rabbit	human	HRP	Jackson ImmunoResearch (309-035-008)
IgG Fc gamma, polyclonal	goat	mouse	HRP	Jackson ImmunoResearch (115-035-008)
IgG Fc gamma, polyclonal	goat	mouse	FITC	Jackson ImmunoResearch (115-095-008)
IgG Fc, monoclonal	mouse	human	HRP	Abcam (ab7499)
IgG, polyclonal	goat	rat	HRP	BioLegend (405405)
Isotype control, IgG2a	mouse	Isotype control		BioLegend (400213)
IZI08 scFv, monoclonal	humanized	EGFR		Prof. Kontermann, University Stuttgart
M13 phage, monoclonal	mouse	phage	HRP	GE Healthcare (27-9421-01)
NRP1, monoclonal	mouse	human		R&D Systems (MAB3870)
PD-1, Nivolumab, monoclonal	human	human		Bristol-Myers Squibb (BMS-936558)

2.1.9 Antibody library

Table 10. List of used antibody library

Antibody library	Description	Supplier (Cat. No.)
Lymph Node Derived Antibody Libraries (LYNDAL)	Phage display library consisting of immune repertoires derived from lymph nodes of 25 head and neck cancer patients, diversity approximately $5x10^9$ clones	In-house, originally generated by Diebolder et al. [152] and extended further by AG Krauss, NCT Heidelberg

2.1.10 Enzymes

Table 11. List of used enzymes and proteins

Enzymes / Proteins	Supplier (Cat. No.)
AgeI-HF	New England Biolabs (R3552S)
Alkaline phosphatase, calf intestinal	New England Biolabs (M0290S)
ApaI	New England Biolabs (R0114S)
ApaLI	New England Biolabs (R0507S)
AscI	New England Biolabs (R0558S)
AvrII	New England Biolabs (R0174S)
BamHI-HF	New England Biolabs (R3136S)
BsiWI-HF	New England Biolabs (R3553S)
CCL11	Peprotech (300-21)
CCL13	Peprotech (300-24)
CCL2	Peprotech (300-04)
CCL7	Peprotech (300-17)
CCL8	Peprotech (300-15)
DNA polymerase I, Large (Klenow) fragment	New England Biolabs (M0210S)
DNase I	Invitrogen (18068-015)
Gateway LR Clonase II	Invitrogen (11791-100)
Gel Filtration Standard	BioRad (1511901)
HindIII-HF	New England Biolabs (R3104S)
Human IL-15	Miltenyi (130-095-765)
Human IL-7	Miltenyi (130-095-363)

KAPA2G Fast Ready Mix with Dye	Roche (KK5103)
Lysozyme	Roche (10837059001)
Mouse IgG, Fc fragment	Jackson ImmunoResearch (015-000-008)
Murine Fc (mFc)	Valentino De Leo, AG Krauss, NCT Heidelberg
NcoI-HF	New England Biolabs (R3193S)
NotI-HF	New England Biolabs (R3189S)
NRP1	ACRO Biosystems (NR1-H5228)
Protein A	Thermo Scientific (21181)
Protein L, biotinylated	GenScript (M00097)
PvuI-HF	New England Biolabs (R3150S)
SalI-HF	New England Biolabs (R3138S)
Sema3A	R&D Systems (1250-S3-025)
SfiI	New England Biolabs (R0123S)
Streptavidin-APC	BioLegend (405207)
Streptavidin-HRP	Thermo Fisher Scientific (21130)
T4 DNA Ligase	Thermo Fisher Scientific (EL0016)
VEGF165, biotinylated	ACRO Biosystems (VE5-H8210)
XbaI	New England Biolabs (R0145S)
XhoI	New England Biolabs (R0146S)

2.1.11 Consumables

Table 12. List of used consumables

Consumable	Supplier
1.5 mm SDS PAGE casette	Invitrogen
24-well plate polystyrene non-treated cell culture plate	Corning
6.5 mm Transwell with 3.0 µm Pore Polyester Membrane Insert	Corning
96 well polypropylene V-bottom plate	Greiner Bio-One
96-deep-well polystrene microtiter plate	Sigma
96-well half area microtiter plate	Nunc
96-well Maxisorp microtiter plate	Nunc
96-well U-bottom polystyrene microtiter plate	Greiner Bio-One
96-well white polystyrene microplate	Corning
AeraSeal breathable sealing film	Excel Scientific

Bacterial culture tube (12 mL)	Greiner Bio-One
Bottle top filter 50 mm	Thermo Fisher Scientific
Cell culture flask for adherent cells (T25, T75, T175)	Greiner Bio-One
Cell culture flask for suspension cells (T75, T175)	Greiner Bio-One
Centricon Plus-70	Merk Millipore
CM5 sensor chip	GE Healthcare
Cryogenic vial with screw cap (2.0 mL)	Greiner Bio-One
Dialysis membrane ZelluTrans	Carl Roth
Electroporation cuvette	BioRad
Erlenmeyer cell culture flask with filter cap (125 mL)	Corning
Erlenmeyer cell culture flask with filter cap (500 mL)	BD Biosciences
Extra thick blot paper / Mini blot size	BioRad
Flow cytometry round-bottom tubes	Falcon
Nitrocellulose western blot membrane	neoLab
PCR tube strip with 8 tubes (0.2 mL)	neoLab
PCR tubes, flat cap (0.2 mL)	AHN Biotechnology
Petri dish 100 mm	Greiner Bio-One
Pipette filter tip (10, 20, 200, 1000 µL)	Greiner Bio-One
Plastic syringe (20 mL, 50 mL)	BD Biosciences
Plastic vials, 11 mm	GE Healthcare
Polypropylene conical tube (15 mL, 50 mL)	Falcon
Polystyrene round bottom tube (5 mL)	Falcon
Reaction tubes (1.5 mL, 2.0 mL)	neoLab
Reagent reservoir (50 mL)	Corning
Rubber caps, type 2	GE Healthcare
Rubber caps, type 5	GE Healthcare
Serological pipette (1, 2, 5, 10, 25 and 50 mL)	Corning
Square dish 120 x 120 x 17 mm	Greiner Bio-One
Syringe filter 0.22 µm	Merk Millipore
Tissue culture dish with 20 mm grid	Corning

2.1.12 Chromatography columns

Table 13. List of used chromatography columns

Column	Supplier (Cat. No.)
HiLoad 16/600 Superdex 75 pg (120 mL)	GE Healthcare (28989333)
HisTrap FF (1 mL)	GE Healthcare (17531901)
HiTrap rProtein A FF (1 mL)	GE Healthcare (17507901)
Superdex 200 Increase 10/300 GL (20 mL)	GE Healthcare (28990944)
Superdex 75 Increase 10/300 GL (20 mL)	GE Healthcare (29148721)

2.1.13 Laboratory equipment

Table 14. List of used laboratory equipment

Instrument	Type	Supplier
Absorbance and fluorescence plate reader	Infinite F200Pro	Tecan
Agarose gel station	Mini Sub-Cell GT Sub-Cell GT	Bio-Rad Laboratories
Automatic dispenser pipette	Multipette Stream	Eppendorf
Automatic multichannel pipette	Xplorer	Eppendorf
Bacteriological incubator	BE 2000 32l Heraeus B6	Memmert Thermo Fisher Scientific
Balance	AJ-2200CE Vibra	Shinko Denshi
Cell culture shaker	Minitron Multitron Pro	Infors HT
Centrifuge	5424 R C5-6R Heraeus Megafuge 40R Megafuge 1.0 Mikro 200R Multifuge 4KR Sorvall RC 6+	Eppendorf Beckmann Thermo Fisher Scientific Heraeus Hettich Thermo Fisher Scientific Thermo Fisher Scientific
Centrifuge mini	3-1810	neoLab

Chemiluminescence visualization system	INTAS Advanced Fluorescence Imager	Intas Science Imaging
CO_2 incubator	Heracell 150 NU-5510E	Thermo Fisher Scientific Ibs Tecnorama
Electroblotting system	Trans Blot Semi-Dry Transfer Cell	Bio-Rad Laboratories
ELISA washer	Elx405	BIO-TEK
Flow cytometer	BD FACS Celesta BD FACS Verse	BD Biosciences
FPLC system	AEKTAFPLC system AEKTApure FPLC system	Amersham Bioscience GE Healthcare
Gel visualization system	Gel Jet Imager	Intas Science Imaging
Heating block	HBT-2 131 TH 21	HLC Biotech
Hemocytometer	Neubauer improved	Karl Hecht
Inverted microscope	CKX41	Olympus
Magnetic stirrer	MR2000 2mag Mix 1 XL	Heidolph Instruments 2mag AG
Magnetic tray	DynaMag-2 Magnet	Thermo Fisher Scientific
Multichannel pipette	Pipetman neo P200	Gilson
Orbital plate shaker	DRS-12	neoLab
PCR thermocycler	peqSTAR 96 Universal Gradient	peqLab
pH meter	PB-11	Sartorius
Photometer	NanoDrop ND-1000 NanoDrop 2000c	Thermo Fisher Scientific
Pipette controller	Pipetus	Hirschmann
Pipettes	Pipetman neo P1000, P200, P20, P10	Gilson
Power supply	PowerPac Basic PowerPac HC peqPower	Bio-Rad Laboratories Bio-Rad Laboratories peqLab
Precision balance	CPA22D-OCE	Sartorius
Rocking plate shaker	DSG 304/M4	Heidolph Instruments

Scanner	Perfection V750 Pro	Epson
SDS gel station	Novex Mini-Cell	Invitrogen
Sonicator	UW 2070	Bandelin electronic
Sterile bench	SAFE2020 HERAsafe KSP 12	Thermo Fisher Scientific
Surface plasmon resonance based instrument	Biacore 2000	GE Healthcare
Vortex	L46 D-6012	GLW neoLab
Water bath	T100	Labortechnik Medingen

2.1.14 Software and online tools

Table 15. List of used software and online tools

Software / Online tool	Description	Supplier/Homepage
BD FACS Diva	Acquisition and analysis of flow cytometric data	BD Biosciences
BD FACS Suite	Acquisition and analysis of flow cytometric data	BD Biosciences
BIACORE Control	BIACORE controlling software	GE Healthcare
BIAevaluation	Sensorgram evaluation	GE Healthcare
Chemo Star Imager 3.14	Fluorescence and ECL visualization	Intas Science Imaging
Epson Scan	Image scan and digitalization	Epson
ExPASy ProtParam	Analysis of physical and chemical parameters of proteins	http://web.expasy.org/protparam/
Fiji	Image processing software for scientific image analysis	ImageJ [153]
FlowJo 10.3	Flow cytometric data evaluation	Tree Star
Geneious 10.1	Cloning manager	Biomatters
GraphPad Prism 7.0	Statistical analysis and graphical illustrations	GraphPad Software
IMGT/V-Quest	Database containing antibody germline sequences	IMGT/V-Quest [154]
Intas GDS 3.3.9	DNA visualization and documentation	Intas Science Imaging

LEGENDplex Data Analysis Software 8.0	Analysis of LEGENDplex data	BioLegend
Mendeley	Reference manager	Elsevier
Microsoft Office 2010	Data evaluation, illustration and text processing	Microsoft
NanoDrop 1000 3.8.1	Spectrophotometer control	Thermo Fisher Scientific
Photoshop Elements 10	Image editing	Adobe Systems
Tecan i-control 3.7.3	Absorbance/fluorescence reader	Tecan Austria
Unicorn 5.10	FPLC control	GE Healthcare
Unicorn 6.3	FPLC control	GE Healthcare
VBASE2	Database containing antibody germline sequences	VBASE2 [155]

2.2 Methods

2.2.1 Phage display

2.2.1.1 Helper phage titer determination

E. coli TG1 were streaked out on minimal agar plates and grown overnight at 37 °C. 4 mL 2x YT medium were inoculated with a single colony and incubated overnight at 37 °C, 225 rpm. 100 µL bacterial culture were used to inoculate 14 mL 2x YT medium and incubated at 37 °C, 180 rpm, until an OD_{600} of 0.5 was reached. 15 µL of a serial dilution (10^{-6} to 10^{-9} for VCSM13 helper phages and 10^{-9} to 10^{-12} for library phages) of phages in 2x YT medium were used to infect 285 µL of log phase *E. coli* TG1 and incubated for 30 min at 37 °C followed by 30 min at 37 °C, 160 rpm. 100 µL of infected *E. coli* TG1 were streaked out in duplicates on 2x YT-K plates or 2x YT-GA plates to amplify helper or library phages, respectively, and grown overnight at 37 °C. Colonies were counted and transducing units per mL (TU/mL) were calculated.

2.2.1.2 Phage display selection of anti-CCL2 scFvs from LYNDAL

CCL2-specific scFvs were selected from our in-house antibody library LYNDAL [152] by means of phage display (*Figure 8*). LYNDAL comprises 20 individual phage display libraries consisting of IgG VH and VL repertoires from lymph node-derived B cells of head and neck cancer patients. VH and VL sequences are cloned as scFvs in the phagemid vector pHENIS which encodes the phage coat protein pIII, thereby enabling presentation of the scFv on the phage surface. LYNDAL constitutes a large source (in total approximately 5×10^9 clones) of human variable antibody domains and is stored as *E. coli* TG1 glycerol stocks at -80 °C.

E. coli TG1 were prepared the day before use by inoculating 4 mL 2x YT medium with a single colony picked from a minimal plate and subsequent overnight growth at 37 °C, 180 rpm.

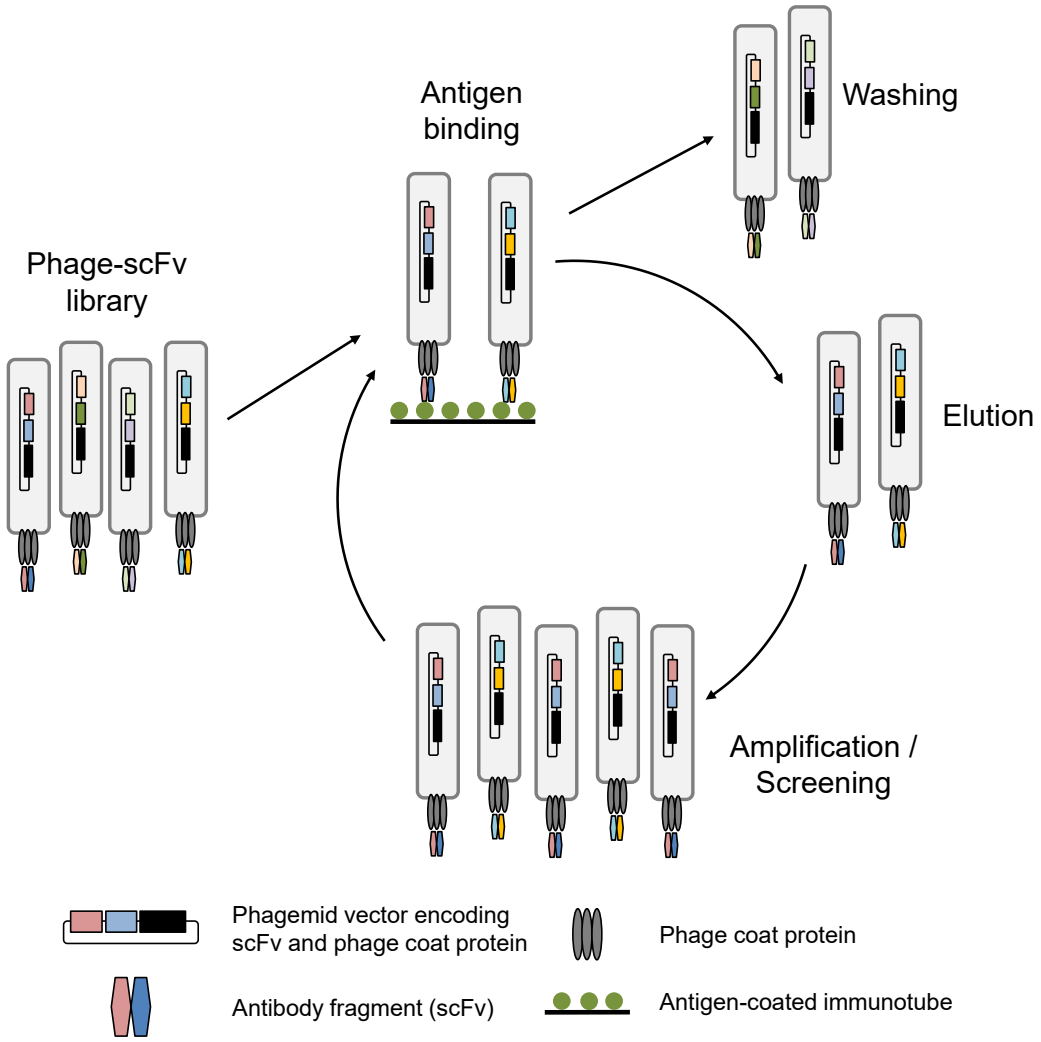

Figure 8. Phage display. Phages presenting the LYNDAL-scFvs were incubated with the antigen of interest coated to an immunotube. Unbound phages were removed by washing and binders were recovered by elution. Binders were further amplified in bacteria and entered another selection round. After three selection rounds, phages were screened for binding.

For the first selection round, phages were produced from the antibody libraries containing bacterial stock. Therefore, 1200 mL 2x YT-GA medium were inoculated with bacterial library stock such that the starting OD_{600} was 0.1. For the following selection rounds, 60 µL infected bacteria from the previous round were used to inoculate 200 mL 2x YT-GA medium. Bacteria were grown at 37 °C, 180 rpm, until an OD_{600} of 0.5 was reached.

Bacteria were infected with VCSM13 helper phages at a multiplicity of infection (MOI) of 15 and incubated for 30 min at 37 °C followed by 30 min at 37 °C, 160 rpm. Infected bacteria were centrifuged for 15 min at 3500 g and resuspended in fresh 2x YT-AK medium supplemented with

0.5 mM isopropyl β-D-1-thiogalactopyranoside (IPTG) to induce phage production. The culture was incubated for 6 h at 28 °C, 130 rpm.

Produced phages were purified by precipitation. For this purpose, the culture was centrifuged for 15 min at 3500 g and 4 °C followed by addition of 20 % (v/v) precipitation buffer and incubation overnight at 4 °C. Phages were pelleted by 45 min centrifugation at 3500 g, 4 °C, and washed with 20 mL ice cold phosphate buffered saline (PBS). For a second precipitation step, the phages were centrifuged for 45 min at 3500 g at 4 °C, 20 % (v/v) precipitation buffer was added to the supernatant and incubated 1 h on ice. Phages were harvested by 45 min centrifugation at 3500 g, 4 °C, and resuspended in 300 µL PBS. Remaining debris was removed by 3 min centrifugation at maximum speed, 4 °C. Phage titer was determined as described in *2.2.1.1*.

The selection of antigen-specific scFv presenting phages was performed in three rounds in immunotubes. For the first selection round 20 µg/mL CCL2-murine fragment crystallizable (mFc) and for the following selection rounds 10 µg/mL CCL2-mFc in 3 mL PBS were incubated in the immunotube overnight at 4 °C. The immunotube was blocked by addition of 2 % MPBS for 2 h at RT. 10^{12} phages in 3 mL 2 % MPBS were added and incubated for 90 min at RT followed by 30 min rotation. Unbound phages were removed by washing 5x with PBS-T and 5x with PBS for the first selection round, 10x with PBS-T and 10x with PBS for the second selection round and 15x with PBS-T and 15x with PBS for the third selection round. Antigen binding phages were recovered by addition of 1 mL elution buffer and rotation for 8 min at RT. Eluted phages were transferred to a new tube and 130 µL neutralization buffer were added.

8.9 mL *E. coli* TG1 culture (OD_{600} = 0.5) were infected with eluted phages for 30 min at 37 °C followed by 30 min at 37 °C, 160 rpm. 10 µL of the infected bacteria were used for titer determination (10^{-2} to 10^{-6} serial dilution) as described in *2.2.1.1*. Remaining bacteria were centrifuged for 10 min at 400 g at 4 °C. The pellet was resuspended in 1 mL 2x YT medium, streaked onto a 2x YT-GA plate (12 cm x 12 cm) and grown overnight at 30 °C. The colonies were harvested with 4 mL 2x YT medium using a glass spatula and stored as glycerol stock (final concentration 15 %) at -80 °C.

Panning round 3 phage-infected glycerol stock of *E. coli* TG1 was plated onto 2x YT-GA plates and incubated overnight at 30 °C. Single colonies were used to inoculate 100 µL 2x YT-GA medium in a 96-well plate using a sterile tip. The same tip was used for colony PCR screening (see *2.2.2.4*). The 96-well plates were incubated overnight at 37 °C, 160 rpm, and stored as “master plate” glycerol stocks (final concentration 15 %) at -80 °C.

2.2.1.3 Polyclonal phage ELISA

Enrichment of antigen specific phages during three panning rounds of phage display was monitored by polyclonal phage enzyme linked immunosorbent assay (ELISA). The working volume was 100 µL/well.

A 96-well ELISA plate was coated overnight at 4 °C with 3 µg/mL antigen and control proteins diluted in PBS. Wells were blocked with 400 µL/well 2 % MPBS for 2 h at RT. 10^{12} phages/well in PBS were added and incubated 1h at RT. The plate was washed 3x with PBS-T and 3x with PBS (350 µL/well). Anti-M13 HRP conjugated antibody diluted in 2% MPBS was added for 1 h at RT. Plate was washed as described before, TMB solution was added and incubated in the dark at RT. Reaction was stopped by addition of 50 µL/well 2 N sulfuric acid. Absorbance was measured at 450 nm wavelength (620 nm reference) using a plate reader.

2.2.1.4 Anti-CCL2 and anti-NRP1 scFvs selected by YUMAB GmbH

Our collaboration partner Yumab GmbH was supplied with internally produced CCL2-mFc and commercially available NRP1-His (ACRO Biosystems). Phage display was performed to select antigen-specific scFvs from their naïve antibody library HAL9/10 [156]. We received five CCL2-specific scFv clones, namely YU109A1, YU109B1, YU109D1, YU109E1 and YU109H1, as well as two NRP1-specific scFv clones, namely YU110B1 and YU110D1.

2.2.2 Molecular biological methods

2.2.2.1 Cloning of antigen, antibody and CAR coding sequences

Antigen coding sequences were codon optimized and synthesized by Eurofins Genomics. The coding sequences were cloned into the mammalian expression vector pCMV6 (AscI x XhoI) which includes a mouse Fc tag 3' of the insertion site. The CCL2-mFc sequence encodes for the full-length protein with P8A substitution. This substitution ablates dimerization of CCL2 and at the same time ensures the same biological activity as the wild type [157]. NRP1 (CUB1)-mFc and NRP1 (CUB1CUB2)-mFc contain amino acids 1-144 and 1-272, respectively, which are described to encompass the Sema3A binding domain. The

recombinant protein domains were produced in HEK293-6E and purified via Protein A affinity chromatography and size exclusion chromatography as described in *2.2.4.4*

ScFv, scFv-hFc and IgG1 antibody formats were used for the analysis of binding characteristics and functional assays. The in-house selected CCL2 specific scFv NB7.E5 carrying a His- and c-myc-tag was cloned into the pAB1 vector (NotI x SfiI) for expression in *E. coli* TG1 (see *2.2.3.1*). Clones received from Yumab GmbH were cloned as scFv-hFc in the mammalian expression vector pCMX2.5 (NotI x NcoI). NB7.E5 was synthesized by Eurofins Genomics to match the restriction sites and linker of the Yumab GmbH derived scFvs and was also cloned as scFv-hFc in the pCMX2.5 vector. All antigen-specific clones were further produced as full length IgG1 with the N297A substitution to ablate antibody effector functions. For this purpose, variable heavy (VH) chain segments and variable light (VL) chain segments were cloned into the corresponding subcloning vector pSCon IgG1 (ApaLI x XhoI), pSCon Lambda (ApaLI x AvrII) or pSCon Kappa (ApaLI x BsiWI), which contained the Kozak and leader sequence. The VH and VL domains were further cloned into the corresponding mammalian expression vectors pConPlus IgG1 [N297A] (HindIII x ApaI), pConPlus Lambda (HindIII x AvrII) or pConPlus Kappa (HindIII x BsiWI). NB7.E5 was additionally cloned as full-length IgG1 antibody carrying the wild-type N297 by using the expression vector pConPlus IgG1 (HindIII x ApaI). For production of the antibodies in HEK293-6E (see *2.2.3.4*) either cotransfection of the pConPlus vectors was performed or digested subcloning vectors were ligated and the double gene vector (DGV) (PvuI x NotI) was transfected.

The CCL2 specific scFv NB7.E5 was further included for soluble expression in an anti-CD22 CAR. Therefore, the NB7.E5 scFv coding sequence was fused to the CAR encoding sequence either at the N-terminus (αCCL2scFv-αCD22CAR) or the C-terminus (αCD22CAR-αCCL2scFv). The “self-cleaving” peptide thosea asigna virus 2A (T2A) was synthesized by Eurofins Genomics and included between CAR and NB7.E5 scFv sequences (NcoI x BamHI) to allow encoding of two proteins on the same open reading frame. The full CAR sequence encompassed the anti-CD22 scFv SGIII (humanized RFB4 antibody, [158]), a CD8α hinge and transmembrane domain as well as the costimulatory domain 4-1BB (CD137) and the activation domain of the CD3-zeta chain (ζ). This backbone corresponds to the clinically approved anti-CD19 CAR tisagenlecleucel [159]. αCD22CAR-αCCL2scFv was generated by restriction digest (AgeI x XbaI) and ligation (see *2.2.2.7* and *2.2.2.9*) of NB7.E5 scFv and CAR sequence encoded on the vector pENTR1a. By gateway cloning (see *2.2.2.5)* from the entry vector pENTR1a the construct was transferred to the expression vector pRRL#5. Since

pRRL#5 contains an unfavorable internal ribosome entry site (IRES) and puromycin resistance, these sequences were removed by restriction digestion (XbaI x SalI), blunting reaction and ligation. To generate αCCL2scFv-αCD22CAR, NB7.E5 scFv was fused to T2A by overlap extension PCR (see *2.2.2.3*) and the construct was cloned into pRRLSIN.cPPT.hEF1a.WPRE by restriction digest (BamHI x XbaI) and ligation. αCD22CAR-αCCL2scFv expression is driven by a phosphoglycerate kinase (PGK) promoter, whereas the vector used for αCCL2scFv-αCD22CAR expression contains a human elongation factor-1 alpha (EF1α) promoter.

2.2.2.2 Polymerase chain reaction

Polymerase chain reaction (PCR) was performed to amplify DNA or introduce new restriction sites. *Table 16* shows the components of the PCR mix and *Table 17* the reaction conditions for use in a thermocycler. The primer melting temperature (Tm) was calculated according to the formula:

$$Tm = 4\,°C\ x\ (C + G) + 2\,°C\ x\ (A + T)$$

DNA was purified using a PCR purification kit according to the manufacturer's recommendations. DNA concentration was quantified photometrically.

Table 16. PCR reaction mix

Component	Final amount/ concentration
Template DNA	100 ng
KAPA HiFi Buffer (5x)	1x
KAPA HiFi Polymerase (1 U/µL)	1 U
dNTP Mix (10 mM)	0.2 mM
Forward primer (25 µM)	0.5 µM
Reverse primer (25 µM)	0.5 µM
ddH_2O	*ad* 50 µL

Table 17. PCR reaction conditions

Step	Temperature [°C]	Time [s]	Cycles
Initial denaturation	95	300	1
Denaturation	98	20	35
Annealing	Tm – 4 °C	15	35
Elongation	72	60 s/kb	35
Final elongation	72	300	1
Cooling	4	∞	1

2.2.2.3 Overlap extension polymerase chain reaction

Overlap extension PCR was used to align two partly complementary DNA templates. The PCR reaction mix and conditions were set up as described in *2.2.2.2* with the following modifications: First, 5 PCR cycles without primers were performed to allow alignment of the overlapping DNA stretches and extension. Afterwards, the primers were added and 16 cycles were run to amplify the aligned DNA template.

2.2.2.4 Polymerase chain reaction from bacterial glycerol stock or colony

PCR from the bacterial glycerol stock was performed to analyze the integrity of phage display selected scFvs from the master plate (see *2.2.1.2*). PCR from bacterial colonies was performed to screen for sequence insertion after cloning.

2 µL bacterial glycerol stock or a single bacterial colony picked with a sterile p10 pipette tip were added to the PCR mix (*Table 18*) and the reaction was run in a thermocycler (*Table 19*). PCR products were analyzed by agarose gel electrophoresis as described in *2.2.2.6*.

Table 18. PCR reaction mix

Component	Final amount/ concentration
Template DNA	2 µL glycerol stock / bacterial colony
2x KAPA2G Fast Ready Mix with Dye	1x
Forward primer (25 µM)	0.5 µM
Reverse primer (25 µM)	0.5 µM
ddH_2O	*ad* 25 µL

Table 19. PCR reaction conditions

Step	Temperature [°C]	Time [s]	Cycles
Initial denaturation	95	300	1
Denaturation	95	15	35
Annealing	60	15	35
Elongation	72	15 s/kb	35
Final elongation	72	300	1
Cooling	4	∞	1

2.2.2.5 Gateway cloning

Lentiviral vectors were generated by transferring the CAR and scFv sequences from the entry clone pENTR1a into the destination vector pRRL by gateway reaction.

200 ng entry clone encoding the attL-flanked CAR and scFv sequence were mixed with 200 ng destination vector. After addition of 1 µL LR clonase enzyme mix and 1 h incubation at RT, the sequence was excised from the entry clone and transferred to the destination vector (*Figure 9*). The reaction was stopped by addition of 1 µg proteinase K and incubation for 10 min at 37 °C. Chemically competent *E. coli* Stbl3 were transformed as described in *2.2.2.10* and positively selected via the ampicillin resistance encoded on the expression clone.

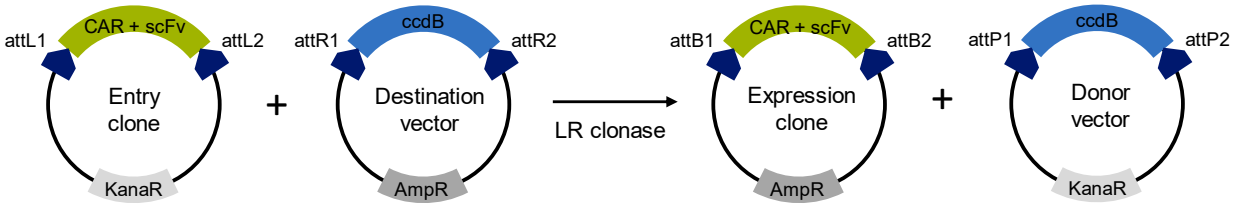

Figure 9. Gateway reaction. CAR and scFv sequence on the entry clone are recombined into the destination vector by the LR clonase enzyme exploiting the recombination sites attL and attR. Expression clones can be positively selected via the ampicillin resistance. Cells containing the original destination vector are killed by the ccdB toxin.

2.2.2.6 Agarose gel electrophoresis, DNA extraction and purification

Agarose gel electrophoresis was performed to isolate target DNA after amplification and digest.

1.0 – 1.5% agarose was dissolved in 1x TAE buffer by boiling and mixed with peqGreen (1:20000) for DNA visualization. Loading dye was added to the samples and applied onto the gel and a standard DNA ladder was loaded in a separate pocket. Electrophoretical separation was carried out at 70 V in 1x TAE running buffer. DNA was visualized on a UV table and target band was excised using a scalpel. DNA was extracted using a gel extraction kit according to the manufacturer's recommendations. DNA concentration was quantified photometrically.

In the case of small (< 100 bp) contaminating DNA fragments, the target DNA was instead purified using a PCR purification kit according to the manufacturer's recommendations.

2.2.2.7 Restriction enzyme digestion

Vector and insert DNA were digested as described in

Table 20 for 2 h at the temperature of maximum enzyme activity. To avoid vector religation, 10 units of alkaline phosphatase from calf intestine (CIP) was added to the vector digest reaction.

Table 20. Restriction digest reaction mix

Component	Final amount/ concentration
DNA	5 µg (vector) / 2 µg (insert)
Buffer	1x
Enzyme I	10 U
Enzyme II	10 U
CIP (vector digest only)	10 U
ddH_2O	*ad* 50 µL

2.2.2.8 DNA blunting reaction

If needed, digested DNA was blunted using DNA polymerase I, Large (Klenow) fragment, as described in *Table 21* for 37 °C for 15 min followed by heat inactivation at 75 °C for 10 min.

Table 21. Blunting reaction mix

Component	Final amount/ concentration
Digested DNA	16 µL
NEB2 Buffer	1x
dNTP Mix (10 mM)	0.5 mM
DNA polymerase I, Large (Klenow) fragment	5 U
ddH_2O	*ad* 20 µL

2.2.2.9 DNA ligation

Digested insert and vector DNA were ligated by setting up the reaction as described in *Table 22* followed by incubation for 1 h at RT.

Table 22. Ligation reaction mix

Component	Final amount/ concentration
Vector	50 ng
Insert	3x molar excess
T4 Ligase Buffer (10x)	1x
T4 Ligase (1 U/ µL)	1 U
ddH_2O	*ad* 20 µL

2.2.2.10 Chemical transformation of bacteria

Chemically competent *E. coli* XL-1 Blue were transformed by heat shock. 100 µL bacteria were thawed on ice, the complete ligation mix or 50 ng plasmid DNA were added and incubated on ice for 30 min. Heat shock was performed for 45 s at 42 °C and immediately 250 µL SOC medium were added to the bacteria. Following recovery of 30 – 60 min at 37 °C, 180 rpm, the bacteria were streaked out on pre-warmed antibiotic-containing LB agar plates. The plates were incubated overnight at 37 °C. Single colonies were picked using a sterile p10 pipette tip to inoculate antibiotic-containing LB medium.

2.2.2.11 Transformation of bacteria by electroporation

DNA was introduced into competent *E. coli* TG1 by electroporation. 50 ng plasmid DNA were added to 50 µL thawed bacteria and transferred to an electroporation cuvette. After electroporation at 1800 V, 25 µF and 200 Ω, 950 µL SOC medium were immediately added and recovery was allowed for 30-60 min at 37 °C, 180 rpm. Bacteria were streaked out on pre-warmed antibiotic-containing LB agar plates. Following overnight incubation at 37 °C, single colonies were picked using a sterile p10 pipette tip to inoculate antibiotic-containing LB medium.

2.2.2.12 Bacterial glycerol stocks

15 % glycerol stocks were prepared for long-term storage of bacteria. Bacteria grown from a single colony in antibiotic-containing LB medium were supplemented with glycerol to a final concentration of 15 %. Cells were immediately mixed by vortexing and frozen at -80 °C.

2.2.2.13 Plasmid DNA preparation

Plasmid DNA was isolated from bacteria cultured in antibiotic-containing LB medium. DNA was extracted using the Mini preparation kit (QIAGEN) or endotoxin free Maxi preparation kit (QIAGEN) according to the manufacturer's instructions. DNA concentration was quantified photometrically.

2.2.2.14 mRNA analysis

Presence of scFv or CCL2 messenger RNA (mRNA) was analyzed by isolation of mRNA using the RNeasy Mini Kit (QIAGEN) according to the manufacturer's instructions, followed by synthesis of complementary DNA (cDNA), sequence specific PCR and visualization on an agarose gel.

mRNA of 1 x 10^7 CAR T cells (see *2.2.3.12*), HEK cells transfected with CAR constructs (see *2.2.3.13*) as well as phytohaemagglutinin P (PHA-P) activated and non-activated PBMCs (see *2.2.3.11*) was isolated according to the manufacturer´s instructions. Genomic DNA was removed in an additional step. Concentration was quantified photometrically and RNA was stored at -80 °C. cDNA synthesis was performed using the RevertAid First Strand cDNA Synthesis (Thermo Fisher Scientific) according to the manufacturer´s recommendations. For this purpose, 1 µg RNA, oligo

(dT) primers, RNase inhibitor, dNTP mix and reverse transcriptase were incubated in reaction buffer for 60 min at 42 °C. The reaction was terminated by incubation at 70 °C for 5 min. 2 µL cDNA were amplified by PCR using scFv or CCL2 sequence-specific primers as well as GAPDH-specific control primers as described in *2.2.2.2*. Samples were separated by agarose gel electrophoresis (see *2.2.2.6*) and target DNA was visualized on a UV table.

2.2.2.15 DNA sequence analysis

Sanger sequencing of plasmid DNA was performed by Eurofins Scientific. Forward and reverse primers are listed in *Table 8*. Sequences were evaluated using Geneious software. Antibody sequence analysis was conducted using IMGT/V-Quest [154] and VBASE2 [155] online tools.

2.2.3 Cell biological methods

2.2.3.1 scFv expression in bacteria

Production of soluble scFvs was performed in a small scale using bacteria transformed with the pHENIS phagemid vector carrying the scFv coding sequence, or in a larger scale using bacteria transformed with the pAB1 vector encoding the scFv. Both pHENIS and pAB1 vectors contain an IPTG inducible lac operon, allowing the production of soluble scFvs upon addition of IPTG.

ScFv expression after phage display was performed in order to screen for antigen-specific clones by ELISA. Although *E. coli* TG1 is an amber stop codon suppressor strain, we found it to generate sufficient amounts of soluble scFv not fused to the phage coat protein pIII. A 96- well plate with 125 µL/well 2x YT-GA (1 g/L glucose) was inoculated with 3 µL glycerol stock of each master plate well (see *2.2.1.2*) and incubated at 37 °C for 2.5 h, 160 rpm (OD_{600} approx. 0.5). ScFv production was induced by addition of IPTG at a final concentration of 1 mM and incubation overnight at 30 °C, 160 rpm. The plate was centrifuged at 2000 g for 15 min at 4 °C. Bacterial pellets were resuspended in 150 µL/well periplasmic preparation buffer and incubated on ice for 25 min. $MgSO_4$ was added to a final concentration of 10 mM and the plate was centrifuged for 15 min at 2000 g, 4 °C. The scFv containing periplasmic supernatants were subjected to ELISA as described in *2.2.4.8.*

For large scale production of scFv, the antibody fragments were cloned into the pAB1 vector, *E. coli* TG1 were transformed by electroporation (see *2.2.2.11*) and scFvs were purified from bacterial periplasm. 500 mL 2x YT-GA (1 g/L glucose) were inoculated with 5 mL of an overnight bacterial culture and incubated at 37 °C, 180 rpm, until an OD_{600} of approximately 0.8 was reached. ScFv production was induced by addition of IPTG (1 mM final concentration) and overnight incubation at 20 °C, 180 rpm. Bacteria were harvested by centrifugation for 15 min at 4000 g and 4 °C. Proteins were isolated from the periplasm by resuspending the pellet in 50 mL periplasmic preparation buffer and adding 50 µg/mL lysozyme. After incubation on ice for 25 min, $MgSO_4$ was added to a final concentration of 10 mM and supernatant was harvested by centrifugation for 15 min at 4000 g and 4 °C. The centrifugation step was repeated until bacterial debris was completely removed. The scFv-containing supernatant was dialyzed against SP10 buffer as described in *2.2.4.1* and scFvs were purified via their His-tag and size exclusion chromatography (see *2.2.4.2* and *2.2.4.4*).

2.2.3.2 Cultivation of eukaryotic cells

Cells were handled under sterile conditions and were cultivated in a humidified incubator at 37 °C, 5% CO_2. Cells were counted using a Neubauer counting chamber and dead cells were visualized by trypan blue staining.

Adherent cell lines HEK293T were cultivated in DMEM (supplemented with 10% FCS and 1% pen/strep), A549 in RPMI-1640 (supplemented with 10% FCS and 1% pen/strep) and HUVEC in EGM2 medium. For passaging, cells were washed with PBS and detached from the plate by adding 1x trypsin-EDTA solution while incubating for 3-5 min at 37 °C. To stop trypsinization, adapted medium was added (at least three times the amount of used trypsin). Cells were counted, the cell density was adjusted to 0.5 x 10^5 cells/mL with fresh medium and cells were seeded into a new flask. Cells were passaged every 2 to 4 days.

Suspension cell lines THP1, Nalm6, Raji and K562 were cultured in RPMI-1640 supplemented with 10% FCS and 1% pen/strep. Cells transduced with lentiviral vectors encoding Gaussia Luciferase (GLuc) were selected by the addition of 1 µg/ml puromycin. To passage cells, cells were counted and the cell density was adjusted to 1.5 x 10^5 cells/mL (except GLuc expressing cells: 5 x 10^5 cells/mL) with fresh medium and cells were seeded into a new flask. Cells were passaged every 2 to 4 days.

HEK293-6E suspension cells were grown in a humidified shaking incubator at 37 °C, 5% CO_2 and 135 rpm in F17 medium supplemented with 4 mM L-Glutamine, 0.1% Kolliphor and 25 µg/mL G418. Cells were passaged every 2 to 3 days to avoid cell densities above 2 x 10^6 cells/mL.

Primary transduced (CAR) and unstransduced (mock) T cells were grown in X-Vivo 15 medium supplemented with 5 % FCS, 10 ng/mL IL-7 and 10 ng/mL IL-15. Cells were passaged ever 2 to 3 days and seeded at 1 x 10^6 cells/mL/cm^2.

2.2.3.3 Freezing and thawing of cells

Cells were centrifuged for 5 min at 300 g and resuspended in freezing medium at a concentration of 0.5 to 1x10^7 cells/mL. 1 mL aliquots were frozen to -80 °C in cryovials by reducing temperature at a rate of 1 °C/min using a freezing container. Cells were stored in a liquid nitrogen tank.

Frozen cells were thawed in a water bath at 37 °C and transferred to a T25 flask containing pre-warmed 9 mL adapted medium. HEK293-6E cells were thawed and transferred to a 125 mL shaking flask containing 16 mL medium without G418. The following day the volume was adjusted to 30 mL using medium without G418.

2.2.3.4 Expression of antigen, scFv-hFc and IgG in HEK293-6E cells

Antigens, scFv-hFc and IgG antibodies were transiently expressed as recombinant proteins in HEK293-6E cells.

Cells at a density of 1.5 – 2.0 x 10^6 cells per mL were used for transfection. 1 µg vector DNA and 2 µg PEI per mL transfection volume was mixed with transfection medium (5 % of the transfection volume) in separate tubes. The PEI solution was transferred to the DNA solution, vortexed thoroughly and incubated for 3 min at RT. The transfection mix was added to the cells and for the expression of NRP1 (CUB1)-mFc $CaCl_2$ was additionally added to a final concentration of 10 mM. After 24 h incubation at 37 °C, shaking at 135 rpm and 5 % CO_2, TN1 feeding medium was added (0.5% final concentration). 4 days after transfection, the culture was harvested by centrifugation for 10 min at 250 g, 4 °C. The antibody containing supernatant was centrifuged again for 10 min at 2300 g, 4°C and dialyzed as described in *2.2.4.1*.

2.2.3.5 Flow cytometry

Intracellular or cell-surface expression of proteins, as well as antibody binding to the surface of target positive cells was analyzed by flow cytometry.

Flow cytometry buffer was used for all staining and washing steps, except for samples that were stained with Protein L where PBS was used during the staining procedure. The staining volume was 100 µL. All reagents were cold (4 °C) and cells were always handled on ice.

For staining of intracellular proteins, cells were first fixed and permeabilized using the Intracellular Fixation and Permeabilization kit (Thermo Fisher Scientific) according to the manufacturer´s recommendations. Staining and washing steps were performed in permeabilization buffer at RT.

0.2 – 1 x 10^6 cells per staining sample were centrifuged for 3 min at 400 g, 4 °C and cells were washed with 200 µL buffer. Fcγ receptors of Fc-receptor expressing myeloid cells were blocked by resuspending the cells in 100 µL PBS supplemented with 1 % (w/v) sodium azide and 10 % (v/v) human serum and incubation for 20 min on ice. Cells were washed twice and antibody (concentration according to manufacturer's recommendations) was added to the cells and incubated for 45 min on ice. Cells were washed twice, followed by addition of labeled secondary antibody (concentration according to manufacturer's recommendations) and incubated for 45 min on ice protected from light. Afterwards, cells were washed twice and resuspended in 300 µL buffer supplemented with SYTOX Blue Dead Cell Stain (1:1000). Fluorescence was analyzed using a flow cytometer and data was evaluated with FlowJo 10.3 software.

2.2.3.6 Ligand-binding competition assay

Flow cytometry was used to investigate the blocking effects of anti-NRP1 antibodies on the Sema3A – NRP1 interaction and of the anti-CCL2 antibody on the CCL2 – CCR2 interaction. Flow cytometry was performed as described in *2.2.3.5* with the following modifications.

For the Sema3A – NRP1 blocking experiment, His-Sema3A-hFc was first labeled via the human Fc tag with APC using the Zenon human IgG APC labeling kit (Thermo Fisher Scientific) according to the manufacturer´s recommendations. NRP1 expressing HUVEC cells were preincubated with 750 nM anti-NRP1 or control IgG antibodies for 45 min at RT. Cells were washed and 75 nM APC-labeled His-Sema3A-hFc was added for 45 min at 4 °C protected from light. Cells were analyzed by flow cytometry.

To analyze the blocking of the CCL2 – CCR2 interaction by our anti-CCL2 antibodies, 100 nM CCL2-mFc and anti-CCL2 antibodies (100 – 1000 nM for IgG antibodies and 100 – 2000 nM for scFvs) were preincubated for 45 min at RT. 100 nM mFc was included as control for unspecific binding to Fc receptors. Fc receptors on CCR2 – expressing THP1 cells were blocked using human serum as described in *2.2.3.5*. The preincubated mixture was added to the THP1 cells for 20 min at 4 °C. FITC-conjugated goat anti-mouse IgG antibody was used for detection of CCL2-mFc binding and cells were analyzed by flow cytometry.

2.2.3.7 CCL2-induced CCR2 signaling

To analyze the effects of anti-CCL2 antibody on CCL2-induced CCR2 downstream signaling, CCR2-expressing THP1 cells were treated with CCL2 in the presence or absence of antibodies. Cell lysates were prepared and mitogen-activated protein kinase (MAPK) pathway was analyzed by investigating phosphorylation of extracellular-signal regulated kinase (ERK).

THP1 cells were washed with PBS, seeded at 3 x 10^5 cells/mL and starved in medium with 1 % FCS for 16 h. 20 nM CCL2 was preincubated with 200 nM anti-CCL2 antibody or without any antibody for 1 h at RT. The mixture was added to the cells and incubated for 3 – 5 min at 37 °C. Cells were centrifuged for 5 min at 2500 g at 4 °C. From this point on cells were always handled on ice. Following two washing steps with 5 mL ice-cold PBS, cells were centrifuged as described before. The pellet was resuspended in 100 µL / 1 x 10^6 cells chilled RIPA buffer supplemented with PhosStop and protease inhibitor. To support cell lysis, sonication was performed for 15 s in 9 cycles with 10 % pulse. Cells were incubated for 15 min on ice while shaking. Cell debris was pelleted by centrifugation for 15 min at 14000 g at 4 °C. The supernatant was transferred to a new tube and protein concentration was measured by BCA analysis using the Pierce BCA Protein Assay Kit (Thermo Fisher Scientific) according to the manufacturer´s recommendations. Supernatants were stored at -80 °C.

SDS gel electrophoresis was performed as described in *2.2.4.5*. Samples were adjusted to equal protein concentrations before loading. Proteins were transferred onto a nitrocellulose membrane by western blotting, see *2.2.4.7*. 4 % BSA - PBS was used for blocking overnight at 4 °C and antibody incubation for 2 h at RT. First, phosphorylated ERK (pERK) was detected by incubation with mouse anti-pERK and HRP-conjugated goat anti-mouse antibody. Next, ERK was detected using rat anti-ERK and HRP-conjugated goat anti-rat antibody. In a last step, the house keeping

gene glyceraldehyde 3-phosphate dehydrogenase (GAPDH) was detected by addition of a HRP-conjugated anti-GAPDH antibody.

Densitometric analysis of data from three independent experiments was performed using Fiji [153].

2.2.3.8 Transwell assay

CCR2-expressing THP1 cells have been described to migrate towards an increasing CCL2 concentration gradient [43], [44]. In order to analyze the effects of the anti-CCL2 antibody on cell migration, a transwell assay was performed.

6.5 mm transwell inserts with 3 µm pore size were coated with 66 µL human fibronectin (50 µg/mL) for 1 h at RT. The inserts were rinsed carefully with 100 µL ddH_2O. For detection of the THP1 cells, the cells were labeled with Calcein-AM. For this purpose, cells were labeled at a density of 2 x 10^6 cells/mL in 1 µM Calcein-AM in PBS for 20 min at 37 °C protected from light. Cells were centrifuged for 5 min at 300 g and washed with PBS. Cells were pelleted as described before and resuspended in serum free cell culture medium at a concentration of 1 x 10^6 cells/mL.

600 µL of CCL2 (final concentration 50 nM) and antibody (final concentration 50 nM and 500 nM) in serum free medium were added to the receiver wells of a 24 well plate. Conditions without CCL2 or antibody were included as controls. The plate was incubated for 30 min at 37 °C. 1.5 x 10^5 cells were added to the transwell inserts and the inserts were carefully placed into the receiver wells. Cell migration was allowed for 3 h at 37 °C. Inserts were removed from the plate and migrated cells were measured using a Tecan fluorescence reader at 485 / 530 nm. Migration in control wells without CCL2 was subtracted as background. All values were calculated relative to the migration in wells containing CCL2, but no anti-CCL2 antibody. All conditions were tested in triplicates.

2.2.3.9 Production of lentiviral particles

Lentiviral particles were produced by cotransfecting HEK293T cells with the lentiviral plasmid pRRL carrying the gene of interest and two helper plasmids encoding for the lentiviral proteins.

HEK293T cells were seeded in 22.5 mL DMEM supplemented with 10% (v/v) FCS and 1% (v/v) pen/strep in 15 cm cell culture dish and cultured at 37 °C, 5 % CO_2, until 80 % confluency was reached. In separate tubes a PEI and DNA mix was prepared, see *Table 23*. The PEI solution was

added to the DNA solution, mixed by vortexing and incubated for 10 min at RT. Half of the medium of the grown cells was replaced with fresh medium and the transfection mix was added dropwise. Cells were incubated at 37 °C, 5 % CO_2, for 24 h. Transfected cells were washed with 5 mL PBS and 14 mL DMEM without phenol red and FCS were added. Cells were incubated for 24 h as described before.

Virus containing supernatant was harvested by centrifugation for 4 min at 300 g and sterilized with a 0.45 µM filter. Supernatant was concentrated using a centrifugal filter unit by centrifugation for 30 min at 3500 g, 4 °C. Concentrated virus was eluted from the filter by centrifugation for 2 min at 900 g, 4 °C, and stored at -80 °C.

Table 23. Transfection mix for lentiviral particle production

Mix	Component	Per plate
DNA mix	Lentiviral plasmid (1 µg/mL)	22.5 µg
	Helper plasmid #1 (1 µg/mL)	7.9 µg
	Helper plasmid #2 (1 µg/mL)	14.6 µg
	NaCl (300 mM)	790 µL
	ddH_2O	790 µL
PEI mix	PEI (323 µg/mL)	352 µL
	NaCl (300 mM)	790 µL
	ddH_2O	438 µL

After production of the lentiviral vectors, the titer was determined. 5 x 10^4 HEK293T cells were seeded in 6 wells of a 24 well plate in 1 mL adapted medium per well and incubated for 24 h at 37 °C, 5 % CO_2. 500 µL of each well were transferred to a 1.5 mL tube. Virus (0, 0.1, 0.3, 1, 3 and 10 µL virus) and 8 µg/mL polybrene, a cationic polymer to increase transduction efficiency, were added, vortexed and returned dropwise to the corresponding well. Cells were incubated for 48 h at 37 °C, 5 % CO_2.

Infected cells were harvested by centrifugation for 4 min at 300 g. Surface expression of CAR was determined by flow cytometry as described in *2.2.3.5* by using biotinylated Protein L and APC conjugated streptavidin.

Estimating a cell number of 1 x 10^5 cells / well at the day of analysis, the mean percentage of CAR positive cells and added virus were used to calculate the virus titer as infectious units (IU) per mL according to the following formula:

$$Titer\ \left[\frac{IU}{mL}\right] = \frac{Cell\ number\ (10^5)\ x\ \%\ positive\ cells}{Volume\ of\ added\ lentivirus\ (0.1\ \mu L)}\ x\ 10^3$$

2.2.3.10 Activation of human T cells with CD3 and CD28 agonists

T cells from human peripheral blood mononuclear cells (PBMCs) were activated and expanded by coincubation with CD3 and CD28 agonists.

2 x 10^7 PBMCs were thawed in X-Vivo15 medium supplemented with 5 % FCS, centrifuged for 5 min at 300 g, washed with medium and centrifuged again. Cells were resuspended in X-Vivo15 supplemented with 5 % FCS, 10 ng/mL IL-7 and 10 ng/mL IL-15. Seeding density was 2 x 10^6 cells/mL in 4 mL per well in a 12 well plate. For T cell activation, 40 µL TransAct (nanomatrix conjugated to humanized CD3 and CD28 agonists) were added per well and incubated for 3 days at 37 °C, 5 % CO_2. Exclusively T cells survive this cultivation and can be further transduced using lentiviral vectors as described in *2.2.3.12*.

2.2.3.11 Activation of human PBMCs with phytohaemagglutinin P

Peripheral blood mononuclear cells (PBMCs) were activated by coincubation with the T cell mitogen PHA-P.

2 x 10^7 PBMCs were thawed in X-Vivo15 medium supplemented with 5 % FCS, centrifuged for 5 min at 300 g, washed with medium and centrifuged again. Cells were resuspended in X-Vivo15 supplemented with 5 % FCS, 10 ng/mL IL-7 and 10 ng/mL IL-15. Seeding density was 2 x 10^6 cells/mL in 4 mL per well in a 12 well plate. Cells were activated by adding 5 µg/mL PHA-P and incubation for 24 h at 37 °C. Cells were further used for mRNA isolation, see *2.2.2.14*, and supernatant was used for analysis as described in *2.2.4.10*.

2.2.3.12 Transduction of activated T cells

T cells were transduced with lentiviral vectors encoding the CAR with or without the anti-CCL2 scFv.

2 x 10^6 activated T cells (see *2.2.3.10*) were seeded in 1 mL X-VIVO15 supplemented with 5 % FCS, 10 ng/mL IL-7 and 10 ng/mL IL-15 per well in a 24 well plate. Per transduction, 1 mL adapted medium, 8 µg/mL polybrene and lentiviral particles at a MOI of 5 were mixed by vortexing. A mock transduction without lentiviral vector was included. The mix was added to the cells and incubated for 24 h at 37 °C, 5 % CO_2. To remove remaining viruses, cells were centrifuged for 5 min at 300 g and washed twice with PBS. Cells were seeded in 2 mL adapted medium in a new 24-well plate. Cells were further cultivated as described in *2.2.3.2*. CAR expression was analyzed by flow cytometry (see *2.2.3.5*). All functional assays were performed at day 14 to 21 after T cell activation.

2.2.3.13 Transfection of HEK293T cells for transient CAR expression

HEK293T cells were transfected with CAR encoding pRRL vectors for transient CAR expression and the analysis of soluble scFv production.

HEK293T cells were seeded in 22.5 mL DMEM supplemented with 10% (v/v) FCS and 1% (v/v) pen/strep in 15 cm cell culture dish and cultured at 37 °C, 5 % CO_2, until 80 % confluency was reached. In separate tubes a PEI and DNA mix was prepared, see *Table 24*. A mock transfection was included as control. The PEI solution was added to the DNA solution, mixed by vortexing and incubated for 10 min at RT. The medium of the grown cells was replaced with fresh serum free medium and the transfection mix was added dropwise. Cells were incubated at 37 °C, 5 % CO_2 for 48 h. CAR expression was analyzed by flow cytometry (see *2.2.3.5)*. Supernatants were harvested and cells were used for mRNA isolation as described in *2.2.3.14* and *2.2.2.14.*

Table 24. Transfection mix for transient CAR expression

Mix	Component	Per plate
DNA mix	CAR plasmid (1 µg/mL)	22.5 µg
	NaCl (300 mM)	790 µL
	ddH_2O	790 µL
PEI mix	PEI (323 µg/mL)	176 µL
	NaCl (300 mM)	790 µL
	ddH_2O	614 µL

2.2.3.14 Preparation of scFv containing supernatants from CAR T cells and HEK293T cells

At day 17 after initial activation and stimulation by coincubation with target positive Nalm6 cells (see *2.2.3.15*), CAR T cells were seeded at 1 x 10^6 cells/mL in 80 mL serum free X-Vivo 15 medium and grown for two days at 37 °C and 5 % CO_2. HEK293T cells transfected with CAR constructs, see *2.2.3.13*, were cultured for two days after transfection. Supernatants were harvested by centrifugation for 5 min at 2500 g. The supernatants were concentrated to 1.5 mL using 10K amicon filters according to the manufacturer´s recommendations and stored at -80 °C. For the analysis of scFv expression, supernatants were subjected to ELISA as described in *2.2.4.8*.

2.2.3.15 CAR T cell proliferation assay

In order to analyze CAR T cell proliferation and to enrich CAR positive cells, CAR T cells were coincubated with CD22 expressing Nalm6 cells. T cells were activated and transduced as described in *2.2.3.10* and *2.2.3.12*. CAR expression was assessed every 4 – 5 days by flow cytometry as described in *2.2.3.5* and cells were counted using a hemocytometer. At day 7 and 10 after activation, CAR T cells were coincubated with Nalm6 cells. Therefore, 5 x 10^5 CAR positive T cells per mL (calculated from flow cytometry data) were incubated with Nalm6 cells at an effector to target ratio of 1:3. Cells were cultured at 37 °C and 5 % CO_2 in 8 mL per well of a 6 well plate in X-Vivo 15 medium supplemented with 5 % FCS and 10 ng/ml IL-7 and IL-15.

2.2.3.16 Cytokine release assay

Cytokine release upon stimulation of CAR T cells with CD22-positive Raji cells was measured by a bead-based sandwich immunoassay (LEGENDplex). This assay employs bead populations of differing size and fluorescence intensity. Each bead population is conjugated with a specific capture antibody, targeting IL-2, IFNγ or TNF. The bead mixture is incubated with a supernatant sample and the analytes are bound by the capture beads. Bound analyte is detected by subsequent incubation rounds with biotinylated detection antibodies and streptavidin-PE. The amount of analyte correlates with the PE fluorescence intensity and can be calculated according to a standard curve.

CAR T cells were generated as described in *2.2.3.12* and CAR expression was assessed by flow cytometry, see *2.2.3.5*. Different CAR T cells were adjusted to have the same percentage of CAR positive cells by addition of mock transduced cells. CAR T cells as well as Raji (CD22-positive) and K562 (CD22 negative) cells were adjusted to 1 x 10^5 cells/mL in X-Vivo 15 medium supplemented with 5 % FCS. 100 µL of each target and effector cells were plated in wells of a 96-well U-bottom plate to get an effector:target ratio of 1:1. Controls without target or without effector cells were included. The plate was incubated for 24 h at 37 °C, 5 % CO_2. Supernatant was harvested by centrifugation for 3 min at 500 g, transferred to a new polypropylene 96-well plate and stored at -80 °C.

Cytokine release into the supernatant was analyzed using the LEGENDplex Kit (Biolegend) according to the manufacturer´s recommendations. In brief, supernatants were diluted in assay buffer to yield an optimal concentration range within the standard curve. In a 96-well polypropylene plate, 12.5 µL assay buffer, 12.5 µL sample or standard and 12.5 µL bead mix per well were incubated overnight at 4 °C while shaking at 800 rpm. The plate was washed twice with wash buffer and centrifuged for 5 min at 300 g. 12.5 µL detection antibodies were added per well and the plate was incubated protected from light for 1 h at RT, 800 rpm. 12.5 µL streptavidin-PE was added per well and incubated as described before for 30 min. The plate was washed once as described before. Pellets were resuspended in 150 µL assay buffer and analysis was performed using a flow cytometer. Data analysis was performed using LEGENDplex data analysis software 8.0.

2.2.3.17 CAR T cell killing assay

Killing of CD22-positive Raji cells by CAR T cells was assessed in a luminescence-based killing assay. For this purpose, Raji-GLuc cells were established in our lab by lentiviral transduction of Raji cells for stable expression of an engineered version of *gaussia princeps* luciferase (GLuc carrying a deletion of the signal peptide sequence to avoid GLuc secretion and M43L/M110L substitutions to convert the luminescence signal from flash-type to glow-type). During lysis of Raji-GLuc cells, luciferase is released into the supernatant and can be detected by addition of its substrate coelenterazine via measurement of the bioluminescent reaction. The bioluminescent signal corresponds to the efficiency of target cell killing.

The different CAR T cell cultures were adjusted to an equal percentage of CAR positive cells by dilution with untransduced (mock) T cells. CD22 positive Raji-GLuc cells (target) were adjusted to 2 x 10^5 cells/mL in X-Vivo 15 medium supplemented with 5 % FCS. CAR positive T cells (effector) were adjusted to 2 x 10^5 cells/mL (effector:target 1:1) and 6 x 10^5 cells/mL (effector:target 3:1) in X-Vivo 15 medium supplemented with 5 % FCS. 50 µL of each target and effector cells were plated in wells of a 96-well U-bottom plate. As negative control (background), 50 µL target cells mixed with 50 µL medium were included. As positive control, 50 µL target cells only were plated for later cell lysis. All samples were prepared in triplicates. The plate was incubated for 15.5 h at 37 °C, 5 % CO_2. 50 µL cell lysis buffer (Thermo Fisher Scientific) (final concentration 1x) was added to the positive control wells and mixed by pipetting. The plate was incubated for 30 min at 37 °C, 5 % CO_2. Supernatant was harvested by centrifugation for 3 min at 300 g and 50 µL were transferred to a new 96-well white plate. 50 µL coelenterazine (20 µM in PBS) substrate were added per well. Bioluminescent signal was measured after 30 s plate shaking using a Tecan plate reader. Percentage of target cell killing was calculated based on the detected bioluminescent signal according to the following formula:

$$Lysis\ [\%] = \frac{(sample\ mean - background\ mean)}{(positive\ control\ mean - background\ mean)} x\ 100$$

2.2.4 Protein biochemical methods

2.2.4.1 Dialysis

After production of proteins in bacteria (see *2.2.3.1*) or mammalian cells (see *2.2.3.4*), buffer exchange was performed by dialysis. In addition, proteins were dialyzed against PBS after purification.

Following production, IgG antibodies and scFvs were dialyzed against 5 L Protein A binding buffer or SP10 buffer, respectively. After purification, proteins were dialyzed against 700 mL PBS. To dialyze NRP1 (CUB1)-mFc, PBS was supplemented with $CaCl_2$ (final concentration of 10 mM). Dialysis was performed using a membrane for exclusion of proteins with a molecular mass below 12 kDa and by overnight incubation at 4 °C under slow stirring. Solutions were sterile filtered using a 0.22 µm low protein binding filter and stored at 4 °C.

2.2.4.2 Immobilized metal affinity chromatography

ScFv antibody fragments carrying a C-terminal c-myc- and His_6-tag were purified by immobilized metal affinity chromatography (IMAC) via a HisTrap FF 1 mL column using the AEKTApure fast protein liquid chromatography (FPLC) system. The flow rate was 1 mL/min and pressure was adjusted according to the column manufacturer's recommendations.

The 1 mL HisTrap FF column was equilibrated with 5 column volumes of ddH_2O and SP10 binding buffer. Following an equilibration step with 20 column volumes SP20 buffer (SP10 buffer supplemented with 2 % SP500 buffer), protein containing supernatant was loaded onto the column. The column was washed with 5 column volumes SP10 binding buffer, followed by elution with 20 column volumes SP500 elution buffer. The column was washed with 5 column volumes of ddH_2O and ethanol and stored at 4 °C. The column flow-through was photometrically (280 nm) analyzed and protein content was blotted over the flow volume. Protein containing 300 µL fractions were pooled and dialyzed against 700 mL PBS as described in *2.2.4.1.* Protein concentration was photometrically determined at 280 nm considering the protein specific molecular weight and extinction coefficient (ExPASy ProtParam online tool). Proteins were concentrated to approximately 2.5 mL using a 10K Amicon filter and further purified by size exclusion chromatography (see *2.2.4.4*).

2.2.4.3 Protein A affinity chromatohgraphy

ScFv-hFc and IgG proteins were purified by Protein A affinity chromatography using the AEKTApure FPLC system. The used flow rate was 1 mL/min and column pressure was adjusted according to the manufacturer's recommendations.

A 1 mL Protein A column was equilibrated with 5 column volumes of each ddH_2O and Protein A binding buffer. Protein containing supernatant was loaded onto the column. The column was washed with 15 column volumes Protein A binding buffer, followed by elution with 9 column volumes Protein A elution buffer. The protein containing 1 mL fractions were collected in tubes supplemented with neutralization buffer (200 µL first two tubes, 300 µL remaining tubes). The column was washed with 5 column volumes of each ddH_2O and ethanol and stored at 4 °C. The column flow-through was photometrically (280 nm) analyzed and protein content was blotted over the flow volume. Protein containing fractions were pooled and dialyzed against 700 mL PBS as described in *2.2.4.1.* Protein concentration was photometrically determined at 280 nm considering the protein specific molecular weight and extinction coefficient (ExPASy ProtParam online tool). Proteins were stored at 4 °C or for long term storage at -80 °C.

2.2.4.4 Size exclusion chromatography

Analytical size exclusion chromatography (SEC) was performed to analyze protein purity and aggregation. The Superdex 200 Increase 10/300 GL column (20 mL column volume) was used for analysis of recombinant antigen, IgG and scFv-hFc, and the Superdex 75 Increase 10/300 GL column (20 mL column volume) for scFv analysis. Preparative SEC was performed to further purify scFvs following IMAC (see *2.2.4.2*) using the Superdex 16/60 75 pg column (120 mL column volume).

The column was washed with 1.5 column volumes H_2O and PBS at a flow rate of 0.3 to 1 mL/min. For analytical SEC, 10 – 30 µg protein were injected into a 25 µL loop. For preparative SEC, total protein amount was injected into a 5 mL loop. Proteins were applied to the column at a flow rate of 0.5 mL/min. Protein elution was photometrically analyzed at 280 nm. Elution time was compared to a protein standard to calculate the approximate molecular weight. After preparative SEC, the fractions containing monomeric protein were pooled, sterile filtered using a 0.22 µm low protein binding filter and stored at 4 °C or long term at -80 °C.

2.2.4.5 Sodium dodecyl sulfate polyacrylamide gel electrophoresis

Proteins were separated according to their molecular weight by sodium dodecyl sulfate polyacrylamide gel electrophoresis (SDS-PAGE). 12 or 15 % separating gels and 5 % stacking gels were prepared as described in *Table 25* and cast into a 1.5 mm cassette.

2 µg protein or maximum protein amount for lysate analysis were mixed with sample buffer (1 x final concentration) and DTT (250 mM final concentration) and adjusted with ddH_2O to 20 – 50 µL sample volume. Samples were denaturated for 3 min at 95 °C. The running chamber was filled with 1x SDS running buffer and proteins were loaded onto the SDS gel. A protein standard was loaded in a separate pocket. Proteins were separated by electrophoresis for 2 h at 140 V.

Table 25. Separating and stacking gel mix

Component	Separating gel [µL]		Stacking gel [µL]
	12 %	15 %	5 %
Rotiphorese A	3110	3890	490
Rotiphorese B	1300	1620	200
Separating gel buffer	1920	1920	-
Stacking gel buffer	-	-	750
10% SDS	80	80	30
TEMED	6.5	6.5	2.2
10% APS	64	64	25
ddH_2O	*ad* 8000	*ad* 8000	*ad* 3000

2.2.4.6 Coomassie blue staining

Coomassie blue staining was used to visualize proteins on a SDS gel.

Following SDS-PAGE (see *2.2.4.5*), the gel was washed with ddH_2O three times for 5 min on a shaker. Coomassie Blue staining solution was added and incubated for 1 to 3 h on a shaker. Destaining of the gel was performed by incubation in ddH_2O overnight on a shaker. Gels were scanned for documentation.

2.2.4.7 Western blot

For visualization of specific poteins after separation in SDS-PAGE (see *2.2.4.5*), proteins were first transferred onto a nitrocellulose membrane by semi-dry western blotting and the membrane was afterwards blocked and stained with protein-specific antibodies.

SDS gel, nitrocellulose membrane and blot paper were equilibrated for 5 min in semi-dry blot buffer on a shaker, assembled and the blot was run for 30 min at 20 volts. Blocking buffers for detecting normal proteins and phospho-proteins were 2 % MPBS and 4 % BSA-PBS, respectively, and specific antibodies were diluted in the respective blocking buffer. After the transfer, the membrane was blocked with blocking buffer for 1 h at RT on a shaker. Primary antibody (dilution according to manufacturer's recommendations) was added to the membrane and incubated overnight at 4 °C on a shaker. The membrane was washed three times 5 min with PBST and PBS under shaking. HRP-conjugated secondary antibody (dilution according to manufacturer's recommendations) was added and incubated for 2 h at RT. The membrane was washed as described before. ECL detection reagents were mixed, added to the membrane and incubated for 1 min protected from light. INTAS advanced fluorescence imager was used for luminescence detection. For phosphorylated proteins, band intensity was evaluated using Fiji (ImageJ).

2.2.4.8 Enzyme-linked immunosorbent assay

Protein binding to the target antigen and cross-reactivity to control proteins was analyzed by ELISA. For conventional ELISA plates the working volume was 100 µL, washing and blocking volume 400 µL. For half area ELISA plates the working volume was 50 µL, washing and blocking volume 200 µL. 2 % MPBS was used for blocking and antibody dilutions, except for assays including cell culture supernatants where 2 % BSA-PBS was used. The different ELISA experimental set ups as well as the used proteins for coating and detection antibodies are listed in *Table 26*. All commercial antibodies were diluted according to the manufacturer´s recommendations.

The ELISA plate was coated overnight at 4 °C with proteins diluted in PBS. After blocking the plate for 2 h at RT with 2 % MPBS/BSA-PBS, the blocking solution was removed, analyte proteins were added and incubated for 2 h at RT. The plate was washed three times with PBST and PBS. HRP-conjugated protein-specific secondary antibody was added and incubated for 1 h at RT, followed by washing as described before. TMB reagents were mixed, added and incubated for up to 10

min protected from light. The reaction was stopped by adding sulfuric acid (50 µL/well ELISA plate or 25 µL/well half area ELISA plate). Using a plate reader, absorbance was measured at 450 nm wavelength (reference wavelength 620 nm).

Table 26. Coating, analyte and detection proteins used for ELISA

Assay	Coating protein	Analyte protein	Detection antibody
Integrity analysis of in-house produced NRP1	3 µg/mL NRP1-His, NRP1 (CUB1)-mFc and NRP1 (CUB1CUB2)-mFc	1 µg/mL His-Sema3A-hFc	HRP-conjugated mouse anti-human Fc
Integrity analysis of in-house produced CCL2	3 µg/mL CCL2-mFc	Rabbit anti-CCL2	HRP-conjugated goat anti-rabbit
Monoclonal scFv analysis after phage display	3 µg/mL CCL2-mFc and mFc	50 µL/well scFv containing bacterial periplasmic preparation	HRP-conjugated anti-c-myc
scFv antigen specificity	3 µg/mL antigen (CCL2, CCL2-mFc, NRP1-His) and control proteins	10 µg/mL scFv	HRP-conjugated anti-c-myc
scFv-hFc antigen specificity	3 µg/mL antigen (CCL2-mFc, NRP1-His) and control proteins	10 µg/mL scFv-hFc	HRP-conjugated mouse anti-human IgG
IgG antigen specificity	3 µg/mL antigen (CCL2, CCL2-mFc, NRP1-His) and control proteins	10 µg/mL IgG	HRP-conjugated mouse anti-human IgG
scFv secretion by HEK293T and CAR T cells	3 µg/mL CCL2	200 µL/well concentrated cell culture supernatant; 13 ng/mL NB7.E5 scFv	HRP-conjugated anti-c-myc

2.2.4.9 Sema3A / VEGF – NRP1 blocking ELISA

In order to investigate if the anti-NRP1 antibodies block the binding of Sema3A or VEGF to NRP1, an ELISA was performed as described in *2.2.4.8* with the following modifications:

For the Sema3A – NRP1 blocking ELISA, 3 µg/mL His-Sema3A-hFc were coated in half-area ELISA plates. After blocking, the plate was washed three times with PBST and PBS. 50 nM NRP1-His were preincubated with 1000 nM anti-NRP1 IgGs or control IgG in 2 % MPBS for 1 h at RT. The mix was added to the plate and incubated for 2 h at RT, followed by washing and addition of mouse anti-NRP1 antibody for 2 h at RT. For detection, HRP-conjugated anti-mouse antibody was used.

For the VEGF – NRP1 blocking ELISA, 3 µg/ml NRP1-His was coated in half-area ELISA plates. After blocking, the plate was washed three times with PBST and PBS. 500 nM anti-NRP1 IgGs in 2 % MPBS were added for 2 h at RT. After washing, 8.4 nM biotinylated VEGF in 2 % MPBS supplemented with 1 µg/mL heparin was added for 2 h at RT. HRP-conjugated streptavidin was used for detection.

2.2.4.10 CCL2 ELISA

CCL2 secretion by CAR T cells, transfected HEK cells, and PHA-activated and resting PBMCs into the cell culture supernatant was analyzed by using the CCL2 ELISA set (BioLegend) with a lower detection limit of 7.8 pg/mL.

For the preparation of CAR T cell supernatants 1 x 10^6 CAR T cells/mL were seeded in 6 mL serum free X-Vivo 15 medium supplemented with 10 ng/mL IL-7 and IL-15 in a 6 well plate and incubated for 48 h at 37 °C, 5% CO_2. HEK293T cells were transduced and cultured for 48 h as described in *2.2.3.13.* PBMCs were activated and cultured as described in *2.2.3.11*. Supernatants of CAR T cells, HEK cells and PBMCs were harvest by centrifugation for 5 min at 300 g. The ELISA was performed according to the manufacturer´s instructions. Therefore, the ELISA plate was coated overnight at 4 °C with an anti-CCL2 capture antibody diluted in coating buffer. The plate was washed and blocked for 1 h at RT on a shaking incubator followed by washing of the plate. Supernatants as well as a standard were added to the plate and incubated for 1h at RT with shaking. Supernatants were diluted in assay buffer to yield optimal results within the standard curve. Samples were removed by washing and bound CCL2 was detected by incubation with a HRP-conjugated detection antibody for 1 h at RT with shaking. Following washing, Avidin-HRP

was added and incubated for 30 min at RT with shaking. The plate was washed and freshly mixed TMB substrate solution was added for 20 min and the plate was incubated in the dark. The reaction was stopped by addition of stop solution and absorbance at 450 nm (reference 570 nm) was immediately measured using a plate reader.

2.2.4.11 Surface plasmon resonance spectroscopy

The binding affinity of scFv-hFc and IgG proteins toward their antigens was determined by surface plasmon resonance spectroscopy. One interaction partner (ligand) is immobilized on a sensor surface and the second interaction partner (analyte) flows over the surface. The interaction between the ligand and the analyte changes the mass concentration leading to a proportional change in refractive index at the sensor surface. Using a laser, the change in reflection angle can be detected in real-time and is quantified as response units (RU).

Protein A was covalently linked to the dextran matrix of a CM5 chip in all four flow cells. Protein A was diluted to 300 µg/mL in 10 mM sodium acetate, pH 4.5. The sensor chip surface was coated using an amine coupling kit (GE Life Sciences) and a flow rate of 5 µL/min and 7 min per step. First, the surface was activated by injection of 1-Ethyl-3-(3-dimethylaminopropyl) carbodiimid/N-Hydroxysuccinimid (EDC/NHS) to form surface esters. Second, Protein A was injected and immobilized via its amine groups by reaction with the esters. Third, the surface was blocked by deactivation of free esters with ethanolamine.

Ligand (diluted in HBS-EP buffer) was immobilized at a flow rate of 10 µL/min to achieve a maximum response (R_{max}) of 10-50 RU. The following formula was used for calculation of the ligand immobilization level (R_L), considering the stoichiometric ratio (S_m) of ligand to analyte binding as well as the protein molecular weight:

$$R_L = \frac{ligand\ MW}{analyte\ MW}\ x\ \frac{R_{max}}{S_m}$$

For kinetic analysis, an analyte concentration series was prepared in HBS-EP buffer and injected onto the surface at a rate of 30 µL/min for 2 min. Analyte injection was stopped and dissociation of the analyte from the ligand was monitored for 5 min while injecting HBS-EP buffer. The surface was regenerated by injection of regeneration buffer for 1 min at 30 µL/min, followed by a stabilization time of 3 min. Flow cell one without analyte was used as reference and subtracted from flow cell two (containing analyte). Double referencing was performed, by additionally

subtracting the 0 nM analyte concentration. Data were evaluated with the BIAevaluation software using a 1:1 Langmuir binding model. For very fast association and dissociation rate constants a steady state affinity model.

2.2.5 Statistical analysis, calculations and graphical illustrations

Statistical analysis was performed using Graph Pad Prism 7.0 software. Unpaired, two-tailed t test was used to calculate statistical significance. P values < 0.05 were considered statistically significant. Graphs were generated using Graph Pad Prism 7.0 software. Error bars indicate standard deviation of the mean.

K_D values of flow cytometric titration curves were calculated using Graph Pad Prism 7.0. Graph Pad Prism defines the K_D value (equilibrium binding constant) as the ligand concentration needed to achieve a half-maximum binding at equilibrium (EC50). A nonlinear fit was included and one site specific binding was used to calculate the EC50.

The SPR-derived K_D (equilibrium dissociation constant) values describe the time-dependent association and dissociation rate constant (K_D = kd/ka) and are calculated based on a steady state or 1:1 Langmuir binding model using the BIAevaluation software as described in *2.2.4.11*.

3 Results

3.1 Selection of CCL2- and NRP1-specific antibody fragments by phage display

Fully human antibody fragments targeting CCL2 and NRP1 were selected by means of phage display from our in-house immune antibody library LYNDAL. In addition, our collaborator Yumab GmbH selected CCL2- and NRP1-specific antibody fragments from their naïve antibody library HAL9/10 by phage display. For the selection of CCL2-specific antibody fragments we produced and purified full-length CCL2 fused to the murine fragment crystallizable (mFc). For the recovery of NRP1-specific antibody fragments, phage display was performed using commercially available NRP1 composed of the CUB1, CUB2, b1 and b2 domains (NRP1 (CUB1CUB2, b1b2)) and carrying a poly-histidine (His) tag at the C-terminus. Antibody selection from LYNDAL led to the recovery of one CCL2-specific scFv. In contrast, no NRP1-specific scFv could be selected due to enrichment of antibody fragments which did not have full sequence integrity. In addition, our collaborator YUMAB GmbH provided us with five anti-CCL2 and two anti-NRP1 clones.

3.1.1 Target antigen design, production and purification

For selection of CCL2- and NRP1-specific antibody fragments by phage display, highly pure antigens are required. To increase the chance of recovery of a NRP1-specific scFv which blocks the NRP1 - Sema3A interaction, we decided to produce only the domain of NRP1 which is involved in Sema3A binding. The NRP1 - Sema3A binding region is described to be localized in the CUB1 domain or the CUB1CUB2 domains of NRP1 [87], [160]. Furthermore, the CUB domains have been described to have binding sites for calcium ions which are important for the formation of the Sema3A – NRP1 complex [161]. In general, it has been found that calcium is required for the stability of CUB domains [162].

We produced and purified the NRP1 CUB1 domain and NRP1 CUB1CUB2 domains fused to the N-terminus of a mouse IgG1 Fc-tag (mFc). Additionally, we produced the NRP1 CUB1 in the presence of calcium in order to account for the described effects of calcium on the stability of CUB domains [162]. The proteins were produced in HEK293-6E cells and purified from the cell culture supernatants by Protein A chromatography. Protein yields ranged from 10 to 18 mg protein per liter production volume. An exception was NRP1 (CUB1CUB2)-mFc with a yield of only 3.8 mg

protein per liter production volume. Purity was determined by analytical size exclusion chromatography (SEC) (*Figure 10*). Only NRP1 (CUB1CUB2)-mFc showed minor aggregation and a higher than expected calculated molecular weight when compared to a protein standard run (*Appendix, Figure 35)*. NRP1 (CUB1)-mFc produced in the presence or absence of calcium was of high purity. Since a biologically intact Sema3A binding site within the produced recombinant NRP1 protein domains is crucial to show blocking effects by antibody fragments, we investigated binding of Sema3A by ELISA (*Figure 11*). Surprisingly, Sema3A only bound to commercially available NRP1 composed of the CUB1, CUB2, b1 and b2 domains (NRP1 (CUB1CUB2, b1b2)) fused to a poly-His tag. The truncated NRP1-mFc fusion proteins which we produced by ourselves did not bind Sema3A, indicating incorrect protein folding and/or inaccessibility due to steric hindrance by the mFc tag. Consequently, commercially available NRP1 (CUB1CUB2, b1b2) was used for further experiments.

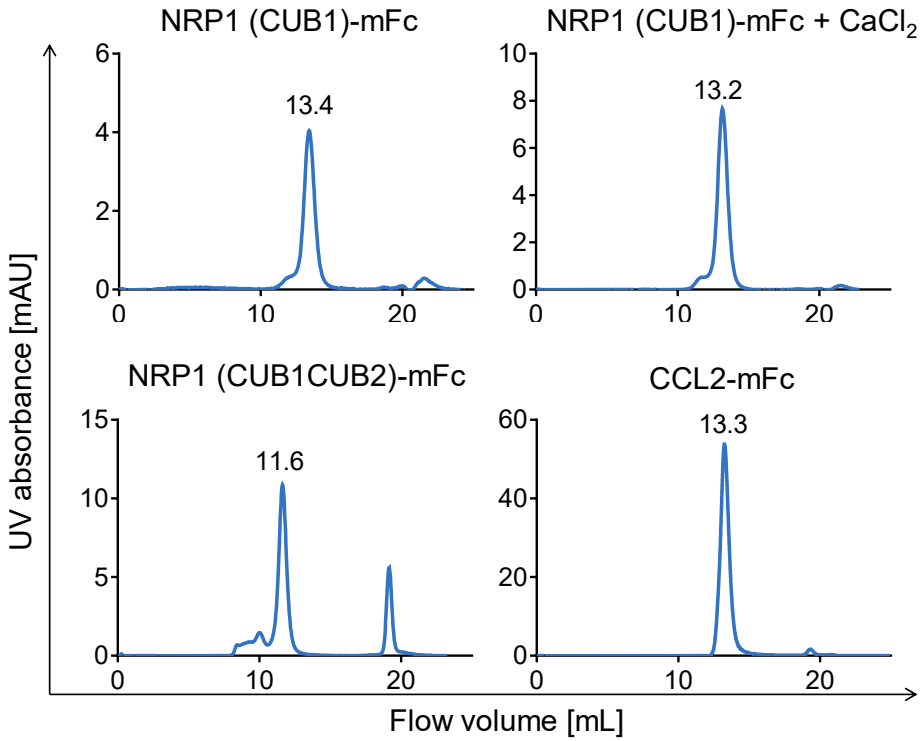

Figure 10. Investigation of NRP1 and CCL2 fusion protein purity by analytical size exclusion chromatography. Using the mammalian expression vector pCMV6, we produced the antigens carrying a C-terminal mFc tag in HEK293-6E cells. NRP1 (CUB1)-mFc was additionally produced and purified in the presence of 10 mM $CaCl_2$. Proteins were purified by Protein A chromatography and purity was analyzed by analytical SEC. Numbers indicate the flow volume in mL of the major peak and were compared to a protein standard (*Appendix, Figure 35*).

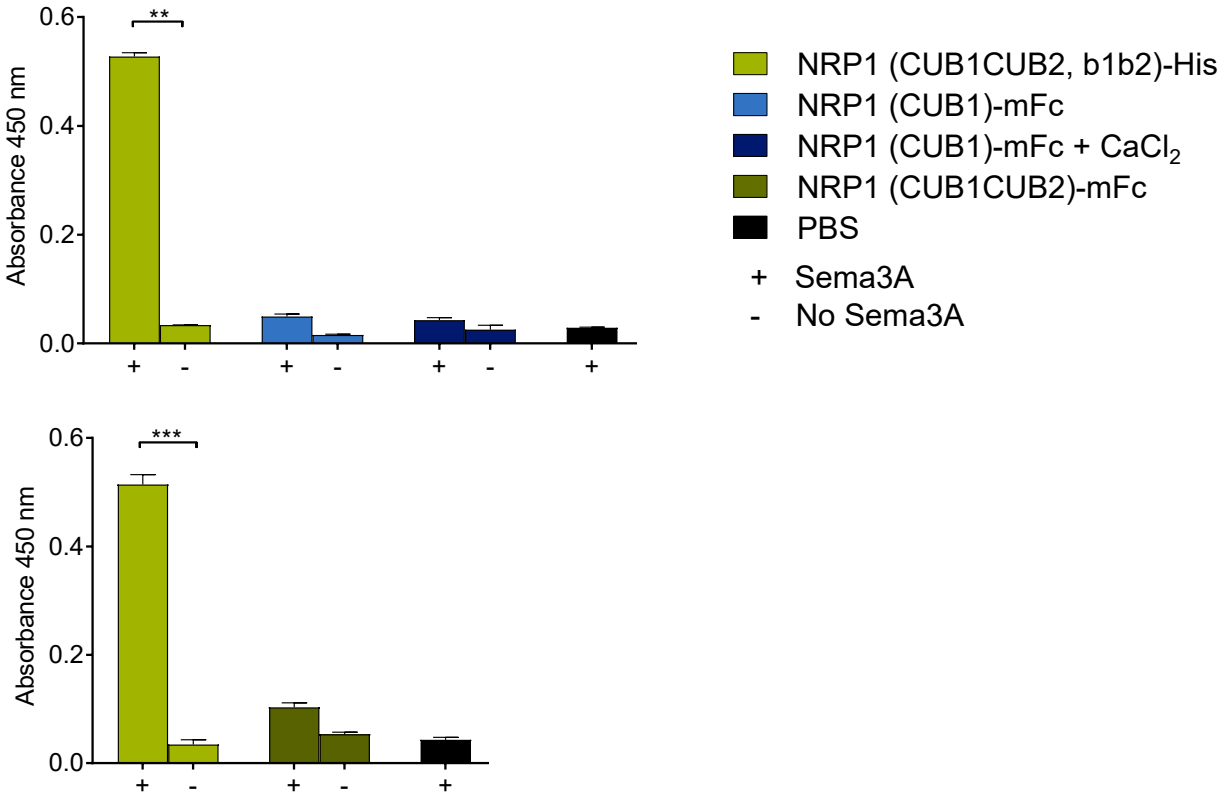

Figure 11. Analysis of binding of Sema3A to NRP1 by ELISA. We investigated binding of Sema3A to our self-produced NRP1-mFc fusion proteins as well as to commercially available, NRP1 (CUB1CUB2, b1b2)-His by ELISA. An ELISA plate was coated with 3 µg/mL NRP1 per well and binding of 1 µg/mL Sema3A fused to a human Fc tag was analyzed (+: with Sema3A; -: without Sema3A). HRP-conjugated mouse anti-human Fc was used for detection. Error bars represent the standard deviation of the mean of duplicates. ** $P \leq 0.01$; *** $P \leq 0.001$.

CCL2 is a rather small protein composed of 76 amino acids, it has a molecular weight of 13 kDa and binding sites for CCR2 are distributed over the whole protein [163]. Hence, we produced full-length CCL2 carrying a C-terminal mFc tag. The CCL2 protein contains the P8A substitution which has been found to ablate dimerization and at the same time ensures equal biological activity as the wild type protein [157]. The P8A substitution has been included to avoid aggregation, as the CCL2-mFc fusion protein dimerizes via the mFc tag. CCL2-mFc was produced in HEK293-6E cells and purified by Protein A chromatography. The protein yield was 7.4 mg per liter production volume. Analytical size exclusion chromatography revealed high protein purity (*Figure 10*). To further investigate protein integrity, western blot and ELISA were performed. Coomassie staining confirmed high protein purity. Multiple bands at approximately

45 kDa are detected by a CCL2-specific antibody on a western blot, which represents variants of the fusion protein with distinct post-translational modifications such as glycosylation of the mFc-tag or CCL2 (*Figure 12A, B*) [164], [165]. In addition, a CCL2-specific antibody could detect our protein in an ELISA (*Figure 12C*). This indicates correct folding and integrity of the CCL2-mFc protein.

In summary, we produced CCL2-mFc to be used for phage display selection of specific antibody fragments. For the selection of NRP1-specific antibody fragments, our truncated NRP1 proteins did not bind to Sema3A, for which reason we proceeded using commercially available NRP1 (CUB1CUB2, b1b2) protein.

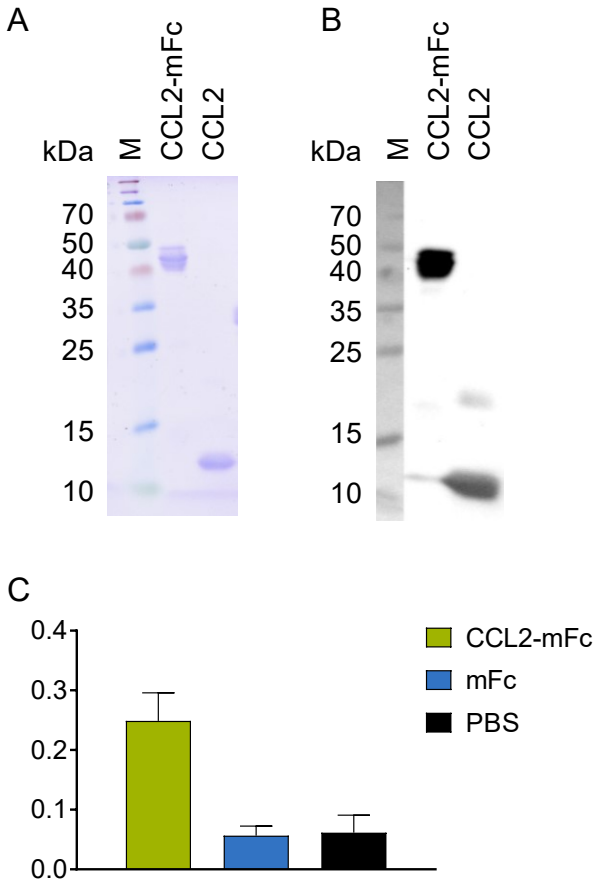

Figure 12. Integrity analysis of CCL2 antigen by western blot and ELISA. The proteins were separated by SDS gel electrophoresis and visualized by (A) coomassie staining and (B) western blotting. For the latter, a rabbit anti-CCL2 primary antibody and a HRP-conjugated goat anti-rabbit antibody were used for detection. M = Marker. (C) CCL2-mFc and mFc were coated onto an ELISA plate and detected using rabbit anti-CCL2 antibody and HRP-conjugated goat anti-rabbit antibody. Error bars represent the standard deviation of the mean of duplicates.

3.1.2 Enrichment of CCL2-specific antibody fragments by phage display

For the selection of fully human CCL2-specific scFvs we performed three rounds of phage display using the antibody library LYNDAL which has been developed in our group by Diebolder *et al.* [152]. LYNDAL comprises 25 individual phage display libraries consisting of IgG VH and VL repertoires from lymph node-derived B cells of head and neck cancer patients. These libraries constitute a large source, in total approximately 5 x 10^9 individual clones, of human monoclonal antibody fragments. The enrichment of CCL2 specific scFvs was monitored by polyclonal phage ELISA and ELISA with soluble monoclonal scFvs (*Figure 13A*). DNA sequence integrity of monoclonal scFvs was analyzed by colony PCR.

Polyclonal phages presenting the scFv on their surface were eluted from the coated antigen after each selection round and subsequently analyzed by ELISA. After selection rounds two and three, phages binding to CCL2-mFc and mFc enriched without cross-reactivity to any of the other tested control proteins (*Figure 13B*). The selection of phages presenting scFvs that bind the mFc tag was expected, therefore binders were further screened on the monoclonal level to identify scFvs specific for CCL2.

Consequently, we picked 540 *E. coli* TG1 individual colonies after infection with round three phages. On the phagemid vector the scFv is separated from the phage coat protein pIII by an amber stop codon. Although *E. coli* TG1 is an amber stop codon suppressor strain, we found that it generates sufficient amounts of soluble scFv not fused to the phage coat protein pIII (data not shown). The integrity of these clones was tested by colony PCR, which revealed that only 37.2 % contained full-length scFv DNA sequences (*Figure 13C*). The enrichment of non-full length antibody fragments was also observed for our NRP1 screening (*Appendix*, *Figure 36*). These non-full-length scFvs may have a propensity to enrich during phage display selection due to “stickiness” to the immunotube plastic surface. We then induced expression of soluble scFv from the full-length clones, isolated the scFvs from the bacterial periplasm and analyzed the specificity by ELISA (data not shown). We decided to repeat this assay with the 35 most promising clones that bound to CCL2-mFc and showed low/no binding to mFc. The repeated ELISA lead to the selection of two scFv clones which showed strong binding to CCL2-mFc and no binding to mFc (clones NB7.C7 and NB7.E5) (*Figure 13D*). The clones NB9.A4, NB9.D6 and NB9.G9 were excluded due to binding to mFc and all other clones were below the cut-off limit (absorbance 450 nm < 1). Sequence analysis of NB7.C7 and NB7.E5 revealed that both clones were identical and we continued with the analysis of anti-CCL2 scFv NB7.E5.

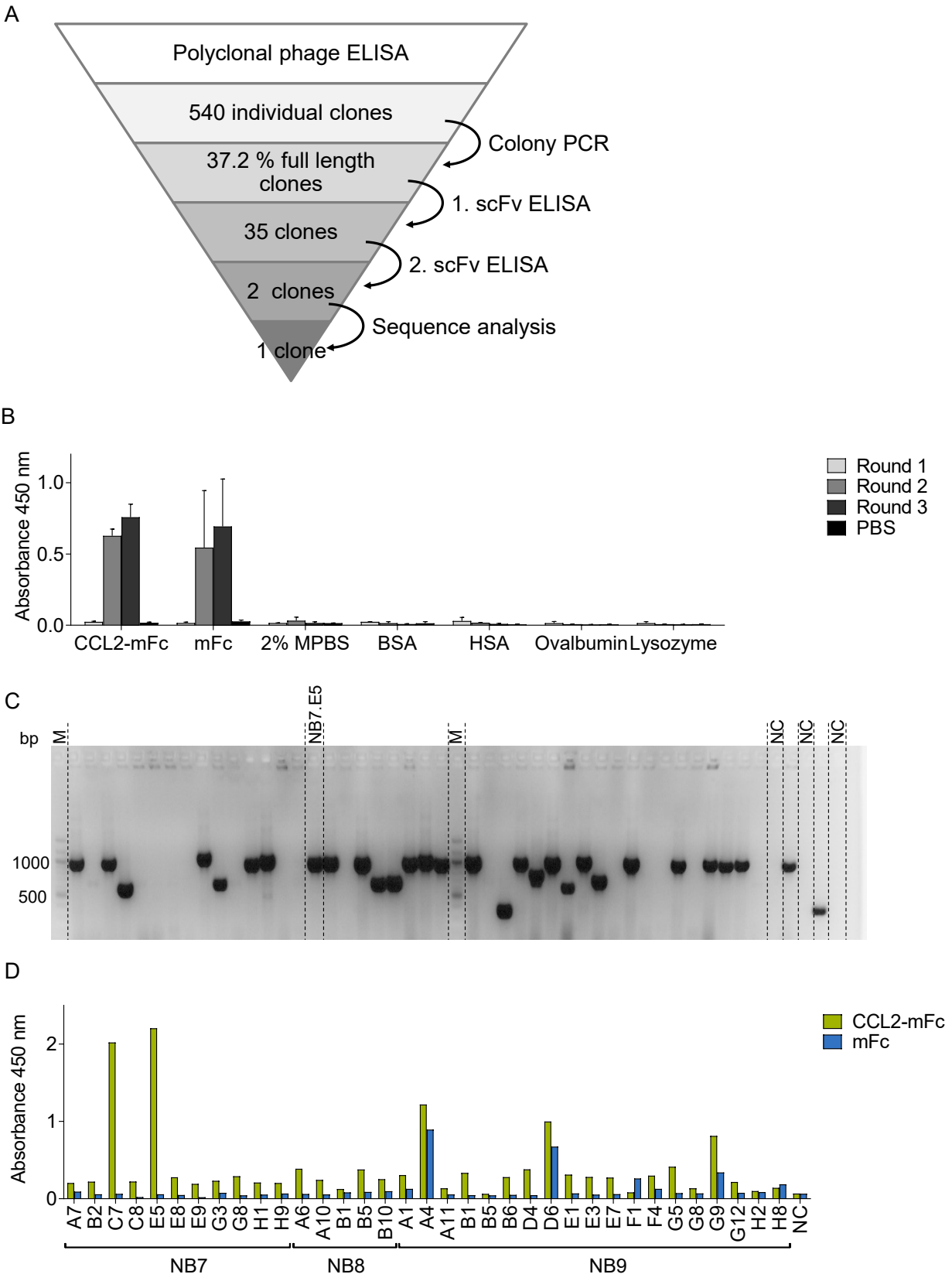
A
Polyclonal phage ELISA
540 individual clones
37.2 % full length clones
35 clones
2 clones
1 clone
Colony PCR
1. scFv ELISA
2. scFv ELISA
Sequence analysis
B
Absorbance 450 nm
1.0
0.5
0.0
CCL2-mFc
mFc
2% MPBS
BSA
HSA
Ovalbumin
Lysozyme
Round 1
Round 2
Round 3
PBS
C
bp
M
NB7.E5
M
NC
NC
NC
1000
500
D
Absorbance 450 nm
2
1
0
A7 B2 C7 C8 E5 E8 E9 G3 G8 H1 H9 A6 A10 B1 B5 B10 A1 A4 A11 B1 B5 B6 D4 D6 E1 E3 E7 F1 F4 G5 G8 G9 G12 H2 H8 NC
NB7
NB8
NB9
CCL2-mFc
mFc

Figure 13. Analysis of CCL2-specific scFvs after the third round of phage display selection. (A) An overview of the analysis and narrowing down of binders on the polyclonal and monoclonal level is presented. After the third round of phage display selection, ELISA using eluted polyclonal phages was performed to analyze the enrichment of antigen-specific phages. Individual bacterial clones infected with phages from selection round three were subjected to colony PCR. Only monoclonal scFvs containing the full-length DNA sequence were analyzed further by ELISA after inducing soluble expression in the bacterial clones. Clones which showed strong binding to CCL2-mFc and low/undetectable binding to mFc were reevaluated in a second ELISA. Promising candidates were subjected to sequence analysis. One unique CCL2-specific clone was identified. (B) Polyclonal phage ELISA was performed to analyze the enrichment of CCL2-specific phages after each selection round. 1 x 10^{12} phages were added per well coated with CCL2 (3 µg/well). Bound phages were detected using a HRP-conjugated anti-M13 phage coat protein antibody. Error bars represent the standard deviation of the mean of duplicates. (C) *E. coli* TG1 were infected with phages after the third round of phage display. Individual clones were subjected to colony PCR with scFv sequence-specific primers and DNA was separated using agarose gel electrophoresis to identify clones carrying a full-length scFv sequence (corresponding to 1000 bp). A representative sample of a total of 540 colony PCRs is presented. The CCL2-specific clone NB7.E5 is indicated. (D) Monoclonal scFvs isolated from bacterial periplasm were analyzed by ELISA. 50 µL of extracted scFvs were added per well to a CCL2-coated ELISA plate. Bound scFvs were detected using a HRP-conjugated anti-c-myc antibody. NB7-NB9 represents the different bacterial glycerol stock master plates. M = marker, NC = negative control.

3.1.3 Sequence analysis of CCL2- and NRP1-specific scFvs selected from immune and naïve libraries

We hypothesized to isolate scFvs with improved specificity and affinity from an immune antibody library like LYNDAL compared to an antigen unexperienced naïve library. To address this question, our collaborator Yumab GmbH selected five CCL2- and two NRP1-specific antibody fragments from their proprietary naïve IgM antibody library HAL9/10 by phage display. HAL9/10 is derived from blood lymphocytes of 98 non-immunized humans and contains a repertoire size of 1.5 x 10^{10} clones [156].

We intended to investigate whether the DNA sequence of antibody fragments derived from an antigen-encountered immune library accumulated more mutations due to affinity maturation than that of antibody fragments selected from a naïve library. For this purpose, we compared the antibody variable heavy (VH) and variable light (VL) chain sequence to the closest related germline sequence using the databases IMGT/V-Quest and VBASE2 [154], [155]. The results are summarized in *Table 27*.

Regarding the VH gene usage, we found three VH1, four VH3 and one VH5 subfamilies within all screened antibody fragments. The VH1 subfamily represents 19 % of the used VH genes *in vivo* and is therefore overrepresented (50 %) in our CCL2-specific antibody fragments. This might indicate preferential binding of VH1 to CCL2 which could be due to similar complementarity determining region (CDR) sequences. The VH3 gene is present in both anti-NRP1 antibody fragments and is the most commonly used VH gene family *in vivo* constituting 49 %. VH4 is not represented in our screened antibody fragments, although this subfamily is the second most frequently used VH region (27 %) *in vivo* [166]. Importantly, the underrepresentation of VH4 has also been found in a large scale antibody analysis of the HAL9/10 library [156]. As expected, we found 36 nucleotide (nt) mutations in the VH region of the LYNDAL-derived clone NB7.E5 leading to 22 amino acid (AA) mutations of which four were located within the CDRs. In contrast, only up to five nucleotide mutations were found in the scFvs selected from the naïve library leading to no or only one amino acid mutation in one of the CDRs (see clone YU109H1). All other mutations were located in the framework regions.

Surprisingly, only two out of the eight antibodies contained κ light chains (NB7.E5 and YU109H1). In humans, κ light chain IgG antibodies are approximately twice as common as antibodies containing a λ light chain [1]. Interestingly, Kuegler *et al.* also found this underrepresentation of κ light chain antibodies (15.9 %) when analyzing the HAL libraries [156]. Moreover, all λ light chain antibodies contained the same V region gene Vλ3 (except for clone YU110D1) and the same J region gene and allele Jλ2*01 F. The Vλ3 gene is only the third most commonly used subfamily *in vivo* (17%) [166]. This might indicate structural advantages of this specific λ light chain subfamily regarding binding to CCL2 or NRP1. Moreover, we found a surprising accumulation of mutations in the VL region of antibody fragments selected from the naïve library (up to 15 amino acid changes) as compared to the immune library-selected antibody fragment (5 amino acid changes).

In summary, we found a total of 27 amino acid changes in the combined VH and VL region of the LYNDAL-derived clone NB7.E5. In contrast, the HAL9/10-derived clones had only 1 - 16 amino acid changes in the VH and VL region.

Table 27. Comparison of antibody sequences with their closest related germline sequence

Clone	NB7.E5	YU109A1	YU109B1	YU109D1	YU109E1	YU109H1	YU110B1	YU110D1
Target	CCL2	CCL2	CCL2	CCL2	CCL2	CCL2	NRP1	NRP1
Heavy chain								
V-gene + allele (identity [%])	IGHV1 24*01 F (87.85)	IGHV5 51*01 F (100.00)	IGHV1 24*01 F (98.96)	IGHV3 20*01 F (99.65)	IGHV1 69*01 F (98.26)	IGHV3 30*03 F (99.31)	IGHV3 30*03 F (98.96)	IGHV3 33*01 F (98.26)
D-gene + allele	IGHD1 26*01 F	IGHD4 17*01 F	IGHD2 21*02 F	IGHD4 17*01 F	IGHD4 17*01 F	IGHD4 17*01 F	IGHD2 8*01 F	IGHD1 26*01 F
J-gene + allele (identity [%])	IGHJ2*01 F (90.57)	IGHJ3*02 F (96.00)	IGHJ3*02 F (100.00)	IGHJ3*02 F (96.00)	IGHJ4*02 F (95.83)	IGHJ4*02 F (89.58)	IGHJ5*02 F (76.47)	IGHJ6*02 F (91.94)
V: Number of nt mutation	36	0	3	1	5	3	3	5
V: Number of AA changes (very dissimilar)	22 (4)	0	1 (0)	1 (0)	2 (0)	3 (0)	1 (0)	4 (1)
CDR1: Number of AA changes (very dissimilar)	3 (1)	0	0	0	0	0	0	0
CDR2: Number of AA changes (very dissimilar)	1 (0)	0	0	0	0	0	0	0
CDR3: Number of AA changes (very dissimilar)	0	0	0	0	0	1 (0)	0	0
Light chain								
V-gene + allele (identity [%])	IGKV1 5*01 F (97.13)	IGLV3 21*02 F (96.06)	IGLV3 19*01 F (100.00)	IGLV3 21*01 F (88.89)	IGLV3 21*03 F (96.06)	IGKV3 20*01 F (92.91)	IGLV3 21*02 F (91.40)	IGLV1 47*02 F (96.49)
J-gene + allele (identity [%])	IGKJ2*01 F (94.87)	IGLJ2*01 F (94.59)	IGLJ2*01 F (100.00)	IGLJ2*01 F (94.59)	IGLJ2*01 F (97.37)	IGKJ3*01 F (100.00)	IGLJ2*01 F (91.89)	IGLJ2*01 F (100.00)
V: Number of nt mutation	8	13	0	31	7	21	27	10
V: Number of AA changes (very dissimilar)	5 (0)	6 (3)	0	14 (5)	4 (2)	11 (8)	15 (7)	8 (4)
CDR1: Number of AA changes (very dissimilar)	0	2 (1)	0	2 (0)	0	2 (1)	0	3 (3)
CDR2: Number of AA changes (very dissimilar)	0	0	0	2 (1)	0	1 (0)	2 (1)	0
CDR3: Number of AA changes (very dissimilar)	3 (0)	1 (0)	0	2 (1)	2 (0)	4 (3)	4 (1)	0

3.2 Characterization of CCL2-specific scFv NB7.E5

The CCL2-specific scFv clone NB7.E5, which was recovered from our in-house antibody library LYNDAL, was cloned into the pAB1 vector for expression in *E. coli* TG1. The pAB1 vector introduced in-frame His- and c-myc-tag sequences 3' to the scFv sequence allowing for later purification and antibody-based detection of the scFv proteins.

3.2.1 Production and purification of anti-CCL2 scFv NB7.E5

E. coli TG1 cells were transformed with pAB1 plasmids encoding the CCL2-specific NB7.E5 scFv fused at the 3' end to a His- and c-myc-tag. ScFv molecules were harvested from the bacterial periplasm and purified by immobilized metal affinity chromatography and SEC. During preparative SEC, we collected only the fractions corresponding to the monomeric peak, which constituted approximately 70 % of the eluted protein (*Figure 14A*). We recovered 1.6 mg protein out of 500 mL production volume that was sufficient for all subsequent analyses. The purity of the NB7.E5 scFv was confirmed by analytical SEC (*Figure 14B*). We observed a highly pure monomeric protein with <10% aggregate content. Compared to a standard protein run, the elution volume of the analyzed scFv corresponded to the expected molecular weight of 29 kDa (*Appendix, Figure 35A*).

We further analyzed the produced NB7.E5 anti-CCL2 scFv by coomassie staining and western blotting (*Figure 14C, D*). We detected one clear band corresponding to the expected molecular weight of approximately 30 kDa on the coomassie stained gel. In addition, the scFv was detected via the C-terminal c-myc-tag by western blotting. The scFv used as control seemed to lose the tag by degradation over time as indicated by the additional band at approximately 25 kDa appearing on the coomassie stained gel and not being detected in the western blot.

In summary, we successfully produced the anti-CCL2 scFv NB7.E5 in bacteria and recovered a highly pure, monomeric protein.

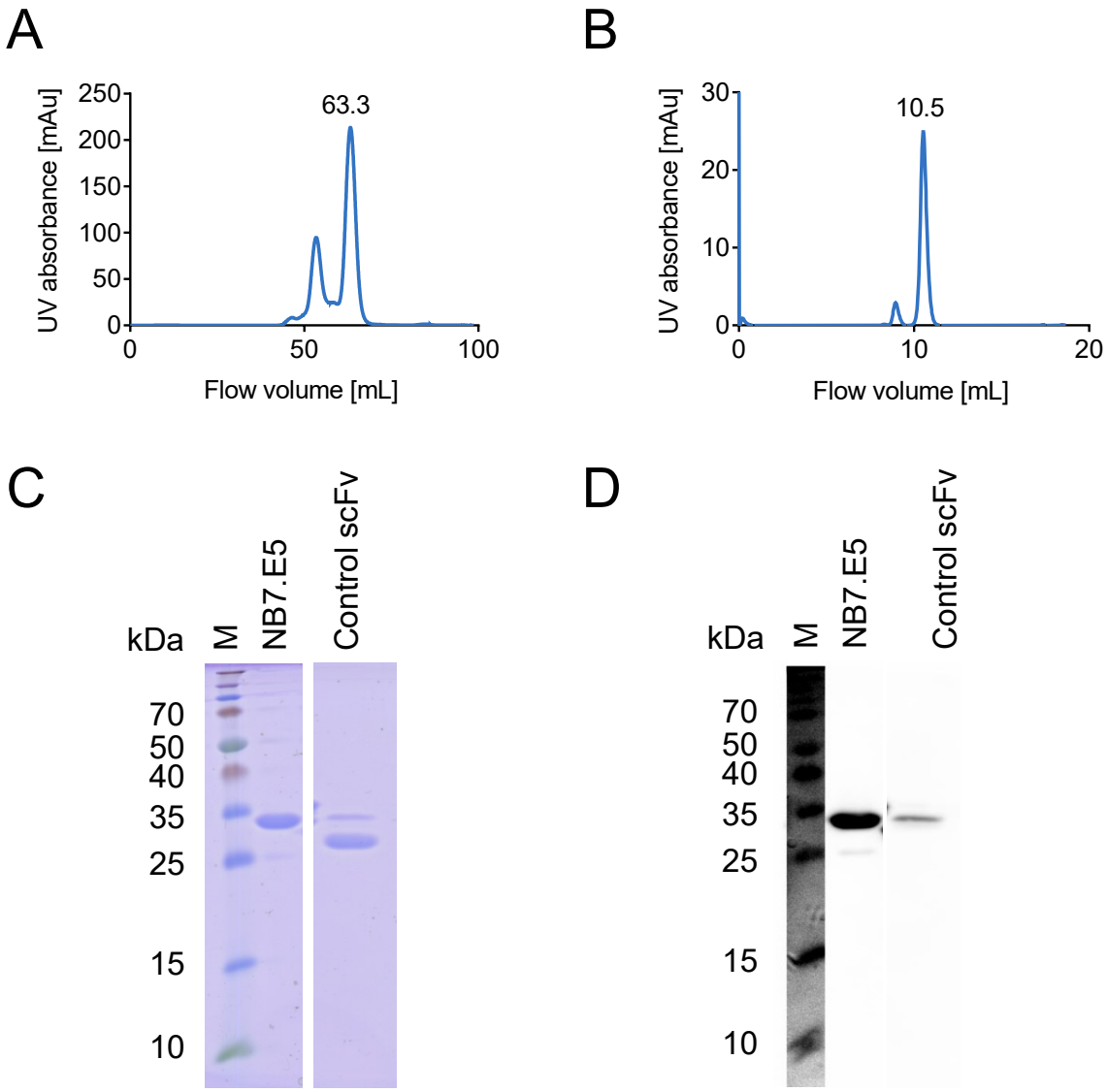

Figure 14. Purification of NB7.E5 anti-CCL2 scFv. After harvesting produced scFv from bacterial periplasm, the protein was purified via the His-tag. (A) During further purification by preparative SEC, only fractions corresponding to monomeric NB7.E5 molecules monomeric scFv were collected. (B) Analytical SEC of NB7.E5 scFv was used to analyze protein purity and elution volumes were compared to a standard run of proteins with known molecular weight, see *Appendix, Figure 35A*. Purified scFv was separated by SDS gel electrophoresis and visualized by (C) coomassie staining and (D) western blotting. ScFvs were detected using an anti-c-myc HRP-conjugated antibody. A control scFv containing a C-terminal myc-tag was included. M = Marker.

3.2.2 Analysis of specificity of anti-CCL2 scFv NB7.E5

We investigated the binding specificity of the LYNDAL-derived anti-CCL2 scFv NB7.E5 by ELISA and western blotting. First, we performed an ELISA including the target antigen and unrelated control proteins and found that the scFv specifically bound to CCL2 and not to the other tested proteins (*Figure 15A*). Importantly, we did not observe any cross-reactivity with mFc which was included as a protein tag in the CCL2-mFc fusion protein used as antigen for phage display selection.

To determine if the NB7.E5 scFv also binds to the linearized CCL2 antigen, we separated CCL2-mFc and commercially available CCL2 in SDS PAGE and probed our anti-CCL2 scFv in western blot analysis (*Figure 15*B). We observed that the NB7.E5 scFv specifically detected CCL2 also in its denatured form.

Since chemokines are a closely related protein family with high sequence homologies, we decided to have a deeper look into the cross-reactivity profile of our anti-CCL2 scFv. Therefore, we identified the chemokines with over 50 % sequence identity compared to CCL2 by using NCBI protein blast, namely CCL7, CCL8, CCL11 and CCL13 [167]. Indeed, as determined by ELISA, we confirmed the specificity of NB7.E5 scFv towards CCL2 as no binding to CCL7, CCL8, CCL11 and CCL13 was detected (*Figure 15C*). Therefore, our NB7.E5 scFv possesses high specificity for CCL2 despite the high sequence homology to other related chemokines.

In conclusion, the NB7.E5 scFv exclusively binds to CCL2 and no binding to the mFc protein tag or related chemokines was observed.

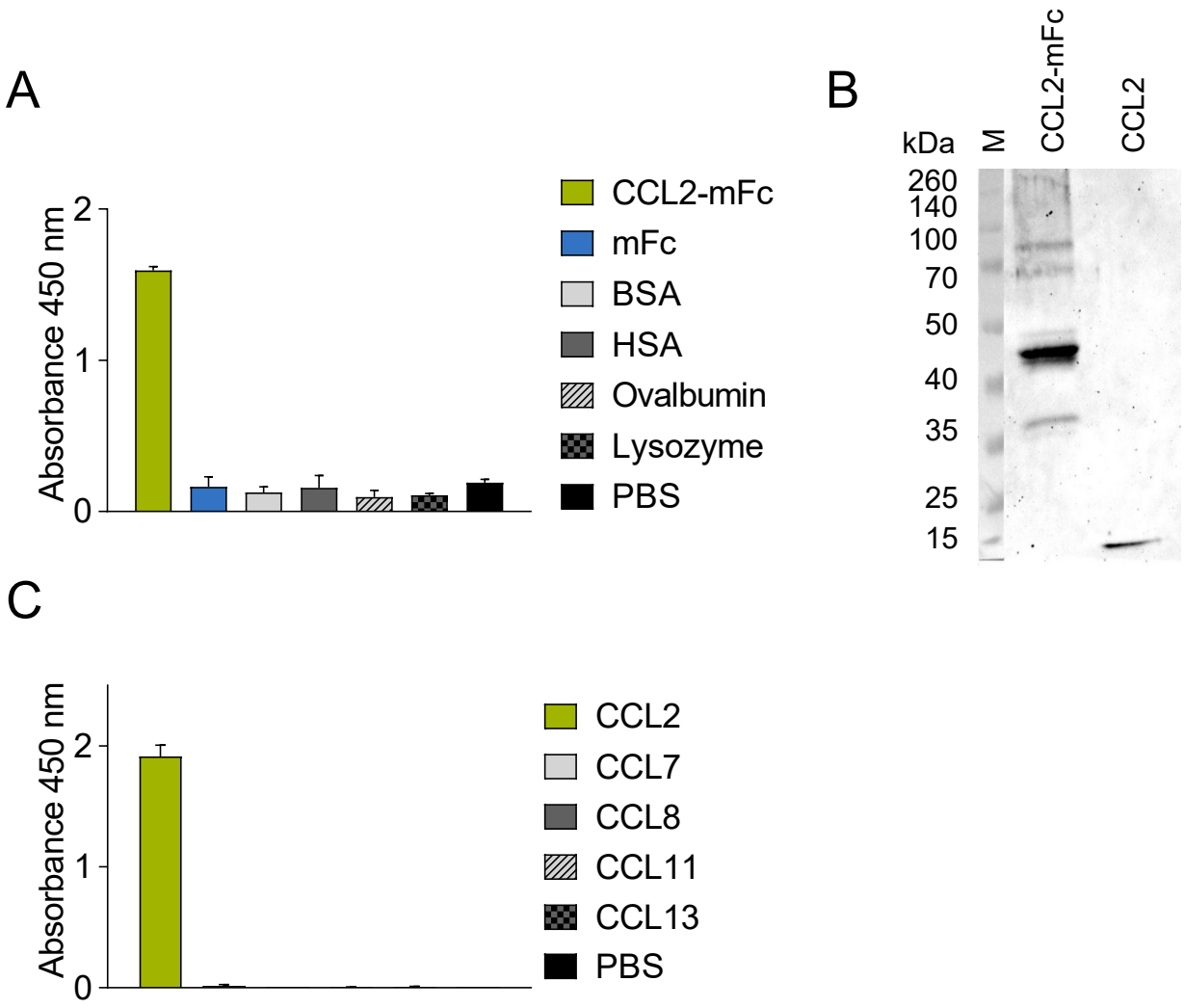

Figure 15. The anti-CCL2 scFv NB7.E5 shows high specificity towards CCL2. (A) ELISA was performed to investigate the binding of the NB7.E5 scFv to CCL2 and to a set of control proteins. ELISA plates were coated with the indicated proteins and 10 µg/mL scFv were added to the coated wells. Bound scFv was detected using a HRP-conjugated anti-c-myc antibody. Error bars represent the standard deviation of the mean of triplicates. (B) CCL2-mFc fusion protein and commercially available CCL2 were separated by SDS gel electrophoresis and binding of NB7.E5 scFv was detected on a western blot. 10 µg/mL NB7.E5 scFv were incubated with the membrane and bound scFv was detected using an anti-c-myc HRP-conjugated antibody. (C) To analyze cross-reactivity of NB7.E5 towards chemokines with > 50 % sequence identity to CCL2, an ELISA was performed. Indicated chemokines were coated to the wells of an ELISA plate and 10 µg/mL scFv were added to the coated wells. Bound scFv was detected using a HRP-conjugated anti-c-myc antibody. Error bars represent the standard deviation of mean values of duplicates.

3.3 Generation and characterization of CCL2- and NRP1-specific IgG1 antibodies

The antibody-like scFv-hFc format was chosen for preliminary analyses of the selected anti-CCL2 and anti-NRP1 scFv molecules in a bivalent context. Therefore, the LYNDAL-derived NB7.E5 scFv was synthesized by Eurofins Genomics in order to include the same restriction sites and VH-VL linker which are used by the HAL9/10-derived scFvs. All CCL2- and NRP1-specific scFv clones were cloned into the mammalian expression vector pCMX2.5 to fuse the scFv sequences to a human IgG1 Fc backbone (scFv-hFc). The scFv-hFc fusion proteins were produced in HEK293-6E cells and purified via the hFc tag. Analytical SEC as well as coomassie staining following SDS PAGE of the purified proteins showed high protein purity with no or low aggregate content (*Appendix*, *Figure 37*). Importantly, CCL2- and NRP1-specific scFv-hFc proteins specifically bound their target antigens without binding to unrelated control proteins as detected by ELISA (*Appendix*, *Figure 38*). Moreover, we analyzed the binding kinetics by surface plasmon resonance spectroscopy. With an equilibrium dissociation constant (K_D) of 5.7 nM, NB7.E5 scFv-hFc showed strong affinity to CCL2. All other scFv-hFc molecules exhibited moderate binding affinities (K_D values ranging from 27 to 105 nM), except anti-CCL2 scFv-hFc YU109H1 for which no affinity could be determined (Appendix, *Figure 39, Table 29*). Due to the promising results, we decided to proceed with the analysis of all selected clones in the IgG1 format. Since the analyses in the IgG1 format confirmed our findings in the scFv-hFc format, only the characterization of the IgG1 antibodies are presented and discussed in greater detail in the following section.

The CCL2- and NRP1-specific scFvs were expressed in the context of a full-length IgG1 antibody containing the N297A substitution. This substitution has been described to result in lack of glycosylation and thereby loss of Fcγ receptor binding and, thus, loss of effector functions [168], [169]. NRP1 is expressed on several immune cell populations, we therefore intended to inhibit antibody mediated effector functions. Although CCL2 is a soluble protein and antibody mediated effector functions might not play an obvious role, chemokines have been found to be sequestered to the cell surface by glycosaminoglycans [170]. To avoid potential off-target effects that may be destructive when applied *in vivo*, we decided to continue with the IgG1 format containing the N297A substitution.

ScFv VH and VL sequences were first separately cloned into the corresponding mammalian expression vectors pConPlus IgG1 [N297A], pConPlus Lambda or pConPlus Kappa. To experimentally show successful ablation of Fcγ receptor binding mediated by the N297A

substitution, we additionally produced the NB7.E5 IgG containing the wild-type N297 amino acid by using the expression vector pConPlus IgG1. Subsequently, IgG antibodies were produced in HEK293-6E cells, purified and binding characteristics were analyzed.

3.3.1 Production and purification of CCL2- and NRP1-specific full-length IgGs

Anti-CCL2 IgG antibodies (NB7.E5, YU109A1, YU109B1, YU109D1, YU109E1 and YU109H1) as well as anti-NRP1 IgG antibodies (YU110B1 and YU110D1) were produced in HEK293-6E cells. The cell culture supernatants were harvested and the antibodies were purified by Protein A affinity chromatography. Protein yields ranged from 5 to 39 mg protein per liter production volume. This difference in production efficiency might be due to different transfection efficiency and/or preferences in codon usage for the various antibody variable regions. All antibody yields were sufficient for subsequent studies.

Purity was determined by analytical SEC as well as separation by SDS gel electrophoresis and coomassie staining (*Figure 16*). Analytical SEC revealed that all proteins were highly pure showing low aggregate content of <5% (*Figure 16A, B*). The only exception was YU110B1 with 16 % aggregate content. We decided not to further purify YU110B1 considering the substantial protein loss which would have occurred by additional purification. Protein elution volume was compared to a standard protein run (*Appendix,Figure 35B*) and the expected antibody molecular weight of approximately 150 kDa was confirmed. Interestingly, YU110D1 showed a reduced calculated molecular weight of 100 kDa. Maybe the binding moiety of YU110D1 in context of the full-length IgG1 molecule leads to a more compact folding of the protein and therefore later elution from the column. This deviation from the expected molecular weight was not observed for YU110D1 in the scFv-hFc format (*Appendix, Figure 37*). Separation of the proteins by SDS gel electrophoresis and coomassie staining (*Figure 16C*) confirmed that all antibodies consisted of heavy and light chain (50 and 25 kDa bands, respectively) and no other additional protein bands were detected.

In summary, we produced anti-CCL2 and anti-NRP1 IgG antibodies in mammalian cells and recovered highly pure proteins.

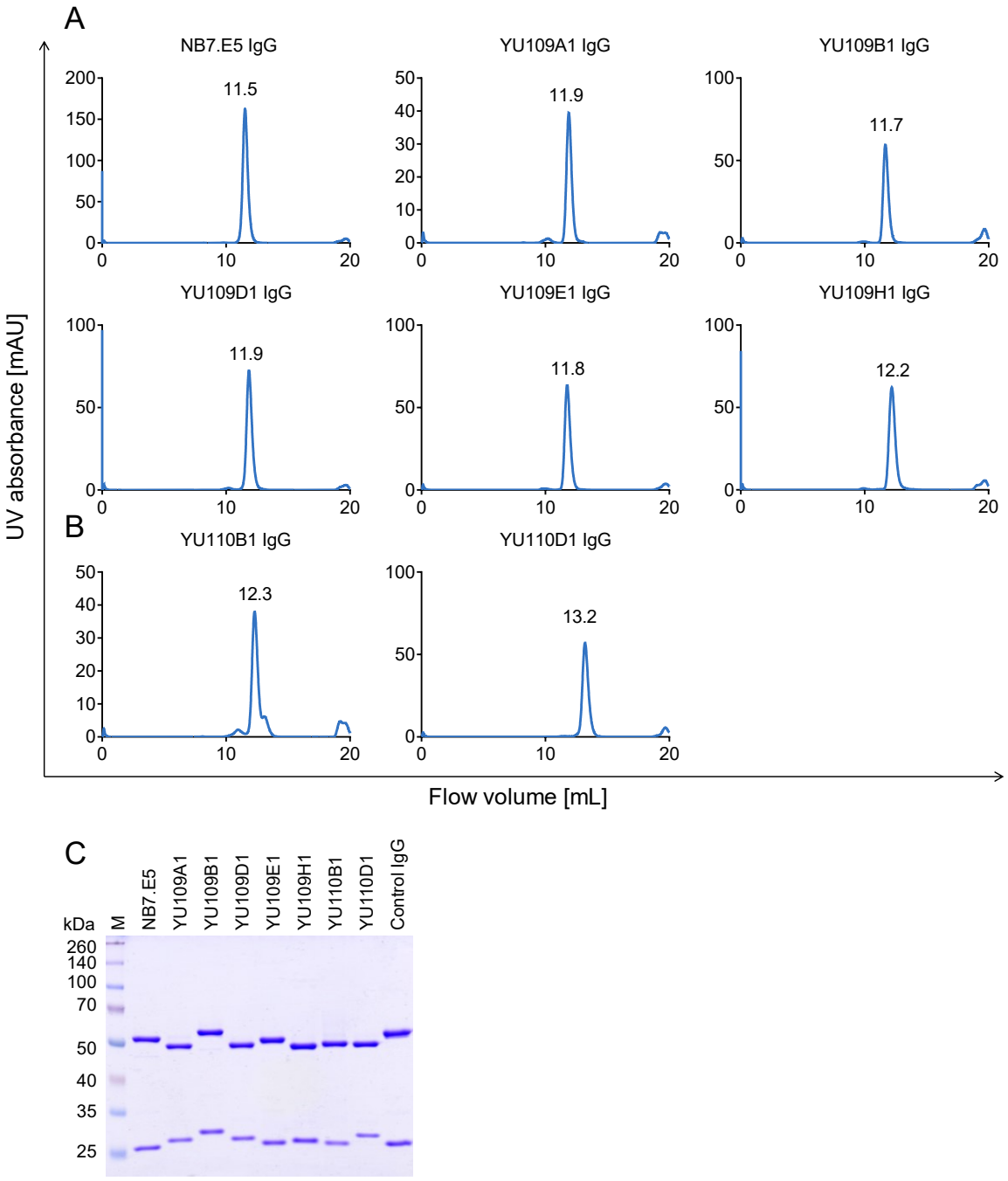

Figure 16. Investigation of IgG antibody purity by analytical size exclusion chromatography and coomassie staining. Following Protein A affinity purification of the IgG antibodies, the purity of the proteins was analyzed. Analytical SEC of anti-CCL2 (A) and anti-NRP1 (B) IgG antibodies was performed to investigate purity and aggregate content. Elution volumes were compared to those of a standard protein run (*Appendix, Figure 35B*). (C) Antibodies were separated by SDS gel electrophoresis and visualized by coomassie staining. A control IgG was included for comparison of antibody heavy and light chain. YU109E1 and YU109H1 purification and coomassie staining were performed by M.Sc. D. Thomas. M = Marker.

3.3.2 Effects of the N297A substitution on Fcγ receptor binding

All our IgG antibodies contain the N297A substitution which is described to ablate antibody effector functions by blocking the binding to the Fcγ receptor [168], [169]. To verify this, we compared their binding to the human monocytic cell line THP1, which expresses high amounts of Fcγ receptor I and II, to a control IgG [171]. Therefore, we cloned, produced and purified the anti-CCL2 NB7.E5 IgG containing the wild-type N297, termed NB7.E5 (N297). Antibody purity and target antigen binding was confirmed as described for the mutated counterpart (*Appendix, Figure 40*).

As expected, the N297A substitution resulted in the ablation of binding of antibodies to Fc receptor expressing cells (*Figure 17*). Based on this finding we also expect reduced effector functions and thereby reduced off-target effects of our antibodies *in vivo,* which needs to be assessed in further experiments.

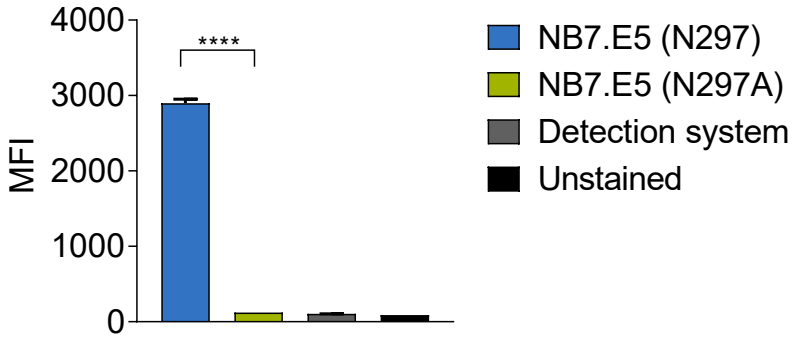

Figure 17. Effect of the N297A substitution on binding of IgG to Fc receptor expressing cells analyzed by flow cytometry. 10 nM NB7.E5 IgG (N297A) or NB7.E5 (N297) were added to Fc receptor expressing THP1 cells. Bound IgG was detected using a FITC-conjugated rabbit anti-human Fc gamma antibody and data was acquired by flow cytometry. MFI = median fluorescence intensity. Error bars represent the standard deviation of mean values of triplicates. **** P ≤ 0.0001.

3.3.3 Binding profiles of CCL2- and NRP1-specific IgGs determined by ELISA

In order to confirm the previously described results in the scFv format, we re-analyzed the specificity of the IgG antibodies by ELISA. Importantly, in contrast to scFv molecules, IgG molecules are bivalent (two antigen binding sites per molecule) which may affect antigen binding characteristics. Moreover, Steinwand *et al.* showed that scFvs retained antigen affinity when

expressed as scFv-hFc molecules which are encoded on a single gene but may lose affinity after conversion into the full-length IgG format [172].

We found specific binding of our anti-CCL2 and anti-NRP1 IgGs toward their cognate antigen without showing any cross-reactivity towards the control proteins by ELISA. Importantly, no binding was detected to the protein tags which were included in the recombinant target antigens used for phage display (*Figure 18A, B*). The weak signals detected for YU109D1 and YU110B1 against mFc and His, respectively, were considered as negligible. Compared to the other CCL2-specific antibodies, the clones YU109B1 and YU109H1 exhibited weaker signals pointing towards weaker binding of the target antigen.

Importantly, we did not detect any binding of the NB7.E5 IgG to chemokines with a sequence homology of > 50% compared to CCL2, thus confirming the results obtained for the NB7.E5 anti-CCL2 scFv (*Figure 18C*).

Therefore, we observed high specificity for all our anti-CCL2 and anti-NRP1 IgG antibodies and did not observe any binding to other control proteins.

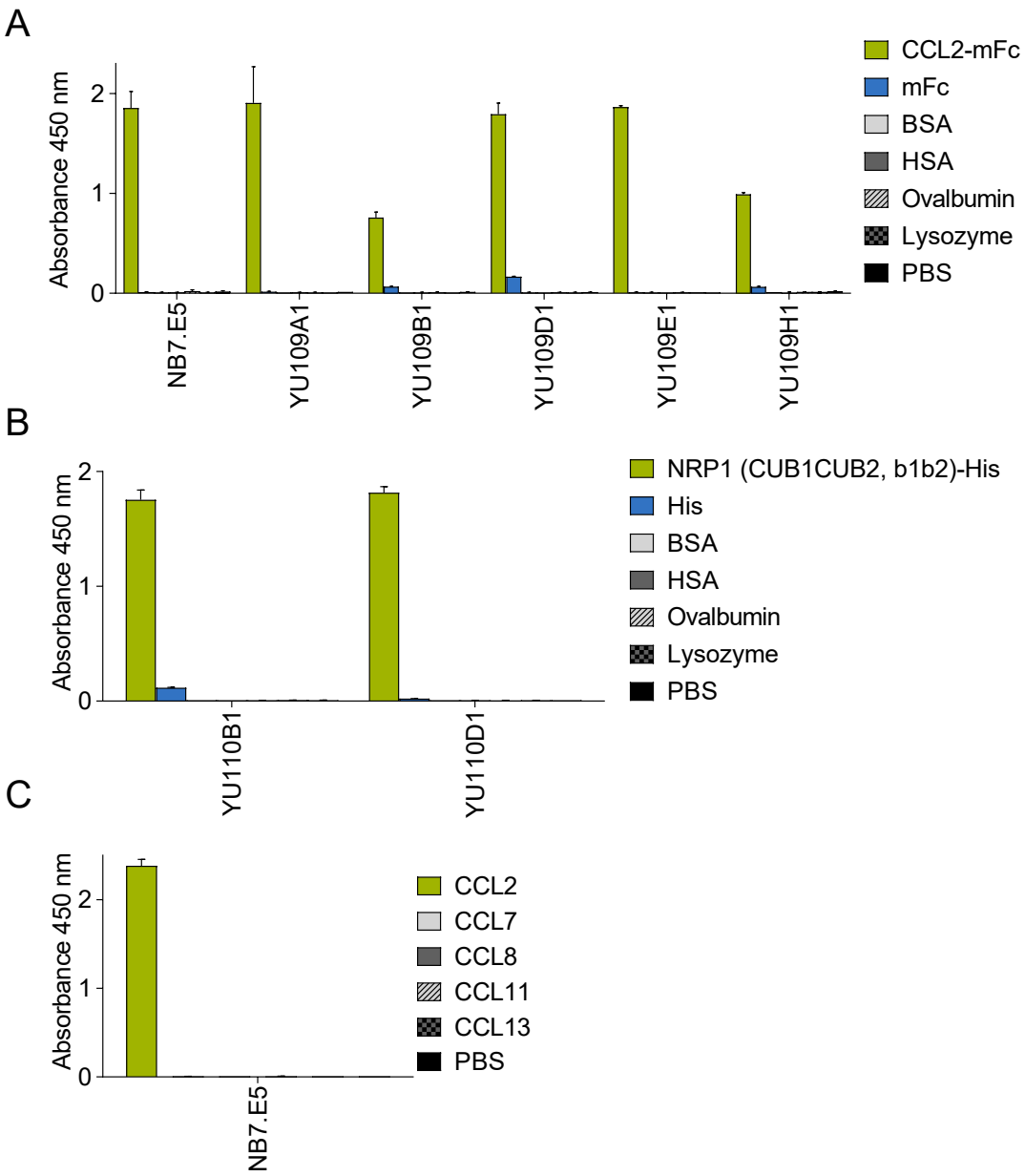

Figure 18. Binding of target antigens by anti-CLL2 and anti-NRP1 IgG antibodies investigated by ELISA. An ELISA was performed using anti-CCL2 (A) or anti-NRP1 (B) IgG antibodies. The wells of an ELISA plate were coated with CCL2 or NRP1, respectively, as well as target antigens and a set of control proteins. mFc and His were included as control proteins since the target antigens used for phage display selection were fused to these tags. His = unrelated scFv antibody fragment fused to a His-tag. (C) Cross-reactivity to chemokines with > 50 % sequence identity to CCL2 was investigated for the NB7.E5 IgG. 10 µg/mL IgG were added to the wells of an antigen-coated ELISA plate. Bound IgG was detected using a HRP-conjugated mouse anti-human IgG antibody. Error bars represent the standard deviation of mean values of triplicates (A, B) or duplicates (C).

3.3.4 Determination of antibody affinity by surface plasmon resonance spectroscopy

We investigated the binding kinetics of our anti-CCL2 and anti-NRP1 IgG antibodies using surface plasmon resonance (SPR) spectroscopy. By SPR spectroscopy, real-time protein interactions can be detected and mathematical modeling allows the calculation of antibody affinities. We immobilized the IgG antibodies on the surface of a Protein A-coated sensorchip and injected increasing concentrations of target antigen (*Figure 19*). Antibody affinities were calculated by fitting the data either to a 1:1 Langmuir binding model or in the case of antibodies with very fast association and dissociation a steady state affinity model (results of two independent experiments are summarized in (*Table 28*)).

For the CCL2-specific antibodies (*Figure 19A*) we observed that the LYNDAL-derived antibody NB7.E5 showed robust binding toward the target antigen CCL2 (K_D = 5.8 nM) with slow dissociation kinetics. In contrast, the clones YU109A1, YU109B1, YU109D1 and YU109E1 showed moderate antigen binding affinities (K_D values ranging from 50 to 334 nM) and possessed very fast association and dissociation rates. YU109H1 showed only low affinity (K_D = 422 nM), which coincides with the weaker binding as previously detected by ELISA (*Figure 18A*). Due to the highest binding affinity towards its target antigen compared to the other antibodies, and because of its proven high specificity for CCL2, we decided to pursue only with NB7.E5 anti-CCL2 IgG in all subsequent functional characterizations.

For the NRP1-specific IgG antibodies we detected comparable binding profiles and K_D values for YU110B1 and YU110D1 of 35.6 nM and 58.3 nM, respectively (*Figure 19B*).

In conclusion, we identified NB7.E5 to be the lead candidate anti-CCL2 IgG antibody with high affinity binding. The anti-NRP1 IgG antibodies YU110B1 and YU110D1 showed moderate affinities to their cognate antigen.

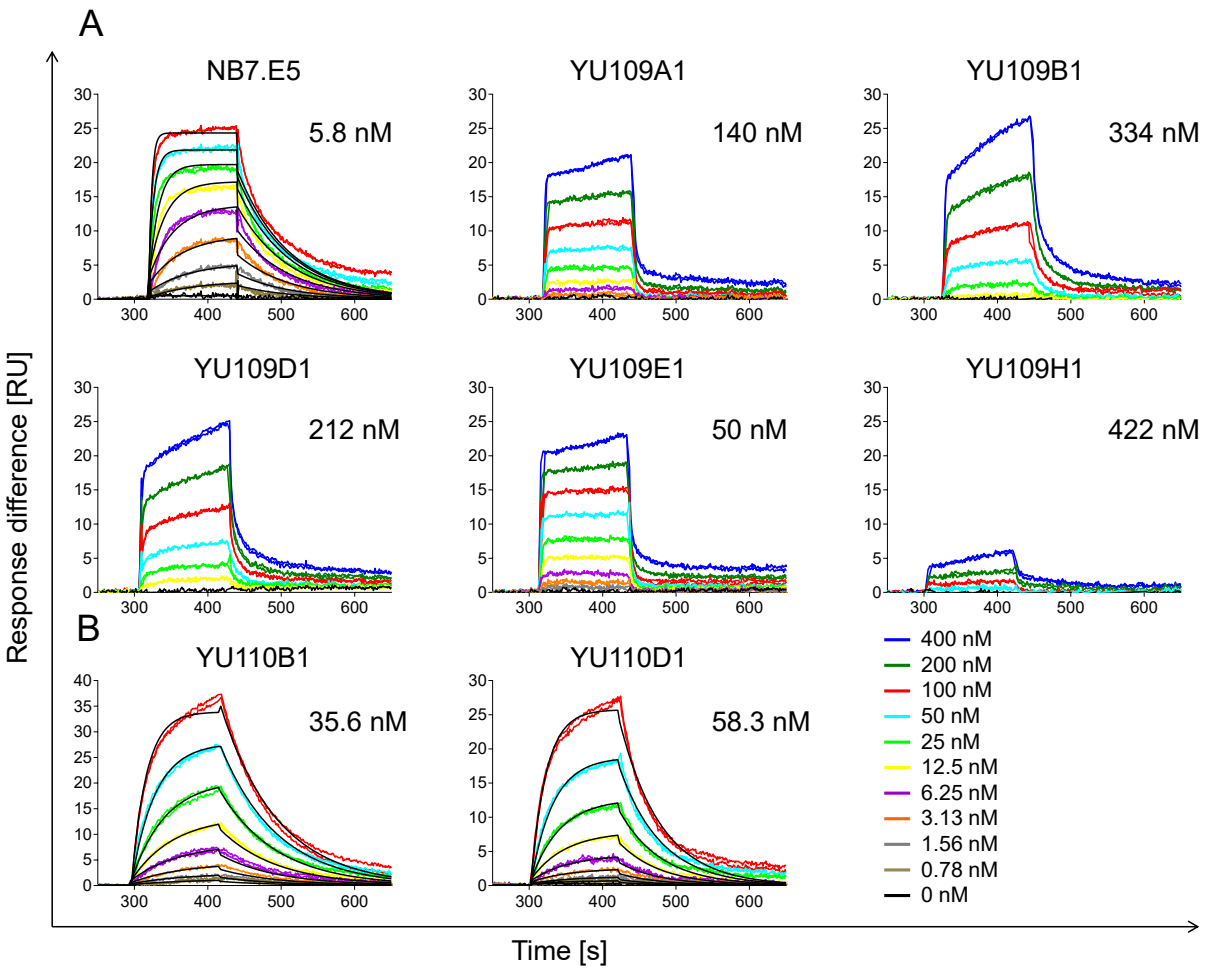

Figure 19. Surface plasmon resonance analyses of CCL2- and NRP1-specific IgGs. (A) Anti-CCL2 and (B) anti-NRP1 IgG molecules were immobilized on a Protein A-coated sensorchip. An antigen concentration series ranging from 0 to up to 400 nM was tested. Black curves represent the 1:1 Langmuir binding model used to calculate antibody affinity. Due to very fast association and dissociation of YU109A1, YU109B1, YU109D1, YU109E1 and YU109H1, these bindings were fitted using a steady state affinity model which only included the equilibrium phase. Numbers indicate the calculated K_D value in nM. Curves represent the mean of duplicates. This is one representative example out of two independent experiments. Performed by M.Sc. D. Thomas.

Table 28. Summary of the mathematical modeling of the IgG binding kinetics determined by surface plasmon resonance spectroscopy

Antigen	IgG1 [N297A]	K_D [nM]		K_D [nM] mean ± SD	Rmax [RU]		Chi^2	
		#1	#2		#1	#2	#1	#2
CCL2	NB7.E5	5.64	5.77	5.7 ± 0.1	19.2	20	0.37	0.47
	YU109A1	115	140	127.5 ± 17.5	23.5	24.6	0.08	0.09
	YU109B1	298	334	nd	33.2	36.9	0.11	0.28
	YU109D1	219	212	215.5 ± 4.9	30.1	29.5	0.07	0.04
	YU109E1	45.2	49.9	47.6 ± 3.3	22.4	22.5	0.10	0.11
	YU109H1	1660	422	nd	20.6	9.33	0.01	0.02
NRP1	YU110B1	42.0	35.6	38.8 ± 4.5	64.1	49.2	0.89	0.29
	YU110D1	73.1	58.3	65.7 ± 10.5	51.6	39.6	0.56	0.21

3.3.5 Binding of anti-NRP1 IgGs to the surface of receptor expressing cells

We next intended to address the question if our anti-NRP1 IgG molecules bind to their cognate antigen when expressed in the context of a cell-surface receptor. For the selection of antibody fragments by phage display, we used recombinant NRP1 protein which included a tag that may have an impact on protein characteristics [173]. Moreover, cell-surface receptors may show different protein folding when expressed as recombinant, soluble proteins [174]. Therefore, antibody binding properties towards the native and the recombinant protein may differ and it is important to study binding of the antibodies to the antigen in its native conformation on the cell surface.

For this purpose, we first confirmed NRP1 expression on human umbilical vein endothelial cells (HUVEC) using a commercially available antibody (*Figure 20A*) and our NRP1-specific IgG antibodies (*Figure 20B*). We then titrated a concentration series of the NRP1-specific IgG molecules on HUVEC cells to determine the antibody affinity by flow cytometry (*Figure 20C*). The K_D was calculated by using a nonlinear curve to fit the data and corresponds to the ligand

concentration needed to achieve half-maximum binding at equilibrium (EC50). We found a K_D of 0.36 nM for YU110B1 and 0.17 nM for YU110D1. Interestingly, these results do not correlate with the K_D values determined by SPR analysis which may be due to the different calculation of the K_D values using these two methods. Additionally, avidity effects in the flow cytometric experiment increases the apparent antibody affinity [175], [176].

Thus, we showed binding of the NRP1-specific IgG molecules to their cognate antigen expressed as cell surface receptor. We observed higher affinity of the antibodies as compared to the previously described surface plasmon resonance analysis.

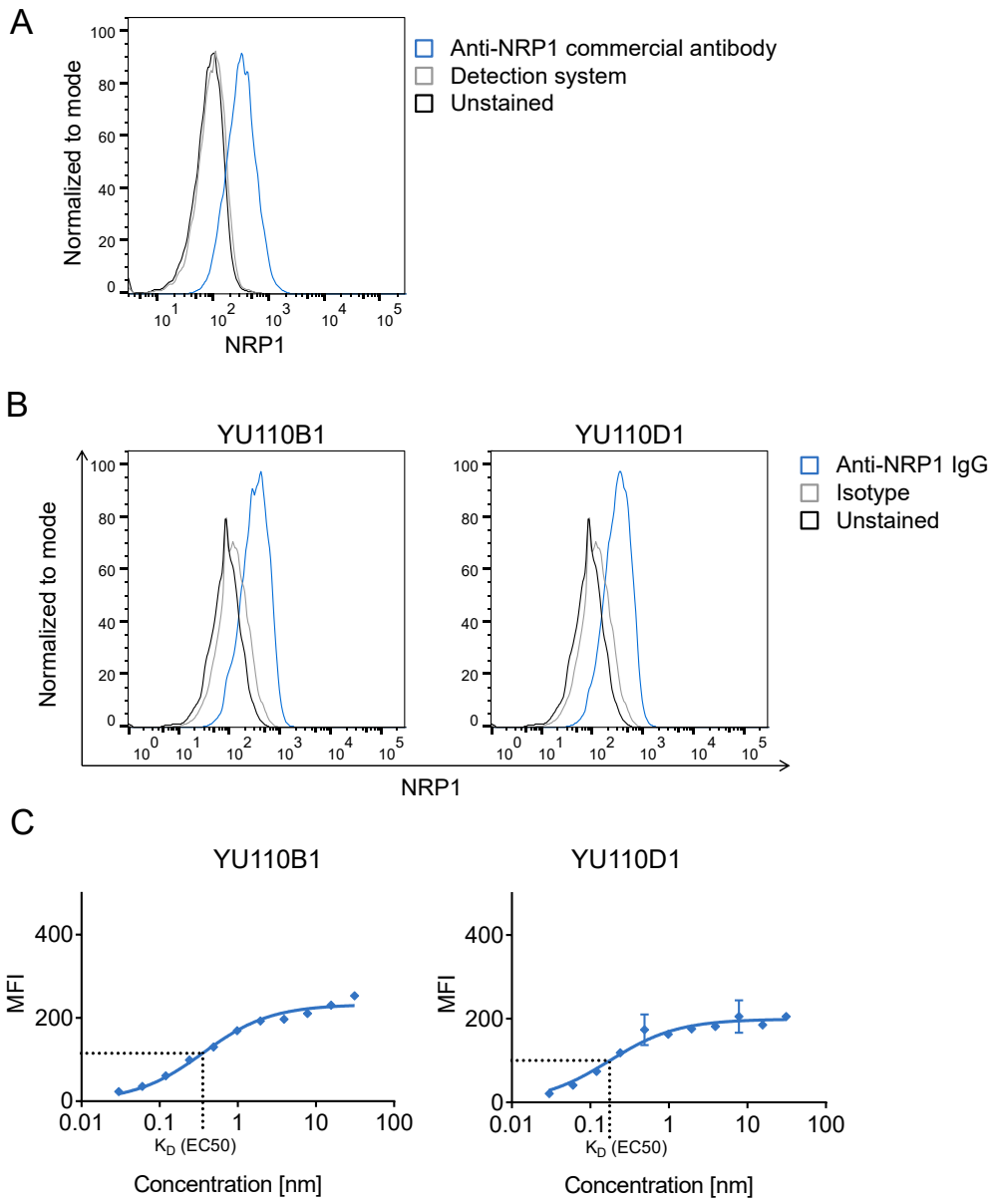

Figure 20. Analysis of binding of anti-NRP1 IgGs to NRP1-expressing cells by flow cytometry. NRP1 expression on HUVEC cells was analyzed by flow cytometry. (A) NRP1 was stained using a commercially available mouse anti-NRP1 antibody and a FITC-conjugated goat anti-mouse IgG detection antibody. (B) Binding of our anti-NRP1 antibodies (30 nM) was detected using a FITC-conjugated rabbit anti-human IgG antibody. An isotype control antibody was included. (C) Anti-NRP1 antibodies were titrated (0-30 nM) on HUVEC cells, binding was detected using a FITC-conjugated rabbit anti-human IgG antibody and data was acquired using a flow cytometer. Error bars represent the standard deviation of mean values of duplicates. The antibody affinity was determined using graph pad prism by including a nonlinear fit and one site specific binding was used to calculate the K_D value (YU110B1 K_D = 0.36 nM; YU110D1 K_D = 0.17 nM).

3.4 Functional characterization of CCL2- and NRP1-specific antibodies and antibody fragments

The anti-NRP1 antibodies YU110B1 and YU110D1 as well as the lead candidate anti-CCL2 antibody NB7.E5 were functionally characterized. To this end, we tested if the NRP1-specific antibodies are able to block the binding of Sema3A to NRP1 by ELISA and flow cytometry. Moreover, we investigated the blocking of the CCL2 – CCR2 interaction mediated by NB7.E5 by flow cytometry and the resulting effects on the downstream signaling cascade. Furthermore, we tested if NB7.E5 is able to block CCL2-dependent cell migration in a transwell assay.

3.4.1 Anti-NRP1 antibodies do not block the Sema3A/VEGF - NRP1 interaction

First, we determined the blocking effects of our antibodies on the receptor - ligand interaction by ELISA. For this purpose, we coated the wells of an ELISA plate with Sema3A and analyzed binding of soluble NRP1 in the presence of anti-NRP1 antibodies, control IgG antibody or the absence of antibodies. Importantly, we detected significant blocking of binding of NRP1 to Sema3A mediated by our antibodies compared to the control (*Figure 21A*). Another ligand of NRP1 is VEGF, thus we wanted to rule out effects of the antibodies on the NRP1 - VEGF interaction. Therefore, we performed an ELISA assay as described before, but with NRP1 being coated to the wells of an ELISA plate and analysis of binding of soluble VEGF. We observed no blocking of this interaction by our antibodies (*Figure 21B*).

To confirm these promising results in a cellular system, we further analyzed the blocking effect of the NRP1-specific antibodies on binding of soluble Sema3A to NRP1 expressed on the cell surface (*Figure 21C*). First, we tested if Sema3A binds to NRP1-expressing HUVEC cells and determined the optimal concentration of Sema3A for use in further experiments. Therefore, we titrated Sema3A on NRP1-expressing HUVEC cells (data not shown). Although we did not reach saturation of cell surface binding, we decided to use the highest feasible Sema3A concentration (75 nM) for further assays. Surprisingly, addition of a 10-fold molar excess (750 nM) of anti-NRP1 antibodies over Sema3A did not block the receptor – ligand interaction on HUVEC cells. Notably, we used antibody concentrations far above which saturation (approximately 10 nM) of antibody binding to NRP1-expressing HUVEC cells was reached, as described previously (*Figure 20B*). Therefore, we expected that all cell surface expressed NRP1 was bound by the anti-NRP1 antibodies and no additional binding of Sema3A would be observed in case the anti-NRP1 antibodies block the Sema3A binding site.

In summary, we observed conflicting results for the blocking capabilities of our antibodies. In an ELISA setting we detected blocking of binding of soluble NRP1 to coated Sema3A mediated by both anti-NRP1 antibodies. In contrast, we did not detect ablation of binding of soluble Sema3A to NRP1-expressing cells in the presence of our antibodies using flow cytometry. Our attempts to further investigate the functionality of our anti-NRP1 antibodies were so far not successful (data not shown), thus we decided not to continue the development of the anti-NRP1 antibodies at this stage.

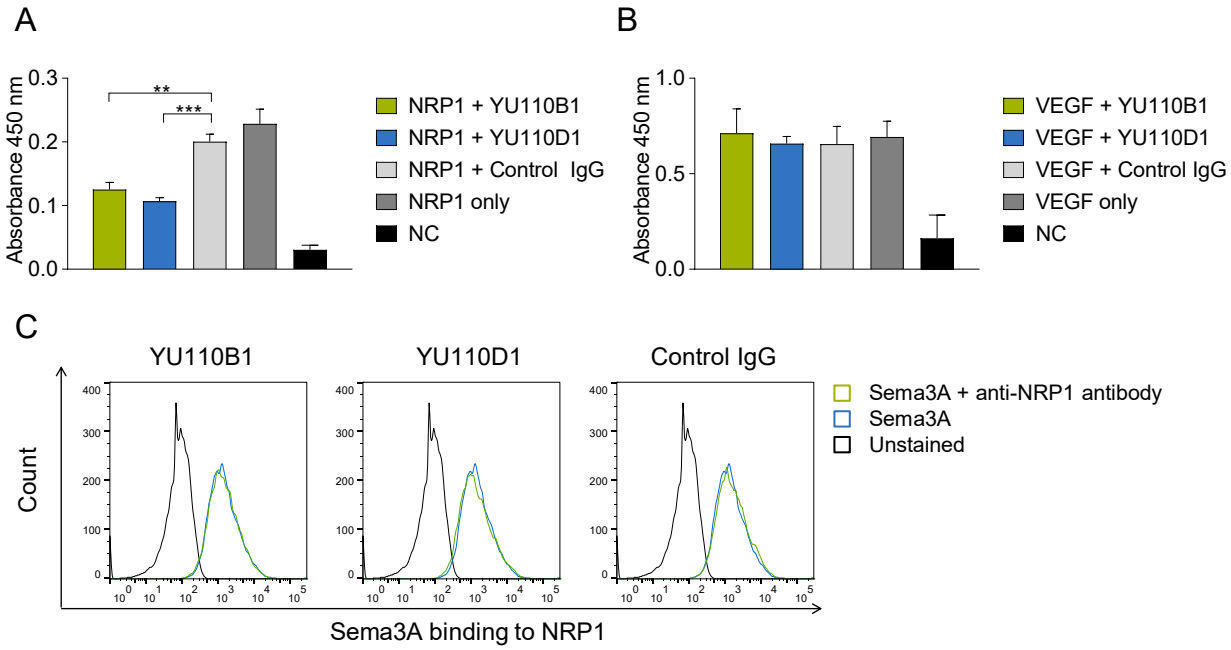

Figure 21. Investigation of blocking of the Sema3A/VEGF – NRP1 interaction mediated by anti-NRP1 IgG antibodies using ELISA and flow cytometry. (A) The effects of the NRP1-specific antibodies on binding of Sema3A to NRP1 were investigated by ELISA. 1000 nM anti-NRP1 and control IgG antibodies were pre-incubated with 50 nM NRP1 (CUB1CUB2, b1b2) and added to a Sema3A-coated ELISA plate. Bound NRP1 was detected using a mouse anti-NRP1 and a HRP-conjugated anti-mouse antibody. NC = negative control: no NRP1 and no IgG. (B) NRP1 - VEGF blocking ELISA was performed to investigate the effect of our antibodies on binding of VEGF to NRP1. 500 nM anti-NRP1 and control IgG antibodies were added to a NRP1 (CUB1CUB2, b1b2)-coated ELISA plate. 8.4 nM biotinylated VEGF was added and detected using HRP-conjugated streptavidin. NC = negative control: no VEGF and no IgG. Error bars represent standard deviation of mean values of triplicates. (C) Blocking of the Sema3A - NRP1 interaction by our NRP1-specific antibodies was investigated by flow cytometry. 750 nM anti-NRP1 antibody or control antibody were incubated with HUVEC cells. 75 nM APC-labeled Sema3A was added and binding was analyzed by flow cytometry.

3.4.2 Anti-CCL2 IgG NB7.E5 blocks binding of CCL2 to CCR2 expressing cells

A prerequisite for the macrophage modulating effects of our CCL2-specific antibody NB7.E5 implies potent neutralizing effects on the interaction between CCL2 and its receptor CCR2. To this end, we investigated the blocking capability by flow cytometry.

First, we confirmed high expression of CCR2 on the cell surface of the monocytic cell line THP1 using a CCR2-specific antibody (*Figure 22A*). Next, THP1 cells were incubated with CCL2-mFc and binding of CCL2 was detected using a fluorescently labeled anti-mFc tag antibody. In addition, we pre-incubated CCL2-mFc with different concentrations (up to 20-fold molar excess) of NB7.E5 scFv or IgG, added the mixture to THP1 cells and analyzed binding of CCL2 by flow cytometry (*Figure 22B*). Since THP1 cells express high levels of Fcγ receptors that can result in unspecific binding of the CCL2-mFc fusion protein, we pre-incubated THP1 cells with human serum and included mFc as control to monitor background binding of CCL2-mFc to the cells. We observed a continuous decrease in binding of CCL2 to THP1 cells that correlates to increasing concentrations of the NB7.E5 antibody. As expected, NB7.E5 IgG showed a stronger blocking capacity of the CCL2 - CCR2 interaction than the monovalent NB7.E5 scFv, which may relate to the bivalent nature of the IgG molecule. A 1:1 molar ratio of CCL2-mFc to NB7.E5 IgG resulted in over 50 % blocking of the receptor - ligand interaction and a 5-fold or higher excess of antibody over CCL2-mFc completely ablated binding of CCL2 to CCR2.

In summary, we successfully demonstrated neutralizing effects of the NB7.E5 IgG and scFv molecules on the CCL2 – CCR2 interaction.

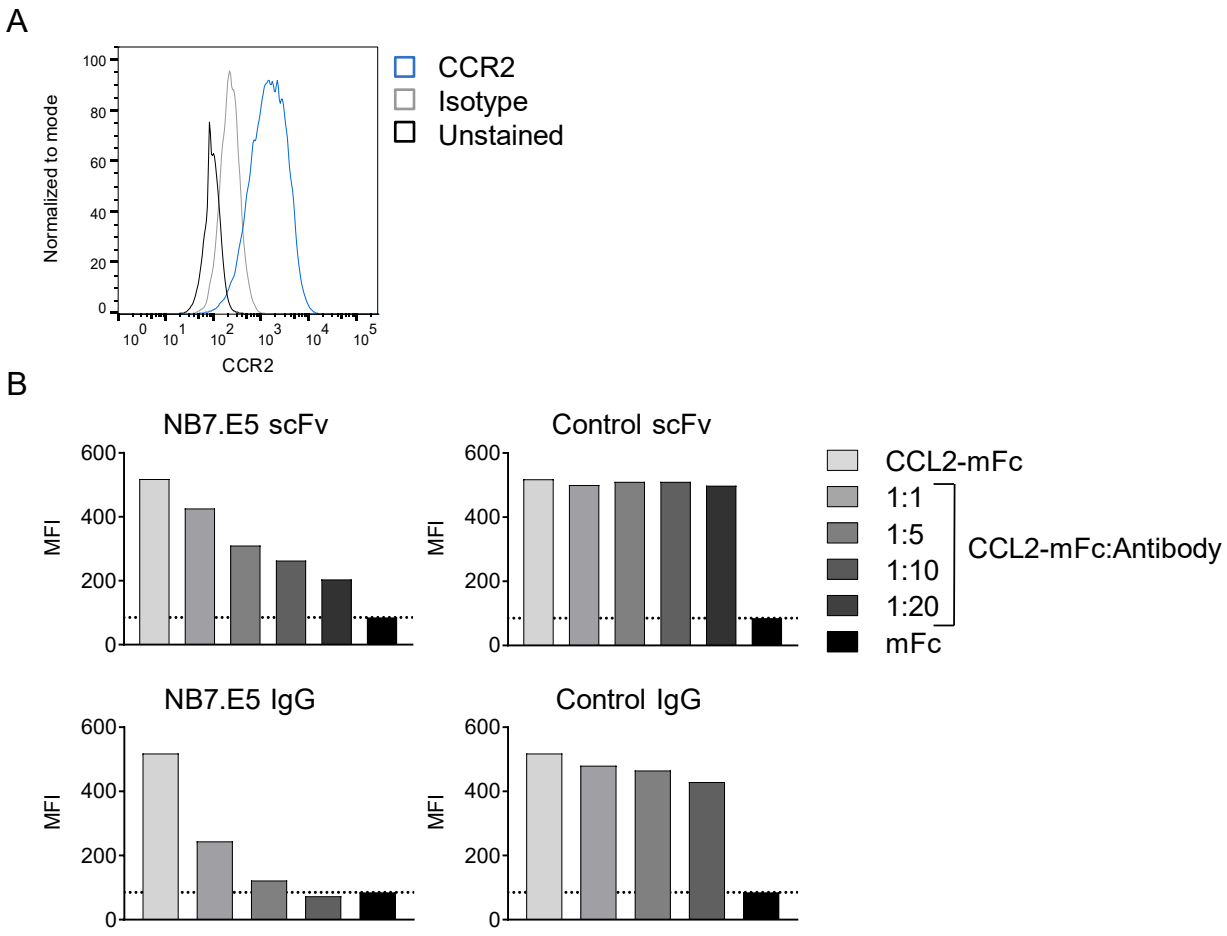

Figure 22. Flow cytometric analyses show the neutralizing effects of anti-CCL2 NB7.E5 on the CCL2 – CCR2 interaction. (A) CCR2 surface expression on THP1 cells was analyzed by flow cytometry. Fc receptors were blocked by preincubation with 10 % human serum and CCR2 was detected using a PE-conjugated anti-CCR2 antibody. A PE-conjugated isotype control antibody was included. (B) CCL2-mFc was pre-incubated at a final concentration of 100 nM with IgG antibodies (100 - 1000 nM) or scFv antibody fragments (100 – 2000 nM) as well as control antibodies. CCL2-mFc without antibodies was used as positive control to determine the maximum binding of CCL2 to its receptor CCR2. mFc at a final concentration of 100 nM was used as control to exclude false positive binding of CCL2-mFc to the Fc receptors on THP1 cells. The mixture was incubated with Fc-blocked (10 % human serum) THP1 cells and FITC-conjugated goat anti-mouse IgG antibody was added to detect CCL2-mFc binding. The dotted lines indicate baseline mFc binding. MFI = median fluorescence intensity.

3.4.3 Impact of the anti-CCL2 antibody NB7.E5 on CCR2 downstream signaling

We investigated the effects on downstream intracellular signaling resulting from the blocking of the CCL2 – CCR2 interaction mediated by the NB7.E5 IgG antibody. CCL2 interacts with the G protein-coupled receptor CCR2, thereby activating several intracellular signaling pathways including the MAPK pathway [69], [70]. This cascade has been found to play an important role in CCL2-driven macrophage chemotaxis [71].

As a readout for MAPK signaling, we studied phosphorylation of extracellular signal-regulated kinase (ERK) in CCL2-treated THP1 cells in the presence and absence of the NB7.E5 IgG (*Figure 23*). Treated cells were lysed and phosphorylated ERK (pERK) and total ERK protein was detected by western blot analysis (*Figure 23A*). THP1 cells without CCL2 treatment were included to assess basal ERK phosphorylation. Glyceraldehyde 3-phosphate dehydrogenase (GAPDH) was included as control and pERK as well was total ERK levels were calculated relative to GAPDH (*Figure 23B*). Importantly, we found a significant reduction of ERK phosphorylation mediated by our CCL2-specific antibody in three independent experiments, while the ratio of total ERK to GAPDH remained constant in all experimental settings.

To summarize, we detected decreased ERK phosphorylation in the presence of the anti-CCL2 NB7.E5 IgG, indicating that NB7.E5 is able to block CCR2 downstream signaling via the MAPK pathway.

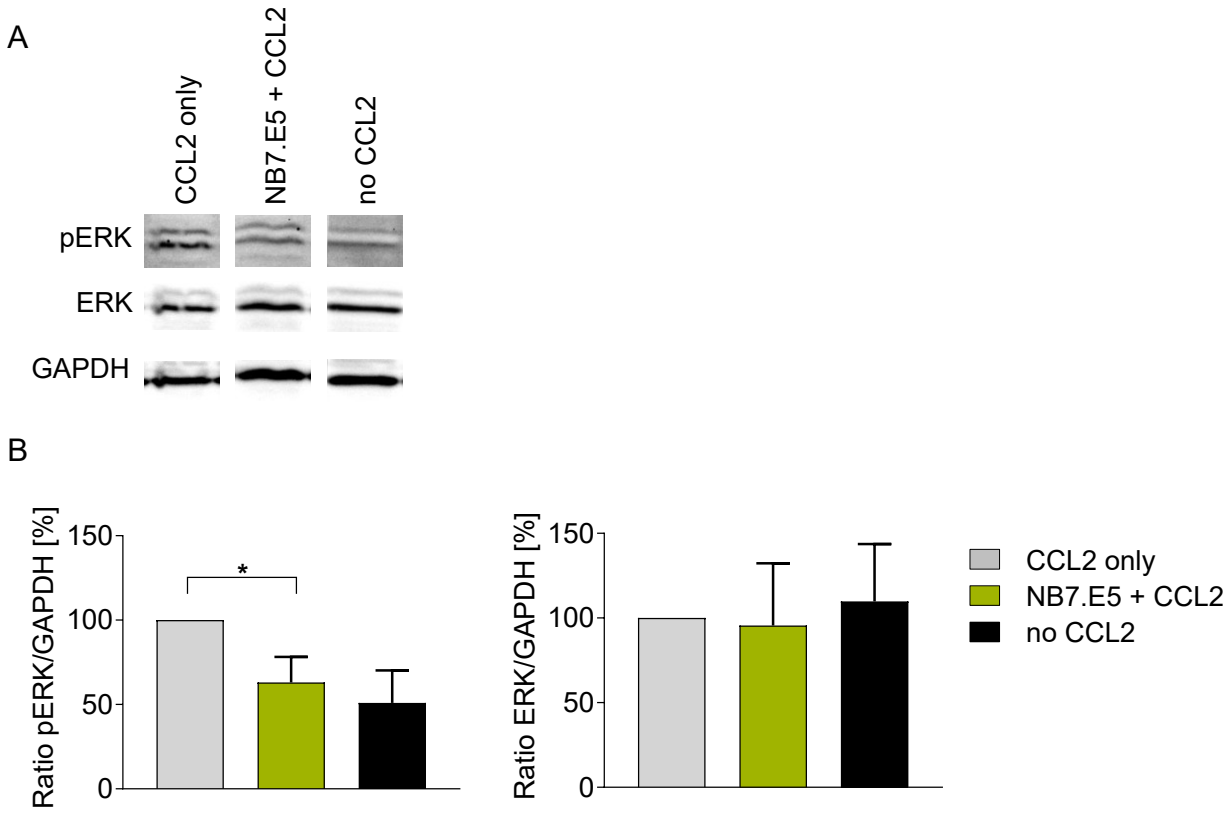

Figure 23. Effects of NB7.E5 IgG on CCL2 - CCR2 downstream signaling. The impact of NB7.E5 IgG on CCR2 downstream MAPK signaling was analyzed by detection of pERK in lysates of THP1 cells. 20 nM CCL2 and 200 nM NB7.E5 IgG were pre-incubated and added to the cells for 3 – 5 min. Cell lysates were prepared and equal amounts of lysate per lane were separated by SDS gel electrophoresis. After western blotting, pERK was detected using a primary mouse anti-pERK and a secondary HRP-conjugated anti mouse antibody. ERK was detected by incubation with primary mouse anti-ERK and secondary HRP-conjugated anti mouse antibody. GAPDH was detected using HRP-conjugated anti-GAPDH antibody. (A) A representative western blot is shown. (B) Densitometric analysis was performed from three independent experiments and statistical significance of pERK/GAPDH ratio was calculated using two-tailed unpaired t test. Error bars represent the standard deviation of the mean values of triplicates. Ratio of ERK/GAPDH was calculated to show equal protein loading in each lane.

3.4.4 The anti-CCL2 IgG NB7.E5 counteracts CCL2-induced monocyte migration

To test the influence of our CCL2-specific NB7.E5 IgG on CCL2-driven monocyte chemotaxis, we performed a transwell assay. In this assay, we analyzed the migration of CCR2-expressing monocyte-like THP1 cells through the pores of the transwell insert towards the receiver well, which contained CCL2 in the presence of NB7.E5 or control IgG in 1:1 or 1:10 molar ratios (*Figure 24A*).

After allowing the cells to migrate for 3 hours along the CCL2 gradient, we observed a significantly reduced number of THP1 cells in the receiver wells in the presence of our anti-CCL2 antibody NB7.E5, but not the control IgG (*Figure 24B*). These results suggest that the NB7.E5 IgG blocks the migration of CCR2-expressing monocytes along the CCL2 chemokine gradient.

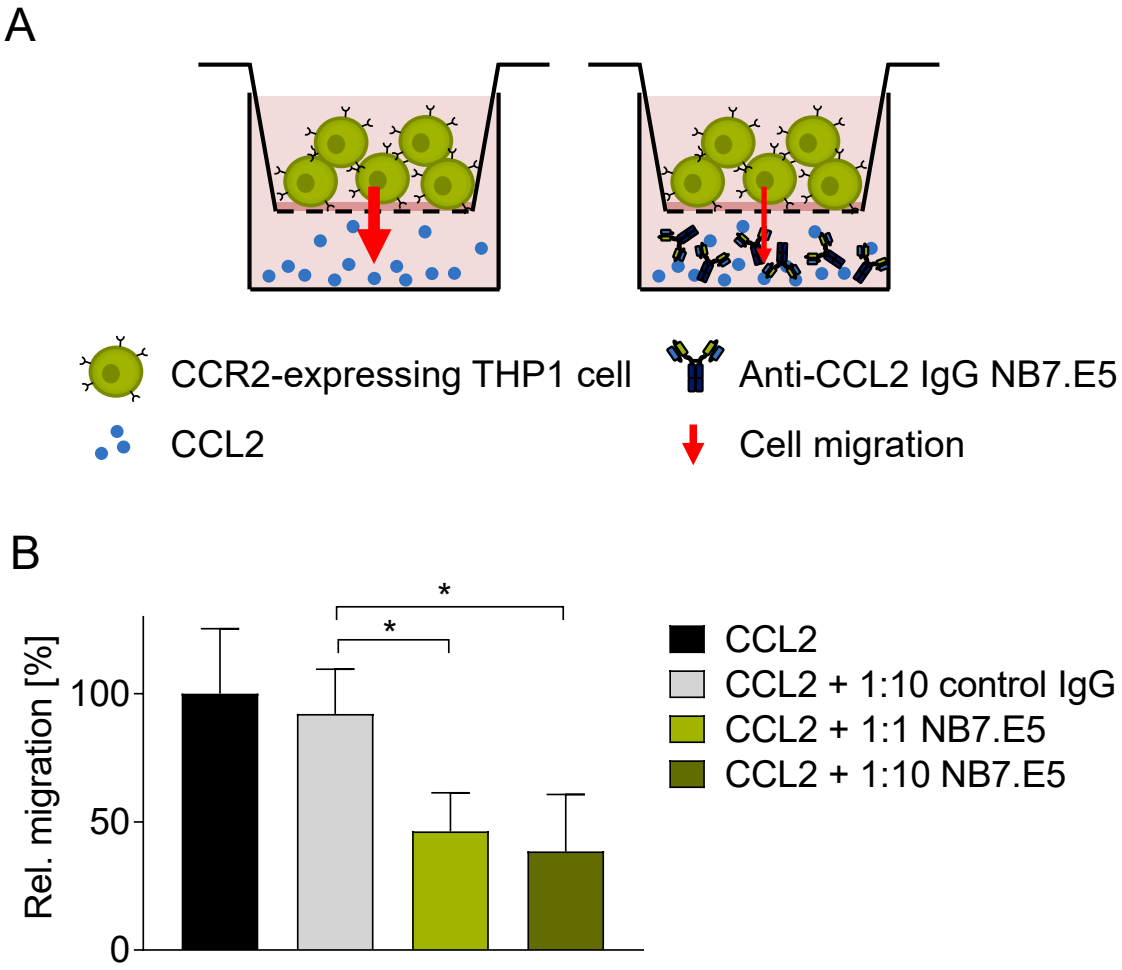

Figure 24. Transwell migration assay to investigate the inhibitory capacity of NB7.E5 IgG on CCL2-mediated monocyte chemoattraction. (A) Schematic representation of the experimental set up of the migration assay. CCR2-expressing THP1 cells were labeled with Calcein-AM for detection and transwell inserts with a defined pore size were coated with human fibronectin to allow attachment of the cells. In the receiver wells, 50 nM CCL2 were pre-incubated in a 1:1 or 1:10 molar ratio with NB7.E5 IgG, a control IgG or without IgG. THP1 cells were added to the transwells and migration was allowed for 3 h. (B) Migrated cells were detected using a fluorescence plate reader. Migration in a control condition without CCL2 was subtracted from all values as background. Relative (rel.) fluorescence was calculated to the control containing only CCL2 without antibody. Error bars represent the standard deviation of mean values of triplicates. Performed by M.Sc. D. Thomas.

3.5 Characterization of anti-CD22 CAR T cells secreting the anti-CCL2 scFv NB7.E5

In a phase I/II clinical study it was found that the systemic administration of the anti-CCL2 antibody carlumab (CNTO 888) led to only minor reductions of serum CCL2 concentrations, even followed by increased CCL2 levels post treatment [45], [47]. We intend to circumvent systemic effects of CCL2-directed therapy such as activation of chemokine compensatory mechanisms including the overexpression of CCL2 by developing a novel vehicle for the targeted delivery of anti-CCL2 scFvs to the tumor site. We set out to generate CD22-directed CAR T cells engineered to secrete soluble anti-CCL2 scFvs since high intratumoral CCL2 concentrations correlate with poor clinical outcomes in CD22 -positive DLBCL patients [151].

We generated a lentiviral CAR construct containing the humanized binding domains derived from the RFB4 hybridoma that recognize human CD22 [158]. The CD22-CAR has the following organization: an extracellular CD22-specific scFv, a CD8α hinge and transmembrane region, and two intracellular domains, 4-1BB (CD137) and CD3zeta. The CD3-zeta chain (ζ) is required for T cell activation and 4-1BB delivers costimulatory signals important for efficient T cell expansion.

Furthermore, we generated so-called “armored” constructs that included the CCL2-specific NB7.E5 scFv for soluble expression in addition to the anti-CD22 CAR. Specifically, the NB7.E5 scFv was introduced either 5’ (αCCL2scFv-αCD22CAR) or 3’ (αCD22CAR-αCCL2scFv) to the anti-CD22 CAR sequence. A schematic representation of the resulting constructs as well as the conventional CAR without secretable CCL2-specific scFv (termed here αCD22CAR) are depicted in *Figure 25*. The “self-cleaving” peptide T2A was cloned between the scFv and CAR sequence to allow encoding of two separate proteins on the same open reading frame.

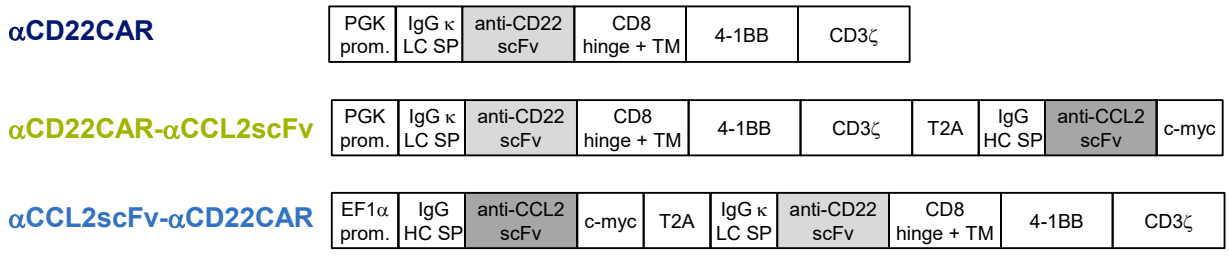

Figure 25. Schematic representation of CAR constructs. The conventional αCD22CAR construct encoded the CD22-targeted CAR without secretable anti-CCL2 scFv and served as control during further

analyses. The CAR consists of the extracellular anti-CD22 scFv targeting domain, a CD8α hinge and transmembrane (TM) domain as well as the intracellular costimulatory domain 4-1BB (CD137) and the activation domain of the CD3-zeta chain (CD3ζ). CAR expression is driven by a phosphoglycerate kinase promoter (PGK prom.) and the protein is destined towards the secretory pathway by the IgG kappa light chain signal peptide (IgG κ LC SP). To generate αCD22CAR-αCCL2scFv, the anti-CCL2 scFv was encoded downstream of the CAR and separated using a T2A "self-cleaving" peptide. The anti-CCL2 scFv is destined for secretion by the IgG heavy chain signal peptide (IgG HC SP) and carries a c-myc tag at its C-terminus. For the αCCL2scFv-αCD22CAR construct, the anti-CCL2 scFv was encoded upstream of the T2A peptide and the CAR downstream. In addition, this construct is regulated by an EF1-alpha promoter (EF1α prom.).

3.5.1 Analysis of anti-CD22 CAR expression and secretion of anti-CCL2 scFvs by HEK293T cells

In order to analyze the functionality of our constructs, CAR expression and scFv secretion was first investigated in HEK293T cells. Therefore, cells were transfected with the lentiviral plasmids encoding the different CAR constructs (*Figure 25*) and transfection efficiency was determined by flow cytometric analysis of CAR surface expression. HEK293T cells transfected with plasmids encoding αCD22CAR-αCCL2scFv, αCCL2scFv-αCD22CAR or the control αCD22CAR showed high transfection efficiencies of 47 % to 80 % (*Figure 26A, B*).

To analyze soluble expression of the CCL2-specific scFv, we harvested supernatant of equivalent numbers of transfected HEK293T cells and concentrated the supernatant. The wells of an ELISA plate were coated with CCL2, concentrated supernatant was added and bound scFvs were detected via their myc-tag (*Figure 26C, D*). We observed significant scFv production in cells transfected with plasmids encoding for αCD22CAR-αCCL2scFv and αCCL2scFv-αCD22CAR compared to cells transfected with plasmids encoding for αCD22CAR or mock transfected cells. As estimated by comparison to defined concentrations of recombinant NB7.E5 scFv, which was used as positive control, the anti-CCL2 scFv concentration in the supernatant was approximately 13 ng/mL, which corresponds to 1.3 ng/mL in the non-concentrated cellular supernatant. The data indicate that HEK293T cells expressing the αCCL2scFv-αCD22CAR construct may secreted a lower amount of the anti-CCL2 scFv compared to cells expressing the αCD22CAR-αCCL2scFv construct. However, since these results were obtained from single separate experiments, one cannot rule out whether factors other than the design of the construct play a role for the differential scFv production, as for instance different transfection efficiencies as shown in *Figure 26A, B*. For

a direct comparison, however, the different constructs should be tested in parallel in repeated experiments under constant conditions.

In summary, we detected CAR cell-surface expression and significant anti-CCL2 scFv secretion from HEK293T cells transfected with αCCL2scFv-αCD22CAR or αCD22CAR-αCCL2scFv constructs indicating the expected functionality of our constructs.

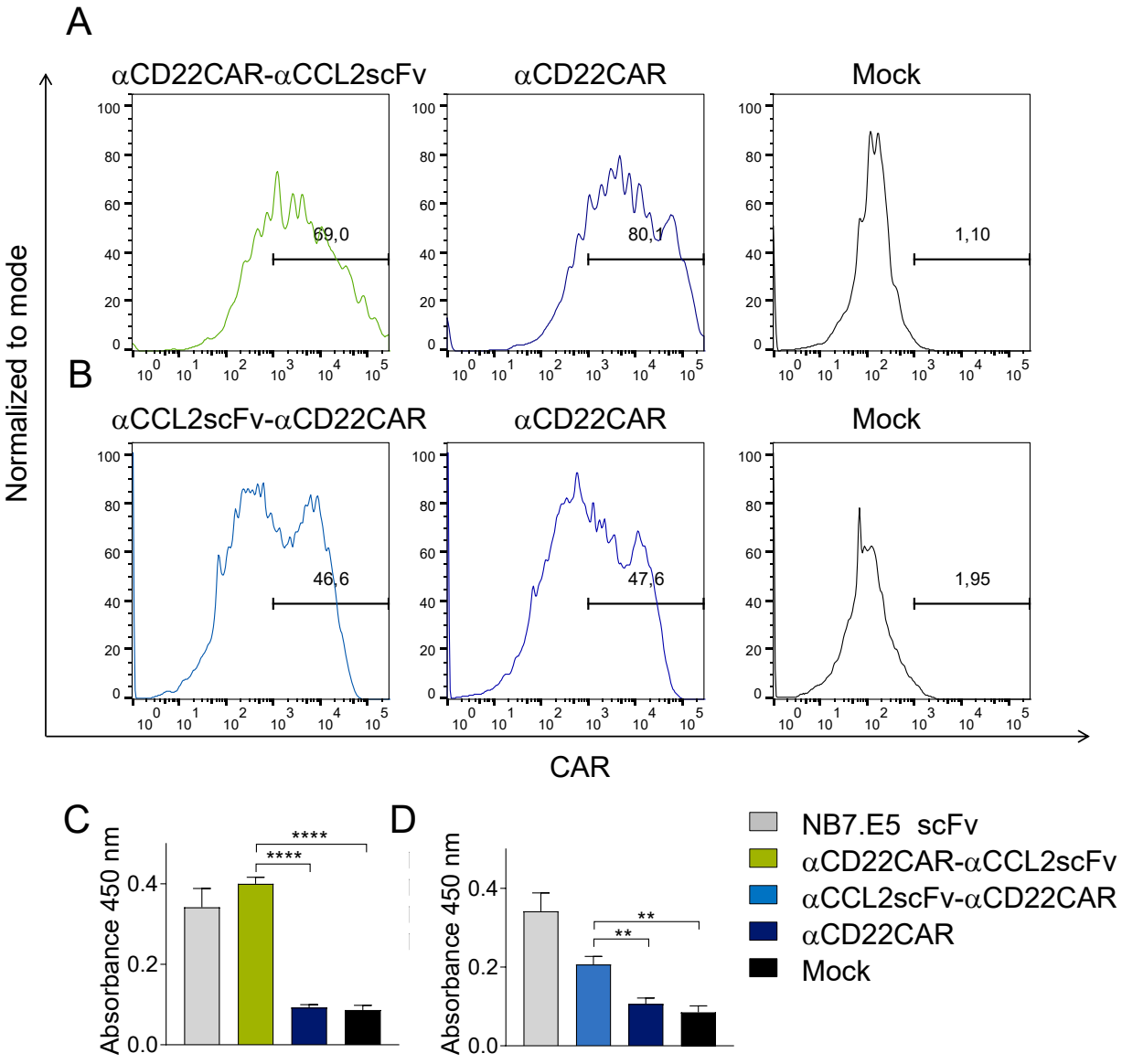

Figure 26. Analysis of CAR expression and scFv secretion by transfected HEK293T cells. CAR expression on the surface of HEK293T cells transfected with (A) αCD22CAR-αCCL2scFv and (B) αCCL2scFv-αCD22CAR was analyzed in two independent experiments by flow cytometry. αCD22CAR and mock transfected cells served as control. Cell surface CAR was stained by incubation with biotinylated Protein L and APC-conjugated streptavidin. Numbers indicate percentage of CAR positive cells. Soluble

scFv expression from HEK293T cells transfected with (C) αCD22CAR-αCCL2scFv and (D) αCCL2scFv-αCD22CAR into the supernatant was analyzed by ELISA. ELISA plates were coated with CCL2, concentrated supernatants were added and bound scFvs were detected by mouse anti-c-myc HRP-conjugated antibody. 13 ng/mL purified NB7.E5 scFv served as positive control. Error bars represent the standard deviation of mean values of triplicates. ** P ≤ 0.01;**** P ≤ 0.0001

3.5.2 Soluble expression of scFvs by CAR T cells

Since we confirmed the functionality of our anti-CD22 CAR constructs as indicated by CAR surface expression and scFv secretion using transfected HEK293T cells, we continued to generate CAR T cells expressing the same constructs. Human PBMCs were activated and T cells were transduced with lentiviral vectors encoding for αCD22CAR-αCCL2scFv, αCCL2scFv-αCD22CAR and αCD22CAR or mock transduced. CAR expression was confirmed by flow cytometry and transduction efficiencies ranged between 40 to 80 % (data not shown). At day 10 after activation, CAR T cells were adjusted to an equal number of CAR positive cells and were seeded at 1 x 10^6 cells/mL in 80 mL serum free medium. Supernatants were harvested two days later, concentrated and the amount of secreted scFv was analyzed by ELISA. Surprisingly, no scFv secretion could be detected in any of the supernatants (data not shown).

We speculated that the levels of secreted scFvs might be below the detection threshold of our ELISA-based assay. Cells transduced with the αCD22CAR-αCCL2scFv and αCCL2scFv-αCD22CAR constructs should express both CAR and anti-CCL2 scFv in a linear fashion, therefore we intended to increase the concentration of scFv in the supernatant by enriching CAR expressing cells. In the previously described experiment supernatant was harvested from cells which were approximately 40 % CAR positive, therefore we set out to enrich the amount of CAR positive cells by stimulation with target cells. At day 7 and 10 after activation transduced T cells were stimulated by coincubation with CD22 positive Nalm6 cells at an effector to target ratio of 1:3 (*Appendix, Figure 41*). CAR expression was monitored by flow cytometry and we observed an increase to 93 % CAR positive cells for T cells expressing αCD22CAR-αCCL2scFv and αCD22CAR and to 89 % CAR positive cells for T cells expressing αCCL2scFv-αCD22CAR (*Figure 27A*). At day 17 after activation, CAR T cells were seeded at 1 x 10^6 cells/mL in 80 mL serum free medium and grown for two days. Supernatants were harvested, concentrated and scFv secretion was analyzed by ELISA. However, we did not detect any secreted scFv molecules by the transduced T cells, although the fraction of CAR-positive cells increased to almost 100 % (*Figure 27B*).

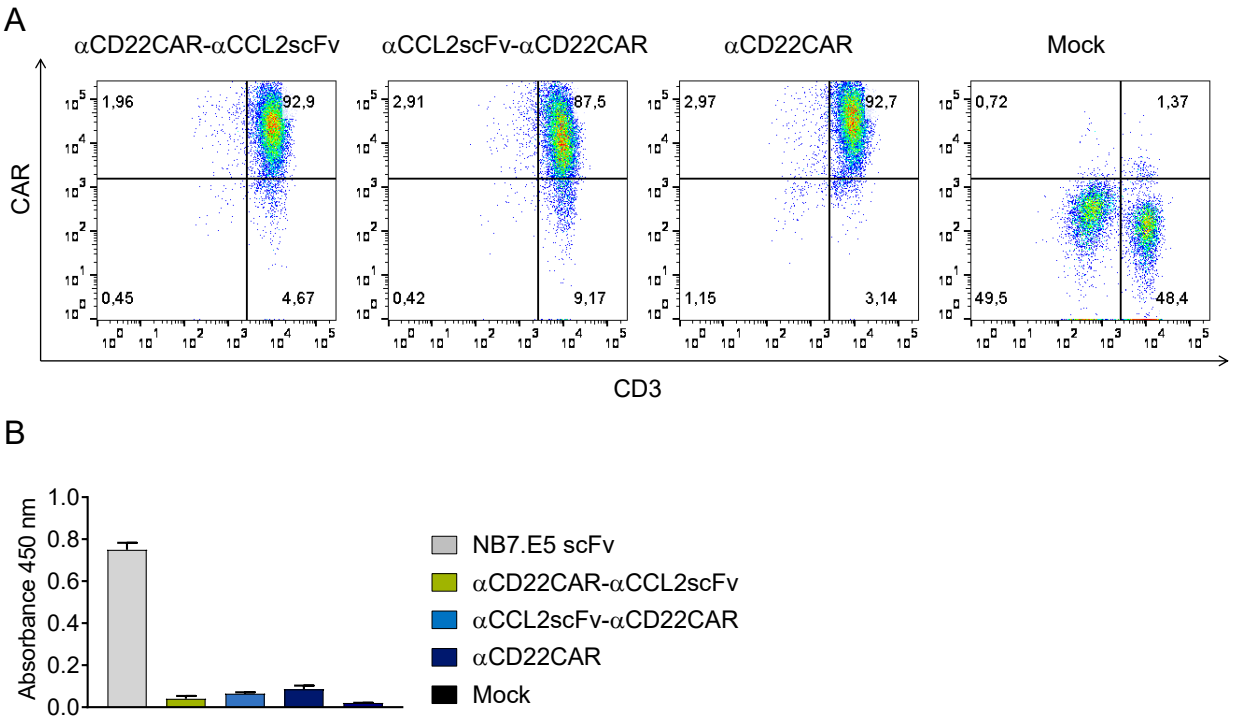

Figure 27. Surface CAR and soluble scFv expression by CAR T cells stimulated via coincubation with target positive cells. (A) Stimulation with CD22-expressing Nalm6 cells enriched CAR positive cells over time. Flow cytometric analysis of CAR expression at day 14 post T cell activation is shown. T cells were identified by staining with FITC-conjugated CD3 antibody. CAR molecules were stained by incubation with biotinylated Protein L and APC-conjugated streptavidin. (B) After CAR T cell stimulation by coincubation with Nalm6 cells, scFv secretion of αCD22CAR-αCCL2scFv and αCCL2scFv-αCD22CAR into the supernatant was analyzed by ELISA. Plates were coated with CCL2, concentrated supernatants were added and bound scFvs were detected by mouse anti-c-myc HRP antibody. NB7.E5 scFv served as positive control. Error bars represent the standard deviation of mean values of triplicates.

We considered several factors that might be involved in the lack of scFv detection in supernatants of CAR T cells: 1. Insufficient “self-cleavage” mediated by the T2A peptide might lead to inefficient separation of scFvs from the CAR, or the anti-CCL2 scFv binds unspecifically to the surface of the T cells; 2. scFvs are not trafficked through the Golgi via the secretory pathway; 3. The scFv coding sequence is not present on the messenger RNA (mRNA); 4. T cells produce endogenous CCL2 which sequesters the scFv and prevents its detection. The investigation of the different possible causes is described in the following section.

The scFv and CAR are encoded on the same plasmid and are separated by a T2A “self-cleaving” peptide. When the 2A peptide is translated, “self-cleavage” occurs at the C-terminal proline by

steric hindrance which induces ribosome skipping [177]. Although T2A has been described to have one of the highest cleavage efficiencies, it is conceivable that the ribosome might read through and the scFv might thus not be efficiently separated from the CAR [178]. In this case, the scFv should be detectable by flow cytometry on CAR T cells transduced with the αCCL2scFv-αCD22CAR construct carrying the anti-CCL2 scFv at the N-terminal extracellular portion of the CAR (*Figure 28A*). Alternatively, the anti-CCL2 scFv may bind to a yet unidentified and unspecific target present on the surface of T cells. Importantly, we detected no anti-CCL2 scFv on the surface of the CAR T cells, indicating correct separation of the anti-CCL2 scFv from the CD22-directed CAR and no unspecific binding of the scFv to the T cell surface (*Figure 28B*).

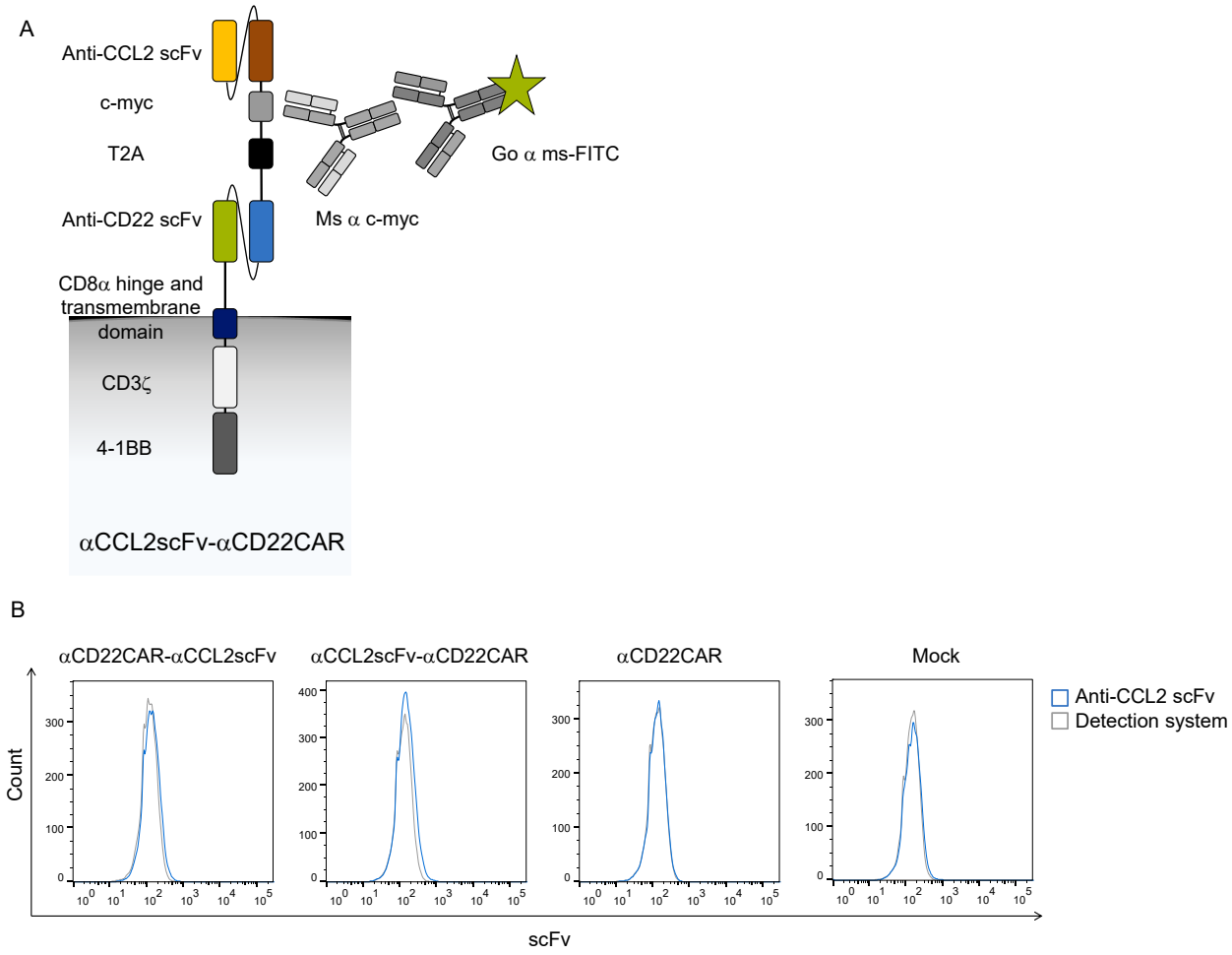

Figure 28. Flow cytometric analysis of the cleavage of anti-CCL2 scFv and anti-CD22 CAR. (A) Schematic representation of the hypothetical scFv expression on the surface of CAR T cells transduced with the αCCL2scFv-αCD22CAR construct following failure of protein separation at the T2A peptide. Anti-CCL2 scFvs were detected by mouse anti c-myc antibody (ms α c-myc) and FITC-conjugated goat anti-mouse antibody (go α ms-FITC). (B) CAR T cells with enriched CAR expression after target cell stimulation

(*Figure 27A*) were used. Anti-CCL2 scFvs were detected using specific antibodies as described above and cells were analyzed using a flow cytometer.

To test whether the scFv is expressed in intracellular compartments, we performed intracellular stainings of transduced T cells and transfected HEK293T cells and analyzed scFv expression by flow cytometry. As expected, we confirmed CAR expression on the HEK293T cell surface and observed staining of intracellularly localized scFvs (*Figure 29A, B*). Surprisingly, however, we could not detect any intracellular anti-CCL2 scFv protein in CAR T cells expressing the corresponding constructs, although transduction was efficient as indicated by cell surface expression of the CAR (*Figure 29C, D*).

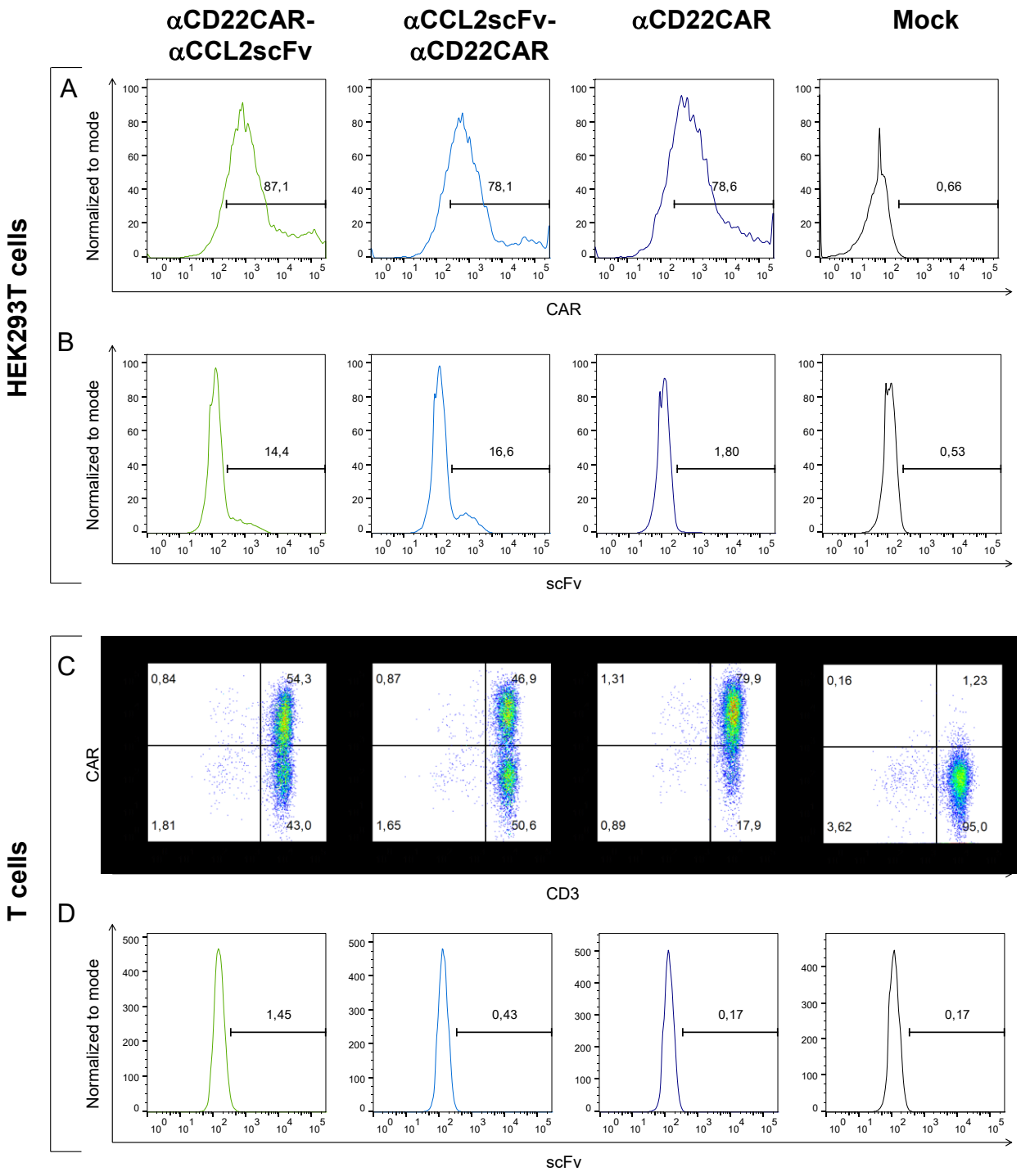

Figure 29. Intracellular localization of anti-CCL2 scFvs analyzed by flow cytometry. HEK293T cells were transfected and T cells were transduced with the lentiviral plasmids encoding the respective CAR constructs. CAR surface expression was analyzed for HEK293T cells (A) and for T cells (C) at day 11 after activation using flow cytometry. T cells were identified by staining with FITC-conjugated CD3 antibody. CAR molecules were stained by incubation with biotinylated Protein L and APC-conjugated streptavidin. The presence of intracellularly localized anti-CCL2 scFvs in HEK293T cells (B) and T cells (D) was analyzed by

flow cytometry. For intracellular staining, cells were fixed and permeabilized. Anti-CCL2 scFvs were detected by anti c-myc antibody and FITC-conjugated goat ant mouse antibody. Numbers indicate % of CAR or scFv positive cells.

Since we were unable to detect the anti-CCL2 scFvs at the protein level in CAR T cells, we investigated the presence of the scFv coding sequence on the mRNA level. To this end, mRNA was isolated from transduced CAR T cells and transfected HEK293T cells. After synthesis of complementary DNA (cDNA) and sequence specific PCR using primers which bind upstream (signal peptide) and downstream (myc-tag) of the anti-CCL2 scFv sequence, the amplified DNA samples were visualized on an agarose gel (*Figure 30*). We detected a clear band corresponding to the scFv coding sequence in cDNA samples derived from T cells and HEK293T cells expressing the αCD22CAR-αCCL2scFv and αCCL2scFv-αCD22CAR constructs, but not from untransduced or untransfected cells or cells solely expressing the CD22 CAR.

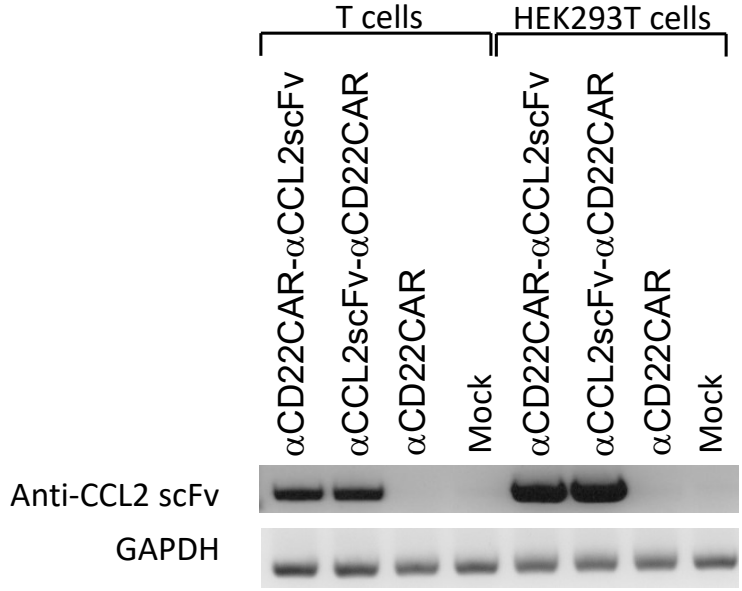

Figure 30. Detection of anti-CCL2 scFv mRNA in T cells and HEK293T cells carrying the CAR constructs. ScFv expression was analyzed on the mRNA level in HEK293T and T cells expressing the indicated CAR constructs. CAR expression was detected by flow cytometry see *Figure 29A, C*. mRNA was isolated from equal cell numbers, cDNA synthesized and sequence specific PCR was performed to amplify anti-CCL2 scFv and GAPDH DNA. For amplification of the anti-CCL2 scFv sequence primers which bind upstream (signal peptide) and downstream (myc-tag) of the anti-CCL2 scFv were used. For amplification of GAPDH encoding DNA primers binding in exons of the GAPDH sequence were used. Samples were separated by agarose gel electrophoresis and visualized on a UV table.

Although there is no compelling evidence on the production of CCL2 by human T cells, reports in the literature described the secretion of CCL2 by murine T lymphocytes of mammary tumor-bearing mice [179], [180]. It is conceivable that CCL2 secreted from T cells might trap the produced anti-CCL2 scFvs and prevent their successful detection in our ELISA-based assay. To address this question, we transduced T cells with the different CAR constructs. Moreover, human peripheral blood mononuclear cells (PBMCs) have been found to secrete high levels of CCL2 upon activation with the polyclonal T cell activating substance Phytohaemagglutinin P (PHA-P) [181]–[183]. Therefore, non-activated and PHA-P activated PBMCs were included as positive control, whereas HEK293T cells transfected with the different CAR constructs were used as negative control. mRNA was isolated from these cells and cDNA was synthesized. Using CCL2 and GAPDH sequence specific primers the DNA was amplified by PCR and analyzed on an agarose gel (*Figure 31A*). As expected, we detected efficient induction of CCL2 mRNA expression in PHA-activated PBMCs, but also mRNA expression in non-activated PBMCs albeit to a lower extend. Interestingly, we detected faintly visible DNA bands corresponding to CCL2 mRNA in CAR T cells that might indicate low CCL2 production in CAR T cells. To verify this, we harvested supernatants of the cells and analyzed secretion of CCL2 using a commercially available CCL2 ELISA kit with an optimized detection threshold of 7.8 pg/mL (*Figure 31B*). We found CCL2 only in the supernatants of PBMCs with a remarkable increase in PHA-activated PBMCs compared to non-activated PBMCs, which is in accordance with previously published results [181], [182]. In contrast, CAR T cells and mock T cells were not found to secrete CCL2, which argues against the possibility that the produced anti-CCL2 scFv may be trapped by simultaneous expression of CCL2.

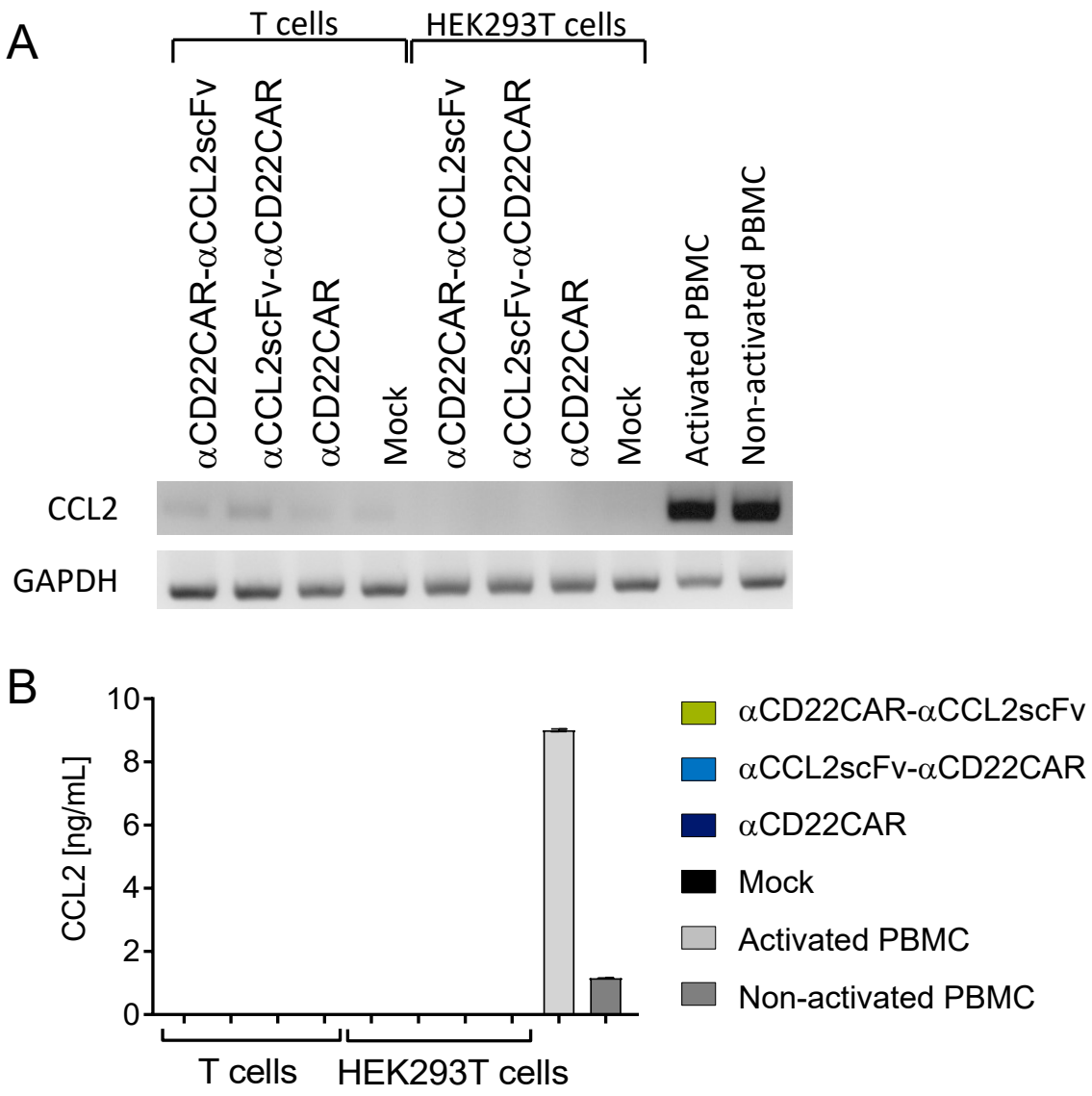

Figure 31. Analysis of CCL2 mRNA and protein levels in CAR expressing T cells, HEK293T cells and PBMCs. Presence of CCL2 mRNA and protein was analyzed in CAR T cells at day 11 after activation. HEK293T cells transfected with the CAR constructs were included as negative and PBMCs as positive control. PBMCs were activated for 24 hours using 5 µg/mL PHA-P. CAR expression of T cells and HEK293T cells was analyzed by flow cytometry before (*Figure 29A, C*). (A) mRNA of equal cell numbers was isolated, cDNA synthesized and PCR was performed using sequence specific primers. Samples were separated by agarose gel electrophoresis and DNA was visualized using a UV table. (B) Supernatants were harvested after 48 h incubation of transduced T cells or transfected HEK293T cells in serum free medium or 24 h after activation of PBMCs using PHA in serum free medium. Secretion of CCL2 was determined using a CCL2 ELISA kit (BioLegend). Based on a standard curve CCL2 levels could be calculated. Error bars represent the standard deviation of mean values of duplicates.

In summary, we excluded various possible causes for not detecting scFvs in the supernatant of CAR T cells. These included the separation of scFv from the CAR, scFv trafficking to the cell surface, presence of scFv mRNA and CCL2 secretion by T cells. We therefore hypothesize that the identification threshold of the used ELISA-based assay did not allow detection of scFvs.

3.5.3 Analysis of CAR T cell functionality

To test whether the T cells transduced with the constructs that allow simultaneous expression of cell-surface CAR and soluble anti-CCL2 scFv were functionally equivalent to T cells solely expressing the anti-CD22 CAR, we performed functional tests including antigen-dependent cell proliferation, cytokine release and target cell killing assays.

We generated T cells expressing the different CAR constructs and cultivated them either alone or stimulated them by co-incubation with CD22-expressing Nalm6 cells (*Appendix, Figure 41*). We added the Nalm6 cells at day 7 and 10 after T cell activation at an effector to target ratio of 1:3. We monitored CAR expression for up to 18 days. CAR expression of unstimulated CAR T cells remained stable over time (*Figure 32A*). Importantly, upon stimulation with target cells, we observed a remarkable increase in the number of CAR positive T cells to up to 93 % (*Figure 32B*). Interestingly, although the initial transduction efficiencies of anti-CCL2 scFv-encoding constructs was lower (approximately 50 %) as compared to the αCD22CAR construct (80%), the number of CAR expressing cells increased to a comparable level upon stimulation with target cells. The increase in number of CAR expressing cells upon target cell stimulation most probably results from increased proliferation of CAR positive cells in stimulated compared to unstimulated CAR T cells.

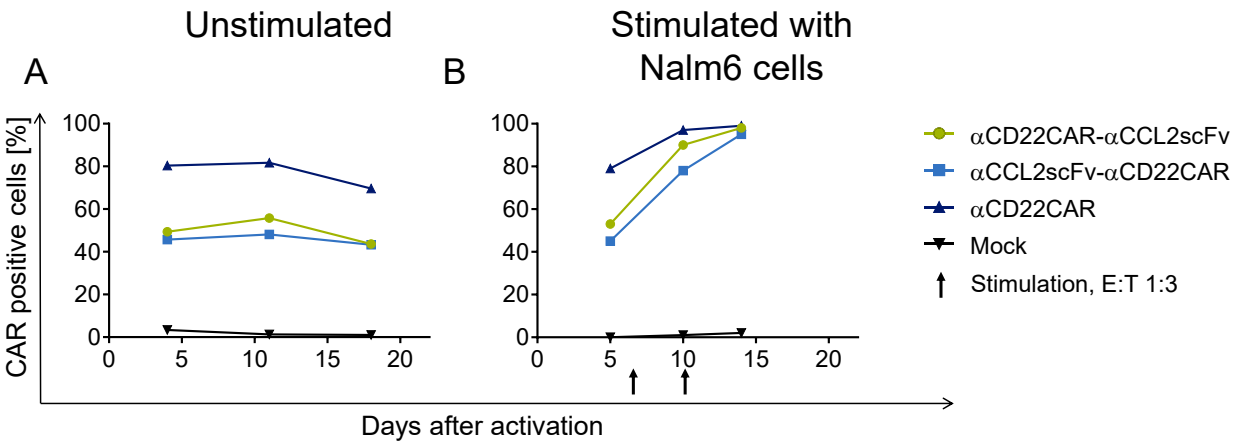

Figure 32. CAR expression during normal CAR T cell cultivation and stimulation by antigen positive cells. CAR T cells were generated and either cultivated without antigen stimulation or were stimulated at day 7 and 10 (indicated by arrows) by co-incubation with CD22-expressing Nalm6 cells in an effector to target ratio of 1:3. Percentage of CAR expressing cells was determined by flow cytometry at different time points after T cell activation during (A) normal CAR T cell cultivation without antigen stimulation and (B) stimulation with target cells.

The release of inflammatory cytokines, including interleukin-2 (IL-2), interferon gamma (IFNγ) and tumor necrosis factor (TNF) upon antigen stimulation plays an important role for the effector functions of CAR T cells. We investigated cytokine release by unstimulated CAR T cells and CAR T cells co-incubated with either CD22-negative K562 cells or CD22-positive Raji cells (*Appendix, Figure 41*). We observed strong release of IL-2, IFNγ and TNF from αCCL2scFv-αCD22CAR and αCD22CAR expressing T cells and low release from αCD22CAR-αCCL2scFv expressing T cells upon co-incubation with CD22-expressing Raji cells. No cytokine release was detected from mock transduced T cells or from unstimulated or K562-stimulated CAR T cells (*Figure 33*). The detected cytokine levels correspond to those described by other groups and indicate successful target antigen-dependent activation of the CAR T cells [184], [185].

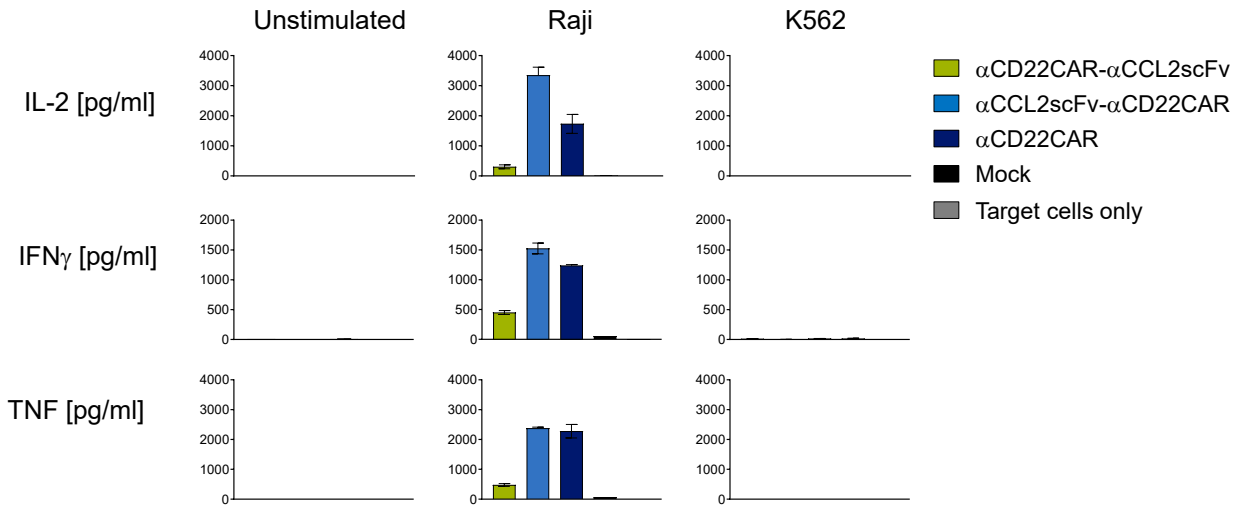

Figure 33. Cytokine release by stimulated and unstimulated CAR T cells. The number of CAR positive cells was adjusted among T cells expressing different CAR constructs by dilution with mock transduced cells. CAR-expressing T cells and target cells were co-incubated at a 1:1 ratio for 24 hours. IL-2, IFNγ and TNF release into the supernatant was investigated using a commercially available bead-based sandwich immunoassay (BioLegend). Cytokine concentrations were calculated relative to an included standard. Mean and standard deviation of triplicates are depicted.

To investigate cytotoxic effects induced by CAR T cells, CAR T cells were co-incubated with target antigen positive Raji cells engineered to express gaussia luciferase (Raji-GLuc) at 1:1 or 3:1 ratios (*Figure 34A*). The killing of target cells was assessed using a luminescence-based assay, where the release of GLuc into the cell supernatant as a result of CAR T cell-induced cell-death served as detection readout. We observed cytotoxic effects for all CAR-expressing cells, whereby αCD22CAR-αCCL2scFv and αCCL2scFv-αCD22CAR expressing T cells showed lower cytotoxicity than the conventional αCD22CAR T cells. In addition, mock transduced T cells also showed minor killing of the target cells.

To investigate the higher killing capacity of αCD22CAR expressing T cells compared to the scFv-carrying CAR T cells, we calculated the CAR surface expression relative to the αCD22CAR expressing T cells based on flow cytometric data from three independent measurements (*Figure 34B*). Interestingly, we found lower levels of CAR expression on the surface of scFv-carrying CAR T cells compared to αCD22CAR expressing T cells. This might be due to the larger size of the constructs leading to expression of fewer CAR molecules per cells. Most probably the higher levels

of CAR on the surface of αCD22CAR T cells might account for the observed increase in cytotoxic effects.

To summarize, we observed that T cells transduced with the constructs that allow simultaneous expression of anti-CD22 CAR and soluble anti-CCL2 scFv were functionally equivalent to T cells expressing the conventional anti-CD22 CAR.

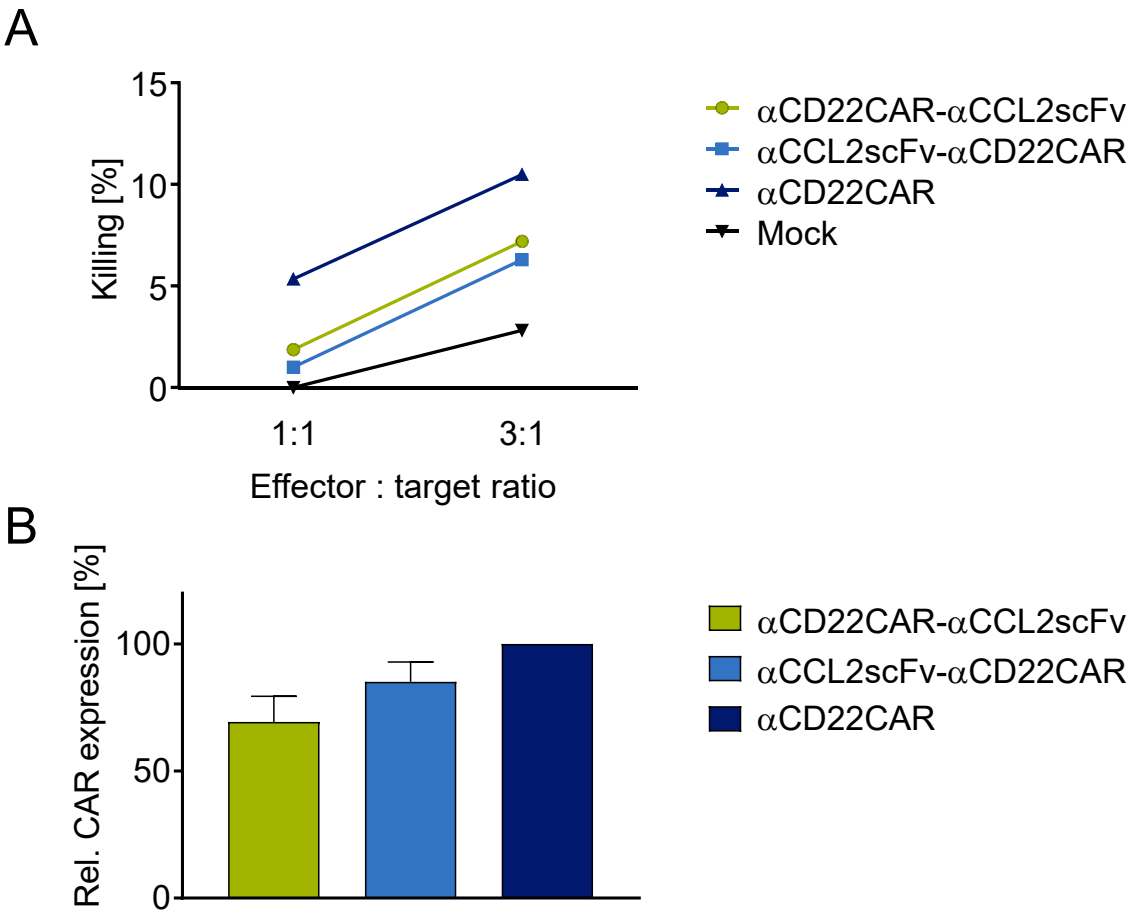

Figure 34. CAR T cell killing and relative CAR expression. (A) Cytotoxicity of CAR T cells was tested using a luminescence-based assay. CAR T cells were generated and percentage of CAR positive cells was determined by flow cytometry (*Figure 29C*). CAR T cells were adjusted to have same levels of CAR positive cells and were incubated at 1:1 or 3:1 ratio with CD22-positive Raji-GLuc cells. The luciferase of eliminated cells is released into the supernatant and can be detected by addition of its substrate coelenterazine. The bioluminescent signal corresponds to the amount of target cell killing. Background signals from target cells only were subtracted and killing was calculated in percent relative to the positive control αCD22CAR. The mean of triplicates is presented. (B) CAR surface expression was calculated relative (rel.) to the αCD22CAR T cells after analysis by flow cytometry at three independent days. Error bars represent the standard deviation of mean values of three independent measurements.

4 Discussion

Over the past years, the field of cancer immunotherapy has advanced rapidly leading to an increased approval of immunotherapeutic drugs. Especially immunomodulatory antibodies have recorded great success. One approach is the modulation of macrophages which constitute the majority of cells of the immune system found in solid tumors. Importantly, tumor-associated macrophages (TAMs) are polarized towards the M2 phenotype which supports tumor growth and metastasis by the secretion of cytokines, chemokines and growth factors. Along this line, several immunotherapy strategies are being developed to target TAMs, including therapeutic antibodies which facilitate macrophage anti-tumor effector functions, repolarization to an anti-tumorigenic M1 phenotype, suppression of TAM survival or blockade of monocyte recruitment to the tumor [186].

We developed NRP1- and CCL2-targeting antibodies for inhibition of monocyte recruitment to tumors in order to reduce the tumor-promoting effects of M2-polarized macrophages. Antigen-specific scFv molecules were selected from the immune antibody library LYNDAL as well as from the naïve antibody library HAL9/10. We demonstrated specific binding of the generated IgG1 antibodies to NRP1 and CCL2 with high to moderate binding affinities towards the cognate target antigen.

For NRP1-specific antibodies we confirmed inhibition of the NRP1 – Sema3A interaction by ELISA, however, we could not demonstrate blocking effects upon binding to NRP1 positive cells. Therefore, the development of NRP1-specific antibodies was not further pursued.

Furthermore, we demonstrated blocking of the CCL2 – CCR2 interaction mediated by the CCL2 – specific NB7.E5 IgG. Additionally, we showed a reduction of intracellular MAPK signaling conferred by the anti-CCL2 IgG. Most importantly, we confirmed our hypothesis of inhibition of monocyte migration mediated by the anti-CCL2 antibody. We further proceeded with the generation of CD22-directed CAR T cells secreting soluble anti-CCL2 scFv molecules. Although we could not confirm secretion of scFvs by the CAR T cells, we successfully demonstrated production of soluble scFvs by HEK293T cells indicating the functionality of our constructs. Additionally, we found that CAR T cells carrying the anti-CCL2 scFv DNA sequence were functionally active, including increased proliferation and inflammatory cytokine release upon stimulation with antigen-positive tumor cells as well as target cell killing.

4.1 Selection and characterization of NRP1- and CCL2-specific scFv and IgG molecules

The chemo-attracting soluble cytokine CCL2 is a key player in monocyte recruitment to the tumor. In fact, several preclinical studies have shown reduced tumor growth and dissemination in response to CCL2 inhibitory treatment [77]–[79]. Preliminary anti-tumor effects were also observed in a phase I clinical trial using the CCL2-specific monoclonal antibody carlumab (CNTO 888) for the treatment of solid cancers, including colorectal, ovarian and uterine cancer. However, no significant tumor response was found in a phase II trial when treating prostate cancer patients with carlumab. Surprisingly, an increase in CCL2 concentration in the serum was observed in both studies following treatment with carlumab [45], [47]. The contrasting results of preclinical and clinical data could derive from compensatory mechanisms (increase in CCL2 concentration), especially in response to the systemic delivery of the CCL2-blocking antibody. The use of a CCL2-specific antibody to target macrophages in combination with an additional approach such as TAM repolarization or checkpoint inhibition seems more promising due to reduced drug resistance. In addition, targeted delivery of the anti-CCL2 antibody to the tumor site might circumvent a systemic increase in CCL2 serum levels following treatment.

Another, although less well-described target for modulation of macrophage recruitment to the tumor, is the membrane surface receptor NRP1. NRP1 is expressed by various immune cells, including macrophages, and is upregulated in multiple tumor types which is often related to disease progression [187]. There is increasing evidence that NRP1 modulates the migration of macrophages to Sema3A-secreting tumors and their switch to a pro-tumorigenic phenotype, thus supporting the concept of targeting NRP1 as a promising treatment approach [54], [93].

Because highly pure antigens are required for the selection of CCL2- and NRP1-specific antibodies by means of phage display, we first set out to produce and purify recombinant CCL2 and NRP1 antigen proteins. CCL2 is a 13 kDa protein composed of 76 amino acids. Since the interaction sites for its cognate receptor CCR2 are distributed over the whole protein [163], we designed a full-length CCL2 protein carrying a C-terminal mFc tag. The extracellular portion of NRP1 consists of a domain essential for Sema3A binding (CUB1CUB2), a domain necessary for VEGF binding (b1b2) and a domain facilitating receptor dimerization (MAM). It has been found that an antibody Fab fragment that interferes with the binding of Sema3A to NRP1 and NRP2 binds specifically to the CUB1 domain of NRP2. This Sema3A binding domain is well conserved between NRP1 and NRP2 [87]. Moreover, seven amino acids in the CUB1 region have been

reported, which when substituted, ablate the binding of Sema3A to NRP1 [160]. Thus, we designed two truncated NRP1 proteins, containing either the CUB1 or the CUB1CUB2 domain, fused to a C-terminal mFc tag to increase the chance of selecting an antibody fragment that blocks the NRP1 – Sema3A interaction site. The fused mFc tag allowed for easy purification by Protein A affinity chromatography and detection via anti-Fc antibodies. HEK293-6E cells were transfected with mammalian expression vectors encoding the antigens and the produced recombinant proteins were purified from the cell culture supernatant by Protein A affinity chromatography. All antigens were produced in sufficient amounts for further analyses and were highly pure with no or little aggregate content. An exception was the NRP1 CUB1CUB2-mFc fusion protein resulting in a lower protein yield and higher aggregate content which could probably derive from the larger size (110 kDa) and complexity (two CUB domains) of this protein. Furthermore, analytical SEC of the CCL2-mFc fusion protein did not show any aggregates for this antigen which may derive from the included P8A substitution omitting CCL2 dimerization [157]. However, we do not have a direct comparison to non-mutated CCL2-mFc fusion protein to confirm the necessity of the P8A substitution.

In order to select an antibody possessing the ability to block the NRP1 – Sema3A interaction, the integrity of the NRP1 CUB domains is of utmost importance. Consequently, we investigated the integrity of the Sema3A binding site on the recombinant NRP1(CUB1)-mFc and NRP1(CUB1CUB2)-mFc fusion proteins by ELISA. Unfortunately, we found that none of the recombinant NRP1 fusion proteins bound to Sema3A. When we used a commercially purchased NRP1 protein containing the CUB1, CUB2, b1 and b2 domains (NRP1 (CUB1CUB2, b1b2)) for coating the ELISA plates, we detected binding of Sema3A, which may indicate incorrect folding of our recombinant NRP1-mFc fusion proteins containing only CUB1 or CUB1CUB2 domains. This was surprising since it was reported that the CUB domains form a beta-barrel structure which was thought to fold independently. Especially the CUB1 domain is in an exposed position and interacts with the neighboring protein domain only via a three residue linker as was found by a crystallography experiment using murine NRP1 [161]. Moreover, Liang *et al.* successfully produced the NRP1 CUB1CUB2 domains in baculovirus Hi5 cells and showed biological activity of this truncated protein by mediating Sema3A-dependent neuronal growth cone collapse [188]. As an alternative for the production of the CUB domains we suggest the design and synthesis of a peptide carrying the Sema3A – NRP1 interaction sites. For this purpose, the section between amino acid 40 and 140 of the NRP1 protein seems to be of special interest. This region is described to contain the epitope of an antibody Fab fragment blocking the Sema3A - NRP1 interaction [87]. In addition, amino acids are located in this region which when substituted ablate

the binding of Sema3A to NRP1 [160]. In contrast, the integrity of the produced CCL2-mFc fusion protein could be successfully confirmed using a commercially acquired CCL2-specific antibody and by subsequent detection via ELISA. Consequently, we used the purchased NRP1 (CUB1CUB2, b1b2) protein and the in-house produced CCL2-mFc fusion protein as antigens for the phage display panning rounds.

The selection of NRP1-specific scFvs from LYNDAL was unsuccessful due to the enrichment of clones which contained only truncated scFv DNA sequences. The enrichment of such clones is most probably due to their unspecific “stickiness” of the presented scFv on the phage surface towards the antigen or immunotube surface [98]. In contrast, after three rounds of phage display selection against CCL2, specific clones enriched that overall contained 37.2 % full-length scFv DNA sequences. Of 540 individually screened clones only two were identified to specifically bind CCL2 but which were found to be identical in sequence analyses (anti-CCL2 clone NB7.E5).

In parallel, our collaborator Yumab GmbH selected fully human scFvs from their naïve antibody library HAL9/10 by phage display using our CCL2-mFc fusion protein as well as the commercially available NRP1 (CUB1CUB2, b1b2) protein [156]. Yumab GmbH provided us with five anti-CCL2 and two anti-NRP1 antibody fragments. A study analyzing antibody affinity maturation and diversification in tetanus toxin vaccinated humans described a mean value of 20.5 amino acid somatic mutations in the combined VH and VL repertoire to indicate affinity maturation [189]. For the LYNDAL-derived clone NB7.E5 we found a total of 27 amino acid changes. In contrast, the HAL9/10-derived clones had only 1 - 16 amino acid changes. In other studies in our laboratory, we found that scFvs with other specificities selected from LYNDAL were more distant to the germline sequence than those selected from HAL9/10. Notably, LYNDAL contains IgG VH and VL repertoires isolated from B cells of tumor draining lymph nodes of head and neck cancer patients, whereas HAL9/10 contains IgM VH and VL repertoires that derive from circulating B cells of healthy donors [152], [156]. Interestingly, we observed an accumulation of mutations in the VL region of antibody fragments selected from the naïve library as compared to the immune library-selected antibody fragment. It has been shown, that IgM^+ memory B cells are somatically mutated and show increased numbers of mutations in the heavy and light chain CDRs [190]. It could be possible that the antibody fragments selected from the HAL9/10 library are derived from these IgM^+ memory B cells. Moreover, it has been shown that antigen-encountered, affinity-matured B cells can be obtained from lymph nodes which are the site of B cell affinity maturation [191], [192]. The selection of high affinity antibodies against autoantigens such as CCL2 from LYNDAL was surprising and we hypothesize that the reason for this may relates to the random combination of antibody heavy chain and light chain genes which allows the creation of completely novel antibody

specificities [152]. Moreover, Tiller *et al.* found that autoantigen-reactive antibodies were expressed by IgG^+ memory B cells. They could identify *de-novo* somatic hypermutation during B cell transition between mature naïve and memory cell to induce expression of these self-reactive antibodies [193]. In addition, overexpression of CCL2 has been described by several studies of head and neck cancer [194]. This enhanced autoantigen expression may promote the formation of autoreactive-antibodies.

To evaluate the binding characteristics of the selected anti-CCL2 scFv NB7.E5, we produced the scFv in *E. coli* TG1 cells. Following purification, the NB7.E5 scFv showed low aggregate content (< 10 %) and correct molecular weight. Remarkably, we showed specific binding of NB7.E5 scFv to CCL2 and did not observe any binding of to other tested members of the chemokine family despite possessing a sequence identity of over 50 % compared to CCL2.

The scFv antibody format is well suited for phage display and can be easily expressed in bacteria. However, most approved therapeutic antibodies are provided in the IgG1 format. IgG antibodies are characterized by longer serum half-live as a result of exceeding the kidney filtration threshold of 70 kDa and binding to the neonatal Fc receptor responsible for recycling of IgG antibodies from endosomes [195], [196]. In contrast to scFv molecules, IgG1 antibodies can mediate effector functions via their Fc region. Antibodies opsonize target antigen-expressing cells, thereby recruiting Fc receptor-expressing effector cells which release cytotoxic molecules such as granzyme and perforin resulting in target cell killing (ADCC: antibody-dependent cellular cytotoxicity). Moreover, Fc receptor-expressing phagocytes are induced to phagocytose antigen-expressing cells (ADCP: antibody dependent cellular phagocytosis). In addition, antibodies bound to target cells may initiate the complement system which can result in killing of the target cell (CDC: complement dependent cytotoxicity) [197]. In this context, it is of utmost importance to carefully consider antigen expression on different cell types in order to prevent off-target effects of the antibodies. Especially for the target NRP1 which is expressed on several cells of the immune system, antibody-mediated effector functions may be detrimental resulting in unwanted killing of healthy cells [86], [87]. In contrast, CCL2 is not associated to the cell membrane but is a soluble protein. However, sequestering of CCL2 to the cell membrane by glycosaminoglycans has been described [170]. CCL2 attached to the cell surface may be bound by anti-CCL2 antibodies which trigger antibody effector functions and killing of the cell. Along this line, we transferred the selected anti-NRP1 and anti-CCL2 scFvs into the IgG1 antibody format containing the N297A substitution which is described to ablate binding to the Fcγ receptor [168], [169]. Blocking of Fcγ receptor-expressing cells to the antibody Fc region has been described to reduce effector functions which can prevent off-target effects such as cell death or unwanted release of cytokines.

Anti-CCL2 and anti-NRP1 IgG antibodies were produced in HEK293-6E cells and showed correct molecular weight and low aggregate content (< 5 %) following purification, except anti-NRP1 YU110B1 (16 % aggregate content). To confirm the ablation of the IgG1 interaction with the Fcγ receptor we compared the binding of NB7.E5 (N297A) and the counterpart containing the wild-tpe N297 (NB7.E5 (N297)) to Fcγ receptor-expressing THP1 cells side-by-side. Importantly, we confirmed inhibition of IgG antibody binding to Fcγ receptor-expressing THP1 cells mediated by the N297A substitution. Thereby, we hypothesize to reduce off-target effects in future *in vivo* studies.

Noteworthy, we observed antigen-specific binding of our IgG antibodies and no cross-reactivity to tested control proteins as determined by ELISA. YU109B1 and YU109H1 showed weaker CCL2 binding compared to our other CCL2-specific antibodies. As for the scFv format, we confirmed no interaction with highly similar (>50% sequence identity compared to CCL2) members of the chemokine family for the CCL2-specific NB7.E5 IgG.

Moreover, we determined antibody binding affinity by SPR spectroscopy. We observed high affinity for our LYNDAL-derived anti-CCL2 IgG NB7.E5 in the low nanomolar range (K_D = 5.8 nM). In comparison, the HAL9/10-derived CCL2-specific IgG antibodies showed lower affinities (K_D value ranging from 50 to 422 nM) with very fast association and dissociation of the soluble antigen. Based on the superior binding affinity of NB7.E5 we pursued this antibody as lead candidate for functional characterization. Regarding the NRP1-specific IgG antibodies, we detected moderate binding affinities (YU110B1 K_D = 35.6 nM, YU110D1 K_D = 58.3 nM). In general, therapeutic antibodies have affinities in the low nanomolar to picomolar range [198]. Accordingly, the two anti-CCL2 antibodies carlumab and ABN912 which have been evaluated in clinical trials have K_D values of 15 and 43 pM, respectively [45], [82]. Remarkably, the LYNDAL-derived antibody NB7.E5 has a strikingly high affinity in regard to being directly selected from the immune antibody library and not having undergone further affinity maturation. Commonly, therapeutic antibodies are comprehensively engineered to optimize biological activity and affinity. Therefore, it should be considered to further enhance antibody affinity which may in turn decrease injection dose, limit adverse effects and finally reduce therapy costs. Affinity maturation can be achieved by *in vitro* techniques like targeted or random mutagenesis or by *in silico*, computer-aided modeling and may be supported by next generation sequencing [198].

We additionally investigated the binding affinity of the anti-NRP1 antibodies to the target expressed in the context of a cell surface receptor on HUVEC cells by flow cytometry. Surprisingly, we measured approximately 10-fold lower K_D values (YU110B1 K_D = 0.36 nM, YU110D1 K_D = 0.17

nM) as determined by SPR spectroscopy. One major difference in the two methods employed to determine the antibody affinity is the fact that flow cytometry measures an end-point and lacks the possibility to acquire real-time antigen association and dissociation. Therefore, the K_D value calculated from flow cytometry data corresponds to the ligand concentration needed to achieve half-maximum binding at equilibrium (EC50). Whereas, the K_D value generated by SPR analysis is calculated from the time-dependent association and dissociation rate constant (K_D = kd/ka). Furthermore, during flow cytometry, an antibody may bind to two antigenic sites simultaneously depending on the antigen surface density [175]. We avoided these antibody avidity effects in the SPR analysis by optimizing the experimental setup to ensure a 1:1 interaction. Antibody avidity may increase the flow cytometry-based calculated affinity of our antibodies in comparison to the data acquired by SPR spectroscopy [176].

4.2 Functional characterization of anti-NRP1 and anti-CCL2 IgG antibodies

A prerequisite of the functionality of the anti-NRP1 and anti-CCL2 antibodies is their ability to block the ligand – receptor interaction. Blockade of the Sema3A – NRP1 or CCL2 – CCR2 interaction has been described to reduce the number of macrophages in the tumor and to support an anti-tumorigenic macrophage phenotype [54], [78], [79], [93], [199].

We investigated the effects of the anti-NRP1 IgG antibodies YU110B1 and YU110D1 on the NRP1 – ligand interaction by ELISA. NRP1 is described to have two ligands, Sema3A and VEGF [87]. We observed blocking of the NRP1 - Sema3A interaction but not of the NRP1 - VEGF interaction mediated by YU110B1 and YU110D1 in an ELISA setting. Furthermore, we studied the blocking capacity of the anti-NRP1 antibodies on binding of Sema3A to NRP1 expressed on the surface of HUVEC cells by flow cytometry. Surprisingly, we did not observe any blocking of the ligand – receptor interaction mediated by YU110B1 or YU110D1 and therefore could not confirm our findings from the ELISA experiment. The ELISA assay using recombinant NRP1 is a rather artificial setting compared to the analysis of the antibody interaction with cell surface expressed NRP1 and might therefore result in contrasting experimental outcomes. Moreover, this discrepancy may be due to binding of Sema3A to another cell surface protein thereby masking the effects of the anti-NRP1 antibodies. Indeed, Sema3A is described to bind to chondroitin sulfate, a glycosaminoglycan and constituent of the extracellular matrix. Chondroitin sulfate is found on different tissues and is present at high levels in the central nervous system and cartilage

[200]. In order to investigate the blocking capacity of our antibodies we further attempted to transfect NRP1-negative HEK293T cells (which are not bound by our antibodies) with a mammalian expression vector encoding full-length NRP1 to induce surface expression of the NRP1 receptor. However, these preliminary attempts were so far not successful due to decreased cell viability following transfection. Another approach could be to develop NRP1-deficient HUVEC cells in order to analyze if Sema3A binding to these cells is only mediated by NRP1 or if Sema3A also binds to other cell surface molecules. However, in the course of this study we decided not to continue the development of the anti-NRP1 antibodies and to prioritize the analysis of the anti-CCL2 lead candidate NB7.E5.

To characterize the effect of NB7.E5 scFv and IgG on the CCL2 – CCR2 interaction we performed a flow cytometry experiment with CCR2-expressing THP1 cells. We observed a remarkable decrease in CCL2 binding to CCR2 correlating to increasing concentrations of NB7.E5 scFv and IgG. The blocking capacity of NB7.E5 IgG was higher compared to NB7.E5 scFv which is most probably due to the bivalent nature of IgG molecules compared to the monovalent scFv.

Furthermore, we investigated whether neutralization of CCL2 by our anti-CCL2 IgG NB7.E5 is able to ablate CCL2-mediated intracellular signaling of CCR2. Interestingly, macrophage chemotaxis has been linked to activation of the MAPK pathway in response to CCL2 – CCR2 interaction [69]–[71]. As a measurement for MAPK signaling we assessed ERK phosphorylation in response to treatment of CCR2-expressing THP1 cells with CCL2 in the presence and absence of the CCL2-specific NB7.E5 IgG. Phosphorylated ERK levels were compared to total ERK and GAPDH levels in cell lysates and were found to be significantly decreased in cells treated with NB7.E5 IgG. These results indicate that the neutralization of CCL2 by NB7.E5 IgG is able to reduce CCL2-induced intracellular signaling of CCR2 via the MAPK pathway and might therefore also affect macrophage chemotaxis.

Next, we addressed the most interesting question of this study: Does CCL2 neutralization by NB7.E5 IgG inhibit monocyte migration towards an increasing CCL2 gradient? For this purpose, we performed a transwell assay which allows to monitor migration of cells through a porous membrane along a chemokine concentration gradient. Alternative assays to assess cell migration are the *in vitro* scratch assay or a microfluidics-based assay. However, a simple scratch assay has the major drawback that no chemokine gradient can be established [201]. Thus, migration rate could merely be monitored in the presence or absence of CCL2. On the other hand, a microfluidics-based migration assay is a more elegant option. This assay would allow real-time single cell tracking during migration along a stable chemokine gradient [202]. However, a transwell

assay is easier to set up, cost effective and does not require special equipment. Consequently, we assessed monocyte (CCR2-expressing THP1 cells) chemotaxis towards a CCL2 gradient in the presence and absence of the anti-CCL2 IgG NB7.E5 in a transwell assay. Remarkably, we observed a decrease in monocyte migration mediated by the anti-CCL2 antibody. At a 1:1 molar ratio of antibody to CCL2 a 50 % reduction in migrated monocytes was shown.

These findings encourage us to further analyze the anti-CCL2 antibody NB7.E5 in future *in vivo* studies. Apart from affecting monocyte migration to the tumor resulting in reduced numbers of pro-tumorigenic TAMs, treatment of CCR2-expressing cancers with an anti-CCL2 antibody may also have direct effects on tumor growth, metastatic spread and disease progression. CCR2 is expressed on breast cancer cells and deletion of CCR2 by transplanting CCR2 negative tumor cells in an orthotopic breast cancer mouse model resulted in reduced tumor growth and two-fold longer survival of the mice. In addition, better tumor control by the immune system was observed including increased infiltration and activation of cytotoxic T cells and dendritic cell maturation, as well as upregulation of MHC class I on tumor cells and downregulation of the immune checkpoint molecule PD-L1 [203]. Moreover, CCL2 - CCR2 signaling can directly promote metastasis in CCR2-expressing tumors such as prostate or breast cancer. Thereby, CCL2 guides the migration of CCR2-expressing cancer cells. In addition, CCL2 can trigger the expression of matrix metalloproteinases in tumor cells, resulting in increased invasion [204]. Furthermore, an *in vitro* experiment using the CCR2-expressing non-small cell lung cancer cell line A549 showed that CCL2 promoted tumor cell viability, motility and invasion by upregulation of matrix metalloproteinases. These CCL2-mediated effects could be abrogated by addition of a CCR2 antagonist [205]. Based on these findings, we would expect similar reduction in tumor growth and metastasis of CCR2-expressing cells by neutralizing CCL2 using our anti-CCL2 antibody.

4.3 CD22-directed CAR T cells as vehicle for anti-CCL2 scFv delivery

Tremendous effort has been put into the development of CAR T cell therapies over the past years leading to the FDA approval of two CD19 targeting CAR T cell therapies for the treatment of leukemia and relapsed and refractory large B cell lymphoma [120], [121]. Although CD19-targeted CAR T cell therapies show potent effects, antigen loss is a frequently observed immune escape mechanism in patients with pre-B cell acute lymphoblastic leukemia (B-ALL) leading to therapy resistance. A promising treatment approach for relapsed patients after CD19-targeted CAR T cell therapy may be targeting alternative antigens using CAR T cells. Along this line, clinical

experience has been gained using a CD22-directed CAR T cell therapy in pre-B-ALL demonstrating a similar safety profile and potency as CD19-targeting CAR T cells [129].

Treatment of hematological tumors with tumor-specific CAR T cells has shown remarkable efficacy. However, regarding solid tumors CAR T cell therapy has so far only shown limited success. Promising results were observed for the treatment of neuroblastoma patients with first-generation disialoganglioside (GD2)-specific CAR T cells in a phase I clinical study which resulted in complete remission in three out of eleven patients [206]. In contrast, all other CAR T cell therapies investigated in phase I clinical studies in the treatment of solid cancers achieved either no anti-tumor effects or only transient or partial tumor responses [207]. Known obstacles to CAR T cell therapy of solid tumors are the identification of true tumor-specific target antigens, reduced trafficking of CAR T cells to the tumor site, inefficient CAR T cell activation, and low proliferation and cytotoxicity capacities. Many of these T cell defects are caued by the immunosuppressive microenvironment within the tumor mass which is maintained by TAMs and regulatory T cells (Tregs). TAMs mediate the immunosuppressive functions by decreasing local levels of tryptophan, an essential amino acid for optimal function of CAR T cells, and the release of inhibitory cytokines such as IL-10 and TGFβ [130], [207].

To overcome the inhibitory environment within the tumor, the development of fourth-generation CAR T cells, which are additionally engineered to secrete cytokines or antibody fragments, has moved into the center of attention. These so called “armored” CAR T cells allow the combination of CAR T cell therapy with targeting of immune checkpoints, activation of costimulatory pathways or modulation of the immunosuppressive tumor microenvironment (TME) [208]. Along this line, innovative studies have been published demonstrating enhanced anti-tumoral effects of CAR T cells secreting antibody fragments or IgG antibodies. CD19- and Mucin 16 (ecto)-directed CAR T cells secreting an anti- programmed cell death protein 1 (PD-1) scFv for checkpoint inhibition resulted in increased anti-tumor activity in mouse models of hematologic and solid cancers [137]. Moreover, in a human glioma mouse model, secretion of an anti-cytotoxic T lymphocyte-associated protein 4 (CTLA4) minibody from interleukin-13 receptor subunit alpha-2 (IL-13Rα2)-recognizing CAR T cells inhibited tumor growth and prolonged T cell function [139]. In an additional study, secretion of anti-PD-L1 IgG antibodies from carbonic anhydrase IX (CAIX)-directed CAR T cells resulted in diminished tumor growth and reduced expression of PD-L1 on tumor cells in a humanized mouse model of clear cell renal cell carcinoma [138].

DLBCL is the most common human lymphoma and current standard-of-care treatment composed of chemotherapy combined with rituximab shows high remission rates (50 – 60 %). However, 40

% of patients with initial remission experience disease relapse and these patients show very poor clinical outcomes [141], [143]. Therefore, novel therapy approaches for DLBCL are of urgent need. Since DLBCL originates from mature B cells, the tumor cells express B cell-specific surface molecules such as CD19 and CD22 [141]. Treatment of 93 patients with relapsed or refractory DLBCL with the CD19-directed CAR T cell therapy tisagenlecleucel resulted in complete remission in 40 % of the patients [144]. Moreover, treatment of 77 DLBCL patients with another CD19-directed CAR T cell therapy, axicabtagene ciloleucel, achieved complete remission in 49 % of the patients [125]. Another targetable B cell marker in DLBCL tumor cells is CD22. In our laboratory we developed a CD22-specific CAR which shows efficient activation, proliferation and potent cytotoxicity in pre-clinical *in vitro* assays.

Also in DLBCL, the immunosuppressive TME has been described to play a significant role in disease outcome. Several studies have confirmed correlation of increased numbers of TAMs, especially of the M2 phenotype, with poor prognosis of DLBCL [146]–[150]. Interestingly, Li *et al.* analyzed CCL2 expression in 221 DLBCL patients and found that high expression of CCL2 correlated with significantly poorer overall survival and progression free survival [151].

Based on these findings, we aimed to employ CD22-directed CAR T cells and DLBCL as model for the analysis of our anti-CCL2 scFv NB7.E5. For this purpose, we engineered CD22-directed CAR T cells to secrete soluble anti-CCL2 scFv molecules. We hypothesized that this novel treatment approach of CAR T cell therapy in combination with macrophage modulation may show improved antitumoral efficacy. Reduced monocyte migration to the tumor induced by targeted delivery of anti-CCL2 scFvs may ablate enrichment of tumor-promoting M2 macrophages in the tumor environment. Additionally, the immunosuppressive environment in solid tumors may be tackled resulting in improved CAR efficacy. Along this line, it has been shown that macrophage depletion in a mouse mammary tumor model led to higher numbers of tumor infiltrating T cells [209]. Moreover, CCL2 blockade in a lung cancer model has been correlated with the activation of CD8+ cytotoxic T cells [78]. Furthermore, this treatment approach may also be useful for other solid tumors where CCL2 contributes to a bad prognosis, depending on the chosen CAR specificity.

We generated two anti-CD22 CAR constructs which additionally encoded the anti-CCL2 NB7.E5 scFv either downstream (αCD22CAR-αCCL2scFv) or upstream (αCCL2scFv-αCD22CAR) of the CAR sequence. In order to encode two proteins on the same open reading frame, we included the “self-cleaving” peptide T2A between the scFv and CAR sequence.

We transfected HEK293T cells with lentiviral plasmids encoding the different CAR constructs and demonstrated CAR surface expression and soluble scFv secretion into the cell culture supernatant. Additionally, we transduced activated primary human T cells with lentiviral vectors encoding the CAR sequences and confirmed CAR expression on the cell surface. However, to our surprise no scFv molecules were detected by ELISA in the supernatant of transduced T cells. This is in contrast to our findings observed in transfected HEK293T cells and we speculated that the scFv concentration in the CAR T cell supernatant might be below the detection threshold of our assay. In an attempt to increase the scFv concentration we first increased the amount of CAR-expressing T cells from initially 40 % to approximately 90 % by stimulation with antigen-positive target cells. After two days of cultivation, we harvested the supernatant from these CAR T cells and analyzed the presence of secreted scFv by ELISA. However, we could not detect scFv molecules in the CAR T cell supernatant.

We speculated that the lack of scFv detection in supernatants of CAR T cells could be caused by several challenges: 1. Insufficient “self-cleavage” mediated by the T2A peptide might lead to inefficient separation of scFvs from the CAR; 2. scFvs are not trafficked via the secretory pathway; 3. The scFv coding sequence is not present on the mRNA; 4. T cells produce endogenous CCL2 which sequesters the scFv and prevents its detection.

First, we investigated scFv cleavage from the CAR by flow cytometry. The “self-cleaving” peptide T2A has been described to have one of the highest cleavage efficiencies, nevertheless it is thinkable that the scFv remains fused to the CAR [178]. In this case the scFv should be detectable by flow cytometry on CAR T cells transduced with the αCCL2scFv-αCD22CAR construct carrying the scFv at the N-terminal extracellular portion of the CAR. Noteworthy, we detected no scFv on the surface of the CAR T cells, indicating correct separation of the scFv and CAR. Based on these findings it is rather unlikely that the problem may be caused by the T2A cleavage peptide, nonetheless an alternative peptide for investigation in future studies might be the P2A peptide. This cleavage peptide has been efficiently used by Rafiq *et al*. for the generation of anti-PD-1 scFv secreting CAR T cells [137].

The protein secretory pathway responsible for delivery of proteins to the extracellular space might be ineffective for the secretion of the scFv from CAR T cells. To investigate whether the scFv can be detected intracellularly, CAR T cells and transfected HEK293T cells were subjected to intracellular flow cytometry analysis. We detected intracellular scFv molecules, in HEK293T cells carrying the αCD22CAR-αCCL2scFv or the αCCL2scFv-αCD22CAR construct. In contrast, we did not detect any scFv antibody fragments in CAR T cells. This could for example be due to

difference in cell size (HEK293T cells are larger than T cells), which results in more cytoplasm, endoplasmatic reticulum and Golgi complex in HEK293T cells. This critically dertermines protein production and secretion as it was found that cell size directly correlates to protein content of cells [210].

After these puzzling results so far, we wanted to confirm the presence of the scFv coding sequence on the mRNA in CAR-expressing T cells. We detected scFv encoding mRNA in T cells and HEK293T cells expressing the αCD22CAR-αCCL2scFv and αCCL2scFv-αCD22CAR constructs, but not in cells expressing the αCD22CAR construct. Thus, although T cells transduced with the respective constructs contain the scFv coding sequence on the mRNA, there is no scFv on the protein level detectable. The mRNA-to-protein ratio is determined by transcription and translation efficiency, mRNA stability and protein degradation [211], [212].

Another possible cause for not detecting anti-CCL2 scFv protein might be that CCL2 secreted from T cells sequesters the scFv molecules, thereby preventing the detection of scFvs in the cell culture supernatant by ELISA. CCL2 expression has been found in T cells of mammary tumor-bearing mice as well as activated PBMCs [179]–[182]. Therefore, we compared CCL2 mRNA levels as well as CCL2 protein in the cell culture supernatant in untransduced T cells, T cells transduced with the CAR constructs, activated and non-activated PBMCs and as negative control, untransfected and transfected HEK293T cells. We detected presence of CCL2 mRNA and CCL2 protein secretion in activated PBMCs but not in T cells or HEK293T cells. These findings rule out the possibility that endogenously produced CCL2 neutralizes the anti-CCL2 scFv in T cells.

Taken together, we explored different possible causes for the lack of detection of scFv molecules in CAR T cells, however none of these proofed to be the cause. We speculate that the scFv concentration in CAR T cell supernatants might be below the detection limit of our ELISA-based assay. Due to the larger cell size of HEK293T cells compared to T cells, it is conceivable that HEK293T cells transfected with αCD22CAR-αCCL2scFv or αCCL2scFv-αCD22CAR constructs produce higher amounts of scFv molecules [210]. Moreover, HEK293T cells are a widely used cell line for protein production whereas T cells are generally not employed for large-scale recombinant protein production [213]. Further analyses need to be performed to prove secretion of soluble scFvs from our CAR T cells.

In this context, Rafiq *et al.* generated constructs encoding a CD19 or Mucin-16 (ecto)-directed CAR and PD-1-specific scFv separated by a T2A cleavage peptide. They demonstrated anti-PD-1 scFv secretion into the supernatant of CAR T cells by western blot analysis. Moreover, they

demonstrated scFv secretion from their Mucin-16 (ecto)-targeted CAR constructs *in vivo*. In this experiment, they injected CAR T cells intraperitoneally into mice with malignant ascites. 48 hours later, ascites were harvested and immunoprecipitation of the scFvs via their c-myc tag was performed. Anti-PD-1 scFvs were subsequently detected by western blot analysis or luminex analysis [137]. By luminex analysis they observed up to 30 pg/mL anti-PD-1 scFv in their samples following immunoprecipitation. Moreover, they injected CAR T cells secreting anti-PD-1 scFvs into mice with tumors established from ovarian SKOV3 tumor cells. In order to quantify the systemic scFv levels Rafiq and colleagues employed targeted mass spectrometry. They reported no scFv in the serum of these mice and therefore hypothesized that the anti-PD-1 scFv remains localized in the TME [137]. In another recent study, Yin *et al.* demonstrated secretion of anti-CTLA4, anti-PD-1 and anti-T cell immunoglobulin and mucin domain containing 3 (TIM3) minibodies from IL-13Rα2-directed CAR T cells. For this purpose, they generated constructs endocing the CAR and minibody separated by a T2A peptide. They harvested and concentrated conditioned medium from transduced cells and detected anti-CTLA4 and anti-PD-1 minibodies by ELISA. Anti-TIM3 minibodies were detected after co-culturing TIM3 minibody secreting CAR T cells with D270 glioma cells by a competitive inhibition assay using fluorochrome-conjugated anti-TIM3 antibodies. They observed lower binding of labeled antibodies in conditions including the anti-TIM3 minibody expressing CAR T cells, indicating efficient secretion of the minibodies from the CAR T cells [139]. Suarez *et al.* generated constructs encoding a CAIX-targeted CAR and anti-PD-L1 IgG separated by an internal ribosomal entry site. They demonstrated anti-PD-L1 IgG antibody secretion from transduced T cells following 48 hours of culturing of these cells [138]. IgG antibodies were purified by Protein A chromatography, biotinylated and detected via binding to PD-1-coated ELISA plates. Thereby, they observed anti PD-L1 antibodies at concentrations of up to 230 ng/mL. However, it needs to be considered that these concentrations are not achieved in the direct supernatant of CAR T cells but following affinity purification.

Taken together, we expect to detect secretion of our anti-CCL2 scFv using higher sensitivity methods such as mass spectrometry or to perform co-immunoprecipitation using a scFv-specific antibody or CCL2 itself to enrich the CCL2-specific scFvs from the cell culture supernatant. Moreover, the observations of Rafiq and colleagues encourage us to study anti-CCL2 scFv secretion by our CAR T cells in future *in vivo* experiments using tumor-bearing mice. In the tumor higher CAR T cell densities per volume may be reached as in *ex vivo* cell culture resulting in higher scFv concentrations in the tumor interstitium than in cell culture supernatant. Consequently, scFv secretion from the CAR T cells may be detectable in the tumor interstitial fluid.

Additionally, it is important to compare systemic anti-CCL2 scFv concentrations with concentrations of the scFv within the TME in a tumor mouse model. As mentioned above, Rafiq *et al.* did not observe anti-PD-1 scFv in the serum and suspected the scFv to remain in the TME [137]. This would also be advantageous in our setting, since local CCL2 inhibition may increase the efficacy of the anti-CCL2 scFvs and reduce off-target effects and compensatory mechanisms. Moreover, anti-CCL2 scFvs explicitly localized in the TME may further increase the efficacy of CAR T cells by direct modulation of the immunosuppressive TME.

In this study, we also showed that our newly designed CAR constructs, αCCL2scFv-αCD22CAR and αCD22CAR-αCCL2scFv, are functionally active, which is a prerequisite for further development of this approach. Following stimulation with CD22-positive target cell lines, we demonstrated equivalent proliferation, cytokine release and killing capabilities of CAR T cells transduced with the anti-CCL2 scFv encoding contructs or the conventional αCD22CAR construct.

Although stimulated αCD22CAR-αCCL2scFv T cells also showed release of the inflammatory cytokines IL-2, IFNγ and TNF, the detected levels were lower than for T cells transduced with the other constructs. Following separation of the CAR and scFv mediated by the T2A peptide, the protein downstream of T2A is left with an additional N-terminal proline, whereas the protein upstream of T2A remains fused to the complete T2A peptide except for the C-terminal proline [178]. We hypothesize that for the αCD22CAR-αCCL2scFv, where the majority of the T2A peptide remains attached to the CAR, the functionality of the CAR might be affected and therefore the release of inflammatory cytokines might be reduced. Notably, all CAR T cells released higher levels of pro-inflammatory cytokines upon stimulation with target cells compared to unstimulated controls, indicating successful antigen-dependent activation of these cells. Further functional studies including the analysis of activation (e.g. CD25 and CD69) and exhaustion (e.g. PD-1) marker expression on stimulated CAR T cells may help to further characterize the αCD22CAR-αCCL2scFv and αCCL2scFv-αCD22CAR constructs [214], [215].

Additionally, we investigated the cytotoxic effects of CAR T cells in comparison to untransduced T cells. Therefore, effector cells and target antigen-positive GLuc-expresssing Raji cells were co-incubated and target cell killing was analyzed using a luminescence-based cytotoxicity assay. All CAR constructs mediated cytotoxicity, whereby strongest killing capacity was detected for T cells expressing the conventional αCD22CAR. Moreover, we found higher levels of CAR expression on the surface of αCD22CAR T cells compared to scFv-carrying CAR T cells which might account for the observed increase in cytotoxic effects.

Taken together, our findings confirm that CAR T cells additionally encoding the anti-CCL2 scFv remain functionally active. Analyses of CAR constructs containing different spacers or signaling domains may further contribute to improved activity of the CAR T cells. It has been reported that CAR T cell potency depends on the spacer which determines the distance between the CAR T cell and the tumor target cell [118], [119]. Additionally, instead of the 4-1BB (CD137) costimulatory domain, a CD28 costimulatory domain could be used. However, a major advantage of 4-1BB over CD28 is the increased CAR T cell persistence which is important for achieving long-term remission [216].

4.4 Outlook

In a novel approach to generate “armored” CAR T cells, we modified CD22-directed CAR constructs for the soluble secretion of anti-CCL2 NB7.E5 scFv molecules. Although we confirmed functional activity of the CAR expressing T cells, it is of utmost importance to successfully demonstrate scFv secretion from T cells transduced with these constructs. We hypothesize that the concentration of secreted scFvs may be below the detection threshold of our assay. Therefore, a more sensitive method for detection of scFvs should be used such as co-immunoprecipitation of scFvs before supernatant analysis or mass spectrometry. Alternatively, scFv secretion may be detected in an *in vivo* mouse model as described by Rafiq *et al.* [137].

We further plan to characterize the functional properties of the NB7.E5 antibody in an adequate *in vivo* mouse tumor model. Investigating the role of human monocytes and macrophages and the impact of their modulation on tumor growth in a mouse model is challenging. There are a few mouse models described for efficient repopulation of immunodeficient mice with human monocytes and macrophages. In this context, Rongvaux and colleagues irradiated immunodeficient MISTRG mice, transplanted them with human hematopoietic stem and progenitor cells and established a human melanoma tumor xenograft. Interestingly, they detected infiltration of the tumor xenografts by human macrophages expressing M2 markers and correlated these findings to increased tumor growth as compared to control mice [217]. Although MISTRG mice have been discontinued due to their short life span, similar immunodeficient mouse models are now commercially available. Notably, efficient engraftment of immunodeficient mice with functional macrophages requires not only the injection of hematopoietic stem cells but also the expression of human cytokines such as granulocyte/macrophage colony-stimulating factor or IL-3. This may be achieved using either huNOG-EXL or NSG-SGM3 mice which are immunodeficient

and express human cytokines required for myeloid cell engraftment [218]. Reconstitution of mice with human macrophages may allow to study the effects of our CCL2-specific antibody on macrophage modulation and the impact on growth of solid tumors.

With our work we contribute to the development of CCL2-specific antibodies with the aim to inhibit monocyte recruitment to the tumor thereby reducing the number of protumorigenic TAMs. Moreover, the combination of macrophage modulation mediated by CCL2-specific scFvs with CAR T cell therapy may increase the treatment efficacy in solid tumors challenged by an immunosuppressive environment.

5 Bibliography

5.1 References

[1] K. Murphy, P. Travers, M. Walport, and C. Janeway, *Janeway's immunobiology*, 8th editio. New York: Garland Science, 2012.

[2] R. Medzhitov and C. A. Janeway, "Decoding the Patterns of Self and Nonself by the Innate Immune System," *Science (80-.).*, no. 296, pp. 298–300, 2002.

[3] J. S. Marshall, R. Warrington, W. Watson, and H. L. Kim, "An introduction to immunology and immunopathology," *Allergy, Asthma Clin. Immunol.*, vol. 14, no. s2, pp. 1–10, 2018.

[4] J. R. Dunkelberger and W. C. Song, "Complement and its role in innate and adaptive immune responses," *Cell Res.*, vol. 20, no. 1, pp. 34–50, 2010.

[5] F. A. Bonilla and H. C. Oettgen, "Adaptive immunity," *J. Allergy Clin. Immunol.*, vol. 125, no. 2 SUPPL. 2, pp. S33–S40, 2010.

[6] J. V Ravetch and J.-P. Kinet, "Fc Receptors," *Annu. Rev. Immunol.*, vol. 9, pp. 457–492, 1991.

[7] H. W. J. Schroeder and L. Cavacini, "Structure and Function of Immunoglobulins," *J. Allergy Clin. Immunol.*, vol. 125, pp. S41–S52, 2010.

[8] S. Tonegawa, "Somatic generation of antibody diversity," *Nature*, vol. 302, pp. 575–581, 1983.

[9] D. Jung and F. W. Alt, "Unraveling V (D) J Recombination : Insights into Gene Regulation V (D) J recombination assembles antigen receptor," *Cell*, vol. 116, no. D, pp. 299–311, 2004.

[10] I. C. M. Maclennan, "Germinal centers," *Annu. Rev. Immunol*, vol. 12, pp. 117–139, 1994.

[11] B. Zheng, W. Xue, and G. Kelsoe, "Locus-specific somatic hypermutation in germinal centre T cells," *Nature*, vol. 372, pp. 556–559, 1994.

[12] S. D. Boyd and S. A. Joshi, "High-Throughput DNA Sequencing Analysis of Antibody Repertoires," *Microbiol. Spectr.*, vol. 2, no. 5, 2014.

[13] R. van Furth and Z. A. Cohn, "The origin and kinetics of mononuclear phagocytes," *J Exp Med.*, vol. 128, no. 3, pp. 415–435, 1968.

[14] R. van Furth, Z. A. Cohn, J. G. Hirsch, J. H. Humphrey, W. G. Spector, and H. L. Langevoort, "The mononuclear phagocyte system : a new classification of macrophages , monocytes , and their precursor cells," *Bull World Heal. Organ.*, vol. 46, no. 6, pp. 845–852, 1972.

[15] G. Hoeffel *et al.*, "C-Myb+ Erythro-Myeloid Progenitor-Derived Fetal Monocytes Give Rise to Adult Tissue-Resident Macrophages," *Immunity*, vol. 42, no. 4, pp. 665–678, 2015.

[16] C. Schulz *et al.*, “A lineage of myeloid cells independent of myb and hematopoietic stem cells,” *Science (80-.).*, vol. 335, no. 6077, pp. 86–90, 2012.

[17] E. Mass *et al.*, “Specification of tissue-resident macrophages during organogenesis,” *Science (80-.).*, vol. 353, no. 6304, pp. 1–32, 2016.

[18] P. Italiani and D. Boraschi, “From monocytes to M1/M2 macrophages: Phenotypical vs. functional differentiation,” *Front. Immunol.*, vol. 5, no. OCT, pp. 1–22, 2014.

[19] A. R. Poh and M. Ernst, “Targeting macrophages in cancer: From bench to bedside,” *Front. Oncol.*, vol. 8, no. MAR, pp. 1–16, 2018.

[20] S. Gordon, “Alternative activation of macrophages,” *Nat. Rev. Immunol.*, vol. 3, no. 1, pp. 23–35, Jan. 2003.

[21] G. Solinas, G. Germano, A. Mantovani, and P. Allavena, “Tumor-associated macrophages (TAM) as major players of the cancer-related inflammation,” *J. Leukoc. Biol.*, vol. 86, no. 5, pp. 1065–1073, 2009.

[22] S. M. Ong *et al.*, “Macrophages in human colorectal cancer are pro-inflammatory and prime T cells towards an anti-tumour type-1 inflammatory response,” *Eur. J. Immunol.*, vol. 42, no. 1, pp. 89–100, 2012.

[23] E. Y. Lin, A. V. Nguyen, R. G. Russell, and J. W. Pollard, “Colony-stimulating factor 1 promotes progression of mammary tumors to malignancy,” *J. Exp. Med.*, vol. 193, no. 6, pp. 727–739, 2001.

[24] Q. wen Zhang *et al.*, “Prognostic Significance of Tumor-Associated Macrophages in Solid Tumor: A Meta-Analysis of the Literature,” *PLoS One*, vol. 7, no. 12, 2012.

[25] S. Yin *et al.*, “The prognostic and clinicopathological significance of tumor-associated macrophages in patients with gastric cancer: A meta-analysis,” *PLoS One*, vol. 12, no. 1, pp. 1–14, 2017.

[26] X. Zhao *et al.*, “Prognostic significance of tumor-associated macrophages in breast cancer: A meta-analysis of the literature,” *Oncotarget*, vol. 8, no. 18, pp. 30576–30586, 2017.

[27] B. Guo, H. Cen, X. Tan, and Q. Ke, “Meta-analysis of the prognostic and clinical value of tumor-associated macrophages in adult classical Hodgkin lymphoma,” *BMC Med.*, vol. 14, no. 1, 2016.

[28] J. Mei *et al.*, “Prognostic impact of tumor-associated macrophage infiltration in non-small cell lung cancer: A systemic review and meta-analysis,” *Oncotarget*, vol. 7, no. 23, pp. 34217–34228, 2016.

[29] A. Henze and M. Mazzone, “The Impact of Hypoxia on tumor-associated macrophages,” *J. Clin. Invest.*, vol. 126, no. 10, pp. 3672–3679, 2016.

[30] L. Cassetta and J. W. Pollard, “Targeting macrophages: Therapeutic approaches in cancer,” *Nature Reviews Drug Discovery*, vol. 17, no. 12. Nature Publishing Group, pp. 887–904, 28-Nov-2018.

[31] T. Schmidt, I. Ben-Batalla, A. Schultze, and S. Loges, “Macrophage-tumor crosstalk: Role of TAMR

tyrosine kinase receptors and of their ligands," *Cellular and Molecular Life Sciences*, vol. 69, no. 9. pp. 1391–1414, May-2012.

[32] D. H. Josephs, H. J. Bax, and S. N. Karagiannis, "Tumour-associated macrophage polarisation and re-education with immunotherapy," 2015.

[33] W. D. Tap *et al.*, "Structure-guided blockade of CSF1R kinase in tenosynovial giant-cell tumor," *N. Engl. J. Med.*, vol. 373, no. 5, pp. 428–437, 2015.

[34] N. Butowski *et al.*, "Orally administered colony stimulating factor 1 receptor inhibitor PLX3397 in recurrent glioblastoma: An Ivy Foundation Early Phase Clinical Trials Consortium phase II study," *Neuro. Oncol.*, vol. 18, no. 4, pp. 557–564, 2016.

[35] B. Von Tresckow *et al.*, "An open-label, multicenter, phase I/II study of JNJ-40346527, a CSF-1R inhibitor, in patients with relapsed or refractory Hodgkin lymphoma," *Clin. Cancer Res.*, vol. 21, no. 8, pp. 1843–1850, 2015.

[36] P. A. Cassier *et al.*, "CSF1R inhibition with emactuzumab in locally advanced diffuse-type tenosynovial giant cell tumours of the soft tissue: A dose-escalation and dose-expansion phase 1 study," *Lancet Oncol.*, vol. 16, no. 8, pp. 949–956, 2015.

[37] G. Germano *et al.*, "Role of Macrophage Targeting in the Antitumor Activity of Trabectedin," *Cancer Cell*, vol. 23, no. 2, pp. 249–262, 2013.

[38] A. N. Barclay and T. K. van den Berg, " The Interaction Between Signal Regulatory Protein Alpha (SIRP α) and CD47: Structure, Function, and Therapeutic Target ," *Annu. Rev. Immunol.*, vol. 32, no. 1, pp. 25–50, 2014.

[39] S. Kaczanowska, A. M. Joseph, and E. Davila, " TLR agonists: our best frenemy in cancer immunotherapy ," *J. Leukoc. Biol.*, vol. 93, no. 6, pp. 847–863, 2013.

[40] G. Van Kooten and J. Banchereau, "CD40-CD40 ligand," *J. Leukoc. Biol.*, vol. 67, no. 1, pp. 2–17, 2000.

[41] R. H. Vonderheide *et al.*, "Clinical activity and immune modulation in cancer patients treated with CP-870,893, a novel CD40 agonist monoclonal antibody," *J. Clin. Oncol.*, vol. 25, no. 7, pp. 876–883, 2007.

[42] R. H. Vonderheide *et al.*, "Phase i study of the CD40 agonist antibody CP-870,893 combined with carboplatin and paclitaxel in patients with advanced solid tumors," *Oncoimmunology*, vol. 2, no. 1, 2013.

[43] B. Teizo Yoshimura, E. A. Robinson, S. Tanaka, I. Ettore Appella, I. Jun-ichi Kuratsu, and E. J. Leonard, "Purification and amino acid analysis of two human glioma-derived monocyte chemoattractants," *J. Exp. Med.*, pp. 1449–1459, 1989.

[44] B. Kouji Matsushima, C. G. Larsen, G. C. DuBOIS, and J. J. Oppenheim, "Purification and

characterization of a novel monocyte chemotactic and activating factor produced by a human myelomonocytic cell line," 1989.

[45] S. K. Sandhu *et al.*, "A first-in-human, first-in-class, phase i study of carlumab (CNTO 888), a human monoclonal antibody against CC-chemokine ligand 2 in patients with solid tumors," *Cancer Chemother. Pharmacol.*, vol. 71, no. 4, pp. 1041–1050, Apr. 2013.

[46] I. Brana *et al.*, "Carlumab, an anti-C-C chemokine ligand 2 monoclonal antibody, in combination with four chemotherapy regimens for the treatment of patients with solid tumors: an open-label, multicenter phase 1b study," *Target. Oncol.*, vol. 10, no. 1, pp. 111–123, 2015.

[47] K. J. Pienta *et al.*, "Phase 2 study of carlumab (CNTO 888), a human monoclonal antibody against CC-chemokine ligand 2 (CCL2), in metastatic castration-resistant prostate cancer," *Invest. New Drugs*, vol. 31, no. 3, pp. 760–768, Jun. 2013.

[48] T. M. Nywening *et al.*, "Phase 1b study targeting tumour associated macrophages with CCR2 inhibition plus FOLFIRINOX in locally advanced and borderline resectable pancreatic cancer HHS Public Access," *Lancet Oncol*, vol. 17, no. 5, pp. 651–662, 2016.

[49] D. Linehan *et al.*, "Overall survival in a trial of orally administered CCR2 inhibitor CCX872 in locally advanced/metastatic pancreatic cancer, Correlation with blood monocyte counts.," *J Clin Oncol*, vol. 36, no. 92, 2018.

[50] J. S. Lewis, R. J. Landers, J. C. E. Underwood, A. L. Harris, and C. E. Lewis, "Expression of vascular endothelial growth factor by macrophages is up-regulated in poorly vascularized areas of breast carcinomas," *J. Pathol.*, vol. 192, pp. 150–158, Jan. 2000.

[51] R. D. Leek, N. C. Hunt, R. J. Landers, C. E. Lewis, J. A. Royds, and A. L. Harris, "Macrophage infiltration is associated with VEGF and EGFR expression in breast cancer," *J. Pathol.*, vol. 190, no. 4, pp. 430–436, Mar. 2000.

[52] S. Matschurat *et al.*, "Regulation of EMAP II by hypoxia," *Am. J. Pathol.*, vol. 162, no. 1, pp. 93–103, 2003.

[53] M. J. Grimshaw, J. L. Wilson, and F. R. Balkwill, "Endothelin-2 is a macrophage chemoattractant: Implications for macrophage distribution in tumors," *Eur. J. Immunol.*, vol. 32, no. 9, pp. 2393–2400, 2002.

[54] A. Casazza *et al.*, "Impeding Macrophage Entry into Hypoxic Tumor Areas by Sema3A/Nrp1 Signaling Blockade Inhibits Angiogenesis and Restores Antitumor Immunity," *Cancer Cell*, vol. 24, no. 6, pp. 695–709, Dec. 2013.

[55] R. Du *et al.*, "Hif1alpha Induces the Recruitment of Bone Marrow-Derived Vascular Modulatory Cells to Regulate Tumor Angiogenesis and Invasion," *Cancer Cell*, vol. 13, no. 3, pp. 206–220, 2008.

[56] C. Tripathi *et al.*, "Macrophages are recruited to hypoxic tumor areas and acquire a Pro-Angiogenic

M2-Polarized phenotype via hypoxic cancer cell derived cytokines Oncostatin M and Eotaxin," *Oncotarget*, vol. 5, no. 14, pp. 5350–5368, 2014.

[57] C. Murdoch, A. Giannoudis, and C. E. Lewis, "Mechanisms regulating the recruitment of macrophages into hypoxic areas of tumors and other ischemic tissues," *Blood*, vol. 104, no. 8, pp. 2224–2234, 2004.

[58] X. Zhang and D. M. Mosser, "Macrophage activation by endogenous danger signals," *J Pathol.*, vol. 214, no. 2, pp. 161–178, 2008.

[59] M. C. Bosco, G. Reffo, M. Puppo, and L. Varesio, "Hypoxia inhibits the expression of the CCR5 chemokine receptor in macrophages," *Cell. Immunol.*, vol. 228, no. 1, pp. 1–7, Mar. 2004.

[60] A. Sica *et al.*, "Defective Expression of the Monocyte Chemotactic Protein-1 Receptor CCR2 in Macrophages Associated with Human Ovarian Carcinoma," *J. Immunol.*, vol. 164, no. 2, pp. 733–738, 2000.

[61] M. N. Ajuebor *et al.*, "Endogenous monocyte chemoattractant protein-1 recruits monocytes in the zymosan peritonitis model," *J. Leukoc. Biol.*, vol. 63, no. 1, pp. 108–116, 1998.

[62] J. Zhang, L. Patel, and K. J. Pienta, "Targeting chemokine (C-C motif) Ligand 2 (CCL2) as an example of translation of cancer molecular biology to the clinic," in *Progress in Molecular Biology and Translational Science*, vol. 95, no. C, Elsevier B.V., 2010, pp. 31–53.

[63] T. Yoshimura, "The chemokine MCP-1 (CCL2) in the host interaction with cancer: A foe or ally?," *Cellular and Molecular Immunology*, vol. 15, no. 4. Chinese Soc Immunology, pp. 335–345, 01-Apr-2018.

[64] S. Prasad, J. Ravindran, and B. B. Aggarwal, "NF-κB and cancer: how intimate is this relationship," *Mol Cell Biochem.*, vol. 336, no. 1–2, pp. 25–37, 2010.

[65] J. F. Zhu, A. J. Valente, J. A. Lorenzo, D. Carnes, and D. T. Graves, "Expression of monocyte chemoattractant protein 1 in human osteoblastic cells stimulated by proinflammatory mediators.," *J Bone Min. Res*, vol. 9, no. 7, pp. 1123–1130, 1994.

[66] S. L. Deshmane, S. Kremlev, S. Amini, and B. E. Sawaya, "Monocyte chemoattractant protein-1 (MCP-1): An overview," *J. Interf. Cytokine Res.*, vol. 29, no. 6, pp. 313–325, 2009.

[67] R. J. Phillips, M. Lutz, and B. Premack, "Differential signaling mechanisms regulate expression of CC chemokine receptor-2 during monocyte maturation," *J. Inflamm.*, vol. 2, pp. 1–14, 2005.

[68] J. Corbisier, C. L. Galès, A. Huszagh, M. Parmentier, and J. Y. Springael, "Biased signaling at chemokine receptors," *J. Biol. Chem.*, vol. 290, no. 15, pp. 9542–9554, 2015.

[69] I. F. Charo, S. J. Myers, A. Herman, C. Franci, A. J. Connollytt, and S. R. Coughlint, "Molecular cloning and functional expression of two monocyte chemoattractant protein 1 receptors reveals alternative splicing of the carboxyl-terminal tails (chemokines/chemotadxs/seven-transmembrane-

domain receptor),” 1994.

[70] S. P. M. Dubois, D. Palmer, M. L. Webb, and J. A. Ledbetter, “Early signal transduction by the receptor to the chemokine monocyte chemotactic protein-1 in a murine T cell hybrid,” *J. Immunol.*, vol. 156, pp. 1356–1361, 1996.

[71] N. Ashida, H. Arai, M. Yamasaki, and T. Kita, “Distinct Signaling Pathways for MCP-1-dependent Integrin Activation and Chemotaxis,” *J. Biol. Chem.*, vol. 276, no. 19, pp. 16555–16560, May 2001.

[72] B. Qian *et al.*, “CCL2 recruits inflammatory monocytes to facilitate breast tumor metastasis,” *Nature*, vol. 475, no. 7355, pp. 222–225, 2011.

[73] K. Mizutani *et al.*, “The chemokine CCL2 increases prostate tumor growth and bone metastasis through macrophage and osteoclast recruitment,” *Neoplasia*, vol. 11, no. 11, pp. 1235–1242, 2009.

[74] R. P. M. Negus *et al.*, “The detection and localization of monocyte chemoattractant protein-1 (MCP-1) in human ovarian cancer,” *J. Clin. Invest.*, vol. 95, no. 5, pp. 2391–2396, 1995.

[75] D. A. Arenberg *et al.*, “Macrophage infiltration in human non-small-cell lung cancer: The role of CC chemokines,” *Cancer Immunol. Immunother.*, vol. 49, no. 2, pp. 63–70, 2000.

[76] E. Sierra-Filardi *et al.*, “CCL2 Shapes Macrophage Polarization by GM-CSF and M-CSF: Identification of CCL2/CCR2-Dependent Gene Expression Profile,” *J. Immunol.*, vol. 192, no. 8, pp. 3858–3867, Apr. 2014.

[77] R. D. Loberg *et al.*, “Targeting CCL2 with systemic delivery of neutralizing antibodies induces prostate cancer tumor regression in vivo,” *Cancer Res.*, vol. 67, no. 19, pp. 9417–9424, 2007.

[78] Z. G. Fridlender *et al.*, “Monocyte chemoattractant protein-1 blockade inhibits lung cancer tumor growth by altering macrophage phenotype and activating CD8+ cells,” *Am. J. Respir. Cell Mol. Biol.*, vol. 44, no. 2, pp. 230–237, 2011.

[79] X. Lu and Y. Kang, “Chemokine (C-C Motif) ligand 2 engages CCR2+ stromal cells of monocytic origin to promote breast cancer metastasis to lung and bone,” *J. Biol. Chem.*, vol. 284, no. 42, pp. 29087–29096, 2009.

[80] R. Arakaki *et al.*, “CCL2 as a potential therapeutic target for clear cell renal cell carcinoma,” *Cancer Med.*, vol. 5, no. 10, pp. 2920–2933, 2016.

[81] K. Yoshinaga *et al.*, “Ig L-chain shuffling for affinity maturation of phage library-derived human anti-human MCP-1 antibody blocking its chemotactic activity,” *J. Biochem.*, vol. 143, no. 5, pp. 593–601, 2008.

[82] J. J. Haringman *et al.*, “A randomized controlled trial with an anti-CCL2 (anti-monocyte chemotactic protein 1) monoclonal antibody in patients with rheumatoid arthritis,” *Arthritis Rheum.*, vol. 54, no. 8, pp. 2387–2392, 2006.

[83] F. Moisan *et al.*, “Enhancement of paclitaxel and carboplatin therapies byCCL2 blockade in ovarian cancers,” *Mol. Oncol.*, vol. 8, no. 7, pp. 1231–1239, 2014.

[84] S. Takagi, T. Hirata, K. Agata, M. Mochii, G. Eguchi, and H. . Fujisawa, “The A5 antigen, a candidate for the neuronal recognition mole- cule, has homologies to complement components and coagulation factors.,” *Neuron*, vol. 7, pp. 295–307, 1991.

[85] G. Beckmann and P. Bork, “An adhesive domain detected in functionally diverse receptors.,” *Trends Biochem Sci*, vol. 18, pp. 40–41, 1993.

[86] S. Roy, A. K. Bag, R. K. Singh, J. E. Talmadge, S. K. Batra, and K. Datta, “Multifaceted role of neuropilins in the immune system: Potential targets for immunotherapy,” *Front. Immunol.*, vol. 8, no. OCT, pp. 1–27, 2017.

[87] B. A. Appleton *et al.*, “Structural studies of neuropilin/antibody complexes provide insights into semaphorin and VEGF binding,” *EMBO J.*, vol. 26, no. 23, pp. 4902–4912, Nov. 2007.

[88] C. Pellet-many, P. Frankel, H. Jia, and I. Zachary, “Neuropilins : structure , function and role in disease,” *Biochem. J.*, vol. 411, pp. 211–226, 2008.

[89] Z. He and M. Tessier-Lavigne, “Neuropilin is a receptor for the axonal chemorepellent semaphorin III,” *Cell*, vol. 90, no. 4, pp. 739–751, 1997.

[90] H. Gitay-Goren *et al.*, “Selective binding of VEGF121 to one of the three vascular endothelial growth factor receptors of vascular endothelial cells,” *J. Biol. Chem.*, vol. 271, no. 10, pp. 5519–5523, 1996.

[91] A. M. Jubb, L. A. Strickland, S. D. Liu, J. Mak, M. Schmidt, and H. Koeppen, “Neuropilin-1 expression in cancer and development,” *J. Pathol.*, vol. 226, no. 1, pp. 50–60, Jan. 2012.

[92] A. Patnaik *et al.*, “A Phase Ib study evaluating MNRP1685A, a fully human anti-NRP1 monoclonal antibody, in combination with bevacizumab and paclitaxel in patients with advanced solid tumors,” *Cancer Chemother. Pharmacol.*, vol. 73, no. 5, pp. 951–960, 2014.

[93] X. J. Chen *et al.*, “The role of the hypoxia-Nrp-1 axis in the activation of M2-like tumor-associated macrophages in the tumor microenvironment of cervical cancer,” *Mol. Carcinog.*, vol. 58, no. 3, pp. 388–397, Mar. 2019.

[94] G. Koehler and C. Milstein, “Continuous cultures of fused cells secreting antibody of predefined specificity,” *Nature*, vol. 256, pp. 495–497, 1975.

[95] F. A. Harding, M. M. Stickler, J. Razo, and R. B. DuBridge, “The immunogenicity of humanized and fully human antibodies: Residual immunogenicity resides in the CDR regions,” *MAbs*, vol. 2, no. 3, pp. 256–265, 2010.

[96] G. P. Smith, “Filamentous Fusion Phage: Novel Expression Vectors That Display Cloned Antigens on the Virion Surface,” *Science (80-.).*, vol. 228, pp. 1315–1316, 1985.

[97] M. A. A. Persson, R. H. Caothien, and D. R. Burton, “Generation of diverse high-affinity human monoclonal antibodies by repertoire cloning,” *Proc. Natl. Acad. Sci. U. S. A.*, vol. 88, no. 6, pp. 2432–2436, 1991.

[98] R. Kontermann and S. Dübel, *Antibody Engineering*, Second edi. Berlin, Heidelberg: Springer Verlag, 2010.

[99] A. Knappik *et al.*, “Fully synthetic human combinatorial antibody libraries (HuCAL) based on modular consensus frameworks and CDRs randomized with trinucleotides,” *J. Mol. Biol.*, vol. 296, no. 1, pp. 57–86, 2000.

[100] C. E. Z. Chan, A. P. C. Lim, P. A. MacAry, and B. J. Hanson, “The role of phage display in therapeutic antibody discovery,” *Int. Immunol.*, vol. 26, no. 12, pp. 649–657, 2014.

[101] H. Kaplon and J. M. Reichert, “Antibodies to watch in 2019,” *MAbs*, vol. 11, no. 2, 2019.

[102] Antibody Society, “Antibody therapeutics approved or in regulatory review in the EU or US.” [Online]. Available: https://www.antibodysociety.org/resources/approved-antibodies/. [Accessed: 05-Nov-2019].

[103] J. Maynard and G. Georgiou, “Antibody engineering,” *Annu. Rev. Biomed. Eng.*, vol. 2, pp. 339–376, 2000.

[104] P. J. Carter, “Potent antibody therapeutics by design,” *Nature Reviews Immunology*, vol. 6, no. 5. pp. 343–357, May-2006.

[105] S. A. Rosenberg, P. Spiess, and R. Lafreniere, “A New Approach to the Adoptive Immunotherapy of Cancer with Tumor-Infiltrating Lymphocytes,” *Science (80-.).*, vol. 233, no. 4770, pp. 1318–1321, 1986.

[106] J. L. Jorgensen, P. A. Reay, E. W. Ehrich, and M. M. Davis, “Molecular components of T-cell recognition,” *Annu. Rev. Immunol*, vol. 10, pp. 835–873, 1992.

[107] M. Sadelain, I. Rivière, and S. Riddell, “Therapeutic T cell engineering,” *Nature*, vol. 545, no. 7655. Nature Publishing Group, pp. 423–431, 24-May-2017.

[108] G. Gross, T. Waks, and Z. Eshhar, “Expression of immunoglobulin-T-cell receptor chimeric molecules as functional receptors with antibody-type specificity,” *Proc. Natl. Acad. Sci. U. S. A.*, vol. 86, no. 24, pp. 10024–10028, 1989.

[109] Z. Eshhar, T. Waks, G. Gross, and D. G. Schindler, “Specific activation and targeting of cytotoxic lymphocytes through chimeric single chains consisting of antibody-binding domains and the γ or ζ subunits of the immunoglobulin and T-cell receptors,” *Proc. Natl. Acad. Sci. U. S. A.*, vol. 90, no. 2, pp. 720–724, 1993.

[110] A. D. Fesnak, C. H. June, and B. L. Levine, “Engineered T cells: The promise and challenges of cancer immunotherapy,” *Nat. Rev. Cancer*, vol. 16, no. 9, pp. 566–581, 2016.

[111] M. Sadelain, R. Brentjens, and I. Rivière, “The basic principles of chimeric antigen receptor design,” *Cancer Discov.*, vol. 3, no. 4, pp. 388–398, 2013.

[112] J. Maher, R. J. Brentjens, G. Gunset, I. Rivière, and M. Sadelain, “Human T-lymphocyte cytotoxicity and proliferation directed by a single chimeric TCRζ /CD28 receptor,” *Nat. Biotechnol.*, vol. 20, pp. 70–75, 2002.

[113] M. A. Pulè, K. C. Straathof, G. Dotti, H. E. Heslop, C. M. Rooney, and M. K. Brenner, “A chimeric T cell antigen receptor that augments cytokine release and supports clonal expansion of primary human T cells,” *Mol. Ther.*, vol. 12, no. 5, pp. 933–941, 2005.

[114] C. Imai *et al.*, “Chimeric receptors with 4-1BB signaling capacity provoke potent cytotoxicity against acute lymphoblastic leukemia,” *Leukemia*, vol. 18, no. 4, pp. 676–684, 2004.

[115] A. H. Long, H. W. M., J. F. Shern, K. M. Wanhainen, and E. Al., “4-1BB Costimulation Ameliorates T Cell Exhaustion Induced by Tonic Signaling of Chimeric Antigen Receptors,” *Nat Med.*, vol. 21, no. 6, pp. 581–590, 2015.

[116] M. C. Milone *et al.*, “Chimeric receptors containing CD137 signal transduction domains mediate enhanced survival of T cells and increased antileukemic efficacy in vivo,” *Mol. Ther.*, vol. 17, no. 8, pp. 1453–1464, 2009.

[117] R. J. Brentjens and K. J. Curran, “Novel cellular therapies for leukemia: CAR-modified T cells targeted to the CD19 antigen.,” *Hematology Am. Soc. Hematol. Educ. Program*, vol. 2012, pp. 143–151, 2012.

[118] M. Hudecek *et al.*, “Antigen Receptors Is Decisive for in Vivo Antitumor Activity,” *Cancer Immunol Res*, vol. 3, no. 2, pp. 125–135, 2015.

[119] R. D. Guest *et al.*, “The Role of Extracellular Spacer Regions in the Optimal Design of Chimeric Immune Receptors,” *J Immunother*, vol. 28, pp. 203–211, 2005.

[120] U. S. Food and Drug Administration, “Kymriah (tisagenlecleucel),” 2019. [Online]. Available: https://www.fda.gov/vaccines-blood-biologics/cellular-gene-therapy-products/kymriah-tisagenlecleucel. [Accessed: 21-Oct-2019].

[121] U. S. Food and Drug Administration, “Yescarta (axicabtagene ciloleucel),” 2018. [Online]. Available: https://www.fda.gov/vaccines-blood-biologics/cellular-gene-therapy-products/yescarta-axicabtagene-ciloleucel. [Accessed: 21-Oct-2019].

[122] M. M. Boyiadzis *et al.*, “Chimeric antigen receptor (CAR) T therapies for the treatment of hematologic malignancies: Clinical perspective and significance,” *J. Immunother. Cancer*, vol. 6, no. 1, pp. 1–12, 2018.

[123] S. L. Maude, N. Frey, P. Chaw, R. Aplenc, and E. Al., “Chimeric Antigen Receptor T Cells for Sustained Remissions in Leukemia,” *N. Engl. J. Med.*, vol. 371, no. 16, pp. 1507–1517, 2014.

[124] S. J. Schuster, J. Svoboda, E. A. Chong, S. D. Nasta, and E. Al., “Chimeric Antigen Receptor T Cells in Refractory B-Cell Lymphomas,” *N. Engl. J. Med.*, vol. 377, no. 26, pp. 2545–2554, 2017.

[125] S. S. Neelapu *et al.*, “Axicabtagene ciloleucel CAR T-cell therapy in refractory large B-Cell lymphoma,” *N. Engl. J. Med.*, vol. 377, no. 26, pp. 2531–2544, 2017.

[126] M. Ruella and M. V. Maus, “Catch me if you can: Leukemia Escape after CD19-Directed T Cell Immunotherapies,” *Comput. Struct. Biotechnol. J.*, vol. 14, pp. 357–362, 2016.

[127] J. Ereño-Orbea *et al.*, “Molecular basis of human CD22 function and therapeutic targeting,” *Nat. Commun.*, vol. 8, no. 764, pp. 1–11, 2017.

[128] F. Naeim, P. Nagesh Rao, S. X. Song, and R. T. Phan, *Atlas of Hematopathology*, Second. Academic Press, 2018.

[129] T. J. Fry *et al.*, “CD22-CAR T Cells Induce Remissions in CD19-CAR Naïve and Resistant B-ALL,” *Nat. Med.*, vol. 24, no. 1, pp. 20–28, 2018.

[130] M. A. Morgan and A. Schambach, “Engineering CAR-T Cells for Improved Function Against Solid Tumors,” *Front. Immunol.*, vol. 9, no. October, p. 2493, 2018.

[131] M. Chmielewski, C. Kopecky, A. A. Hombach, and H. Abken, “IL-12 release by engineered T cells expressing chimeric antigen receptors can effectively muster an antigen-independent macrophage response on tumor cells that have shut down tumor antigen expression,” *Cancer Res.*, vol. 71, no. 17, pp. 5697–5706, 2011.

[132] D. Chinnasamy *et al.*, “Local delivery of interleukin-12 using T cells targeting VEGF receptor-2 eradictaes multiple vascularized tumors in mice,” *Clin Cancer Res*, vol. 18, no. 6, pp. 1672–1683, 2012.

[133] B. Hu *et al.*, “CAR T Cells Secreting IL18 Augment Antitumor Immunity and Increase T Cell Proliferation and Costimulation,” *bioRxiv 111260 [Preprint]. https://doi.org/10.1101/111260*, 2017.

[134] M. P. Avanzi *et al.*, “Engineered Tumor-Targeted T Cells Mediate Enhanced Anti-Tumor Efficacy Both Directly and through Activation of the Endogenous Immune System,” *Cell Rep.*, vol. 23, no. 7, pp. 2130–2141, May 2018.

[135] G. Krenciute *et al.*, “Transgenic expression of IL15 improves antiglioma activity of IL13Rα2-CAR T cells but results in antigen loss variants,” *Cancer Immunol. Res.*, vol. 5, no. 7, pp. 571–581, 2017.

[136] L. V. Hurton *et al.*, “Tethered IL-15 augments antitumor activity and promotes a stem-cell memory subset in tumor-specific T cells,” *Proc. Natl. Acad. Sci. U. S. A.*, vol. 113, no. 48, pp. E7788–E7797, 2016.

[137] S. Rafiq *et al.*, “Targeted delivery of a PD-1-blocking scFV by CAR-T cells enhances anti-tumor efficacy in vivo,” *Nat. Biotechnol.*, vol. 36, no. 9, pp. 847–858, Oct. 2018.

[138] E. R. Suarez *et al.*, “Chimeric antigen receptor T cells secreting anti-PD-L1 antibodies more effectively regress renal cell carcinoma in a humanized mouse model,” *Oncotarget*, vol. 7, no. 23, pp. 34341–34355, 2016.

[139] Y. Yin *et al.*, “Checkpoint Blockade Reverses Anergy in IL-13Rα2 Humanized scFv-Based CAR T Cells to Treat Murine and Canine Gliomas,” *Mol. Ther. - Oncolytics*, vol. 11, pp. 20–38, Dec. 2018.

[140] R. L. Siegel, K. D. Miller, and A. Jemal, “Cancer statistics, 2019,” *CA Cancer J. Clin.*, vol. 69, no. 1, pp. 7–34, 2019.

[141] Y. Liu and S. K. Barta, “Diffuse large B-cell lymphoma: 2019 update on diagnosis, risk stratification, and treatment,” *Am. J. Hematol.*, vol. 94, no. 5, pp. 604–616, 2019.

[142] Shipp, “A predictive model for aggressive non-Hodgkins lymphoma,” *N. Engl. J. Med.*, vol. 329, no. 14, pp. 987–994, 1993.

[143] L. V. Pham, E. Pogue, and R. J. Ford, “The role of macrophage/B-cell interactions in the pathophysiology of B-cell lymphomas,” *Frontiers in Oncology*, vol. 8, no. MAY. Frontiers Media S.A., 08-May-2018.

[144] S. J. Schuster *et al.*, “Tisagenlecleucel in adult relapsed or refractory diffuse large B-cell lymphoma,” *N. Engl. J. Med.*, vol. 380, no. 1, pp. 45–56, Jan. 2019.

[145] T. Giavridis, S. J. C. Van Der Stegen, J. Eyquem, M. Hamieh, A. Piersigilli, and M. Sadelain, “CAR T cell-induced cytokine release syndrome is mediated by macrophages and abated by IL-1 blockade letter,” *Nat. Med.*, vol. 24, no. 6, pp. 731–738, 2018.

[146] F. Marchesi *et al.*, “High density of CD68+/CD163+ tumour-associated macrophages (M2-TAM) at diagnosis is significantly correlated to unfavorable prognostic factors and to poor clinical outcomes in patients with diffuse large B-cell lymphoma,” *Hematological Oncology*, vol. 33, no. 2. John Wiley and Sons Ltd, pp. 110–112, 01-Jun-2015.

[147] H. Ji *et al.*, “Ratio of Immune Response to Tumor Burden Predicts Survival Via Regulating Functions of Lymphocytes and Monocytes in Diffuse Large B-Cell Lymphoma,” *Cell. Physiol. Biochem.*, vol. 45, no. 3, pp. 951–961, Feb. 2018.

[148] G. Lenz *et al.*, “Stromal Gene Signatures in Large-B-Cell Lymphomas,” 2008.

[149] T. Tadmor *et al.*, “Monocyte count at diagnosis is a prognostic parameter in diffuse large B-cell lymphoma: Results from a large multicenter study involving 1191 patients in the pre- and post-rituximab era,” *Haematologica*, vol. 99, no. 1, pp. 125–130, Jan. 2014.

[150] S. J. Nam *et al.*, “Prognostic implications of tumor-infiltrating macrophages, M2 macrophages, regulatory T-cells, and indoleamine 2,3-dioxygenase-positive cells in primary diffuse large B-cell lymphoma of the central nervous system,” *Oncoimmunology*, vol. 7, no. 7, pp. 1–12, 2018.

[151] Y. L. Li, Z. H. Shi, X. Wang, K. S. Gu, and Z. min Zhai, “Prognostic significance of monocyte

chemoattractant protein-1 and CC chemokine receptor 2 in diffuse large B cell lymphoma," *Ann. Hematol.*, vol. 98, no. 2, pp. 413–422, Feb. 2019.

[152] P. Diebolder *et al.*, "Generation of LYmph Node Derived Antibody Libraries (LYNDAL) for selecting fully human antibody fragments with therapeutic potential," *MAbs*, vol. 6, no. 1, pp. 130–142, Jan. 2014.

[153] J. Schindelin *et al.*, "Fiji: An open-source platform for biological-image analysis," *Nature Methods*, vol. 9, no. 7. pp. 676–682, Jul-2012.

[154] X. Brochet, M. P. Lefranc, and V. Giudicelli, "IMGT/V-QUEST: the highly customized and integrated system for IG and TR standardized V-J and V-D-J sequence analysis.," *Nucleic Acids Res.*, vol. 36, no. Web Server issue, pp. 503–508, 2008.

[155] I. Retter, H. H. Althaus, R. Münch, and W. Müller, "VBASE2, an integrative V gene database," *Nucleic Acids Res.*, vol. 33, no. DATABASE ISS., pp. 671–674, 2005.

[156] J. Kügler *et al.*, "Generation and analysis of the improved human HAL9/10 antibody phage display libraries," *BMC Biotechnol.*, vol. 15, no. 1, Feb. 2015.

[157] C. D. Paavola *et al.*, "Monomeric Monocyte Chemoattractant Protein-1 (MCP-1) Binds and Activates the MCP-1 Receptor CCR2B*," *J. Biol. Chem.*, 1998.

[158] J. Krauss, M. A. E. Arndt, A. C. R. Martin, H. Liu, and S. M. Rybak, "Specificity grafting of human antibody frameworks selected from a phage display library: generation of a highly stable humanized anti-CD22 single-chain Fv fragment," *Protein Eng. Des. Sel.*, vol. 16, no. 10, pp. 753–759, Oct. 2003.

[159] Novartis, "'Novartis receives European Commission approval of its CAR-T cell therapy, Kymriah® (tisagenlecleucel),'" 2018. [Online]. Available: https://www.novartis.com/news/media-releases/novartis-receives-european-commission-approval-its-car-t-cell-therapy-kymriah-tisagenlecleucel. [Accessed: 16-Sep-2019].

[160] C. Gu *et al.*, "Characterization of neuropilin-1 structural features that confer binding to semaphorin 3A and vascular endothelial growth factor 165," *J. Biol. Chem.*, vol. 277, no. 20, pp. 18069–18076, May 2002.

[161] B. J. C. Janssen, T. Malinauskas, G. A. Weir, M. Z. Cader, C. Siebold, and E. Y. Jones, "Neuropilins lock secreted semaphorins onto plexins in a ternary signaling complex," *Nat. Struct. Mol. Biol.*, vol. 19, no. 12, pp. 1293–1299, Dec. 2012.

[162] C. Gaboriaud, L. Gregory-Pauron, F. Teillet, N. M. Thielens, I. Bally, and Ǵerard J. Arlaud, "Structure and properties of the Ca 2+ -binding CUB domain, a widespread ligand-recognition unit involved in major biological functions," *Biochemical Journal*, vol. 439, no. 2. pp. 185–193, 15-Oct-2011.

[163] S. Hemmerich *et al.*, "Identification of residues in the monocyte chemotactic protein-1 that contact the MCP-1 receptor, CCR2," *Biochemistry*, vol. 38, no. 40, pp. 13013–13025, Oct. 1999.

[164] Y. Jiang, A. J. Valente, M. J. Williamson, L. Zhang, and D. T. Graves, “Post-translational modification of a monocyte-specific chemoattractant synthesized by glioma, osteosarcoma, and vascular smooth muscle cells,” *J. Biol. Chem.*, vol. 265, no. 30, pp. 18318–18321, 1990.

[165] B. J. Rollins, P. Stier, T. Ernst, and G. G. Wong, “The human homolog of the JE gene encodes a monocyte secretory protein.,” *Mol. Cell. Biol.*, vol. 9, no. 11, pp. 4687–4695, 1989.

[166] T. Tiller *et al.*, “A fully synthetic human Fab antibody library based on fixed VH/VL framework pairings with favorable biophysical properties,” *MAbs*, vol. 5, no. 3, pp. 445–470, 2013.

[167] Bethesda, “National Center for Biotechnology Information (NCBI), Protein Blast. Available from: https://www.ncbi.nlm.nih.gov/,” 1998. .

[168] M. H. Tao and S. L. Morrison, “Studies of aglycosylated mouse-human IgG. Role of carbohydrate in the structure and effector functions mediated by the human IgG constant region.,” *J. Immunol.*, vol. 143, pp. 2595–2601, 1989.

[169] S. Bolt *et al.*, “The generation of a humanized, non-mitogenic CD3 monoclonal antibody which retains in vitro immunosuppressive properties,” *Eur. J. Immunol.*, vol. 23, no. 2, pp. 403–411, 1993.

[170] A. J. Hoogewerf *et al.*, “Glycosaminoglycans Mediate Cell Surface Oligomerization of Chemokines,” *Biochemistry*, vol. 36, pp. 13570–13578, 1997.

[171] H. B. Fleit and C. D. Kobasiuk, “The human monocyte-like cell line THP-1 expresses Fc gamma RI and Fc gamma RII,” *J Leukoc Biol.*, vol. 49, no. 6, pp. 556–565, 1991.

[172] M. Steinwand, P. Droste, A. Frenzel, M. Hust, S. Dübel, and T. Schirrmann, “The influence of antibody fragment format on phage display based affinity maturation of IgG,” *MAbs*, vol. 6, no. 1, pp. 204–218, 2014.

[173] M. E. Kimple, A. L. Brill, and R. L. Pasker, “Overview of affinity tags for protein purification,” *Curr. Protoc. Protein Sci.*, no. SUPPL.73, pp. 608–616, 2013.

[174] B. D. Lipes, Y. Chen, H. Ma, H. F. Staats, D. J. Kenan, and M. D. Gunn, “An Entirely Cell-based System to Generate Single-Chain Antibodies Against Cell Surface Receptors,” *J Mol Biol.*, vol. 379, no. 2, pp. 261–272, 2008.

[175] D. M. Crothers and H. Metzger, “The influence of polyvalency on the binding properties of antibodies,” *Immunochemistry*, vol. 9, pp. 341–357, 1972.

[176] G. Vauquelin and S. J. Charlton, “Exploring avidity: Understanding the potential gains in functional affinity and target residence time of bivalent and heterobivalent ligands,” *Br. J. Pharmacol.*, vol. 168, no. 8, pp. 1771–1785, 2013.

[177] M. L. L. Donnelly, G. Luke, A. Mehrotra, X. Li, L. E. Hughwa, D. Gani and M. D. Ryan, “Analysis of the aphthovirus 2A/2B polyprotein ’ cleavage ’ mechanism indicates not a proteolytic reaction, but a novel translational effect : a putative ribosomal ’ skip ’,” *J Gen Virol*, vol. 82, pp. 1013-1026, 2001.

[178] Z. Liu *et al.*, “Systematic comparison of 2A peptides for cloning multi-genes in a polycistronic vector,” *Sci. Rep.*, vol. 7, no. 1, Dec. 2017.

[179] J. L. Owen *et al.*, “The expression of CCL2 by T lymphocytes of mammary tumor bearers: Role of tumor-derived factors,” *Cell. Immunol.*, vol. 235, no. 2, pp. 122–135, Jun. 2005.

[180] J. L. Owen, M. Torroella-Kouri, M. E. Handel-Fernandez, and V. Iragavarapu-Charyulu, “GM-CSF up-regulates the expression of CCL2 by T lymphocytes in mammary tumor-bearing mice,” *Int. J. Mol. Med.*, vol. 20, no. 1, pp. 129–136, 2007.

[181] D. Miotto *et al.*, “CC ligand 2 levels are increased in LPS-stimulated peripheral monocytes of patients with non-small cell lung cancer,” *Respir. Med.*, vol. 101, no. 8, pp. 1738–1743, 2007.

[182] M. Reale, C. Iarlori, C. Feliciani, and D. Gambi, “Peripheral chemokine receptors, their ligands, cytokines and Alzheimer’s disease,” *J. Alzheimer’s Dis.*, vol. 14, no. 2, pp. 147–159, 2008.

[183] A. Movafagh, H. Heydary, S. A. R. Mortazavi-Tabatabaei, and E. Azargashb, “The significance application of indigenous Phytohemagglutinin (PHA) mitogen on metaphase and cell culture procedure,” *Iran. J. Pharm. Res.*, vol. 10, no. 4, pp. 895–903, 2011.

[184] L. Alabanza *et al.*, “Function of Novel Anti-CD19 Chimeric Antigen Receptors with Human Variable Regions Is Affected by Hinge and Transmembrane Domains,” *Mol. Ther.*, vol. 25, no. 11, pp. 2452–2465, Nov. 2017.

[185] J. Zhou, L. Jin, F. Wang, Y. Zhang, B. Liu, and T. Zhao, “Chimeric antigen receptor T (CAR-T) cells expanded with IL-7/IL-15 mediate superior antitumor effects,” *Protein Cell*, 2019.

[186] A. Mantovani, F. Marchesi, A. Malesci, and L. Laghi, “Tumor-Associated Macrophages as Treatment Targets in Oncology,” *Nat Rev Clin Oncol*, vol. 14, no. 7, pp. 399–416, 2017.

[187] N. Guttmann-Raviv, O. Kessler, N. Shraga-Heled, T. Lange, Y. Herzog, and G. Neufeld, “The neuropilins and their role in tumorigenesis and tumor progression,” *Cancer Letters*, vol. 231, no. 1. pp. 1–11, 08-Jan-2006.

[188] W. C. Liang *et al.*, “Function Blocking Antibodies to Neuropilin-1 Generated from a Designed Human Synthetic Antibody Phage Library,” *J. Mol. Biol.*, vol. 366, no. 3, pp. 815–829, Feb. 2007.

[189] T. R. Poulsen, A. Jensen, J. S. Haurum, and P. S. Andersen, “Limits for Antibody Affinity Maturation and Repertoire Diversification in Hypervaccinated Humans,” *J. Immunol.*, vol. 187, no. 8, pp. 4229–4235, 2011.

[190] M. Tsuiji, K. Yurasov, K. Velizon, S. Thomas, M. C. Nussenzweig, and H. Wardemann, “A checkpoint for autoreactivity in human IgM+ memory B cell development,” *J Exp Med.*, vol. 203, no. 2, pp. 393–400, 2006.

[191] Y. Yip, N. Hawkins, M. Clark, and R. Ward, “Evaluation of different lymphoid tissue sources for the construction of human immunoglobulin gene libraries,” *Immunotechnology*, vol. 3, no. 3, pp. 195–

203, 1997.

[192] M. A. Oropallo and A. Cerutti, “Germinal center reaction: antigen affinity and presentation explain it all,” *Trends Immunol.*, vol. 35, no. 7, pp. 287–289, 2014.

[193] T. Tiller, M. Tsuiji, S. Yurasov, K. Velinzon, M. C. Nussenzweig, and H. Wardemann, “Autoreactivity in human IgG+ memory B cells,” *Immunity*, vol. 26, no. 2, pp. 205–213, 2007.

[194] J. M. Da Silva *et al.*, “Significance of chemokine and chemokine receptors in head and neck squamous cell carcinoma: A critical review,” *Oral Oncol.*, vol. 56, no. February 2019, pp. 8–16, 2016.

[195] R. Graham and M. . Karnovsky, “Glomerular permeability,” *J Exp. med*, vol. 124, no. 6, pp. 1123–1134, 1966.

[196] R. P. Junghans and C. L. Anderson, “The protection receptor for IgG catabolism is the beta2-microglobulin-containing neonatal intestinal transport receptor,” *Proc. Natl. Acad. Sci.*, vol. 93, pp. 5512–5516, 1996.

[197] K. O. Saunders, “Conceptual Approaches to Modulating Antibody Effector Functions and Circulation Half-Life,” *Front. Immunol.*, vol. 10, no. June, p. 1296, 2019.

[198] M. Tabasinezhad, Y. Talebkhan, W. Wenzel, H. Rahimi, E. Omidinia, and F. Mahboudi, “Trends in therapeutic antibody affinity maturation: From in-vitro towards next-generation sequencing approaches,” *Immunology Letters*, vol. 212. Elsevier B.V., pp. 106–113, 01-Aug-2019.

[199] X. Li, W. Yao, and Y. Yuan, “Targeting of tumour-infiltrating macrophages via CCL2/CCR2 signalling as a therapeutic strategy against hepatocellular carcinoma,” *Gut*, vol. 66, pp. 157–167, 2017.

[200] L. Djerbal, H. Lortat-Jacob, and J. Kwok, “Chondroitin sulfates and their binding molecules in the central nervous system,” *Glycoconj. J.*, vol. 34, no. 3, pp. 363–376, 2017.

[201] C. C. Liang, A. Y. Park, and J. L. Guan, “In vitro scratch assay: A convenient and inexpensive method for analysis of cell migration in vitro,” *Nat. Protoc.*, vol. 2, no. 2, pp. 329–333, 2007.

[202] Y. C. Chen, S. G. Allen, P. N. Ingram, R. Buckanovich, S. D. Merajver, and E. Yoon, “Single-cell migration chip for chemotaxis-based microfluidic selection of heterogeneous cell populations,” *Sci. Rep.*, vol. 5, no. March, pp. 1–13, 2015.

[203] M. R. Fein, X. He, A. S. Almeida, E. Bružas, A. Pommier, and R. Yan, “Cancer cell CCR2 orchestrates suppression of the adaptive immune response,” *Prepr. BioRxiv*, 2018.

[204] S. Y. Lim, A. E. Yuzhalin, A. N. Gordon-Weeks, and R. J. Muschel, “Targeting the CCL2-CCR2 signaling axis in cancer metastasis,” *Oncotarget*, vol. 7, no. 19, pp. 28697–28710, 2016.

[205] J. An, Y. Xue, M. Long, G. Zhang, J. Zhang, and H. Su, “Targeting CCR2 with its antagonist suppresses viability, motility and invasion by downregulating MMP-9 expression in non-small cell lung cancer cells,” *Oncotarget*, vol. 8, no. 24, pp. 39230–39240, 2017.

[206] C. U. Louis *et al.*, “Antitumor activity and long-term fate of chimeric antigen receptor-positive T cells in patients with neuroblastoma,” *Blood*, vol. 118, no. 23, pp. 6050–6056, 2011.

[207] O. Yeku, X. Li, and R. J. Brenjens, “Adoptive T-Cell Therapy for Solid Tumors Oladapo,” *Am Soc Clin Oncol Educ B.*, vol. 37, pp. 193–204, 2017.

[208] S. Mardiana, B. J. Solomon, P. K. Darcy, and P. A. Beavis, “Supercharging adoptive T cell therapy to overcome solid tumor-induced immunosuppression,” *Sci Transl Med*, vol. 11, no. 495, 2019.

[209] E. Peranzoni *et al.*, “Macrophages impede CD8 T cells from reaching tumor cells and limit the efficacy of anti–PD-1 treatment,” *Proc. Natl. Acad. Sci. U. S. A.*, vol. 115, no. 17, pp. E4041–E4050, 2018.

[210] H. A. Crissman and J. A. Steinkamp, “Rapid, simultaneous measurement of DNA, protein, and cell volume in single cells from large mammalian cell populations,” *J. Cell Biol.*, vol. 59, no. 3, pp. 766–771, 1973.

[211] Y. Liu, A. Beyer, and R. Aebersold, “On the Dependency of Cellular Protein Levels on mRNA Abundance,” *Cell*, vol. 165, no. 3, pp. 535–550, 2016.

[212] R. Sousa Abreu, L. O. Penalva, E. M. Marcotte, and C. Vogel, “Global signatures of protein and mRNA expression levels,” *Bone*, vol. 5, no. 12, pp. 1512–1526, 2009.

[213] S. Dietmair, M. P. Hodson, L. E. Quek, N. E. Timmins, P. Gray, and L. K. Nielsen, “A multi-omics analysis of recombinant protein production in Hek293 cells,” *PLoS One*, vol. 7, no. 8, 2012.

[214] T. Gargett *et al.*, “GD2-specific CAR T Cells Undergo Potent Activation and Deletion Following Antigen Encounter but can be Protected from Activation-induced Cell Death by PD-1 Blockade,” *Mol. Ther.*, vol. 24, no. 6, pp. 1135–1149, 2016.

[215] T. Kamiya, D. Wong, Y. T. Png, and D. Campana, “A novel method to generate T-cell receptor-deficient chimeric antigen receptor T cells,” *Blood Adv.*, vol. 2, no. 5, pp. 517–528, 2018.

[216] R. Weinkove, P. George, N. Dasyam, and A. D. McLellan, “Selecting costimulatory domains for chimeric antigen receptors: functional and clinical considerations,” *Clin. Transl. Immunol.*, vol. 8, no. 5, pp. 1–14, 2019.

[217] A. Rongvaux *et al.*, “Development and function of human innate immune cells in a humanized mouse model,” *Nat. Biotechnol.*, vol. 32, no. 4, pp. 364–372, 2014.

[218] K. S. M. Yong, Z. Her, and Q. Chen, “Humanized Mice as Unique Tools for Human-Specific Studies,” *Arch. Immunol. Ther. Exp. (Warsz).*, vol. 66, no. 4, pp. 245–266, 2018.

6 Appendix

6.1 Supplementary data

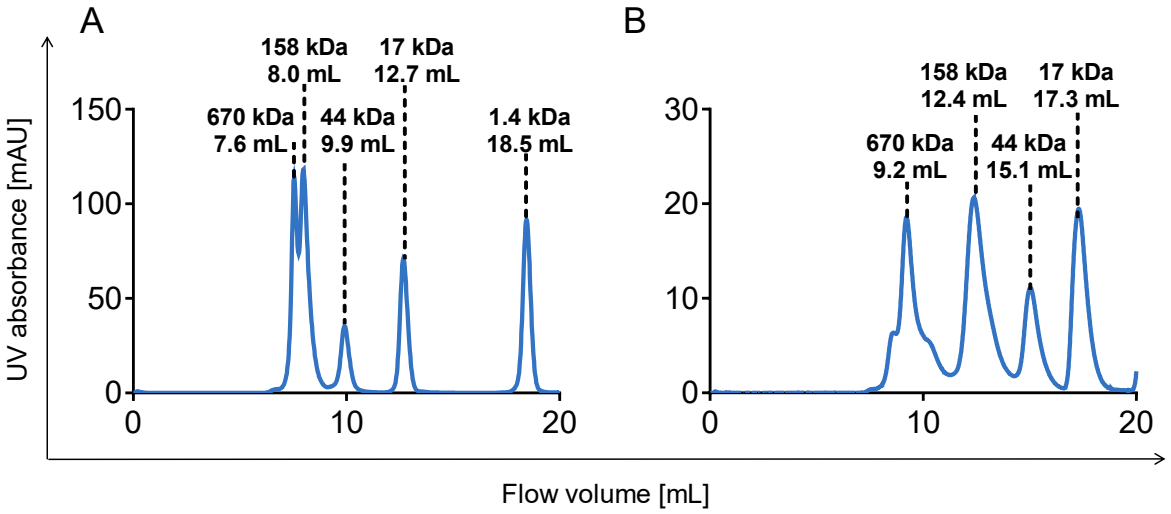

Figure 35. Protein standard used in size exclusion chromatography. A gel filtration standard with proteins of known molecular size was used to determine corresponding flow volumes by analytical SEC using a (A) Superdex 75 Increase 10/300 GL or (B) Superdex 200 Increase 10/300 GL column (performed by E. Exner).

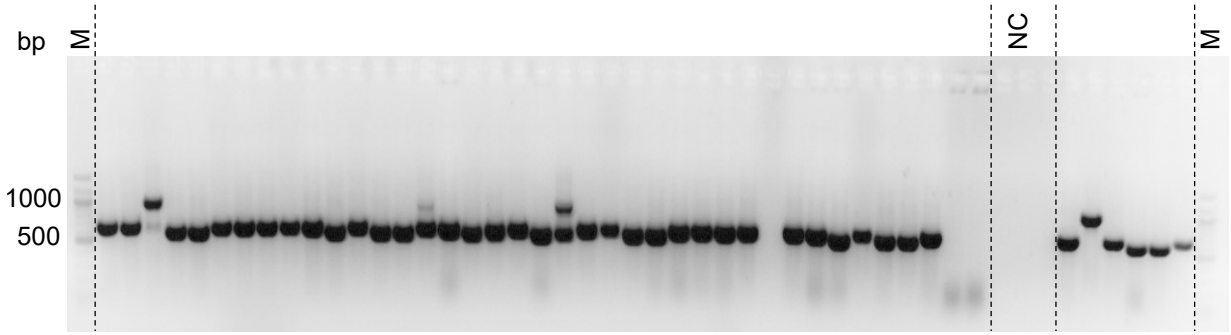

Figure 36. Analysis of NRP1-specific scFvs by colony PCR after the third round of phage display. *E. coli* TG1 were infected with phages after the third round of phage display. Individual clones were subjected to colony PCR with scFv sequence-specific primers and DNA was separated using agarose gel electrophoresis to identify clones carrying a full-length scFv sequence (corresponding to 1000 bp). A representative sample of a total of 110 colony PCRs is presented. M = marker, NC = negative control.

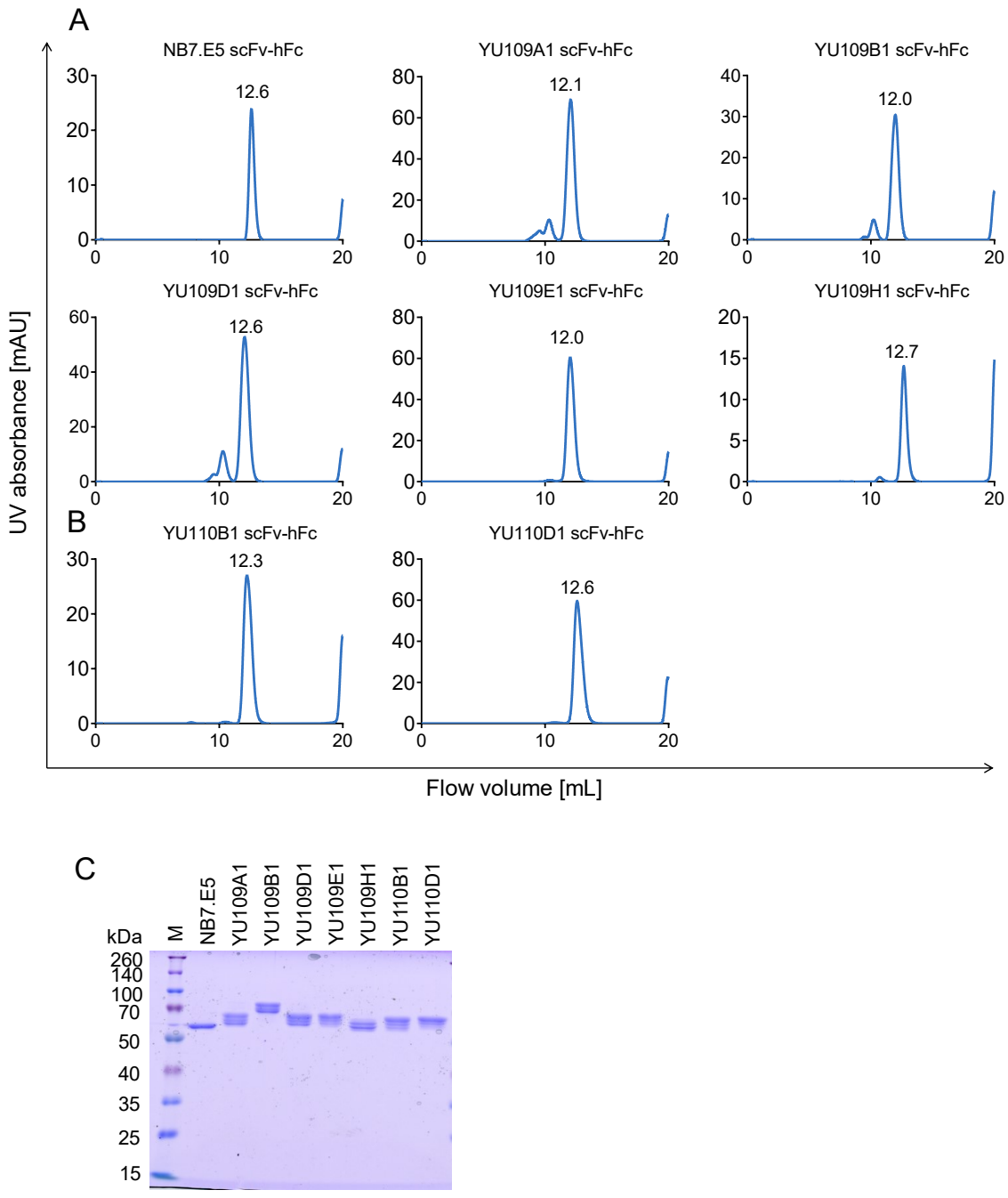

Figure 37. Investigation of scFv-hFc protein purity by analytical size exclusion chromatography and coomassie staining after SDS PAGE. Following Protein A affinity purification of the scFv-hFc antibodies the purity of the proteins was analyzed. Analytical SEC of (A) anti-CCL2 and (B) anti-NRP1 scFv-hFc antibodies was performed to investigate purity and protein aggregation. Elution volumes were compared to a standard protein run (*Appendix, Figure 35B*). (C) Antibodies were separated by SDS gel electrophoresis and visualized by coomassie staining. M = Marker.

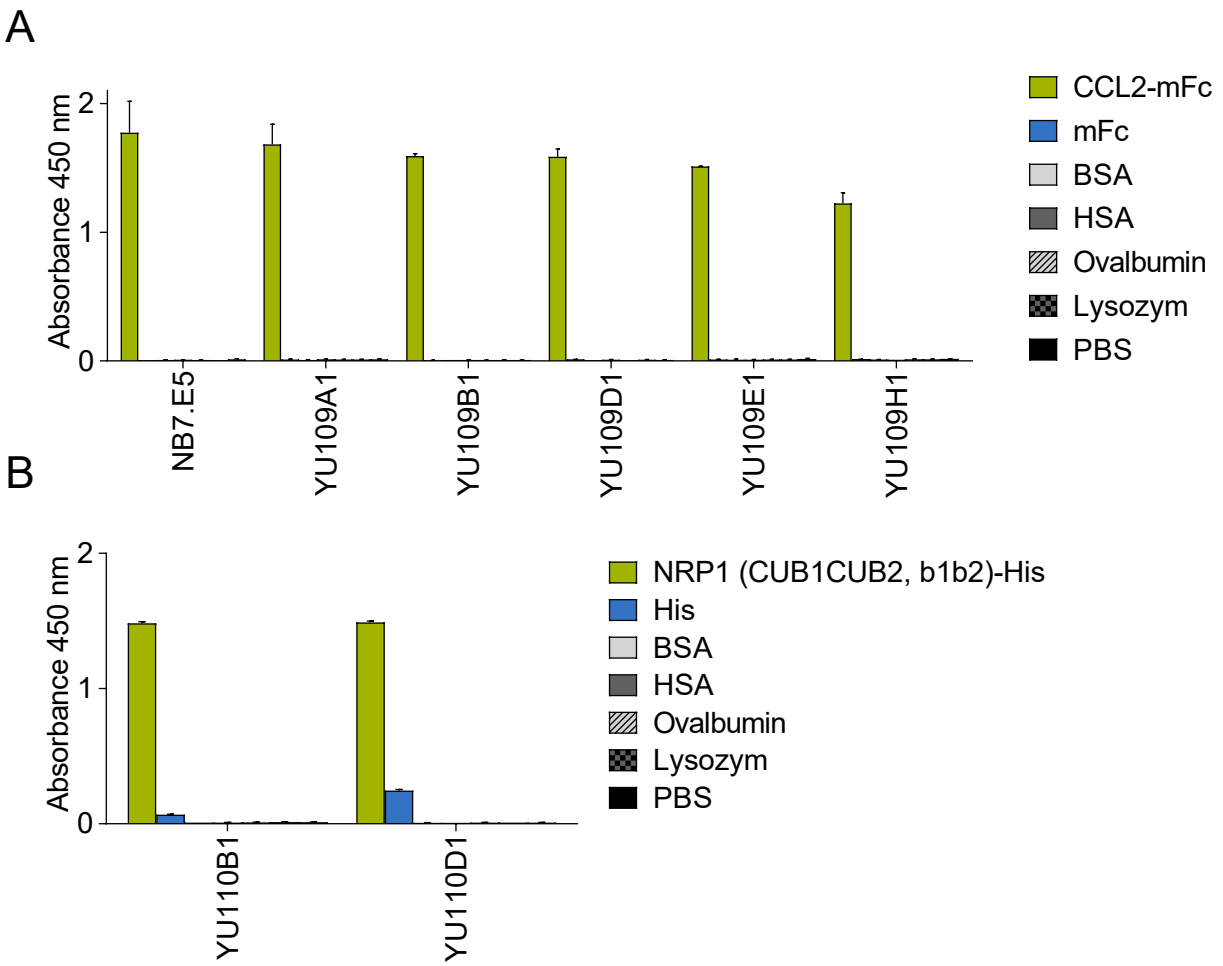

Figure 38. Binding analysis of scFv-hFc antibodies by ELISA. ELISA including a set of control proteins was carried out for (A) anti-CCL2 and (B) anti-NRP1 scFv-hFc antibodies. mFc and His were included since the proteins used for phage display selection were fused to one of these tags. His = scFv antibody fragment fused to a His tag. 10 µg/mL scFv-hFc were added to the wells of an antigen-coated ELISA plate. Bound scFv-hFc was detected using a HRP-conjugated mouse anti-human IgG antibody. Error bars represent the standard deviation of mean values of duplicates.

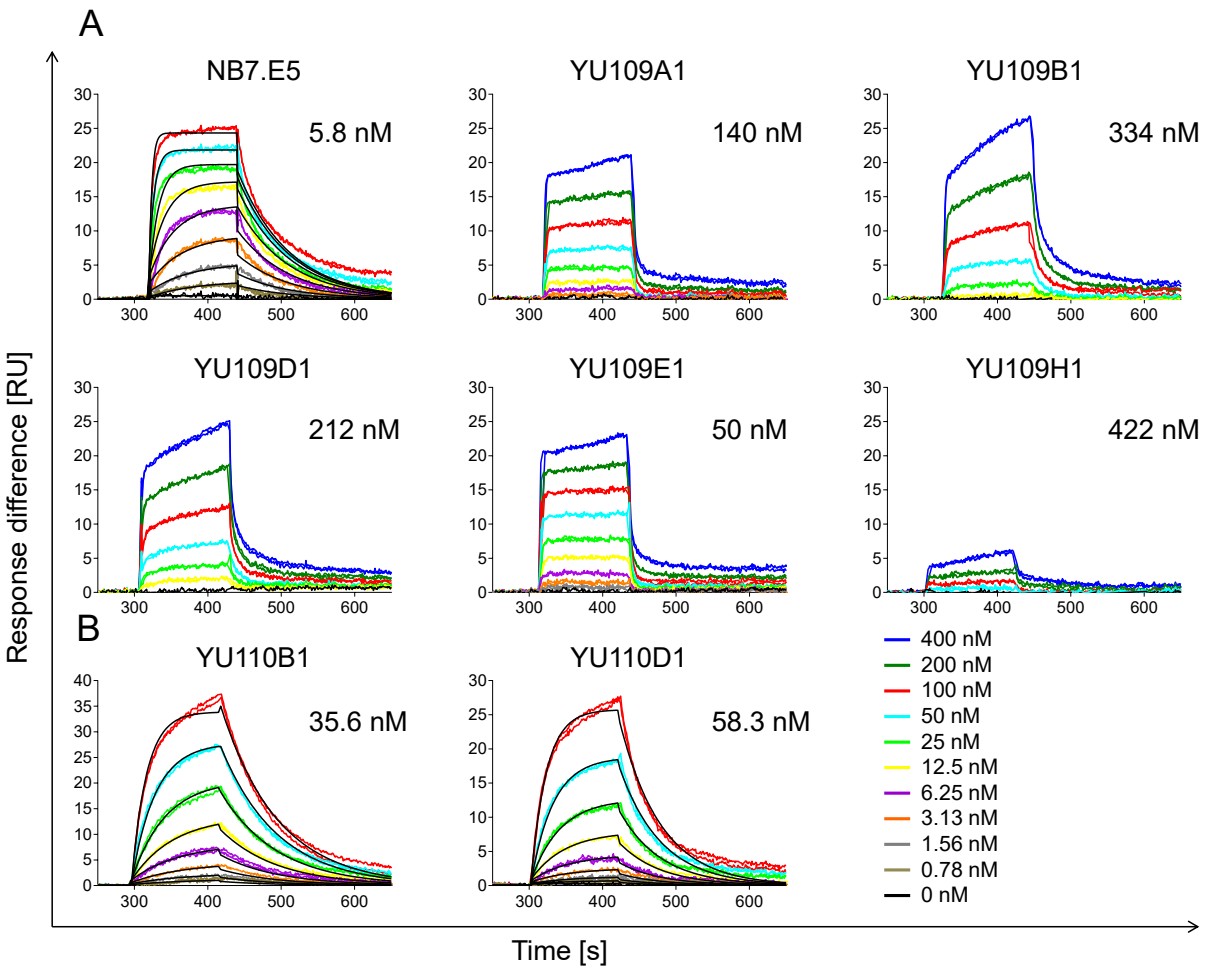

Figure 39. Characterization of binding kinetics of scFv-hFc antibodies by surface plasmon resonance analysis. Surface plasmon resonance analysis was performed to determine scFv-hFc affinity. (A) Anti-CCL2 and (B) anti-NRP1 scFv-hFcs were immobilized on a Protein A-coated sensorchip. An antigen concentration series ranging from 0 to up to 100 nM was tested. Black curves represent the 1:1 Langmuir binding model used to calculate antibody affinity. Due to very fast association and dissociation of YU109A1, YU109E1 and YU109H1, these kinetics were fitted using a steady state affinity model which only included the equilibrium phase. Numbers indicate the calculated K_D values in nM. Curves represent the mean of duplicates.

Table 29. Summary of the mathematical modeling of the scFv-hFc binding kinetics determined by surface plasmon resonance spectroscopy.

Antigen	scFv-hFc	K_D [nM]	Rmax [RU]	Chi^2
CCL2	NB7.E5	5.16	107	4.24
	YU109A1	64.5	101	0.08
	YU109B1	105	113	2.41
	YU109D1	64.2	73	1.73
	YU109E1	22.1	91	0.11
	YU109H1	nd	nd	nd
NRP1	YU110B1	27	72	1.31
	YU110D1	40.1	53	0.59

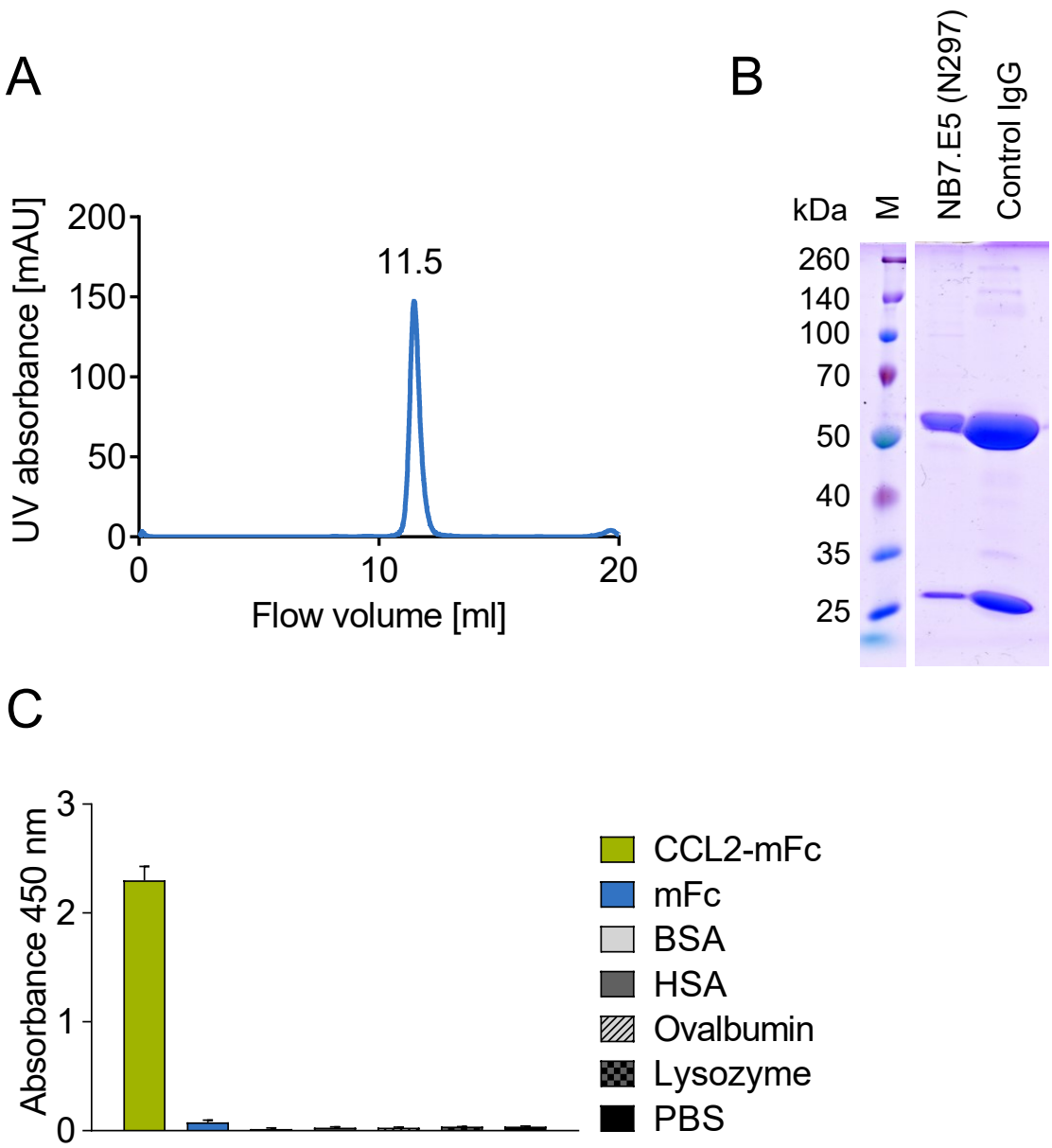

Figure 40. NB7.E5 (N297) IgG production, purification and binding analysis. After production of NB7.E5 (N297) IgG in HEK293-6E cells, the antibody was purified by Protein A affinity chromatography. The purity was further analyzed by (A) analytical size exclusion chromatography and (B) separation by SDS gel electrophoresis and visualization by coomassie staining. (C) Binding of NB7.E5 (N297) IgG to CCL2-mFc and a set of control proteins was investigated by ELISA. mFc was included as control since the protein used for phage display selection was fused to this tag. 10 µg/mL NB7.E5 (N297) IgG was added to the wells of an antigen-coated ELISA plate. Bound IgG was detected using a HRP-conjugated mouse anti-human IgG antibody. Error bars represent the standard deviation of mean values of duplicates.

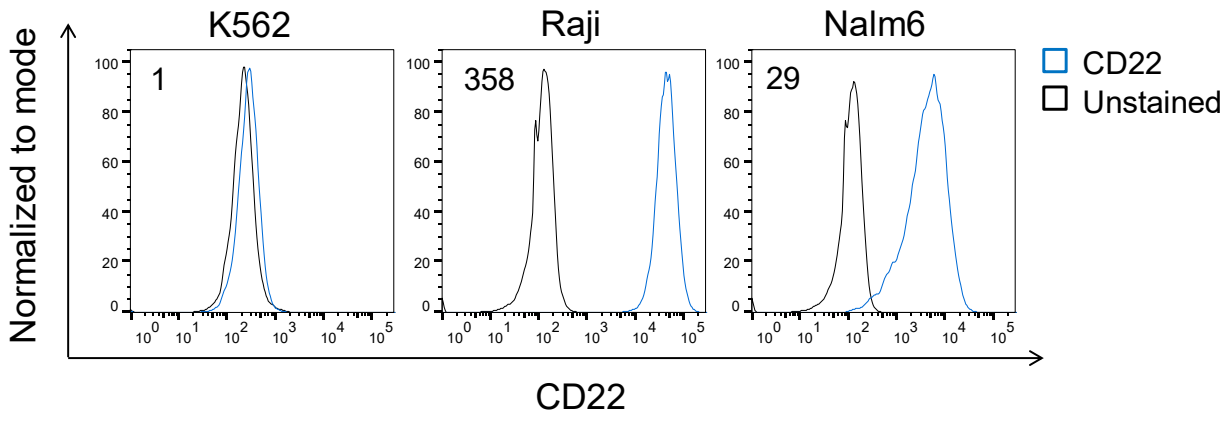

Figure 41. CD22 surface expression on the tumor cell lines K562, Raji and Nalm6. CD22 expression on the surface of K562, Raji and Nalm6 cells was analyzed by flow cytometry. Cells were stained with a PE-conjugated anti-CD22 antibody. Numbers indicate the ratio of CD22 stained to unstained.

6.2 Vector maps

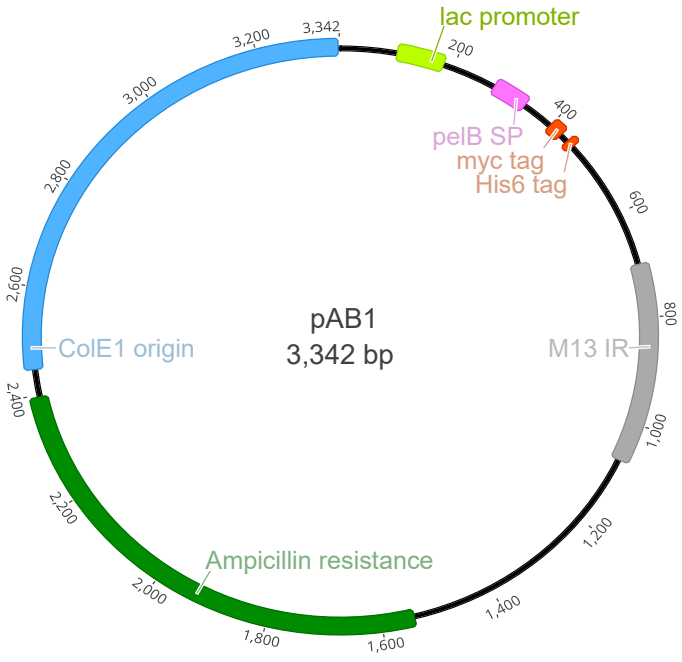

Figure 42. Map of the bacterial expression vector pAB1.

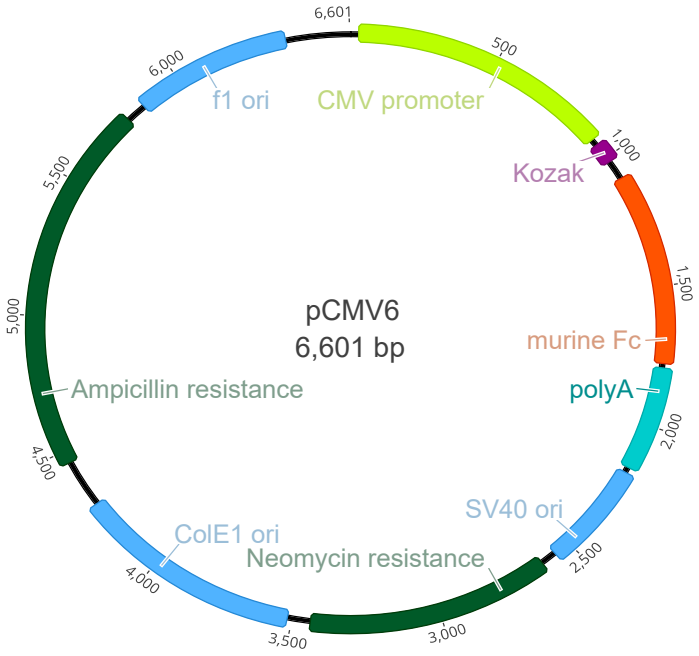

Figure 43. Map of the mammalian expression vector pCMV6.

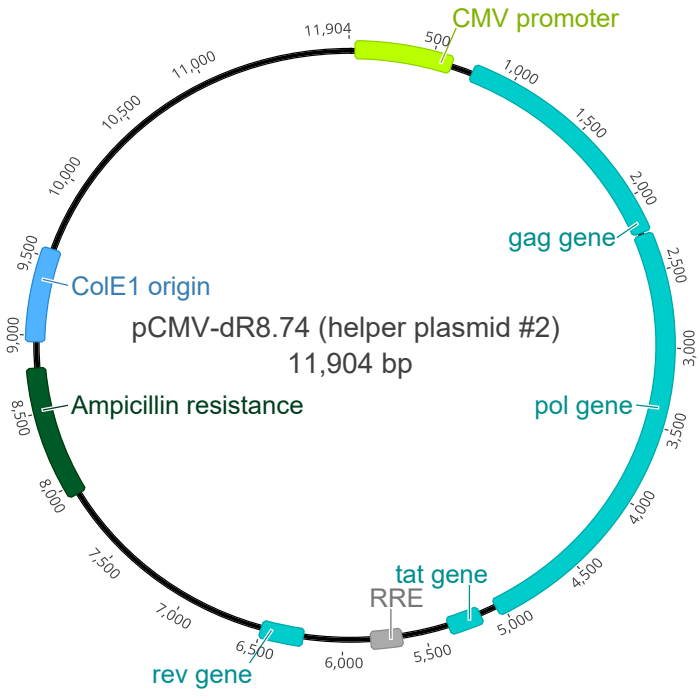

Figure 44. Map of the lentiviral helper plasmid pCMV-dR8.74 (helper plasmid #2).

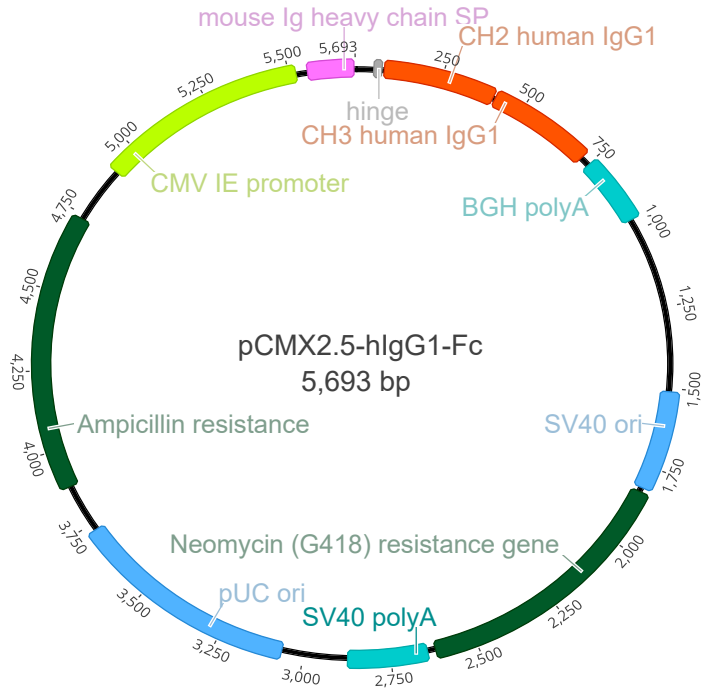

Figure 45. Map of the mammalian expression vector pCMX2.5-hIgG1-Fc.

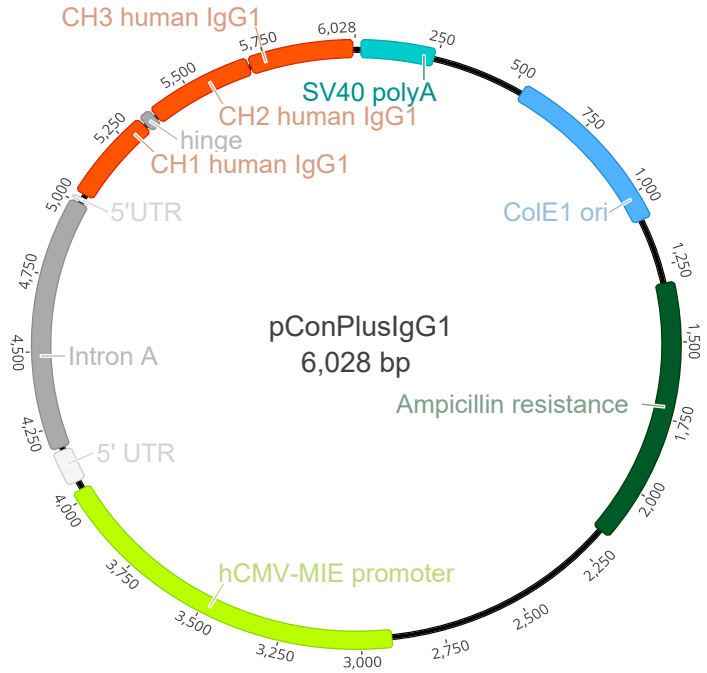

Figure 46. Map of the mammalian expression vector pConPlusIgG1.

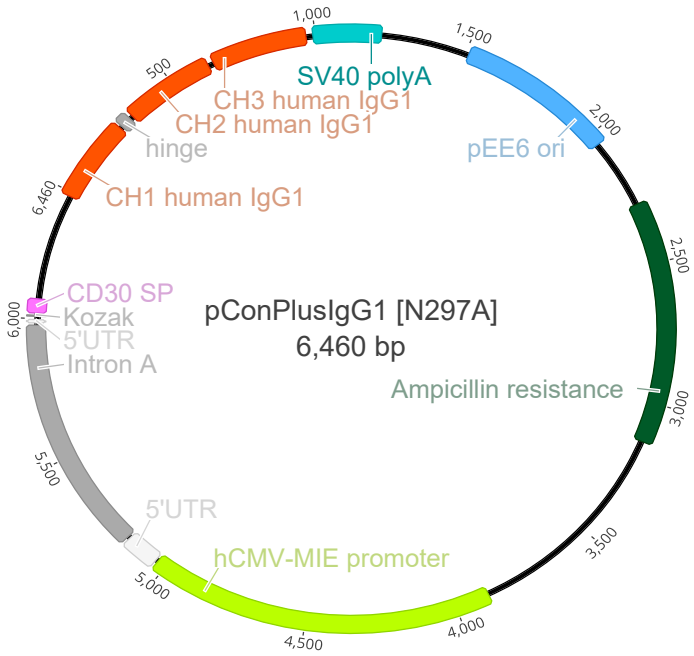

Figure 47. Map of the mammalian expression vector pConPlusIgG1 [N297A].

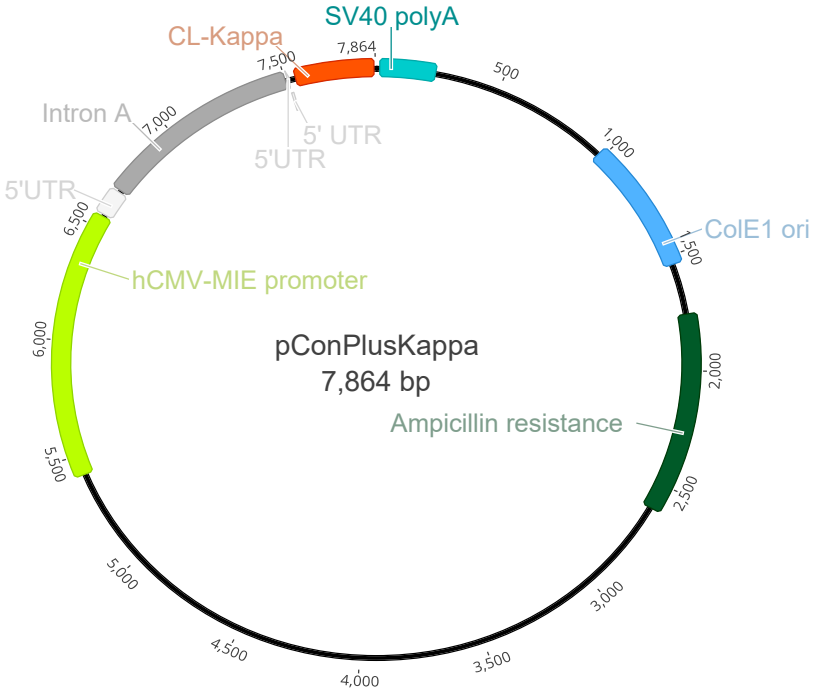

Figure 48. Map of the mammalian expression vector pConPlusKappa.

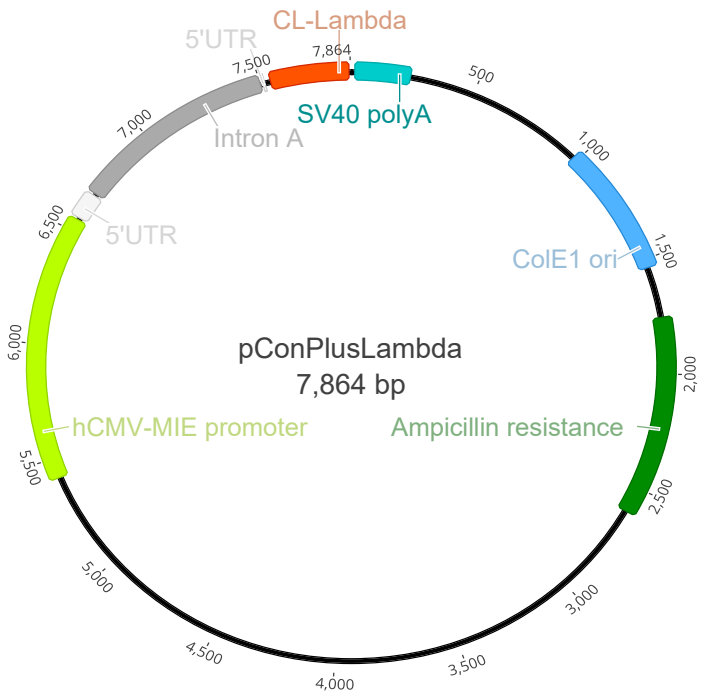

Figure 49. Map of the mammalian expression vector pConPlusLambda.

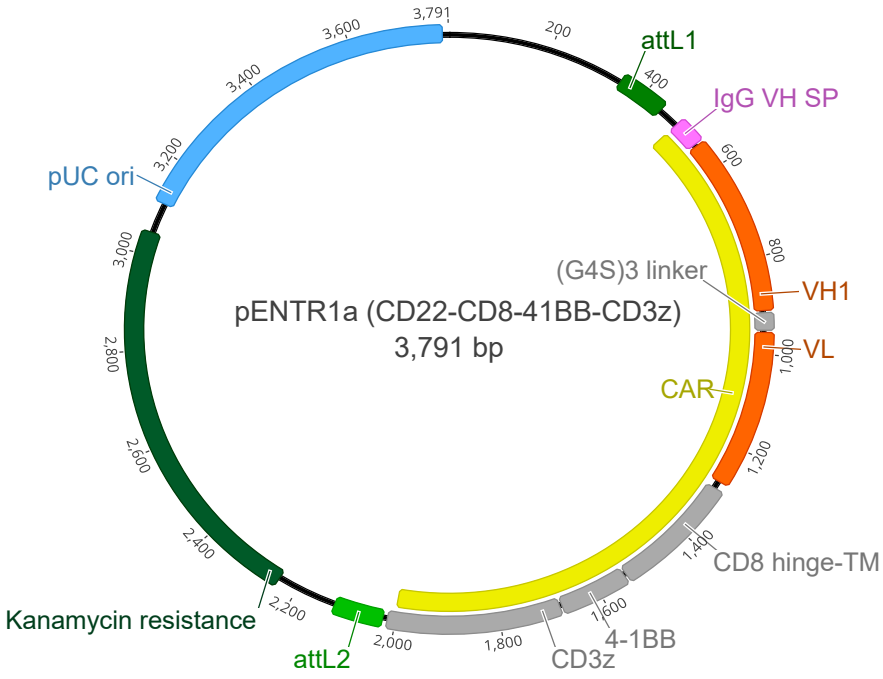

Figure 50. Map of the gateway entry vector pENTR1a (CD22-CD8-41BB-CD3z).

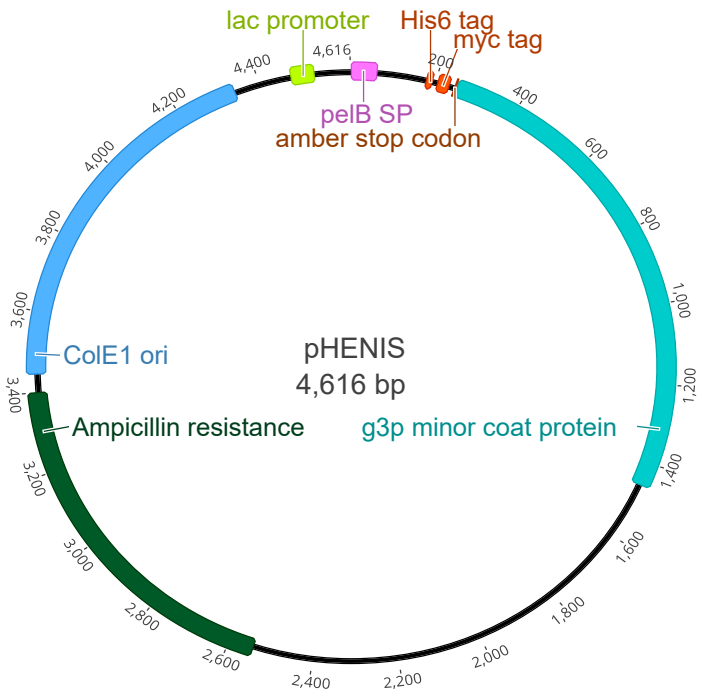

Figure 51. Map of the phagemid vector pHENIS.

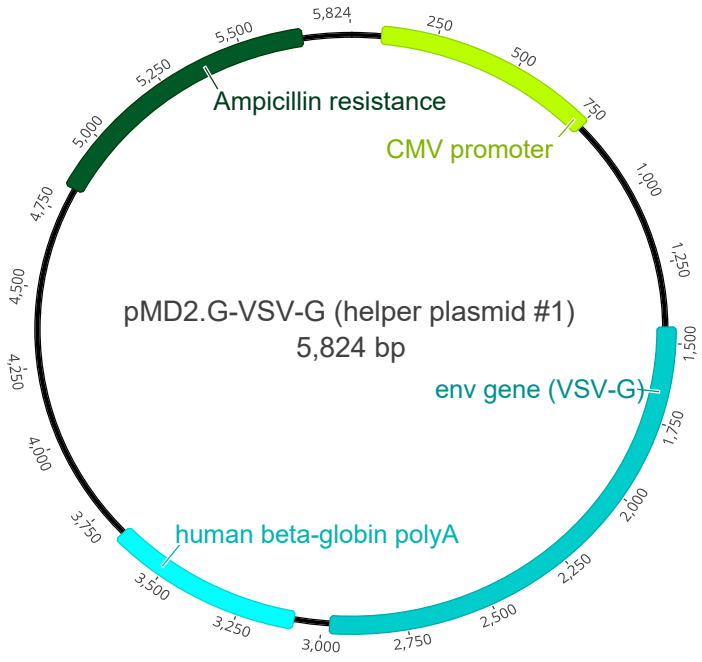

Figure 52. Map of the lentiviral helper plasmid pMD2.G-VSV-G (helper plasmid #1).

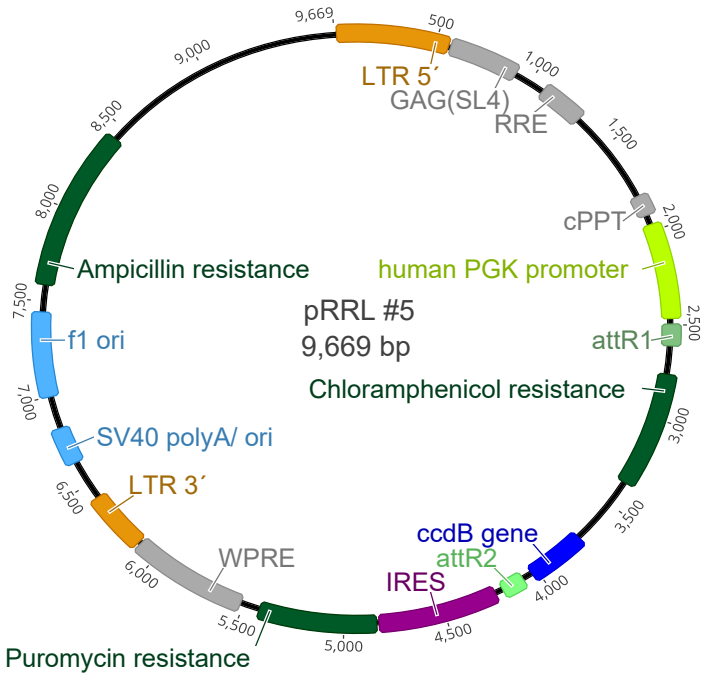

Figure 53. Map of the gateway destination vector pRRL#5.

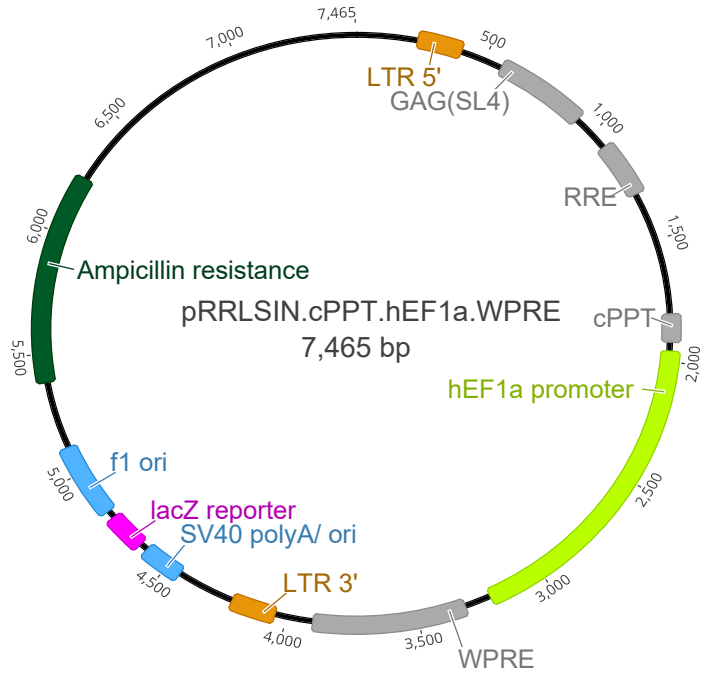

Figure 54. Map of the lentiviral vector pRRLSIN.cPPT.hEF1a.WPRE.

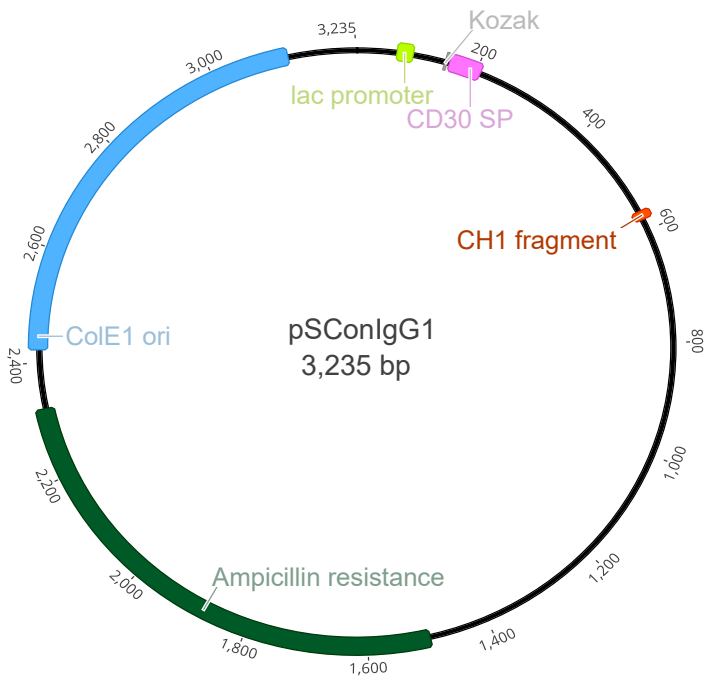

Figure 55. Map of the subcloning vector pSConIgG1.

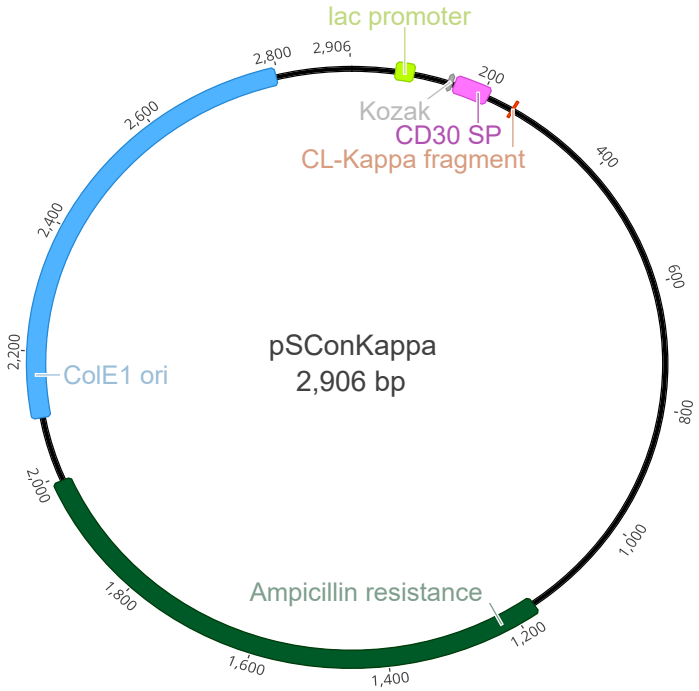

Figure 56. Map of the subcloning vector pSConKappa.

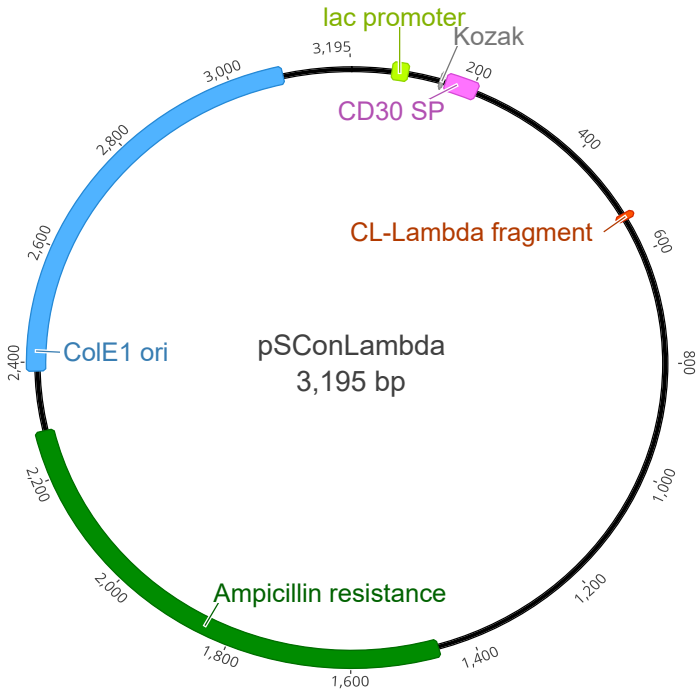

Figure 57. Map of the subcloning vector pSConLambda.

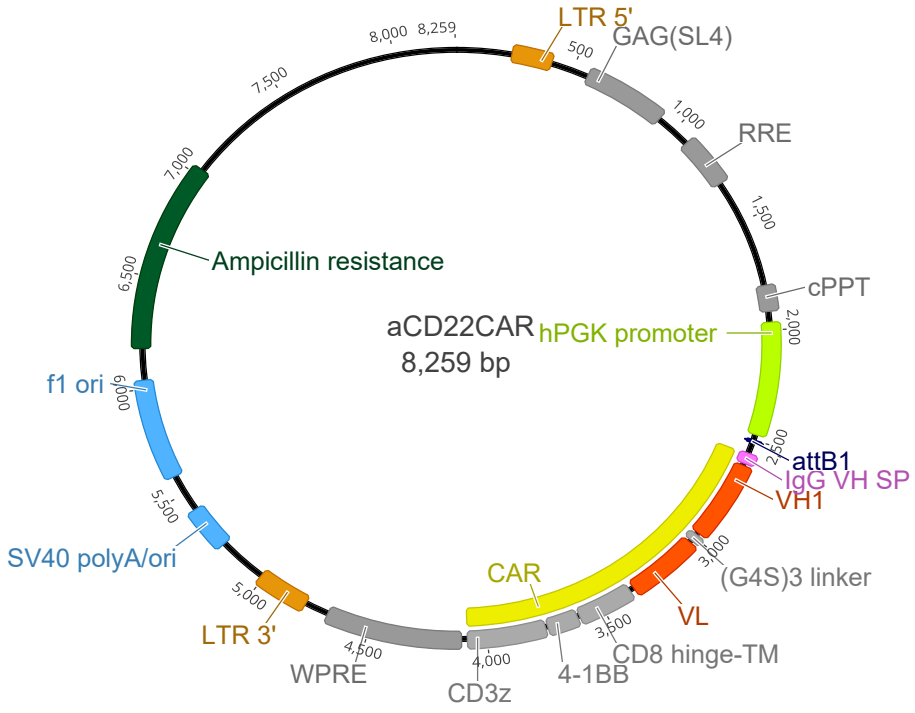

Figure 58. Map of the lentiviral vector encoding the anti-CD22 CAR.

6.3 List of figures

6.4 List of tables

7 Acknowledgements

I especially would like to express my gratitude to Dr. Michaela Arndt and Prof. Dr. Juergen Krauss for giving me the opportunity to perform my doctoral thesis in their group “Antibody-based Immunotherapeutics” at the NCT, Heidelberg. They continuously supported me with their scientific advice and guided me throughout my thesis.

My sincere thanks go to Dr. Rudolf Uebelhart for the supervision of my research project, scientific discussions and support.

Special thanks to my first examiner Prof. Dr. Peter Angel for the scientific guidance as member of my Thesis Advisory Committee and the evaluation of my doctoral thesis.

Furthermore, I thank our collaboration partners Prof. Dr. Stefan Duebel and Dr. Thomas Schirrmann (Yumab GmbH, Braunschweig), for providing us with phage display-derived antibody fragments.

Many thanks to Daniel Thomas, who successfully contributed to my research project in the course of his Master`s thesis.

I express my gratitude to all my former and current colleagues of the “Antibody-based Immunotherapeutics” group for the great atmosphere, teamwork and motivation. I really enjoyed our private (and work) related conversations.

I am especially grateful to Alex, Victoria, my parents, my brother and my friends for all their love, support and encouragement. Without you, I would not be the person I am today.